Theorical modelling and numerical simulation of compressible dense and dilute two-phase flows

Quentin Carmouze

UNIVERSITÉ CÔTE D'AZUR

ÉCOLE DOCTORALE
SCIENCES FONDAMENTALES ET APPLIQUÉES

THÈSE DE DOCTORAT

MODELISATION ET SIMULATION NUMERIQUE DES ECOULEMENTS DIPHASIQUES COMPRESSIBLES DENSES ET DILUES

Theoretical modelling and numerical simulation of compressible dense and dilute two-phase flows

Quentin CARMOUZE

Laboratoire de Mécanique et d'Acoustique, UMR CNRS 7031
Laboratoire J.A Dieudonné, UMR CNRS 7351

Présentée en vue de l'obtention du grade de docteur en Sciences Fondamentales Appliquées **d'Université Côte d'Azur**
Dirigée par : Pr. Boniface NKONGA**,** Pr. Richard SAUREL.
Soutenue le : 28/11/2019

Devant le jury, composé de :
Héloïse BEAUGENDRE (Rapporteur)
Dominique EYHERAMENDY (Examinateur)
Hervé GUILLARD (Examinateur)
Lazhar HOUAS (Examinateur)
Boniface NKONGA (Directeur)
Richard SAUREL (Co-directeur)
Eric SCHALL (Rapporteur)

RS2N

Aix*Marseille université
Initiative d'excellence

cnrs

MODELISATION ET SIMULATION NUMERIQUE DES ECOULEMENTS DIPHASIQUES COMPRESSIBLES DENSES ET DILUES

Theoretical modelling and numerical simulation of compressible dense and dilute two-phase flows

Rapporteurs

Héloïse BEAUGENDRE, Maître de Conférences – Bordeaux INP – Université de Bordeaux

Eric SCHALL, Maître de Conférences – UPPA – Université de Pau et du Pays de l'Adour

Examinateurs

Dominique EYHERAMENDY, PR ECM – Directeur du LMA – Ecole Centrale de Marseille

Hervé GUILLARD, Directeur de Recherche – INRIA – Sophia Antipolis

Lazhar HOUAS, Directeur de Recherche CNRS – IUSTI – Marseille

Directeurs

Boniface NKONGA, Professeur des universités – LJAD – Unice

Richard SAUREL, Professeur des universités – LMA – Aix-Marseille Université

Résumés et mots clés

Titre : Modélisation et simulation numérique des écoulements compressibles denses et dilués

Résumé (de 1700 à 4000 caractères espaces compris)

Cette thèse apporte quelques contributions et voies d'amélioration dans la modélisation et la simulation numérique d'écoulements diphasiques compressibles dans les régimes denses et dilués en particules.

Un nouveau modèle diphasique, hyperbolique dégénéré et thermodynamiquement consistant est construit. La nouveauté repose sur la reconsidération de l'équation sur la fraction volumique. Celle-ci implique des modifications majeures sur la propagation acoustique par rapport au modèle de Baer & Nunziato (1986) et semble plus physique par rapport à la topologie de l'écoulement.

Dans le but de résoudre de manière précise ce nouveau modèle, un solveur de Riemann avec reconstruction interne des états (RSIR) est construit, basé sur la méthode de Linde (2002). D'abord développée et améliorée dans le cadre des équations d'Euler, cette méthode est étendue au modèle diphasique dense – dilué hors d'équilibre développé précédemment. Ce nouveau modèle pose de sérieuses difficultés pour la recherche d'un solveur de Riemann, étant hyperbolique dégénéré et seulement valide dans le cadre de la relaxation raide des pressions (rendant les solutions non-autosimilaires). Grâce à l'approche avec reconstruction interne, un solveur de Riemann faiblement diffusif est développé. Cette nouvelle méthode numérique (RSIR) est utilisée pour résoudre une situation complexe d'instabilité de jets de particules solide dans un milieu granulaire et montre une explication plausible du processus de formation de ces instabilités ou jets de particules.

Dans la suite on s'intéresse à l'écoulement multidimensionnel qui se développe autour de quelques particules discrètes. Une méthode de type Level-Set est développée dans le but de décrire la translation de solides indéformables sur un maillage non-structuré fixe. Grâce à l'utilisation du limiteur de pente Overbee développé par Chiapolino et al. (2017) une méthode simple et robuste de couplage solide/fluide de type Ghost-Cell est construite, puis vérifiée. Cette approche, simple à développer permet une amélioration de la convergence de la méthode à l'aide de considérations également simples. La méthode est ensuite étendue en 2D et validée à l'aide de comparaisons dans le cadre d'un écoulement supersonique autour d'un objet cylindrique immobile. La méthode est ensuite étendue au cas du couplage fort, utilisé pour observer la mise en mouvement de plusieurs particules solides par onde de choc et la formation d'amas de particules.

Mots clés : écoulements diphasiques / dense – dilué / hyperbolique dégénéré / solveur de Riemann

Title: Theorical modelling and numerical simulation of compressible dense and dilute two-phases flows

Abstract (from 1700 to 4000 prints including spaces)

This thesis presents some contributions to the theoretical modelling and numerical simulation of compressible dense and dilute two-phase flows.

A new two-phase flow model is built, weakly hyperbolic and thermodynamically consistent. The novelty come from a modification of the volume fraction equation. It implies major consequences on the acoustic waves' propagation, compared to the Baer & Nunziato (1986) model, which seems more physical compared to the flow topology.

Numerical resolution of the new model is addressed through a new Riemann solver with internal reconstruction (RSIR) is built, based on the Linde (2002) method. First, this method is reconsidered and improved in the frame of the Euler equations. Then this method is extended to the new compressible dense and dilute two-phase flows model. This model poses serious difficulties as it is weakly hyperbolic and only valid in the limit of stiff pressure relaxation, implying non self-similar solutions. Thanks to the internal reconstruction approach, a low dissipative Riemann solver is built for the new model. The RSIR method is used to solve solid particles jet instabilities, showing possible explanation of their creation process.

Then a study on the multidimensional flow around some discrete particles is done. A Level-Set type method is developed to describe the translation of a rigid body on an unstructured mesh. Thanks to the Overbee limiter developed by Chiapolino et al., (2017) a simple and robust solid/fluid coupling method is built. This method is then extended to 2D and validated through comparisons in the frame of a supersonic flow around a static blunt body. Two-way coupling is then addressed to observe motion of particles induced by shock and creation of clusters.

Keywords: two-phase flows / dense and dilute / weakly hyperbolic / Riemann solver

À Jacques Carmouze,

Remerciements

Je tiens à remercier mon directeur de thèse le professeur Boniface Nkonga ainsi que mon codirecteur de thèse le professeur Richard Saurel pour ces trois années de travail et de partage. Ils m'ont transmis avec rigueur leur passion pour la modélisation et la simulation numérique dans le domaine de la mécanique des fluides. Durant ma thèse, ils sont restés disponibles malgré leurs obligations respectives, tout en me permettant de m'épanouir personnellement et professionnellement. Pour ces années, merci.

Je remercie également les docteurs Jeaniffer Vides, Alexandre Chiapolino, François Fraysse et Damien Furfaro ainsi que le futur docteur Lucas David pour leur accueil, leur gentillesse, leur aide et les nombreux échanges au sein de l'équipe.

Je souhaiterais aussi remercier l'ensemble du Laboratoire de Mécanique et d'Acoustique pour leur accueil.

Tout ceci a fait de ces trois années une aventure scientifique et humaine hors du commun, pour moi c'est sûr !

Je remercie Héloise Beaugendre et Eric Schall, tous deux maîtres de conférences et qui ont accepté de juger ce travail en tant que rapporteurs, ainsi que Dominique Eyheramendy, professeur et directeur du Laboratoire de Mécanique et d'Acoustique, Hervé Guillard, directeur de recherche et Lazhar Houas, directeur de recherche qui ont accepté de participer au jury.

Je tiens également à remercier le professeur Stéphane Fuentes du service de neurochirurgie de l'hôpital de la Timone pour son acte chirurgical salvateur sans lequel cette thèse n'aurait pu aboutir.

Ce travail représente l'aboutissement d'un cursus universitaire que je n'aurais pas pu faire sans l'aide et le soutient de ma famille. Merci énormément.

Enfin, je remercie ma compagne ainsi que tous mes proches pour avoir su, chacun à leur manière, me donner la force et le courage durant cette aventure.

Table of content

Table of Figures

Introduction Générale

Cette thèse porte sur la modélisation et la simulation numérique d'écoulements hétérogènes en régime dynamique. Ces écoulements sont étudiés dans des conditions extrêmes, notamment en présence d'ondes de choc. Cette thèse traite l'aspect théorique de la modélisation avec le développement d'un modèle diphasique dense-dilué capable de traiter un très large spectre de fractions volumiques, ainsi que l'aspect numérique avec le développement d'un solveur de Riemann adapté à ce modèle. Plus précisément, on s'intéresse dans cette thèse aux processus de mise en mouvement et de formation d'amas de particules solides ou liquides par interaction avec un fluide.

Motivation et contexte de l'étude

Dès l'apparition de la simulation numérique les communautés scientifiques et industrielles se sont intéressées aux problématiques de modélisation des écoulements diphasiques. Cet engouement s'explique par la nécessité de compréhension de phénomènes complexes et la réduction des coûts de développements des systèmes industriels par rapport aux approches basées sur des expériences uniquement.

Les écoulements multiphasiques se rencontrent dans de nombreuses problématiques industrielles et académiques, telles que la combustion, le génie chimique, la production d'énergie, les phénomènes naturels (mouvements des dunes, tsunamis, éruptions volcaniques, inondations…), les études de sûreté et beaucoup d'autres domaines. De plus, la quantité croissante des ressources informatiques permet d'envisager le traitement numérique de situations de plus en plus complexes. Pour ces raisons les communautés scientifiques cherchent à approfondir les performances des modélisations et des simulations existantes pour apporter des solutions aux situations réelles.

Le travail réalisé durant cette thèse est motivé par le soin d'amélioration des modèles et méthodes numériques dans les écoulements diphasiques hors d'équilibre. Un travail de recherche portant sur la modélisation et la simulation d'écoulements diphasiques compressibles denses et dilués a été effectué. Plus précisément, les phénomènes qui nous intéressent s'inscrivent dans le cadre des instabilités de

jets diphasiques, dont quelques exemples concrets sont la fragmentation dynamique de liquides et la dispersion de particules solides.

Les problèmes d'instabilités de jets diphasiques se rencontrent dans plusieurs secteurs. Pour le secteur de la Défense, ils se rencontrent dans l'explosion de charges entourées de particules (voir Figure 1), pour la conception par exemple de charges à effet de souffle renforcé mais également pour la prédiction des zones de concentration en agents nocifs dans les engins improvisés, et dans la destruction par ondes de choc d'amas liquides.

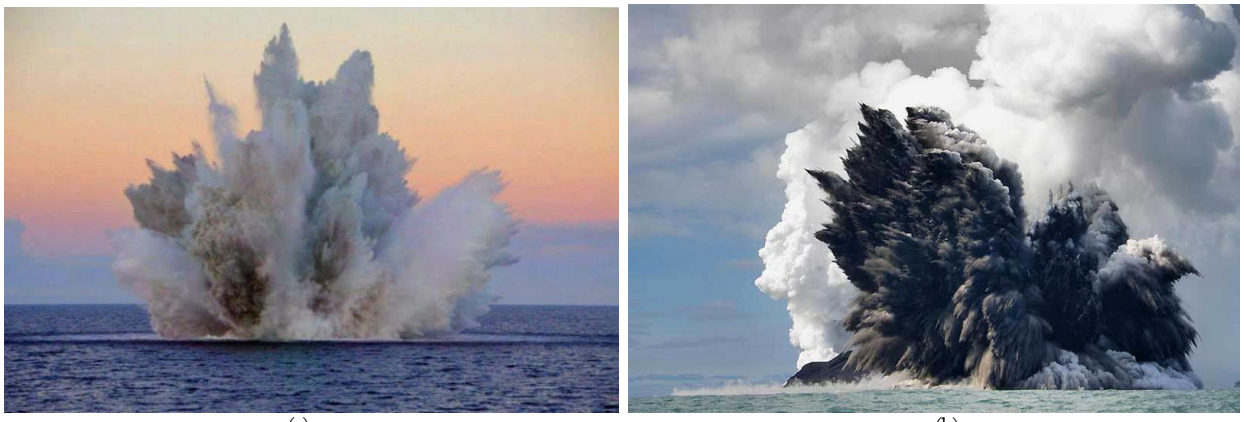

(a) (b)

Figure 1 – Observation du phénomène de dispersion de particules sous forme de « doigts » dans le cas d'explosions sous-marines. Cas (a) : dispersion de gouttes d'eau liquide lors d'une explosion sous-marine. Cas (b) : dispersion d'un mélange de particules de cendre et de gouttes d'eau liquide lors d'une éruption volcanique sous-marine.

Dans le secteur civil, ils se rencontrent dans la quasi-totalité des moteurs thermiques qui utilisent des combustibles liquides. L'efficacité de la combustion et donc du rendement énergétique, ainsi que les émissions de polluants, sont en effet fonction directement de la qualité du mélange combustible – comburant (voir Figure 2).

De ce fait, les applications potentielles du présent projet de recherche sont nombreuses, du secteur des Transports à l'Aéronautique et à l'Espace.

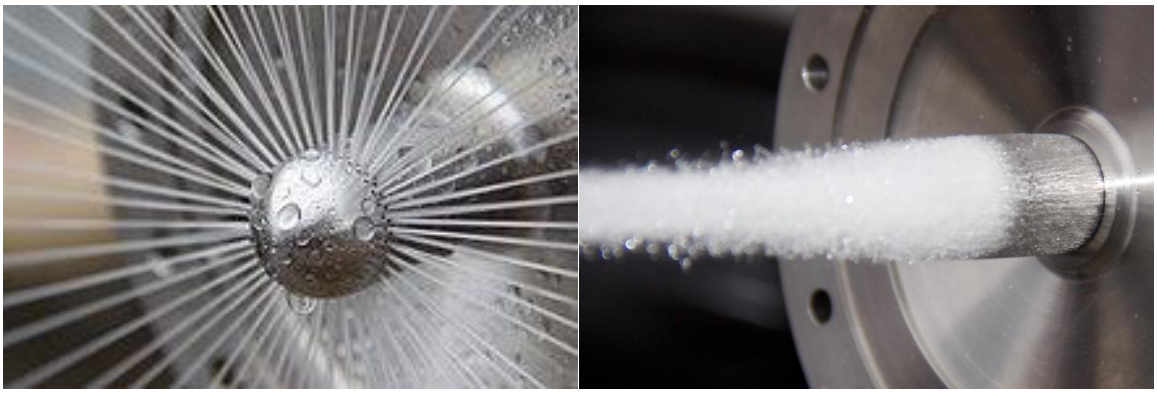

Figure 2 – Deux exemples de géométries de systèmes d'injection pour moteurs thermiques, utilisés dans l'industrie. L'écoulement en sortie de l'injecteur est un jet de combustible (dans un milieu confiné) qui se fragmente en s'éloignant de la source d'injection.

Pour modéliser ces phénomènes, deux types d'approches sont couramment employées :

- L'approche Lagrangienne où chaque particule ou macro particule est suivie dans l'espace et dans le temps.
- L'approche continue où l'ensemble des particules est décrit par un modèle Eulérien d'équations au dérivées partielles.

L'approche qui est préférée ici est la seconde : nous choisissons de modéliser les écoulements denses et dilués par une méthode Eulérienne. La première approche a été étudiée dans la littérature et donne des résultats satisfaisants, mais exige une puissance de calcul importante. En effet, si on considère un problème de fragmentation de jet diphasique, la première approche nécessiterait de suivre une quantité très importante de particules ou macro particules. Numériquement, cela engendre des calculs longs, et par conséquents couteux. Des difficultés apparaissent également dans le couplage dans l'écoulement « continu », entre un liquide pur et un gaz pur, séparés par des interfaces, et le brouillard qui apparait ensuite. Pour ces raisons, on choisit de modéliser ces écoulements denses et dilués par un modèle Eulérien qui sera résolu sur une grille fixe.

Modélisation des écoulements denses et dilués

Les écoulements diphasiques font toujours l'objet d'études approfondies. Cela se traduit par l'existence de plusieurs modèles diphasiques hors d'équilibre. Dans certaines situations, une phase lourde (liquide, solide) est dispersée au sein d'une autre phase continue, souvent un gaz. A l'opposé, on rencontre également des situations ou des bulles de gaz sont dispersées dans un liquide.

Dans la limite dense, les particules sont en contact les unes avec les autres. Un modèle compressible diphasique à 7 équations comprenant 6 ondes a été développé par Baer & Nunziato (1986) dénoté BN pour la suite. Une version alternative du modèle de BN à 7 ondes a été développée par Abgrall et Saurel (2003), Saurel et al., (2003). Ce modèle est hyperbolique et respecte la seconde loi de la thermodynamique. La symétrie du modèle facilite la résolution du problème de Riemann (voir aussi Ambroso et al., 2012) ainsi que l'extension de la formulation à un nombre arbitraire de phases. Ce modèle est utilisé pour un grand nombre de situations dans le cadre d'ondes de détonations dans les explosifs hétérogènes (Chinnayya et al., 2004) ou de chocs en milieux multiphasiques (Saurel et al., 2007) ou encore la combustion de milieux granulaires (Saurel et al., 2014 ; Saurel et al., 2017).

Dans la limite diluée les particules (gouttes de liquide, particules solides ou bulles de gaz) deviennent éloignées les unes des autres et ne sont plus en mesure de propager les ondes de pression (voir Figure 3). Cependant, le modèle de BN ne tient pas compte de cette particularité.

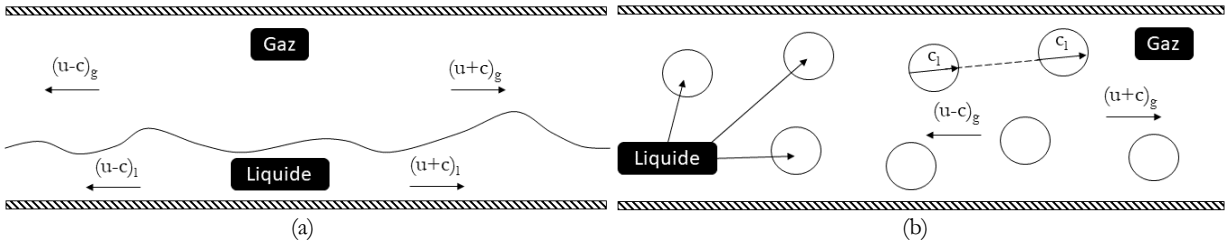

Figure 3 – Schématisation de la propagation des ondes dans deux mélanges diphasiques. Dans le mélange présenté en (a) les deux phases, liquide et gazeuse sont continues. Ainsi, les deux phases propagent les ondes de pressions. Dans le mélange présenté en (b) des gouttes de liquides sont dispersée au sein du gaz. Ainsi, le gaz propage les ondes de pressions mais le liquide ne peut pas les propager. En termes de modélisation, cela signifie que le modèle de BN est utilisable dans le cas (a) mais n'est plus adapté pour résoudre une situation telle que schématisée dans (b).

Ce problème a été clairement identifié par Lhuillier et al., (2013), et rend le modèle de BN discutable pour des situations où une des phases est dispersée. La phase continue propage les chocs, les détentes et les ondes de contact tandis que la phase dispersée ne devrait pas propager le son. Dans la limite des très faibles concentrations de la phase dispersée le modèle de Marble (1963) respecte ces propriétés acoustiques. Ce modèle correspond aux équations d'Euler avec des termes sources pour la phase gazeuse, et une équation de quantité de mouvement sans pression pour la phase dispersée (particules) (voir aussi Zeldovich, 1970). Ce modèle est hyperbolique, respecte la seconde loi de la thermodynamique et comprend 4 ondes. Ce modèle a été grandement utilisé et donne de très bons

résultats, dans la mesure où la phase condensée reste diluée, soit pour une fraction volumique des particules inférieure au pourcent.

Cependant, aucun modèle existant assure la transition d'un écoulement dense vers un écoulement dilué en particulier vis-à-vis de la propagation des ondes de pression, couvrant ainsi toute la gamme de fraction volumiques. Ce problème est important lorsque l'on souhaite traiter tout le spectre de fractions volumiques, du liquide pur au gaz pur, en passant par des mélanges diphasiques denses et dilués. Ce type de problématique se rencontre par exemple dans l'atomisation et la fragmentation d'un jet de liquide dans un gaz. L'approche qui est habituellement considérée dans ces problèmes consiste à utiliser un modèle mono-vitesse (reposant souvent sur un modèle de fluide incompressible) dans la phase de fragmentation primaire, puis de poursuivre la simulation par un modèle Eulérien ou Lagrangien à deux vitesses, celle du gaz et celle des gouttes. Autrement dit, la modélisation de la fragmentation primaire (avant laquelle deux fluides distincts : le liquide et le gaz sont denses) nécessite un modèle à une vitesse alors que la fragmentation secondaire (après laquelle la phase liquide se retrouve très dispersée) nécessite l'utilisation d'un modèle à deux vitesses (voir Figure 4). En effet, le changement d'échelle entre les différentes tailles de goutes fragmentées, initiales et finales, varie de plusieurs ordres de grandeur, rendant impossible la poursuite de la simulation avec un modèle mono-vitesse.

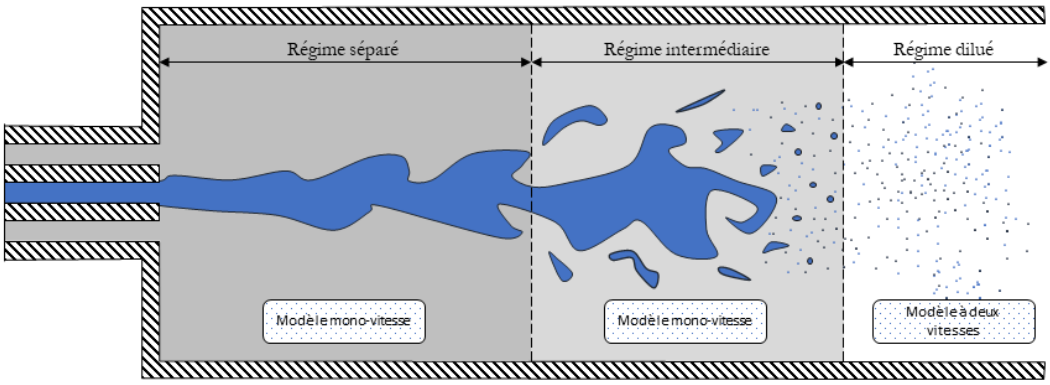

Figure 4 – Schématisation des différents régimes du mélange diphasique liquide-gaz rencontrés lors de l'atomisation d'un jet de liquide.

Deux faiblesses se dégagent de ces modélisations : premièrement la continuité de la modélisation n'est pas satisfaite. Cette faiblesse se traduit par une discontinuité du volume occupé par les phases au niveau du changement de modélisation, oubliant brutalement le volume occupé par le liquide. De plus,

la transition entre le modèle mono-vitesse et le modèle à deux vitesses est elle aussi discutable, puisque généralement arbitraire. La communauté scientifique est alors en recherche d'une modélisation adaptée à la transition de tels écoulements.

Sans prétendre résoudre le problème de la transition d'un modèle à une vitesse vers un modèle à deux vitesses dans un milieu dispersé, on offre une piste de réflexion permettant la considération des deux limites et s'affranchissant ainsi du problème apporté par la discontinuité du volume occupé par les phases lors du couplage. Le modèle qui a été développé respecte les propriétés acoustiques discutées ci-dessus. Basé sur le modèle de BN, le nouveau modèle contient 7 équations. Il comprend 4 ondes, ce qui le rapproche du modèle de Marble, tout en permettant le traitement de problèmes à interface entre fluides. Il respecte les propriétés acoustiques du modèle de Marble dans la limite diluée et tend vers le modèle de Kapila et al., (2001) dans la limite de la relaxation raide des pressions et des vitesses, permettant ainsi le traitement de problèmes à interfaces entre fluides. Liant de manière continue les deux limites, il permet d'envisager des situations telles que les instabilités de jets diphasiques, et notamment les cas sévères d'explosion de charges entourées de particules (voir Figure 5).

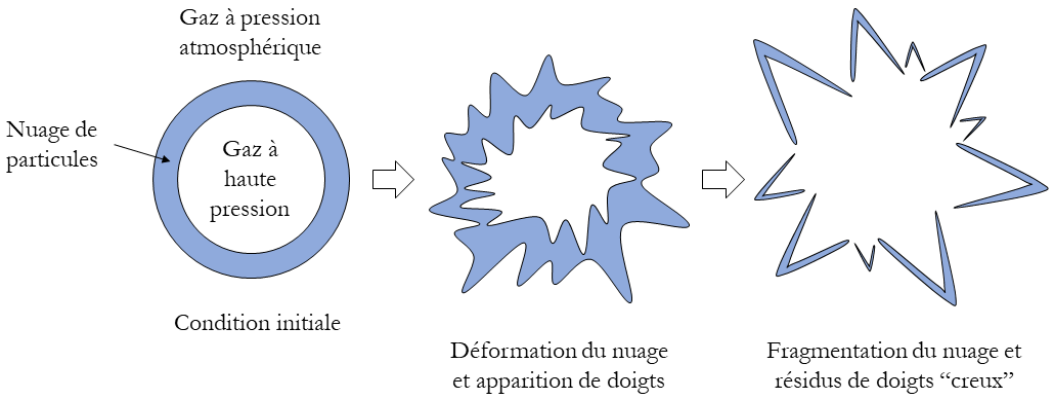

Figure 5 – Schématisation des différents états du nuage de particules au cours d'une explosion. A l'instant initial, la configuration est celle d'un « tube à choc cylindrique ». A t=0s, le gaz va se mettre en mouvement et entrainer les particules dans des zones préférentielles et on observe l'apparition de doigts ou jets de particules. Au fur et à mesure que l'instabilité s'installe, le nuage se fragmente et des doigts de particules remplis de gaz sont formés.

Afin de pouvoir observer au moins qualitativement les phénomènes ayant lieux dans ces problèmes d'instabilités de jets diphasiques, la modélisation est importante, tout comme la méthode numérique. Un schéma numérique adapté au nouveau modèle dense-dilué doit être développé.

Méthodes numériques

Beaucoup de méthodes numériques sont actuellement référencées dans la littérature. La plupart du temps pour les modèles diphasiques, ces solveurs numériques sont des extensions des solveurs développés dans le cas monophasique des équations d'Euler. Les systèmes considérés étant hyperboliques, il est alors nécessaire de résoudre le problème de Riemann sur chaque bord de maille. Par exemple pour le modèle BN un solveur de type HLLC (Toro et al., 1994) a été développé dans Tokareva and Toro (2010), une autre version étant développée dans Furfaro and Saurel (2017).

Pour les modèles diphasiques, de nombreuses ondes caractéristiques sont présentes comme c'est le cas par exemple dans la magnétohydrodynamique (MHD).

Des différences fondamentales apparaissent cependant. En effet, dans la MHD les modèles développés sont conservatifs. La résolution du problème de Riemann peut être alors conduite par une approche type Rusanov (1961) ou HLL (Harten et al., 1983) par exemple comme cela été réalisé dans Gurski (2004) ou encore Balsara et al. (2014). Dans le cas du nouveau modèle, cinq équations sont non-conservatives : l'équation de la fraction volumique des particules, et les équations du mouvement et de l'énergie totale des deux phases. La gestion des termes non-conservatifs est alors importante, et cela représente un problème à surmonter dans le cas du nouveau modèle. Ce point est traité grâce à une formulation conservative locale.

Une autre différence fondamentale émerge entre ces deux domaines. Dans la MHD, les systèmes d'équations sont strictement hyperboliques, c'est-à-dire que les valeurs propres de la Jacobienne du système sont distinctes, ce qui permet la détermination de relations de passages au travers de ces ondes (voir Figure 6). Dans le cadre du nouveau modèle dense-dilué développé dans cette thèse, la vitesse de la phase dispersée est valeur propre multiple, ce qui rend ce modèle hyperbolique dégénéré (Figure 6). La recherche d'un solveur approché de Riemann devient alors difficile.

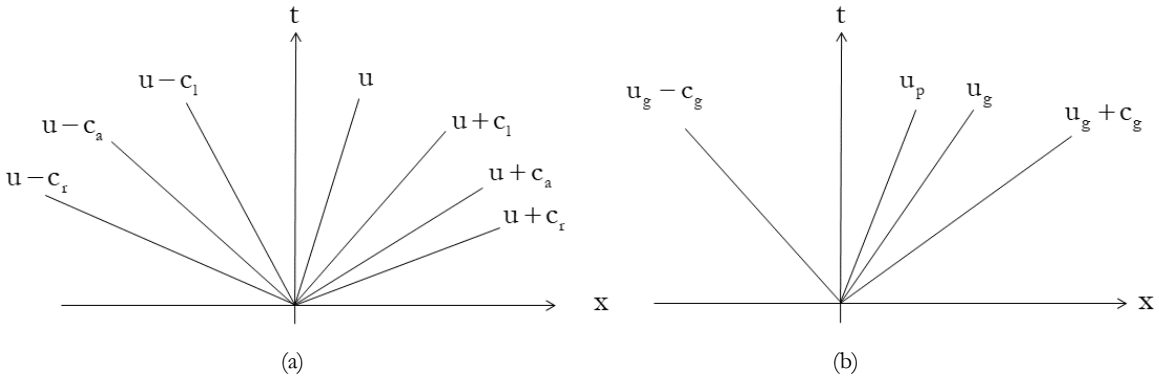

Figure 6 – Représentation en diagramme (x,t) des configurations d'ondes dans le problème de Riemann dans le cas d'un problème de MHD (a) et dans le cas du nouveau modèle dense-dilué (b).

Le diagramme (x,t) présenté en (a) est tiré de Li, S. (2005) : les ondes indicées « a », « r » et « l » correspondent respectivement à des ondes de Alfvèn, des ondes magnéto-acoustiques rapides et lentes. Dans ce problème de MHD, toutes les vitesses d'ondes sont distinctes. Dans le cas du nouveau modèle dense-dilué, la vitesse d'onde u_P est valeur propre multiple.

La vitesse des particules étant valeur propre multiple, la détermination d'un ensemble de relations permettant la détermination des états intermédiaires du problème de Riemann n'est pas possible. Cette difficulté est amplifiée par la présence d'un terme de relaxation des pressions raide, indispensable à la validité du modèle, et conduisant à des solutions non-autosimilaires. Ce problème est important et reste à surmonter.

Les tentatives d'écriture d'un solveur adapté au nouveau modèle dense-dilué basées sur une méthode de type HLLC ont échoués pour les raisons décrites ci-dessus. La recherche d'une méthode numérique s'est alors orientée vers une méthode à « reconstruction interne » des états. Le but de cette démarche est de créer deux états intermédiaires dans le problème de Riemann au lieu d'un seul. Un exemple d'un tel solveur est celui de Linde (2002) basant la reconstruction de deux états intermédiaires à partir de l'approximation HLL pour les équations d'Euler. Ce solveur est reconsidéré et amélioré dans le cas des équations d'Euler. Il est ensuite étendu au modèle diphasique à l'aide de considérations physiques.

Plan du manuscrit

Le manuscrit est organisé de la façon suivante.

Le premier chapitre présente la construction d'un nouveau système d'équation pouvant être considéré comme une variante du modèle BN, du fait de la reconsidération de l'équation sur la fraction volumique. Dans le modèle BN, l'équation sur la fraction volumique est une équation de transport :

$$\frac{\partial \alpha_p}{\partial t} + \overrightarrow{u_p}.\vec{\nabla}\alpha_p = 0 .$$

Dans le cadre du nouveau modèle cette équation devient conservative :

$$\frac{\partial \alpha_p}{\partial t} + \vec{\nabla}.\left(\alpha_p \overrightarrow{u_p}\right) = 0 .$$

Ce changement mineur, justifié dans ce chapitre, a des conséquences majeures sur la considération de la propagation des ondes acoustiques. Un premier modèle est ainsi obtenu. Ce modèle est hyperbolique dégénéré et thermodynamiquement consistant dans la limite de la relaxation raide des

pressions. Les valeurs propres de la Jacobienne du nouveau système sont identiques à celles de la Jacobienne du système de Marble : $\lambda_{1\to4} = u_p$; $\lambda_5 = u_g$; $\lambda_6 = u_g - c_g$; $\lambda_7 = u_g + c_g$, et très différentes de celles du système BN qui en comprend 7.

En considérant la situation inverse de bulles de gaz dispersées dans un liquide un modèle symétrique est également obtenu avec une autre équation sur la fraction volumique :

$$\frac{\partial \alpha_g}{\partial t} + \vec{\nabla}.\left(\alpha_g \overrightarrow{u_g}\right) = 0 \ .$$

Pour le modèle symétrique, la Jacobienne du système a également 4 valeurs propres, mais différentes du premier : $\lambda_{1\to4} = u_g$; $\lambda_5 = u_p$; $\lambda_6 = u_p - c_p$; $\lambda_7 = u_p + c_p$.

Un modèle englobant les deux cas limites est alors construit, la bascule étant basée sur une « limite de fluidisation ». Ce modèle contient 6 ondes mais en comporte seulement 4 en un point donné de l'espace.

La validation du modèle est réalisée à l'aide de cas tests 1D : transport d'une discontinuité, tube à chocs quasi-monophasiques, tube à chocs diphasique et résultats expérimentaux de Rogue et al., (1998) pour la mise en mouvement d'un lit de particules par onde de choc. Ces simulations sont réalisées à l'aide d'un solveur de Riemann rudimentaire qui est celui de Rusanov.

Le deuxième chapitre de cette thèse présente un solveur approché de Riemann, adapté au modèle précédemment développé. La résolution de ce modèle présente quelques difficultés :

- L'équation sur la fraction volumique des particules, ainsi que les équations de quantité de mouvement et d'énergie de chaque phase sont non-conservatives ;
- Le caractère multi-évalué de la solution (Saurel et al., 1994) rend la détermination des états intermédiaires problématique ;
- La présence des termes de relaxation raide des pressions, nécessaires à la validité du modèle implique des solutions dépendantes du temps, non-autosimilaires.

Ces problèmes représentent des difficultés majeures pour la recherche d'un solveur de Riemann approché de type HLLC. Le caractère non-conservatif des équations est contourné au moyen d'une formulation conservative locale. Plusieurs tentatives d'écriture d'un solveur ont été entreprises, en se basant d'abord sur les relations de passage de la phase dense, les conditions de sauts de la phase dispersée et aussi sur l'approximation HLLC, sans donner de résultats concluants. La recherche du solveur de Riemann est alors conduite vers une approche avec reconstruction interne : un état

intermédiaire moyennée est calculé (par exemple par HLL ou Rusanov) puis cette solution est reconstruite à l'aide d'une paramétrisation effectuée sur chaque variable conservative. Des travaux dans ce sens ont été entrepris par Linde (2002) et Miyoshi and Kusano (2005). Dans le cas des équations d'Euler, un solveur est développé et montre des résultats similaires à ceux obtenus avec HLLC. Cette approche est donc poursuivie pour le nouveau modèle diphasique. Testé sur de nombreux cas 1D, ce solveur dénoté RSIR (*Riemann Solver with Internal Reconstruction*) présente des résultats satisfaisants. En effet, le solveur est maintenant capable de préserver une discontinuité de fraction volumique immobile, ce qui n'est pas possible avec un solveur de type Rusanov ou HLL. Ce nouveau solveur permet notamment d'étudier et de résoudre des problèmes de formation de doigts de particules (Figure 1). En effet, beaucoup de résultats expérimentaux ont été obtenus montrant le processus de formation des instabilités dans les jets diphasiques : Rodriguez et al., (2013), McGrath et al., (2018), Osnes et al., (2018) et Xue et al., (2018) parmi tant d'autres. L'implémentation en 2D du solveur RSIR dans le code non structuré DALPHADT de la société RS2N permet de résoudre des cas d'explosions sphériques en milieux granulaires et d'obtenir les premiers résultats numériques de formation de doigts de particules, qualitativement en accord avec les résultats expérimentaux.

Le troisième chapitre de cette thèse présente une approche discrète du problème de dispersion de particules solides dans un mélange multiphasique, afin de caractériser la formation de cluster de particules. Le modèle résolu dans cette partie est le modèle d'Euler multi-constituant (appelé UPT car en équilibre de vitesses, de pressions et de températures).

Dans cette approche, une particule solide est modélisée et suivie à l'aide d'une fonction Level-Set. Cette étude traite principalement du couplage hydrodynamique ayant lieu à l'interface solide/fluide. Utilisant une approche de type Ghost-Cell développée par Fedkiw et al., (1999), une méthode simple robuste et précise de couplage solide/fluide est développée sur des maillages non-structurés. Cette méthode est validée en 1D à l'aide de cas tests élémentaires dont les résultats numériques ont été comparés aux solutions exactes. L'extension de cette méthode en 2D est également étudiée, nécessitant des considérations supplémentaires dans la direction tangentielle à l'interface notamment.

La méthode permet de considérer des cas tests de mise en mouvement d'un ensemble de particules solides par onde de choc et d'observer qualitativement la formation de clusters due à la mise en mouvement des particules discrètes.

Valorisation de la thèse – Liste des publications de l'auteur

Publications by the author

Saurel, R., Chinnayya, A. & Carmouze, Q. (2017) Modelling compressible dense and dilute two-phase flows. *Physics of Fluids*, 29(6), 063301

Carmouze, Q., Fraysse, F., Saurel, R. & Nkonga, B. (2018) Coupling rigid bodies motion with single phase and two-phase compressible flows on unstructured meshes . *Journal of Computational Physics*, 375, 1314-1338

Carmouze, Q., Saurel, R., Chiapolino, A. & Lapebie, E. (2019) Riemann solver with internal reconstruction (RSIR) for compressible single-phase and non-equilibrium two-phase flows. *Journal of Computational Physics (minor revisions)*

Chapter I

Modelling compressible dense and dilute two-phase flows

This chapter focuses on the building of a compressible flow model to address both dense and dilute regimes. Existing flow models of Marble (1963) and Baer & Nunziato (1986) in these limits are first recalled.

The new model is then derived on the basis of a new volume fraction equation, in conservative form with stiff pressure relaxation. Being weakly hyperbolic and thermodynamically consistent, it is validated in 1D thanks to a dissipative but robust numerical method.

The new model and its symmetric alternative are generalized into a single formulation. The general model is able to solve flows in both limits of dispersed droplets particles in a gaz and dispersed bubbles particles in a liquid. It is validated in 1D thanks to exact solutions and experimental results.

Abstract

Many two-phase flow situations, from engineering science to astrophysics, deal with transition from dense (high concentration of the condensed phase) to dilute concentration (low concentration of the same phase), covering the entire range of volume fractions. Some models are now well accepted at the two limits, but none is able to cover accurately the entire range, in particular regarding waves propagation. In the present work an alternative to the Baer & Nunziato (BN) model (1986), initially designed for dense flows, is built. The corresponding model is hyperbolic and thermodynamically consistent. Contrarily to the BN model that involves 6 wave speeds, the new formulation involves 4 waves only, in agreement with the Marble model (1963) based on pressureless Euler equations for the dispersed phase, a well-accepted model for low particle volume concentrations. In the new model, the presence of pressure in the momentum equation of the particles and consideration of volume fractions in the two phases render the model valid for large particle concentrations. A symmetric version of the new model is derived as well for liquids containing gas bubbles. This model version involves 4 characteristic wave speeds as well, but with different velocities. Last, the two sub-models with 4 waves are combined in a unique formulation, valid for the full range of volume fractions. It involves the same 6 wave's speeds as the BN model, but at a given point of space 4 waves only emerge, depending on the local volume fractions. The non-linear pressure waves propagate only in the phase with dominant volume fraction. The new model is tested numerically on various test problems ranging from separated phases in a shock tube to shock – particle cloud interaction. Its predictions are compared to BN and Marble models as well as against experimental data showing clear improvements.

I.1 – Introduction

It is well accepted that hyperbolic models are mandatory to deal with phenomena involving wave propagation. This is the case for multiphase flow mixtures in many situations such as in particular shocks and detonations propagation in granular explosives and in fuel suspensions, as well as liquid-gas mixtures with bubbles, cavitating and flashing flows, as soon as motion is intense and governed by pressure gradients. This is thus the case of most unsteady two-phase flow situations.

Wave propagation is important as it carries pressure, density and velocity disturbances. Sound propagation is also very important as it determines critical (choked) flow conditions and associated mass flow rates. It has also fundamental importance on sonic conditions of detonation waves when the two-phase mixture is exothermically reacting (Petitpas et al., 2009).

Hyperbolicity is also related to the causality principle, meaning that initial and boundary conditions are responsible of time evolution of the solution. When dealing with first-order partial differential equations it means that the Riemann problem must have a solution, and the Riemann problem is correctly posed only if the equations are hyperbolic.

However, only a few two-phase flow models are hyperbolic in the whole range of parameters. The Baer and Nunziato (1986) model seems to be the only formulation able to deal with such requirement. Its symmetric extension (Saurel et al., 2014) facilitates the Riemann problem resolution as the corresponding model involves 7 wave's speeds (instead of 6 in the original version). See also Ambroso et al. (2012) for similar conclusions.

However, in the dilute limit at least, the acoustic properties of this model seem inconsistent (Lhuillier et al., 2013). Indeed with this model, the dispersed phase sound speed corresponds to the one of the pure phase, while this phase is not continuous and unable to propagate sound in reality, at least at a scale larger than particle's one. When the phase is not continuous (dispersed drops in a gas, dispersed bubbles in a liquid), the associated sound speed should vanish, such effect being absent in the formulation.

In the low particles concentration limit, the Marble (1963) model is preferred. This model corresponds to the Euler equations with source terms for the gas phase and pressureless gas dynamic equations for the particle phase (see also Zeldovich, 1970). This model is thermodynamically consistent and hyperbolic as well, except that the particle phase equations are hyperbolic degenerate. In this model, contrarily to the BN model, sound doesn't propagate in the particles phase, this behaviour being more physical in this limit. However, the Marble model has a limited range of validity as the volume of the dispersed phase is neglected, this assumption having sense only for low (less than per cent) condensed phase volume fraction.

There are thus fundamental differences between these two models:

- The volume occupied by the condensed phase is considered in BN while it is neglected in the dilute model, restricting its validity to low dispersed phase volume fractions.
- Condensed phase compressibility is considered in BN while incompressible particles are assumed in the dilute formulation.
- Acoustic properties of the BN model are well accepted in the dense domain but seem inappropriate in the dilute limit.

Even if these two models can be used in the entire space of two-phase flow variables without yielding computational failure (this is characteristic of thermodynamically consistent hyperbolic models)

validity of their results is questionable when they are used out of their range of physical validity. This issue has been clearly understood in Lhuillier et al. (2013), McGrath et al. (2016) and Houim and Oran (2016) where various attempts to build new formulations are reported. In Lhuillier et al. (2013) discussion on the volume fraction equation is done, but no explicit flow model is given. In McGrath et al. (2016) a model is given with conditional hyperbolicity. The same issue is present with different cause in Houim and Oran (2016).

The aim of the present paper is to build an alternative to the BN model with improved acoustic properties, while remaining unconditionally hyperbolic and thermodynamically consistent.

The new model is derived from number density and particle radius (or bubble radius) evolution equations resulting in a volume fraction evolution equation expressed in conservation form with pressure relaxation. Replacing the transport equation in the conventional balance equations of mass, momentum and energy of the phases has dramatic influence on wave's propagation and structure of the equations.

The paper is organised as follows. The well-known BN and Marble models are recalled in Section II to present the main alternatives of existing two-phase hyperbolic models. Derivation of the volume fraction equation of the new model is addressed in Section 3. The new model is then derived in Section 4 and its hyperbolicity demonstrated. Its compatibility with the model of Kapila et al. (2001) is demonstrated as asymptotic limit of the new model, in the limit of stiff mechanical relaxation. Computed results are then examined in Section 5, compared to exact and experimental solutions when available. A symmetric variant of the new flow model, aimed to model bubbly liquids, is considered and tested in the same section. A general model, aimed to address the full spectrum of volume fractions is then derived in Section 6. Conclusions are given in Section 7.

I.2 – Well-known limit models of two-phase flows

Two hyperbolic models are widely used in the two-phase flow literature and their main characteristics are recalled hereafter.

I.2.a) BN type model (1986)

The Baer and Nunziato (1986) model is recalled hereafter, in the absence of granular effects ('configuration' pressure and energy) as well as heat and mass transfers. Mechanical relaxation effects only are considered in addition to waves' dynamics. A variant of this model is available as well in Romenski and Toro (2004), where a conservative formulation is obtained.

The symmetric variant of Saurel et al. (2003) is presented hereafter rather than the original BN. The evolution equations for phase 1 read,

$$\frac{\partial \alpha_1}{\partial t} + u_I \frac{\partial \alpha_1}{\partial x} = \mu(p_1 - p_2)$$

$$\frac{\partial (\alpha\rho)_1}{\partial t} + \frac{\partial (\alpha\rho u)_1}{\partial x} = 0 \qquad \text{(I.2.1)}$$

$$\frac{\partial (\alpha\rho u)_1}{\partial t} + \frac{\partial (\alpha\rho u^2 + \alpha p)_1}{\partial x} = p_I \frac{\partial \alpha_1}{\partial x} + \lambda(u_2 - u_1)$$

$$\frac{\partial (\alpha\rho E)_1}{\partial t} + \frac{\partial (\alpha(\rho E + p)u)_1}{\partial x} = p_I u_I \frac{\partial \alpha_1}{\partial x} + \lambda u_I'(u_2 - u_1) - \mu p_I'(p_1 - p_2)$$

The evolution equations of the second phase are,

$$\frac{\partial (\alpha\rho)_2}{\partial t} + \frac{\partial (\alpha\rho u)_2}{\partial x} = 0 \qquad \text{(I.2.2)}$$

$$\frac{\partial (\alpha\rho u)_2}{\partial t} + \frac{\partial (\alpha\rho u^2 + \alpha p)_2}{\partial x} = p_I \frac{\partial \alpha_2}{\partial x} - \lambda(u_2 - u_1)$$

$$\frac{\partial (\alpha\rho E)_2}{\partial t} + \frac{\partial (\alpha(\rho E + p)u)_2}{\partial x} = p_I u_I \frac{\partial \alpha_2}{\partial x} - \lambda u_I'(u_2 - u_1) + \mu p_I'(p_1 - p_2)$$

The following definitions and notations are used:

- α_k, ρ_k, u_k, E_k, p_k denote respectively the volume fraction, material density, velocity, total energy and pressure of the phase k (k=1,2).

- The total energy of the phases reads, $E_k = e_k + \frac{1}{2} u_k^2$.

- The pressures are given by convex equations of state of the form $p_k = p_k(\rho_k, e_k)$.

- The velocities relax each other to a common equilibrium one at a rate controlled by λ, modelled by conventional drag force correlations and specific interfacial area.

- The pressure relax each other to a common equilibrium one at a rate controlled by μ.

Estimates for this relaxation parameter are given in the references above: $\mu = \frac{A_I}{Z_1 + Z_2}$,

where A_I represents the interfacial exchange area. The specific interfacial area is given by

$A_I = \frac{3\alpha_1}{R_1}$ if phase 1 represents the dispersed phase made of particles or bubbles of radius R_1.

Obviously, more sophisticated models of interfacial area are possible.

- The interfacial variables are estimated by,

$$u_I = u_I' + \mathrm{sgn}\left(\frac{\partial\alpha_1}{\partial x}\right)\frac{p_2 - p_1}{Z_1 + Z_2} \qquad \text{with } u_I' = \frac{Z_1 u_1 + Z_2 u_2}{Z_1 + Z_2},$$

$$p_I = p_I' + \mathrm{sgn}\left(\frac{\partial\alpha_1}{\partial x}\right)\frac{Z_1 Z_2}{Z_1 + Z_2}(u_2 - u_1) \quad \text{with } p_I' = \frac{Z_2 p_1 + Z_1 p_2}{Z_1 + Z_2},$$

where $Z_k = \rho_k c_k$ represents the acoustic impedance of phase k.

This symmetric formulation of the BN model has some advantages:

-Its extension to more than two phases is quite easy.

-It is able to deal with contact and permeable interfaces (Saurel et al., 2003, Saurel et al., 2014).

-It involves an extra wave, not aligned with the condensed phase velocity, this property having benefits at least for numerical resolution (Ambroso et al., 2012, Furfaro and Saurel, 2015).

This system admits the following mixture entropy equation, showing non-negative production:

$$\frac{\partial(\alpha\rho)_1 s_1 + (\alpha\rho)_2 s_2}{\partial t} + \frac{\partial(\alpha\rho)_1 u_1 s_1 + (\alpha\rho)_2 u_2 s_2}{\partial x} =$$

$$\frac{1}{T_1}\left\{\frac{Z_1}{(Z_1+Z_2)^2}\left((p_2-p_1)+\mathrm{sgn}\left(\frac{\partial\alpha_1}{\partial x}\right)Z_2(u_2-u_1)\right)^2\left|\frac{\partial\alpha_1}{\partial x}\right| + \lambda\frac{Z_2}{Z_1+Z_2}(u_2-u_1)^2 + \mu\frac{Z_1}{Z_1+Z_2}(p_2-p_1)^2\right\}$$

$$+\frac{1}{T_2}\left\{\frac{Z_2}{(Z_1+Z_2)^2}\left((p_2-p_1)+\mathrm{sgn}\left(\frac{\partial\alpha_1}{\partial x}\right)Z_2(u_2-u_1)\right)^2\left|\frac{\partial\alpha_2}{\partial x}\right| + \lambda\frac{Z_1}{Z_1+Z_2}(u_2-u_1)^2 + \mu\frac{Z_2}{Z_1+Z_2}(p_2-p_1)^2\right\}$$

Its 7 associated wave speeds are:

$\lambda_I = u_I$, $\lambda_1 = u_1$, $\lambda_2 = u_1 + c_1$, $\lambda_3 = u_1 - c_1$, $\lambda_4 = u_2$, $\lambda_5 = u_2 + c_2$, $\lambda_6 = u_2 - c_2$.

This model is consequently hyperbolic, thermodynamically consistent and symmetric. However, the wave speeds are independent of the volume fraction, meaning that in the dilute limit, the sound speed in the condensed phase is unchanged, this behaviour being questionable as this phase is no longer continuous.

I.2.b) Dilute two-phase flow model (Marble, 1963)

As the model that follows is no longer symmetric it is necessary to precise the phases. Phase 1 is considered to be the condensed one and the gas phase is denoted by the subscript 2. The 'apparent density' of the dispersed phase is introduced as, $\overline{\rho}_1 = (\alpha\rho)_1$.

In this approach, $\alpha_1 < 0.01$ and volume fraction effects are neglected in the gas phase equations. Its validity is therefore clearly restricted to flows with low concentrations of particles.

Phase 1 (dispersed)

$$\frac{\partial \overline{\rho}_1}{\partial t} + \frac{\partial \overline{\rho}_1 u_1}{\partial x} = 0$$

$$\frac{\partial \overline{\rho}_1 u_1}{\partial t} + \frac{\partial \overline{\rho}_1 u_1^2}{\partial x} = \lambda(u_2 - u_1) \qquad \text{(I.2.3)}$$

$$\frac{\partial \overline{\rho}_1 e_1}{\partial t} + \frac{\partial \overline{\rho}_1 e_1 u_1}{\partial x} = 0 \text{ or alternatively } \frac{\partial \overline{\rho}_1 E_1}{\partial t} + \frac{\partial \overline{\rho}_1 E_1 u_1}{\partial x} = \lambda u_1 (u_2 - u_1).$$

Phase 2 (gas)

$$\frac{\partial \rho_2}{\partial t} + \frac{\partial \rho_2 u_2}{\partial x} = 0 \qquad \text{(I.2.4)}$$

$$\frac{\partial \rho_2 u_2}{\partial t} + \frac{\partial \rho_2 u_2^{\,2} + p_2}{\partial x} = -\lambda(u_2 - u_1)$$

$$\frac{\partial \rho_2 E_2}{\partial t} + \frac{\partial (\rho_2 E_2 + p_2) u_2}{\partial x} = -\lambda u_1 (u_2 - u_1)$$

This system admits the following mixture entropy equation:

$$\frac{\partial \overline{\rho}_1 s_1 + \rho_2 s_2}{\partial t} + \frac{\partial \overline{\rho}_1 s_1 u_1 + \rho_2 s_2 u_2}{\partial x} = \frac{\lambda (u_1 - u_2)^2}{T_2}$$

Its associated wave speeds are:

$\lambda_1 = u_1$, $\lambda_2 = u_2$, $\lambda_3 = u_2 + c_2$, $\lambda_4 = u_2 - c_2$.

As $\lambda_1 = u_1$ is fold three times, the equations of phase 1 are hyperbolic and linearly degenerate, while the ones of the gas phase are strictly hyperbolic.

These two models are thus well posed in the sense that they are thermodynamically consistent, frame invariant and hyperbolic. Both models can be solved by Godunov type methods as the Riemann problem has been addressed for both (Saurel et al., 1994, Saurel and Abgrall, 1999, Schwendeman et al., 2006, Deledicque and Papalexandris, 2010, Furfaro and Saurel, 2015). However, well posedness is a necessary condition but not a sufficient one for physical validity. In particular, considering again the

BN model, the condensed phase sound speed c_1 is well defined as a thermodynamic variable and sound disturbances propagate at the particle or grain level. But sound cannot propagate in the mixture at speed c_1 as the continuum approximation is no longer valid for the condensed phase as soon as the mixture becomes dilute enough. See also Lhuillier et al. (2013) and McGrath et al. (2016) for further arguments.

I.3 – Alternative volume fraction equations

The volume fraction equation of the BN model is the first equation of System (I.2.1) and can be derived from averaging methods considering the transport of a characteristic function, equal to 1 in a given phase and 0 in the other phase. See for example Abgrall and Saurel (2003), Drew and Passman (2006).

Let us now consider another point of view as done by Lhuillier et al. (2013) and consider liquid drops (or condensed phase particles) suspended in a gas. The radius R_1 of a single spherical compressible liquid drop surrounded by a gas evolves, under acoustic approximation ($\Delta u \approx \Delta p / \rho c$) with the following transport equation (Chinnayya et al., 2004),

$$\frac{d_1 R_1}{dt} \approx \frac{p_1 - p_2}{\rho_1 c_1}, \tag{I.3.1}$$

where $\frac{d_1}{dt} = \frac{\partial}{\partial t} + u_1 \frac{\partial}{\partial x}$ denotes the Lagrangian derivative of phase 1.

Estimate of the pressure relaxation time τ_1 is given by the time needed for an acoustic wave to travel the particle radius,

$$\tau_1 \approx \frac{R_1}{c_1}.$$

For a liquid drop of 1 mm radius suspended in air the pressure relaxation time is therefore of the order of 1 microsecond. This is very small in most practical situations compared to the other characteristic times related to drag, heat exchange, most situations of wave propagation and fluid motion.

With this definition (I.3.1) becomes,

$$\frac{d_1 R_1}{dt} \approx \frac{R_1}{\tau} \frac{p_1 - p_2}{\rho_1 c_1^2}$$

Trivial transformation of the former equation implies,

$$\frac{d_1 V_1}{dt} \approx 4\pi R_1^2 \frac{R_1}{\tau_1} \frac{p_1 - p_2}{\rho_1 c_1^2} \qquad \text{(I.3.2)}$$

where $V_1 = \frac{4}{3}\pi R_1^3$ denotes the volume of the drop.

In absence of fragmentation and coalescence, the specific number of drops per unit volume obeys the following balance equation:

$$\frac{\partial N_1}{\partial t} + \frac{\partial N_1 u_1}{\partial x} = 0, \qquad \text{(I.3.3)}$$

where N_1 represents the specific number of drops.

Multiplying (I.3.2) by N_1 yields,

$$\frac{\partial \alpha_1}{\partial t} + \frac{\partial \alpha_1 u_1}{\partial x} = \frac{3\alpha_1}{\tau_1} \frac{p_1 - p_2}{\rho_1 c_1^2} \qquad \text{(I.3.4)}$$

as $\alpha_1 = N_1 V_1$.

The volume fraction equation is now in conservative form with a pressure relaxation term.

It is interesting to consider the symmetric situation of liquid containing spherical bubbles.

In this situation the bubble radius evolves according to,

$$\frac{d_2 R_2}{dt} \approx \frac{p_2 - p_1}{\rho_1 c_1},$$

as the acoustic impedance of the less compressible phase ($\rho_1 c_1$) controls the interface velocity.

The specific number of bubbles per unit volume obeys the balance law,

$$\frac{\partial N_2}{\partial t} + \frac{\partial N_2 u_2}{\partial x} = 0,$$

and the corresponding volume fraction equation now reads,

$$\frac{\partial \alpha_2}{\partial t} + \frac{\partial \alpha_2 u_2}{\partial x} = \frac{3\alpha_2}{\tau_2} \frac{p_2 - p_1}{\rho_1 c_1 c_2} \qquad \text{(I.3.5)}$$

with $\tau_2 \approx \frac{R_2}{c_2}$.

We now examine the implications of such volume fraction equations (I.3.4 and I.3.5) on the flow model. The analysis begins with a model based on (I.3.4) to start with a concrete example.

I.4 – The new model

For the sake of simplicity in the notations and compatibility with (I.2.1), Equation (I.3.4) is expressed as

$$\frac{\partial \alpha_1}{\partial t} + \frac{\partial \alpha_1 u_1}{\partial x} = \mu(p_1 - p_2), \tag{I.4.1}$$

with $\mu = \dfrac{3\alpha_1}{\tau_1 \rho_1 c_1^2}$.

The same mass, momentum and energy equations of Systems (I.2.1)-(I.2.2) are reconsidered as,

$$\begin{aligned}
&\frac{\partial (\alpha\rho)_1}{\partial t} + \frac{\partial (\alpha\rho u)_1}{\partial x} = 0 \\
&\frac{\partial (\alpha\rho u)_1}{\partial t} + \frac{\partial (\alpha\rho u^2 + \alpha p)_1}{\partial x} = p_I \frac{\partial \alpha_1}{\partial x} + \lambda(u_2 - u_1) \\
&\frac{\partial (\alpha\rho E)_1}{\partial t} + \frac{\partial (\alpha(\rho E + p)u)_1}{\partial x} = -p_I \frac{\partial \alpha_1}{\partial t} + \lambda u_I(u_2 - u_1) + H(T_2 - T_1) \\
&\frac{\partial (\alpha\rho)_2}{\partial t} + \frac{\partial (\alpha\rho u)_2}{\partial x} = 0 \\
&\frac{\partial (\alpha\rho u)_2}{\partial t} + \frac{\partial (\alpha\rho u^2 + \alpha p)_2}{\partial x} = p_I \frac{\partial \alpha_2}{\partial x} - \lambda(u_2 - u_1) \\
&\frac{\partial (\alpha\rho E)_2}{\partial t} + \frac{\partial (\alpha(\rho E + p)u)_2}{\partial x} = p_I \frac{\partial \alpha_1}{\partial t} - \lambda u_I(u_2 - u_1) - H(T_2 - T_1)
\end{aligned} \tag{I.4.2}$$

The right hand side of the phase energy equations has been modified with the presence of $p_I \dfrac{\partial \alpha_1}{\partial t}$, the interstitial pressure work, present in (I.2.1-2) differently.

The new model just consists in (I.4.1), derived in Section I.3 and System (I.4.2), that doesn't need extra derivation. It represents balance equations of mass, momentum and energy of each phase. These equations are present in almost any Eulerian two-phase flow models, derived with various methods, all giving the same result:

- Time and volume average methods (Anderson and Jackson, 1967, Delhaye and Achard, 1976);
- Ensemble average methods (Drew and Passman, 2006);
- Variational methods (Gavrilyuk and Saurel, 2002);
- Discrete Equations Method (Saurel et al., 2003).

System (I.4.2) obviously satisfies mixture mass, mixture momentum and mixture energy conservation, for any model of interfacial pressure p_I and interfacial velocity u_I. Possible estimates are for example (Saurel et al., 2003):

$$p_I = \frac{Z_2 p_1 + Z_1 p_2}{Z_1 + Z_2};\ u_I = \frac{Z_1 u_1 + Z_2 u_2}{Z_1 + Z_2} \tag{I.4.3}$$

Convective heat exchange ($H(T_2 - T_1)$) has been inserted for the sake of generality where H denotes the product of the specific interfacial area and heat exchange coefficient, related to the Nusselt number.

Balance equations (I.4.2) are considered not only in the BN formulation, but in any two-phase Eulerian model when the effects of volume fraction are considered. The only point to underline is that the various pressures are distinct at this level.

Two questions arise immediately, regarding the fulfilment of the second law of thermodynamics and the hyperbolicity of (I.4.1-2). In this aim, the equations are expressed in a set of appropriate variables.

I.4.a) Physical variables formulation

System (I.4.1-2) is expressed with 'physical variables': volume fraction, density, velocity, internal energy and entropy for each phase:

$$\frac{d_1\alpha_1}{dt} + \alpha_1 \frac{\partial u_1}{\partial x} = \mu(p_1 - p_2) \tag{I.4.4}$$

$$\frac{d_1\rho_1}{dt} = -\frac{\mu\rho_1}{\alpha_1}(p_1 - p_2)$$

$$\frac{d_1 u_1}{dt} + \frac{1}{\rho_1}\frac{\partial p_1}{\partial x} = \frac{(p_I - p_1)}{(\alpha\rho)_1}\frac{\partial \alpha_1}{\partial x} + \frac{\lambda(u_2 - u_1)}{(\alpha\rho)_1}$$

$$\frac{d_1 e_1}{dt} + \frac{p_1 - p_I}{\rho_1}\frac{\partial u_1}{\partial x} = -\frac{\mu}{\alpha_1\rho_1}p_I(p_1 - p_2) + \frac{\lambda(u_I - u_1)(u_2 - u_1)}{(\alpha\rho)_1} + \frac{H(T_2 - T_1)}{(\alpha\rho)_1}$$

$$\frac{d_1 s_1}{dt} + \frac{p_1 - p_I}{\rho_1 T_1}\frac{\partial u_1}{\partial x} = -\frac{\mu}{\alpha_1\rho_1 T_1}(p_I - p_1)(p_1 - p_2) + \frac{\lambda(u_I - u_1)(u_2 - u_1)}{(\alpha\rho)_1 T_1} + \frac{H(T_2 - T_1)}{(\alpha\rho)_1 T_1}$$

$$\frac{d_2\rho_2}{dt} + \frac{\rho_2}{\alpha_2}(u_1 - u_2)\frac{\partial \alpha_1}{\partial x} + \frac{\alpha_1}{\alpha_2}\rho_2\frac{\partial u_1}{\partial x} + \rho_2\frac{\partial u_2}{\partial x} = \frac{\rho_2}{\alpha_2}\mu(p_1 - p_2)$$

$$\frac{d_2 u_2}{dt} + \frac{1}{\rho_2}\frac{\partial p_2}{\partial x} = \frac{p_I - p_2}{(\alpha\rho)_2}\frac{\partial \alpha_2}{\partial x} - \frac{\lambda(u_2 - u_1)}{(\alpha\rho)_2}$$

$$\frac{d_2 e_2}{dt} + \frac{p_2}{\rho_2}\frac{\partial u_2}{\partial x} + \frac{\alpha_1 p_I}{\alpha_2 \rho_2}\frac{\partial u_1}{\partial x} + \frac{p_I(u_1 - u_2)}{\alpha_2 \rho_2}\frac{\partial \alpha_1}{\partial x} = \frac{\mu p_I (p_1 - p_2)}{\alpha_2 \rho_2} - \frac{\lambda (u_I - u_2)(u_2 - u_1)}{(\alpha\rho)_2} - \frac{H(T_2 - T_1)}{(\alpha\rho)_2}$$

$$\frac{d_2 s_2}{dt} + \frac{\alpha_1 (p_I - p_2)}{\alpha_2 \rho_2 T_2}\frac{\partial u_1}{\partial x} + \frac{(p_I - p_2)(u_1 - u_2)}{\alpha_2 \rho_2 T_2}\frac{\partial \alpha_1}{\partial x} = \frac{\mu (p_1 - p_2)(p_I - p_2)}{\alpha_2 \rho_2 T_2} - \frac{\lambda (u_I - u_2)(u_2 - u_1)}{(\alpha\rho)_2 T_2} - \frac{H(T_2 - T_1)}{(\alpha\rho)_2 T_2}$$

The second equation of this system is particularly interesting. It means that phase 1 density is independent of velocity divergence. As phase 1 is dispersed, there is no reason that droplet cloud contraction (or expansion) induces density variations. In the present formulation, it varies only as a consequence of drop contraction or expansion, due to pressure differential $(-\frac{\mu\rho_1}{\alpha_1}(p_1 - p_2))$ and not to velocity divergence, as in the BN model. However, at this level, there is no chance that the entropy production of the system be non-negative in any flow condition, as the entropy equations involve space derivatives of velocities and volume fraction that have undefined sign. This ambiguity vanishes in the stiff pressure relaxation limit that follows.

I.4.b) Stiff pressure relaxation limit

Former system dramatically simplifies in the stiff pressure relaxation limit, as shown hereafter. Let us consider first-order expansions for the pressures,

$$p_k = \rho_1 c_1^2 \left(p_k^0 + \varepsilon p_k^1 + ...\right) \qquad \text{(I.4.5)}$$

Where,

- ε is of the order of the pressure relaxation time ($\varepsilon \approx \tau_1$), tending to zero in most situations($\varepsilon \to 0^+$),
- p_k^0 and p_k^1 are respectively the dimensionless pressures at leading and first-order of the Taylor expansion.

Inserting these definitions in (I.3.4) it becomes,

$$\frac{\partial \alpha_1}{\partial t} + \frac{\partial \alpha_1 u_1}{\partial x} = \frac{3\alpha_1}{\varepsilon}(p_1^0 + \varepsilon p_1^1 - p_2^0 - \varepsilon p_2^1)$$

This equation implies two relations, as ε is arbitrarily small,

$$p_1^0 = p_2^0 \qquad \text{(I.4.6)}$$

and,

$$\frac{\partial \alpha_1}{\partial t} + \frac{\partial \alpha_1 u_1}{\partial x} = p_1^1 - p_2^1. \qquad \text{(I.4.7)}$$

The equilibrium condition (I.4.6) is valid at leading order only and is different of the strict pressure equilibrium condition,

$$p_1 = p_2, \qquad \text{(I.4.8)}$$

widely used in two phase flow literature. Such strict equality results in non-hyperbolic models (see for example Guidaglia et al., 2001).

Equation (I.4.7) means that pressure fluctuations are still present in the flow model, each time the relaxation coefficient μ appears in factor of the pressure differential $(p_1 - p_2)$.

Let us for example examine the entropy equation of the first phase that becomes, after inserting (I.4.5):

$$\frac{d_1 s_1}{dt} + \frac{c_1^2\left(p_1^0 - p_I^0\right)}{T_1}\frac{\partial u_1}{\partial x} + \varepsilon\frac{c_1^2\left(p_1^1 - p_I^1\right)}{T_1}\frac{\partial u_1}{\partial x} =$$

$$-\frac{3c_1^2}{\varepsilon T_1}\left(p_1^0 - p_I^0 + \varepsilon(p_1^1 - p_I^1)\right)\left(p_1^0 - p_2^0 + \varepsilon(p_1^1 - p_2^1)\right) + \frac{\lambda(u_I - u_1)(u_2 - u_1)}{(\alpha\rho)_1 T_1} + \frac{H(T_2 - T_1)}{(\alpha\rho)_1 T_1}$$

With the help of (I.4.6) simplifications appear,

$$\frac{d_1 s_1}{dt} + \varepsilon\frac{c_1^2\left(p_1^1 - p_I^1\right)}{T_1}\frac{\partial u_1}{\partial x} = -\frac{3c_1^2}{T_1}\varepsilon(p_1^1 - p_I^1)^2 + \frac{\lambda(u_I - u_1)(u_2 - u_1)}{(\alpha\rho)_1 T_1} + \frac{H(T_2 - T_1)}{(\alpha\rho)_1 T_1}.$$

Under the assumption of smooth solutions and as $\varepsilon \to 0^+$, it reduces to:

$$\frac{d_1 s_1}{dt} = \frac{\lambda(u_I - u_1)(u_2 - u_1)}{(\alpha\rho)_1 T_1} + \frac{H(T_2 - T_1)}{(\alpha\rho)_1 T_1}$$

Therefore all terms involving pressure differential vanish, except those related to first-order pressure relaxation effects (quadratic pressure differential terms vanish). The resulting limit system reads,

$$\frac{d_1 \alpha_1}{dt} + \alpha_1 \frac{\partial u_1}{\partial x} = \mu(p_1 - p_2) \qquad \text{(I.4.9)}$$

$$\frac{d_1 \rho_1}{dt} = -\frac{\mu \rho_1}{\alpha_1}(p_1 - p_2)$$

$$\frac{d_1 u_1}{dt} + \frac{1}{\rho_1}\frac{\partial p_1}{\partial x} = \frac{\lambda(u_2 - u_1)}{(\alpha\rho)_1}$$

$$\frac{d_1 e_1}{dt} = -\frac{\mu}{\alpha_1 \rho_1} p_I (p_1 - p_2) + \frac{\lambda(u_I - u_1)(u_2 - u_1)}{(\alpha\rho)_1} + \frac{H(T_2 - T_1)}{(\alpha\rho)_1}$$

$$\frac{d_1 s_1}{dt} = \frac{\lambda(u_I - u_1)(u_2 - u_1)}{(\alpha\rho)_1 T_1} + \frac{H(T_2 - T_1)}{(\alpha\rho)_1 T_1}$$

$$\frac{d_2 \rho_2}{dt} + \frac{\rho_2}{\alpha_2}(u_1 - u_2)\frac{\partial \alpha_1}{\partial x} + \frac{\alpha_1}{\alpha_2}\rho_2 \frac{\partial u_1}{\partial x} + \rho_2 \frac{\partial u_2}{\partial x} = \frac{\rho_2}{\alpha_2}\mu(p_1 - p_2)$$

$$\frac{d_2 u_2}{dt} + \frac{1}{\rho_2}\frac{\partial p_2}{\partial x} = -\frac{\lambda(u_2 - u_1)}{(\alpha\rho)_2}$$

$$\frac{d_2 e_2}{dt} + \frac{p_2}{\rho_2}\frac{\partial u_2}{\partial x} + \frac{\alpha_1 p_1}{\alpha_2 \rho_2}\frac{\partial u_1}{\partial x} + \frac{p_I(u_1 - u_2)}{\alpha_2 \rho_2}\frac{\partial \alpha_1}{\partial x} = \frac{\mu p_I (p_1 - p_2)}{\alpha_2 \rho_2} - \frac{\lambda(u_I - u_2)(u_2 - u_1)}{(\alpha\rho)_2} - \frac{H(T_2 - T_1)}{(\alpha\rho)_2}$$

$$\frac{d_2 s_2}{dt} = -\frac{\lambda(u_I - u_2)(u_2 - u_1)}{(\alpha\rho)_2 T_2} - \frac{H(T_2 - T_1)}{(\alpha\rho)_2 T_2}$$

With the help of interfacial variables estimates (I.4.3) the entropy equations become,

$$\frac{d_1 s_1}{dt} = \frac{\lambda}{(\alpha\rho)_1 T_1}\frac{Z_2}{Z_1 + Z_2}(u_2 - u_1)^2 + \frac{H(T_2 - T_1)}{(\alpha\rho)_1 T_1}$$

$$\frac{d_2 s_2}{dt} = \frac{\lambda}{(\alpha\rho)_2 T_2}\frac{Z_1}{Z_1 + Z_2}(u_2 - u_1)^2 - \frac{H(T_2 - T_1)}{(\alpha\rho)_2 T_2}$$

Combination of these equations with the mass equations results in the following mixture entropy equation, that guarantees non-negative evolutions,

$$\frac{\partial \alpha_1\rho_1 s_1 + \alpha_2\rho_2 s_2}{\partial t} + \frac{\partial \alpha_1\rho_1 s_1 u_1 + \alpha_2\rho_2 s_2 u_2}{\partial x} = \left(\frac{Z_2}{T_1} + \frac{Z_1}{T_2}\right)\frac{\lambda}{Z_1 + Z_2}(u_2 - u_1)^2 + \frac{H(T_2 - T_1)^2}{T_1 T_2} \qquad \text{(I.4.10)}$$

System (I.4.9) is consequently entropy preserving.

It is interesting to note that, in the present limit, the internal energy equation of the first phase expresses in conservation form:

$$\frac{\partial \alpha_1\rho_1 e_1}{\partial t} + \frac{\partial \alpha_1\rho_1 e_1 u_1}{\partial x} = -\mu p_I(p_1 - p_2) + \lambda(u_I - u_1)(u_2 - u_1) + H(T_2 - T_1) \qquad \text{(I.4.11)}$$

Another interesting remark emerges with respect to the interfacial variable estimates u_I and p_I in the present context. The entropy equations of System (I.4.9) indicate that simple estimates of the interfacial velocity,

$u_I = u_1$ or $u_I = u_2$,

are admissible.

It is also interesting to note that in the present stiff pressure relaxation limit associated to (I.4.9) the interfacial pressure estimate for p_I has no importance with respect to the entropy production. Therefore, simple estimates such as,

$p_I = p_1$ or $p_I = p_2$,

are admissible as well.

We now check hyperbolicity of this flow model.

I.4.c) Hyperbolicity

System (I.4.9) in absence of relaxation effects, is expressed as,

$$\frac{\partial W}{\partial t} + A(W)\frac{\partial W}{\partial x} = 0,$$

with,

$$W = (\rho_1, \ s_1, \ s_2, \ \alpha_1, \ u_1, \ \rho_2, \ u_2)^T.$$

The Jacobian matrix reads,

$$A(W) = \begin{pmatrix} u_1 & 0 & 0 & 0 & 0 & 0 & 0 \\ 0 & u_1 & 0 & 0 & 0 & 0 & 0 \\ 0 & 0 & u_2 & 0 & 0 & 0 & 0 \\ 0 & 0 & 0 & u_1 & \alpha_1 & 0 & 0 \\ \frac{c_1^2}{\rho_1} & \frac{1}{\rho_1}\frac{\partial p_1}{\partial s_1}\Big)_{\rho_1} & 0 & 0 & u_1 & 0 & 0 \\ 0 & 0 & 0 & \frac{\rho_2}{\alpha_2}(u_1 - u_2) & \frac{\alpha_1}{\alpha_2}\rho_2 & u_2 & \rho_2 \\ 0 & 0 & \frac{1}{\rho_2}\frac{\partial p_2}{\partial s_2}\Big)_{\rho_2} & 0 & 0 & \frac{c_2^2}{\rho_2} & u_2 \end{pmatrix}.$$

The wave speeds, solution of $|A - \lambda I| = 0$ are,

$$\lambda_{1-4} = u_1, \ \lambda_5 = u_2, \ \lambda_6 = u_2 - c_2 \text{ and } \lambda_7 = u_2 + c_2 \ . \qquad \text{(I.4.12)}$$

All roots being real the system is unconditionally hyperbolic. The wave speeds correspond to the one of the dilute model of Marble (1963) (Systems I.2.3 – I.2.4) and not those of Baer and Nunziato (1986), as expected.

The absence of sound propagation in the dispersed phase is obviously more physical, as there is no material to support sound propagation in this phase. In the BN formulation, sound propagates in the dispersed phase even in the absence of contacts, i.e. without material support, such behavior being physically questionable.

I.4.d) Model summary

The flow model thus consists in System (I.4.1-2) with the condition:

$$\tau_1 \to 0^+ \tag{I.4.13}$$

Alternatively it can be expressed as,

$$\frac{\partial \alpha_1}{\partial t} + \frac{\partial \alpha_1 u_1}{\partial x} = \mu(p_1 - p_2), \qquad \text{with} \quad \mu \to +\infty$$

$$\frac{\partial (\alpha\rho)_1}{\partial t} + \frac{\partial (\alpha\rho u)_1}{\partial x} = 0,$$

$$\frac{\partial \alpha_1\rho_1 u_1}{\partial t} + \frac{\partial \alpha_1\rho_1 u_1^2 + \alpha_1 p_1}{\partial x} = p_I \frac{\partial \alpha_1}{\partial x} + \lambda(u_2 - u_1),$$

$$\frac{\partial \alpha_1\rho_1 e_1}{\partial t} + \frac{\partial \alpha_1\rho_1 u_1 e_1}{\partial x} = -\mu p_I (p_1 - p_2) + \lambda \frac{Z_2}{Z_1 + Z_2}(u_2 - u_1)^2 + H(T_2 - T_1),$$

$$\frac{\partial (\alpha\rho)_2}{\partial t} + \frac{\partial (\alpha\rho u)_2}{\partial x} = 0, \tag{I.4.14}$$

$$\frac{\partial (\alpha_1\rho_1 u_1 + \alpha_2\rho_2 u_2)}{\partial t} + \frac{\partial (\alpha_1\rho_1 u_1^2 + \alpha_1 p_1) + (\alpha_2\rho_2 u_2^2 + \alpha_2 p_2)}{\partial x} = 0,$$

$$\frac{\partial (\alpha_1\rho_1 E_1 + \alpha_2\rho_2 E_2)}{\partial t} + \frac{\partial \alpha_1 u_1(\rho_1 E_1 + p_1) + \alpha_2 u_2(\rho_2 E_2 + p_2)}{\partial x} = 0.$$

In this formulation there is a single non-conservative equation (the momentum one of the liquid phase) as the momentum of the second phase is deduced from the mixture momentum equation. The conservative internal energy equation for the liquid phase is a consequence of the second equation of (4.4) and stiff pressure relaxation limit. This is a nice property that simplifies shock conditions determination. Obviously, System (I.4.14) can be complemented by mass transfer.

I.4.e) Shock relations

A major issue of two-phase flow literature is addressed hereafter as most two-phase flow models being non-conservative, determination of weak solutions is challenging.

Let us denote with upper-script 0 the undisturbed state and σ the shock speed. Most equations of System (I.4.14) being conservative, associated jump relations are determined easily as:

$$\alpha_1(u_1-\sigma)=\alpha_1^0(u_1^0-\sigma),$$

$$\rho_1=\rho_1^0,$$

$$e_1=e_1^0, \qquad \text{(I.4.15)}$$

$$\alpha_2\rho_2(u_2-\sigma)=\alpha_2^0\rho_2^0(u_2^0-\sigma),$$

$$\alpha_1\rho_1u_1(u_1-\sigma)+\alpha_2\rho_2u_2(u_2-\sigma)+(\alpha_1p_1+\alpha_2p_2)=\alpha_1^0\rho_1^0u_1^0(u_1^0-\sigma)+\alpha_2^0\rho_2^0u_2^0(u_2^0-\sigma)+(\alpha_1^0p_1^0+\alpha_2^0p_2^0)$$

$$\alpha_1\rho_1E_1(u_1-\sigma)+\alpha_2\rho_2E_2(u_2-\sigma)+\left(\alpha_1u_1p_1+\alpha_2u_2p_2\right)=\alpha_1^0\rho_1^0E_1^0(u_1^0-\sigma)+\alpha_2^0\rho_2^0E_2^0(u_2^0-\sigma)+\left(\alpha_1^0u_1^0p_1^0+\alpha_2^0u_2^0p_2^0\right)$$

Indeed, for any conservation law,

$$\frac{\partial U}{\partial t}+\frac{\partial F}{\partial x}=0,$$

jump conditions are obtained as,

$$F-\sigma U=F^0-\sigma U^0.$$

In the undisturbed state, the mixture is in mechanical equilibrium,

$$u_1^0=u_2^0=u^0,$$

$$p_1^0=p_2^0=p^0,$$

and System (I.4.15) simplifies as,

$$\alpha_1(u_1-\sigma)=\alpha_1^0(u^0-\sigma),$$

$$\rho_1=\rho_1^0 \quad ,$$

$$e_1=e_1^0, \qquad \text{(I.4.16)}$$

$$\alpha_2\rho_2(u_2-\sigma)=\alpha_2^0\rho_2^0(u^0-\sigma),$$

$$\alpha_1\rho_1u_1(u_1-\sigma)+\alpha_2\rho_2u_2(u_2-\sigma)+(\alpha_1p_1+\alpha_2p_2)=\left(\alpha_1^0\rho_1^0+\alpha_2^0\rho_2^0\right)u^0(u^0-\sigma)+p^0$$

$$\alpha_1\rho_1E_1(u_1-\sigma)+\alpha_2\rho_2E_2(u_2-\sigma)+\left(\alpha_1u_1p_1+\alpha_2u_2p_2\right)=\left(\alpha_1^0\rho_1^0E_1^0+\alpha_2^0\rho_2^0E_2^0\right)(u^0-\sigma)+u^0p^0$$

To close System (I.4.16) it is necessary to integrate the non-conservative momentum equation of the dispersed phase. This is usually a major issue with existing flow models, due to the lack of definition of the product $p_I \frac{\partial \alpha_1}{\partial x}$, involving both Heaviside and Dirac functions.

Here this issue vanishes. Indeed, as $\rho_1 = \rho_1^0$ and $e_1 = e_1^0$, necessarily,

$$p_1 = p_1^0 = p^0 . \tag{I.4.17}$$

The pressure of the dispersed phase is invariant across the shock. It will vary in the relaxation zone, but is constant through the discontinuity.

Consequently, assuming $p_I = p_1$ (an admissible estimate, as discussed previously) and integrating the dispersed phase momentum equation, the following result is obtained,

$$\alpha_1\rho_1 u_1 (u_1 - \sigma) + \alpha_1 (p_1 - p^0) = \alpha_1^0\rho_1^0 u_1^0 (u_1^0 - \sigma) + \alpha_1^0 (p_1^0 - p^0),$$

and simplifies significantly as,

$$u_1 = u^0 \tag{I.4.18}$$

The Rankine-Hugoniot system thus consists in (I.4.16) – (I.4.18). Thanks to (I.4.18) it simplifies as,

$$\begin{aligned}
&\alpha_1 = \alpha_1^0 ,\\
&\rho_1 = \rho_1^0 \quad ,\\
&e_1 = e_1^0 ,\\
&u_1 = u^0 , \qquad\qquad (I.4.19)\\
&\rho_2 (u_2 - \sigma) = \rho_2^0 (u^0 - \sigma) ,\\
&\rho_2 u_2 (u_2 - \sigma) + p_2 = \rho_2^0 u^0 (u^0 - \sigma) + p^0 ,\\
&\rho_2 E_2 (u_2 - \sigma) + u_2 p_2 = \rho_2^0 E_2^0 (u^0 - \sigma) + u^0 p^0 .
\end{aligned}$$

This system means that the continuous phase (with index '2') is governed by single phase Rankine-Hugoniot conditions and clearly sees shock compression while the dispersed phase is invariant. This seems again physical, as the dilute phase being discontinuous, shocks cannot compress this phase directly. It is compressed in the relaxation zone, as a consequence of pressure differential among phases.

It is worth to mention that with (I.4.19) the so called 'piston problem' is well posed. Indeed a single shock propagates at speed σ. This is very different of the jump conditions associated to the BN

model, that involves two independent shocks, propagating at speeds σ_1 and σ_2, when relaxation effects are omitted in the equations.

I.4.f) Stiff mechanical relaxation limit

We now address both stiff pressure and velocity relaxation limit to check compatibility of the model with the Kapila et al. (2001) one. This is important for the computation of material interfaces with capturing methods (Saurel and Pantano, 2017). Here, only pressure and velocity relaxation processes are considered. They are considered to relax at infinite rate.

The pressure evolution equations read,

$$\frac{\partial p_1}{\partial t} + u_1 \frac{\partial p_1}{\partial x} = -\frac{\rho_1 c_1^2}{\alpha_1} \mu (p_1 - p_2)$$

$$\frac{\partial p_2}{\partial t} + u_2 \frac{\partial p_2}{\partial x} + \frac{\rho_2 c_2^2}{\alpha_2} \frac{\partial \alpha_1 u_1 + \alpha_2 u_2}{\partial x} = \frac{\rho_2 c_2^2}{\alpha_2} \mu (p_1 - p_2)$$

Taking the difference,

$$u_1 \frac{\partial p_1}{\partial x} - u_2 \frac{\partial p_2}{\partial x} - \frac{\rho_2 c_2^2}{\alpha_2} \frac{\partial \alpha_1 u_1 + \alpha_2 u_2}{\partial x} = -\left(\frac{\rho_1 c_1^2}{\alpha_1} + \frac{\rho_2 c_2^2}{\alpha_2} \right) \mu (p_1 - p_2).$$

In the stiff pressure ($p_1^0 = p_2^0 = p^0$) and velocity relaxation limits ($u_1^0 = u_2^0 = u^0$),

$$\mu (p_1 - p_2) \to \frac{\dfrac{\rho_2 c_2^2}{\alpha_2}}{\dfrac{\rho_1 c_1^2}{\alpha_1} + \dfrac{\rho_2 c_2^2}{\alpha_2}} \frac{\partial u}{\partial x}$$

Inserting this result in the volume fraction equation,

$$\frac{\partial \alpha_1}{\partial t} + u \frac{\partial \alpha_1}{\partial x} = \frac{\rho_1 c_1^2 - \rho_2 c_2^2}{\dfrac{\rho_1 c_1^2}{\alpha_1} + \dfrac{\rho_2 c_2^2}{\alpha_2}} \frac{\partial u}{\partial x},$$

the volume fraction equation of the Kapila et al. (2001) model is recovered.

The mixture sound speed at mechanical equilibrium is thus that of Wood (1930), $\frac{1}{\rho c^2} = \frac{\alpha_1}{\rho_1 c_1^2} + \frac{\alpha_2}{\rho_2 c_2^2}$ while for the Marble model with stiff velocity relaxation, the mechanical equilibrium sound speed is $c^2 = \left(\frac{\rho_2}{\rho}\right) c_2^2$, which is very different.

As the Kapila model is recovered in the stiff mechanical relaxation limit, it means that the present flow model is able to compute interfacial flows with the help of stiff velocity and pressure relaxation solvers. This feature is particularly important for the sake of generality of the formulation.

The present model is hyperbolic but not symmetric, as sound propagates only with the second phase. It is therefore interesting to compute relevant test problems to examine typical solutions and particularly those where sound must propagate in the first phase, to examine robustness of the formulation outside its range of design. To do this, an appropriate flow solver is derived in Appendix I.A.

I.5 – Computed results

Several test problems are addressed, some giving relevant illustrations of model's capabilities, other serving for validation as compared to exact solutions as well as experimental data.

I.5.a) Shock tube tests

The first test corresponds to the simple transport of a volume fraction discontinuity in a flow field in uniform pressure and velocity conditions. The method of Appendix A is extended to higher order thanks to the MUSCL algorithm (see for example Toro, 1997). Present computations use the Minmod limiter. The ideal gas equation of state is used to model thermodynamics of the gas phase, while the liquid is modeled by the stiffened gas EOS. These two EOS are summarized as follows,

$$p_k(\rho_k, e_k) = (\gamma_k - 1)\rho_k e_k - \gamma_k p_{\infty k}, \qquad \text{(I.5.1)}$$

with following sets or parameters,

$\gamma_{air} = 1.4$, $p_{\infty,air} = 0$, k=air,

$\gamma_{liquid} = 4.4$, $p_{\infty,liquid} = 6.10^8 Pa$, k=liquid.

These equations of state and associated parameters are used in all test problems of the present section. A volume fraction discontinuity separating two mixtures is transported at 100 m/s in a uniform pressure flow field of 0.1 MPa. The initial discontinuity is located at 0.5 m initially and computed results are compared to the exact solution at time 1 ms in the Figure I.1.

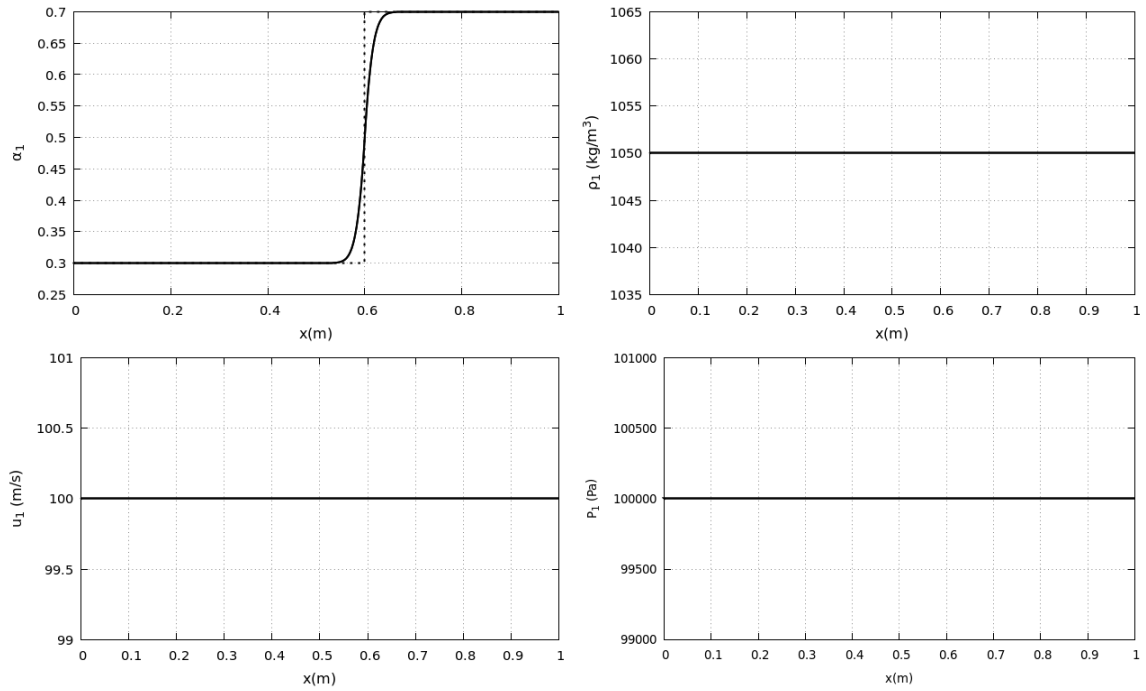

Figure I.1 – Volume fraction transport in uniform pressure and velocity fields. The mesh involves 500 cells and the time step is computed with CFL=0.5. The Minmod flux limiter is used in the MUSCL method. Initial velocities are set to 100m/s and pressures are constant and equal to 10^5 Pa. The volume fraction discontinuity is initially set at 0.5 m. The numerical solution is plotted at 1ms. The exact solution for the volume fraction is presented in dot symbols showing perfect agreement. Flow variables of phase 1 only are shown and are oscillation free. The same observation holds for the second phase, not shown for the sake of space restriction.

Another test is now addressed and corresponds to a two-phase shock tube, as shown in Figure I.2. In this test, stiff pressure relaxation is not used, while the flow model is hyperbolic and entropy preserving only when stiff pressure relaxation is done. Consequently, the present computations should fail. They however produce results with quite significant pressure disequilibrium, showing robustness of the formulation.

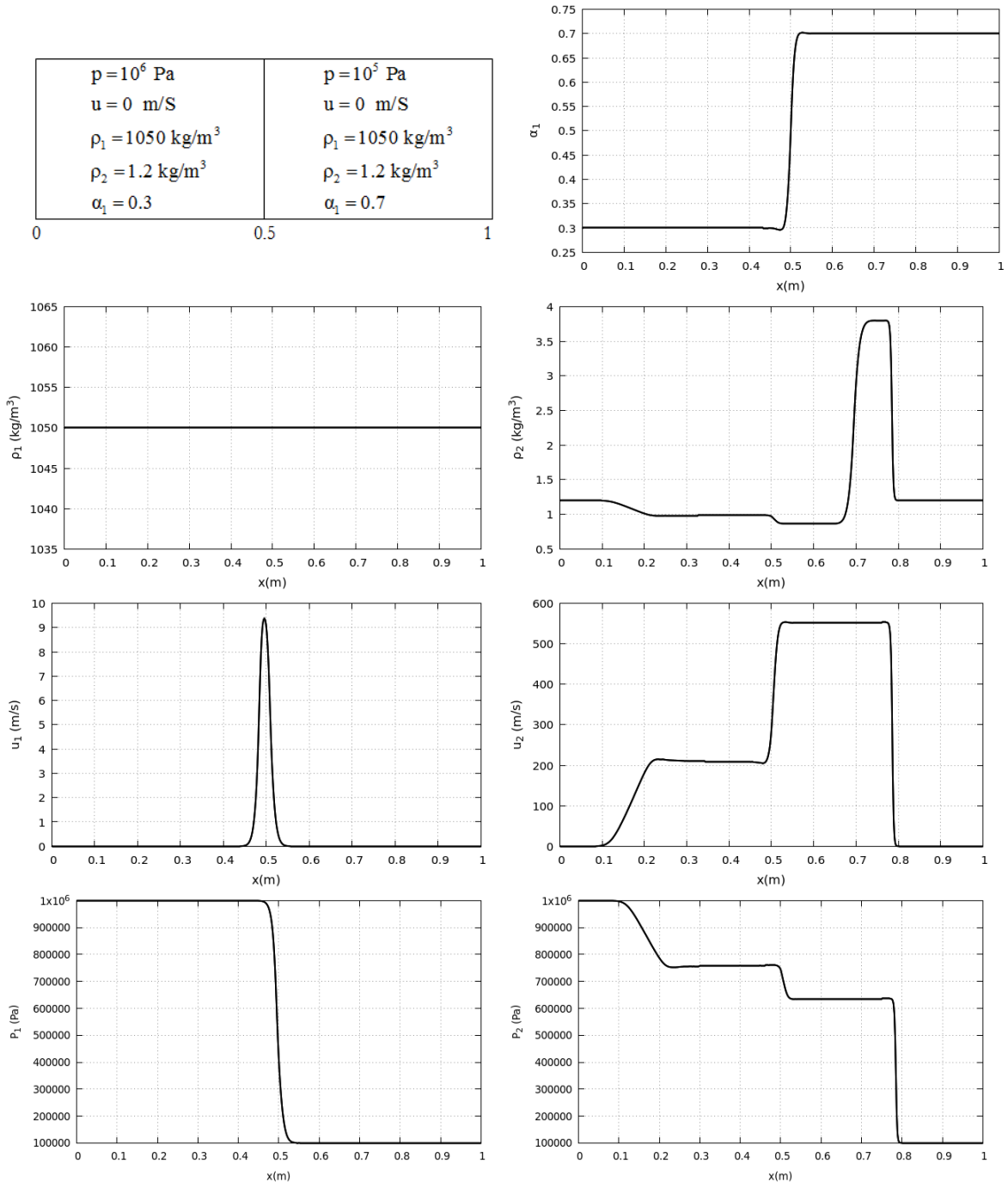

Figure I.2 – "Smooth shock tube test case". Computations are made in the absence of relaxation terms, with 500 cells and CFL=0.5. Results are shown at time 350µs. The Minmod flux limiter is used in the MUSCL method. Four waves are visible, in spite of the simplified Riemann solver that considers two only. It is interesting to note the discontinuous profile of pressure in the phase 1: no pressure wave is present in this phase. Phase 1 shows slight velocity creation (compared to the velocity of the gas phase) even in absence of drag, the pressure term in the momentum equation being responsible for that. These results also show the absence of volume fraction, density and velocity jumps across the shock, in agreement with shock relations (I.4.19), not explicitly used in the

flow solver of Appendix I.A. These results give a first validation of the two-phase Rankine-Hugoniot model (I.4.19).

These typical profiles are very different to those expected with BN and Marble models (without relaxation terms). For example, the pressure profiles of the phases are very different and even unphysical, but the model and algorithm stay robust.

To recover acceptable pressure evolutions in the condensed phase, stiff pressure relaxation is used. Pressure and velocity relaxation solvers are detailed in the appendixes C and D of Furfaro and Saurel (2016).

The same run as the one defined in Figure I.2 is reconsidered hereafter with pressure relaxation. Results are shown in Figure I.3.

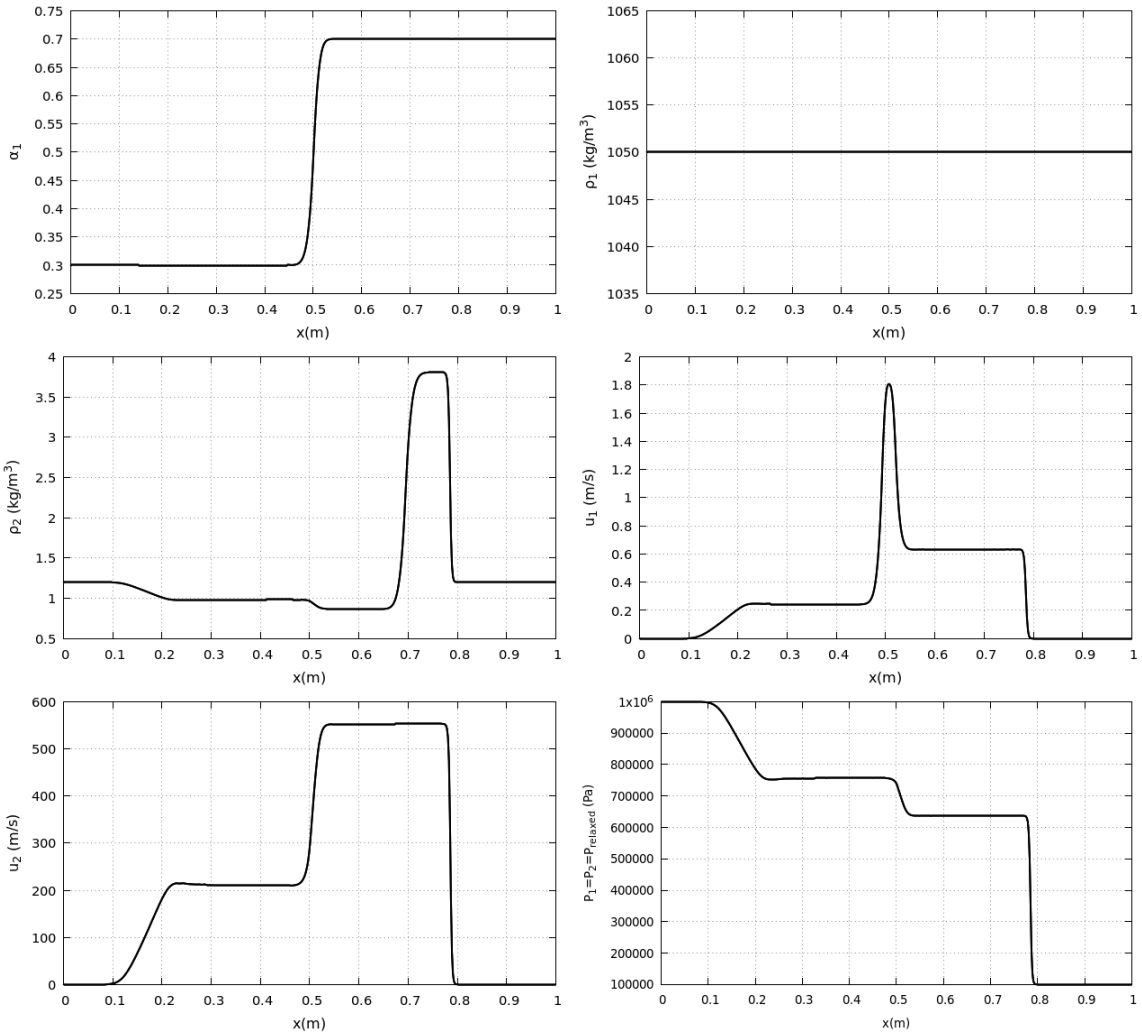

Figure I.3 – Smooth shock tube computations in the absence of velocity relaxation but with stiff pressure relaxation. Computations made with 500 cells and CFL=0.5. Computed results are shown at time 350µs. The Minmod flux limiter is used in the MUSCL method. All pressures are now equal, modifying significantly the phase 1 velocity profile.

With the help of both velocity and pressure relaxation solvers it is possible to address interfaces separating (nearly) pure liquid and (nearly) pure gas. The aim is to analyze the behavior of the flow model in another limit case, having in mind it has been derived for clouds of droplets, not interfaces. The initial conditions are given in Figure I.4 and correspond to a liquid at right set to motion by a pressurized gas at left. The exact solution is available for this test case and used to check accuracy of computations.

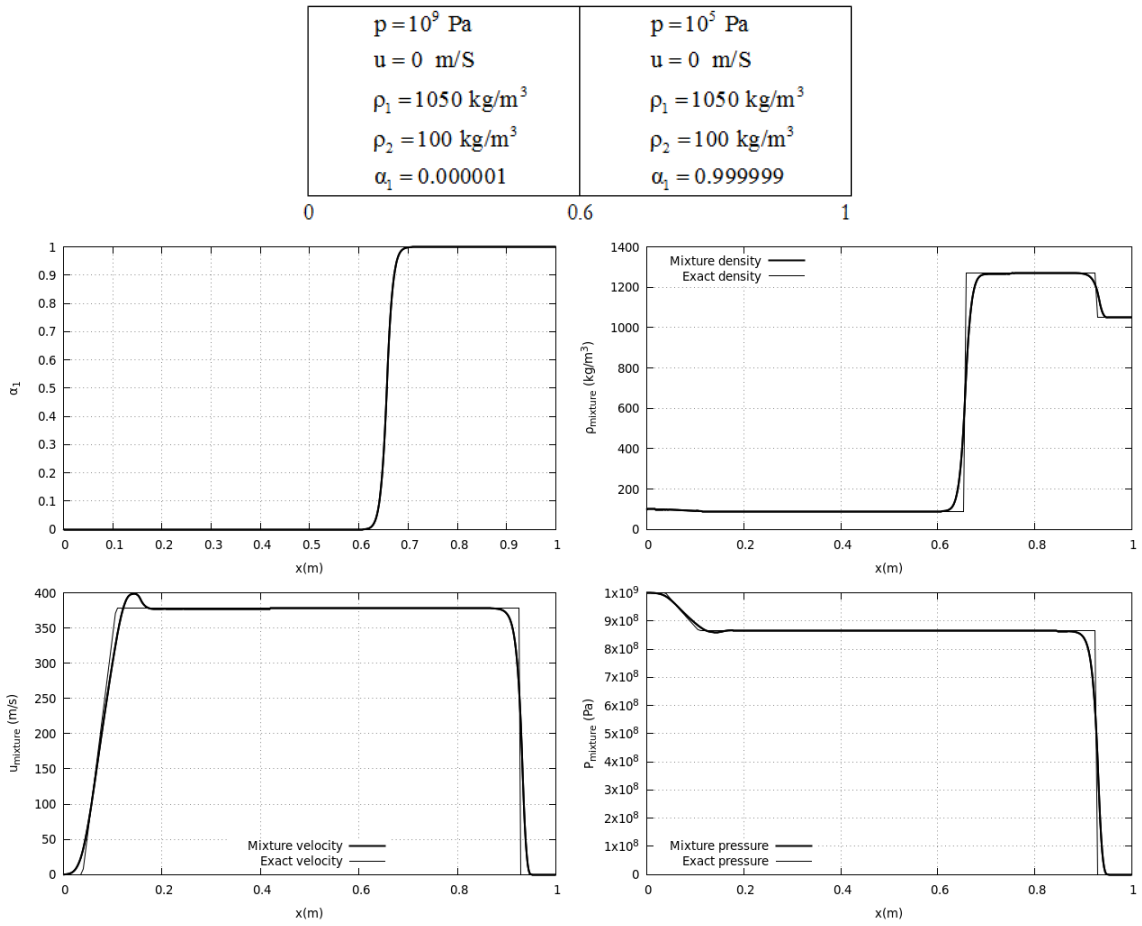

Figure I.4 – Shock tube with gas-liquid interface: High pressure gas at left and low pressure liquid at right. Computations done with 500 cells and CFL=0.5. Computed results shown at time 150µs. The Minmod flux limiter is used in the MUSCL method. Both velocities and pressure are relaxed, making the interface condition of equal pressures and velocities fulfilled.

The same test is considered but with fluids in reverse order: High pressure liquid at left and low pressure gas at right. This test is more severe as maintaining pressure positivity during liquid expansion is hard to manage. Corresponding results are shown in Figure I.5 and compared to the exact solution.

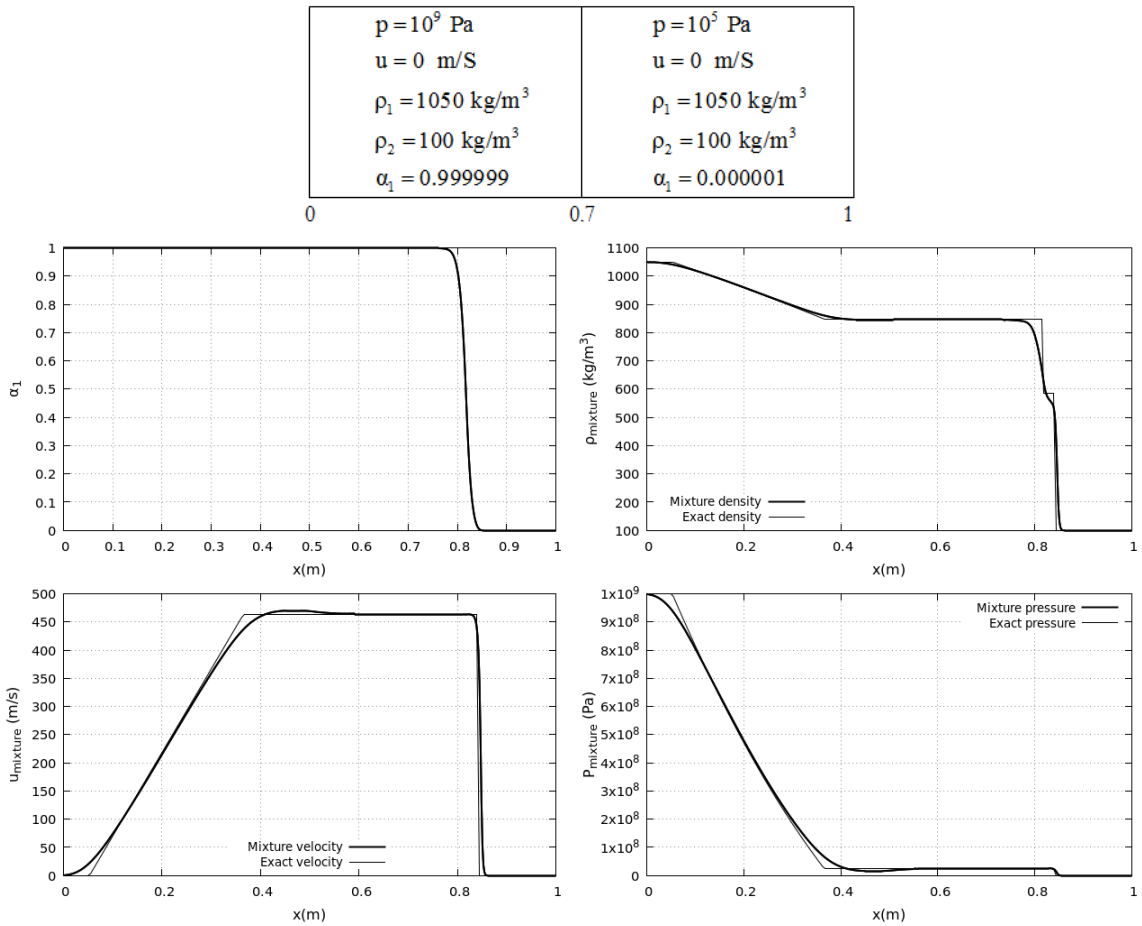

Figure I.5 – Shock tube with liquid-gas interface: high pressure liquid at left and low pressure gas at right. Computations done with 500 cells and CFL=0.5. Computed results shown at time 250µs. The Minmod flux limiter is used in the MUSCL method. Both velocities and pressure are relaxed, making the interface condition of equal pressures and velocities fulfilled.

These various results illustrate method's capabilities in several configurations far from the original design of the model, based on clouds of droplets suspended in air. It is also interesting to note that even if the liquid acoustic wave is absent of the formulation, its dynamics is correctly computed thanks to relaxation effects.

I.5.b) Shock interaction with a fluidized bed – Rogue test

We now consider a test more appropriate to the model. It consists in the fluidization of a particle cloud under shock wave interaction. Such a configuration has been studied experimentally by Rogue et al. (1998) and is summarized in Figure I.6.

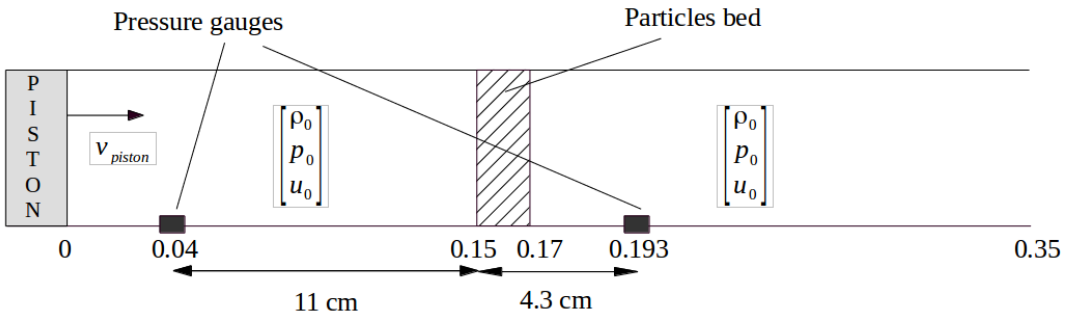

Figure I.6 – Rogue et al. (1998) fluidization shock tube test. A shock tube is filled with gas at density 1.2 kg/m^3. A dense cloud of nylon particles ($\rho_0 = 1050 \text{kg/m}^3$) is set in a cross section of the tube, with 2 cm width. The initial solid volume fraction in the particle bed is 0.65. The initial pressure is uniform initially and set at 10^5 Pa. A shock at Mach number 1.3 is created by the expansion of the high pressure gas, equivalent to a shock created by a piston moving at 151 m/s.

In this experiment pressure signals are recorded before and after the particles cloud, to examine reflected and transmitted waves through the granular media as well as its dilution and dispersion.

To account for drag effects the following correlation is used, combination of Ergun (1952) and Bernecker and Price (1974),

$$F = \frac{r_2}{d_1} C_d \left| u_2 - u_1 \right| \left(u_2 - u_1 \right)$$

with,

$$C_d = \begin{cases} \dfrac{150 a_1}{\text{Re}} + 1.75 & \text{if} \quad a_1 \geq a_{cr} \\ \dfrac{150 a_1}{\text{Re}} + 1.75 \left[\dfrac{(1 - a_{cr}) a_1}{a_1 a_2} \right]^{0.45} & \text{if} \quad (1 - a_s) \leq a_1 \leq a_{cr}, \\ \dfrac{150 a_1}{\text{Re}} + 0.3 & \text{if} \quad a_1 \leq (1 - a_s) \end{cases}$$

$R_e = \dfrac{\alpha_2 \rho_2 \left| u_2 - u_1 \right| d_1}{\mu_2}$ the particulate Reynolds number, $\alpha_{cr} = 0.63$ and $\alpha_s = \left(1 + 0.02 \dfrac{1 - \alpha_{cr}}{\alpha_{cr}} \right)^{-1}$.

The particle diameter appearing in these relations is constant ($d_1 = 1.5mm$) and the gas viscosity is $\mu_2 = 18.10^{-6}$ Pa.s.

The granular bed is made of nylon particles, treated as compressible material, governed by the SG EOS (I.5.1) with the same EOS parameters as liquid water.

Predictions of the BN, Marble and new model are compared with the same modeling of drag effects given above. The BN model, or more precisely its symmetric version with 7 waves is solved with the Furfaro and Saurel (2015) method. The Marble model is solved with the Saurel et al. (1994) method and the new model is solved with the method given in Appendix I.A.

Let us first comment Rogue et al. (1998) experimental data, typical pressure signals being shown in Figure I.7.

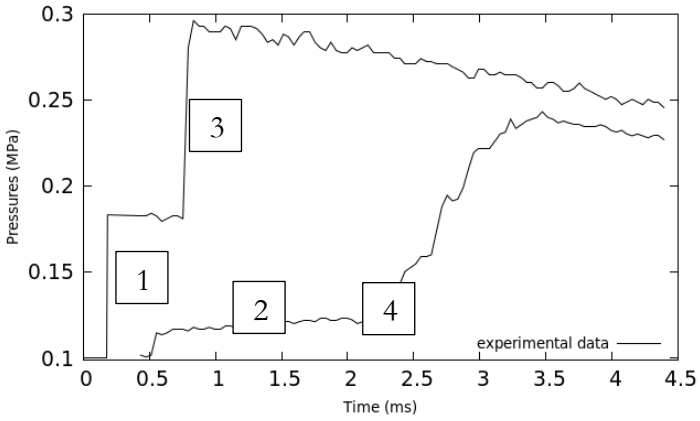

Figure I.7 – Experimental pressures signals of Rogue (1998): 1 denotes the incident shock wave, 2 denotes the transmitted shock wave/fan of compression waves, 3 denotes the reflected shock wave on the particles cloud, 4 corresponds to the arrival of the cloud upper front at the pressure gauge location.

Computed results with the various flow models are shown in Figure I.8.

(Marble) *(BN)*

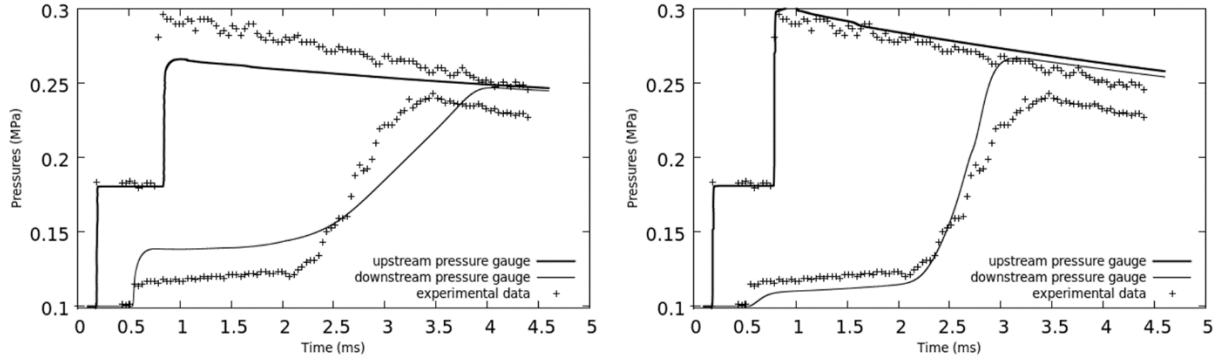

(Present model with two different options for the volume fraction equation)

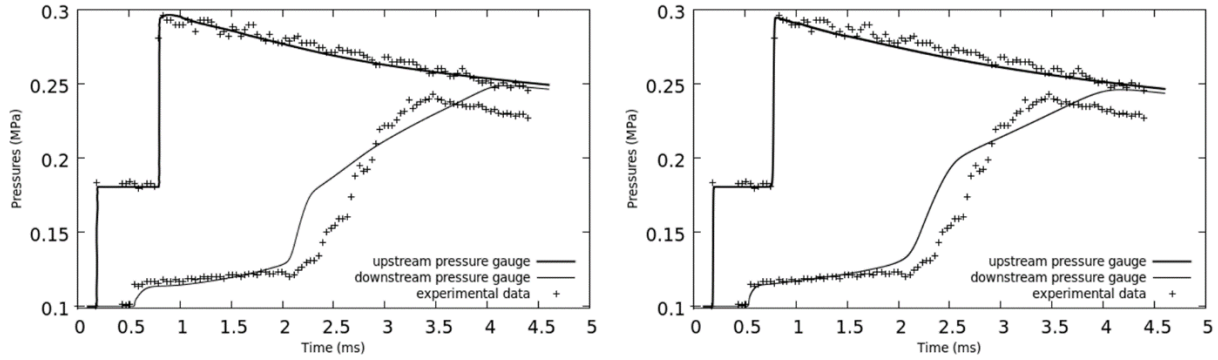

Figure I.8 – Comparison of computed results with the various models (lines) versus experimental data (symbols) for the Rogue test problem. Computations are done with 1000 cells and CFL=0.5. The Minmod flux limiter is used in the MUSCL method. Transmitted and reflected waves are badly predicted with the Marble model, and corresponding relative errors are respectively 191% and 25%. Wave transmission and reflection are better predicted with the BN model where corresponding relative errors of 35% and 4%. Wave's dynamics is considerably improved with the new model. On the figure at left, computations are done with the present model with the volume fraction equation (I.3.4). The relative errors on transmitted and reflected waves are respectively 5% and 0.9%. However, the pressure evolution in the particle cloud is still perfectible. On the graph at right equation (I.3.5) has been used instead of (I.3.4). The relative errors on transmitted and reflected waves are respectively 0.9% and 1.3%, while the pressure evolution in the particle cloud seems more accurate but again still perfectible.

It is also interesting to compare computed particle's cloud trajectories with the various models against experimental data of Rogue et al. (1998). Corresponding results are shown in Figure I.9.

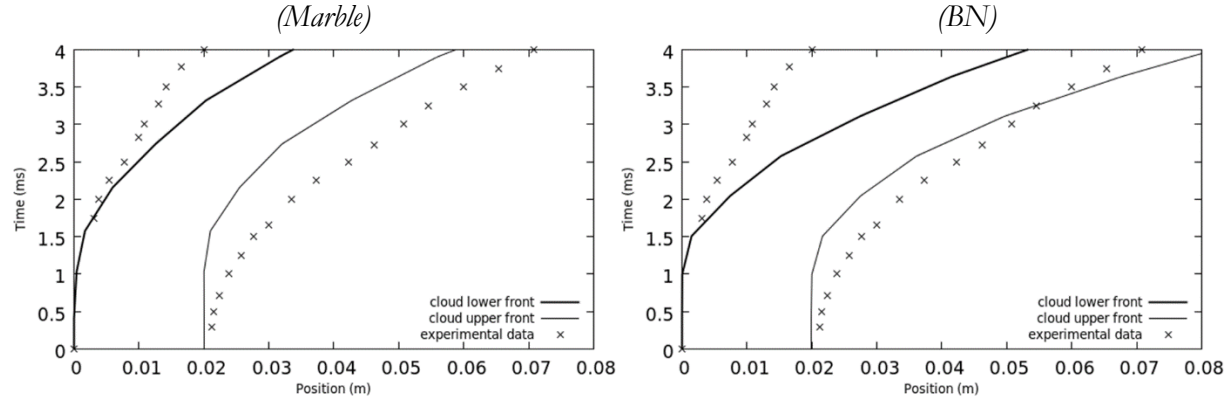

(Present model with two different options for the volume fraction equation)

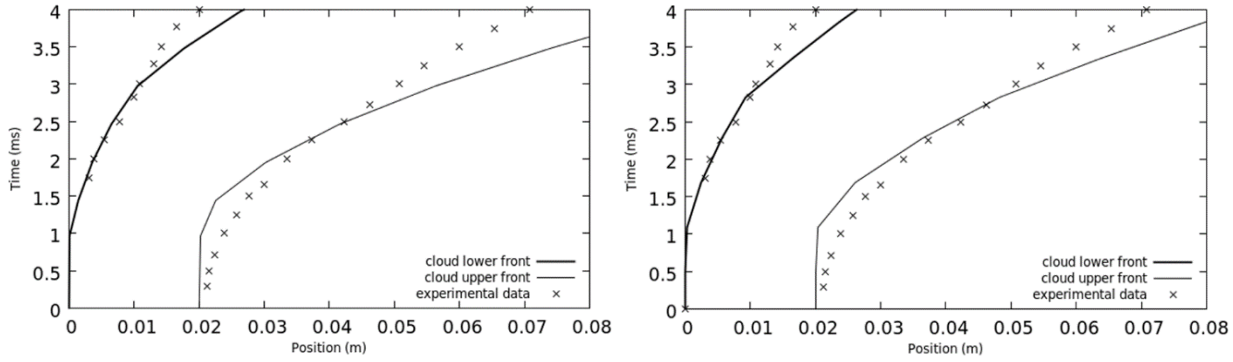

Figure I.9 – Comparison of computed results of cloud fronts trajectories with the various models (lines) versus experimental data (symbols) for the Rogue test problem. Computations are done with 1000 cells and CFL=0.5. The Minmod flux limiter is used in the MUSCL method. Both Marble and BN models present large deviations regarding cloud front trajectories while the new model, with its two variants, produces results in better agreement. On the figure at left, computations are done with the new model with the volume fraction equation (I.3.4) while on the graph at right equation (I.3.5) has been used instead.

Figure I.8 shows computed results with both equations (I.3.4) and (I.3.5) as alternatives for the volume fraction equation. When (I.3.4) is replaced by (I.3.5), in the same set of balance equations (I.4.2) the resulting wave's speeds dramatically change as,

$\lambda_{1-4} = u_2$, $\lambda_5 = u_1$, $\lambda_6 = u_1 - c_1$ and $\lambda_7 = u_1 + c_1$.

Sound now propagates in the first phase but pressure relaxation effects restore quite correct wave dynamics in both phases.

For the sake of generality, attempt for an extended formulation is addressed hereafter.

I.6 – Towards a general formulation

The new model and its symmetric variant are embedded in a general formulation. Parameters 'a' and 'b' are defined as,

$$a = \begin{cases} 1 & \text{if} \quad \alpha_1 < \alpha^{\text{fluidization}} \\ 0 & \text{otherwize} \end{cases} \qquad \text{(I.6.1)}$$

$$b = a - 1$$

Parameter $\alpha^{\text{fluidization}}$ corresponds to some fluidization limit, for example $\alpha^{\text{fluidization}} \approx 0.5$. This parameter has been used in the various computations that will be examined later. The various tests done haven't shown clear dependence of the results to this parameter.

Therefore, in this formulation 'a' and 'b' are local constants, but they vary in space as $a = a(\alpha_1)$.

The general flow model reads,

$$\frac{\partial \alpha_1}{\partial t} + a\frac{\partial \alpha_1 u_1}{\partial x} + b\frac{\partial \alpha_2 u_2}{\partial x} = \mu(p_1 - p_2), \tag{I.6.2}$$

$$\frac{\partial (\alpha\rho)_1}{\partial t} + \frac{\partial (\alpha\rho u)_1}{\partial x} = 0$$

$$\frac{\partial \alpha_1\rho_1 u_1}{\partial t} + \frac{\partial \alpha_1\rho_1 u_1^2 + \alpha_1 p_1}{\partial x} = p_I\frac{\partial \alpha_1}{\partial x} + \lambda(u_2 - u_1)$$

$$\frac{\partial \alpha_1\rho_1 E_1}{\partial t} + \frac{\partial \alpha_1\rho_1 u_1 E_1}{\partial x} + \frac{\partial \alpha_1 u_1 p_1}{\partial x} = p_I\left(a\frac{\partial \alpha_1 u_1}{\partial x} + b\frac{\partial \alpha_2 u_2}{\partial x}\right) - p_I\mu(p_1 - p_2) + \lambda u_I(u_2 - u_1) + H(T_2 - T_1)$$

$$\frac{\partial (\alpha\rho)_2}{\partial t} + \frac{\partial (\alpha\rho u)_2}{\partial x} = 0$$

$$\frac{\partial \alpha_2\rho_2 u_2}{\partial t} + \frac{\partial \alpha_2\rho_2 u_2^2 + \alpha_2 p_2}{\partial x} = p_I\frac{\partial \alpha_2}{\partial x} - \lambda(u_2 - u_1)$$

$$\frac{\partial \alpha_2\rho_2 E_2}{\partial t} + \frac{\partial \alpha_2\rho_2 u_2 E_2}{\partial x} + \frac{\partial \alpha_2 u_2 p_2}{\partial x} = -p_I\left(a\frac{\partial \alpha_1 u_1}{\partial x} + b\frac{\partial \alpha_2 u_2}{\partial x}\right) + p_I\mu(p_1 - p_2) - \lambda u_I(u_2 - u_1) - H(T_2 - T_1)$$

It admits the following additional mixture entropy equation,

$$\frac{\partial \alpha_1\rho_1 s_1 + \alpha_2\rho_2 s_2}{\partial t} + \frac{\partial \alpha_1\rho_1 s_1 u_1 + \alpha_2\rho_2 s_2 u_2}{\partial x} = \mu(p_1 - p_2)^2\left(\frac{1}{T_1} + \frac{1}{T_2}\right) + \lambda\frac{(u_2 - u_1)^2}{Z_1 + Z_2}\left(\frac{Z_2}{T_1} + \frac{Z_1}{T_2}\right) + \frac{H(T_2 - T_1)^2}{T_1 T_2}$$

guaranteeing thermodynamic consistency.

System (I.6.2) can also be written as,

$$\frac{\partial W}{\partial t} + A(W)\frac{\partial W}{\partial x} = 0,$$

with,

$$W = \left(s_1,\ \ s_2,\ \ \alpha_1,\ \ \rho_1,\ \ u_1,\ \ \rho_2,\ \ u_2\right)^T,$$

and,

$$A(W)=\begin{pmatrix} u_1 & 0 & 0 & 0 & 0 & 0 & 0 \\ 0 & u_2 & 0 & 0 & 0 & 0 & 0 \\ \frac{1}{\rho_1}\frac{\partial p}{\partial s_1}\Big)_{\rho_1} & 0 & u_1 & \frac{c_1^2}{\rho_1} & 0 & 0 & 0 \\ 0 & 0 & -b\rho_1 & u_1 & b\frac{\rho_1}{\alpha_1}(u_2-u_1) & 0 & -b\rho_1\frac{\alpha_2}{\alpha_1} \\ 0 & 0 & a\alpha_1 & 0 & (au_1-bu_2) & 0 & b\alpha_2 \\ 0 & 0 & a\rho_2\frac{\alpha_1}{\alpha_2} & 0 & a\frac{\rho_2}{\alpha_2}(u_1-u_2) & u_2 & a\rho_2 \\ 0 & \frac{1}{\rho_2}\frac{\partial p}{\partial s_2}\Big)_{\rho_2} & 0 & 0 & 0 & \frac{c_2^2}{\rho_2} & u_2 \end{pmatrix}$$

This matrix has a nice structure. Eigenvalues are given by $\det(A-\lambda I)=0$, which results in the following polynomial,

$$\Big[(u_2-\lambda)^2(u_1-\lambda)^2\big((au_1-bu_2)-\lambda\big)+(u_2-\lambda)^2bc_1^2\big((a-b)u_2-\lambda\big)+(u_1-\lambda)^2ac_2^2\big(\lambda+(b-a)u_1\big)\Big]=0$$

When a=1, b=0 it reduces to,

$$(u_1-\lambda)^3\Big[(u_2-\lambda)^2-c_2^2\Big]=0$$

with the wave speeds of the first model.

When a=0, b=-1 it reduces to,

$$\big(u_2-\lambda\big)^3\Big[(u_1-\lambda)^2-c_1^2\Big]=0$$

with the wave speeds of the symmetric model.

Therefore the flow model (I.6.2) has the following wave speeds:

$\lambda_1=u_1$, $\lambda_2=u_1+c_1$, $\lambda_3=u_1-c_1$, $\lambda_4=u_2$, $\lambda_5=u_2+c_2$ and $\lambda_6=u_2-c_2$. (I.6.3)

However, these wave speeds are not present at any point of space. They change when the volume fraction crosses the fluidization limit ($\alpha^{\text{fluidization}}$) somewhere in the domain. In nearly all computational examples considered previously, such instance happens.

Let us mention that other guesses have been considered for parameters 'a' and 'b'. For example $a=\frac{1}{2}$, $b=-\frac{1}{2}$ yields imaginary wave speeds. Same observation appeared with $a=\alpha_2$, $b=-\alpha_1$.

For numerical computations, the first equation of System (I.6.2) is expressed as,

$$\frac{\partial \alpha_1}{\partial t} + \frac{\partial \left(a \alpha_1 u_1 + b \alpha_2 u_2 \right)}{\partial x} - \left(\alpha_1 u_1 + \alpha_2 u_2 \right) \frac{\partial a}{\partial x} = 0 ,$$

It is solved with the hyperbolic solver of Appendix I.A based on the Rusanov flux. However, the wave speed estimate,

$$S = \mathrm{Max}_k \left(|\lambda_k|_{i+1}, |\lambda_k|_i \right),$$

now involves the six eigenvalues (I.6.3).

The volume fraction equation in (I.6.2) being non-conservative, appropriate scheme is needed. Similar analysis as the one described in Section V is reused. Details are given in Appendix I.B.

Let us examine typical solutions of the general model on some test problems, as those considered previously. A shock tube test case with liquid at left and gas at right is considered, in the same conditions as the test in Figure 5. Computed results are compared against exact solution in Figure I.10.

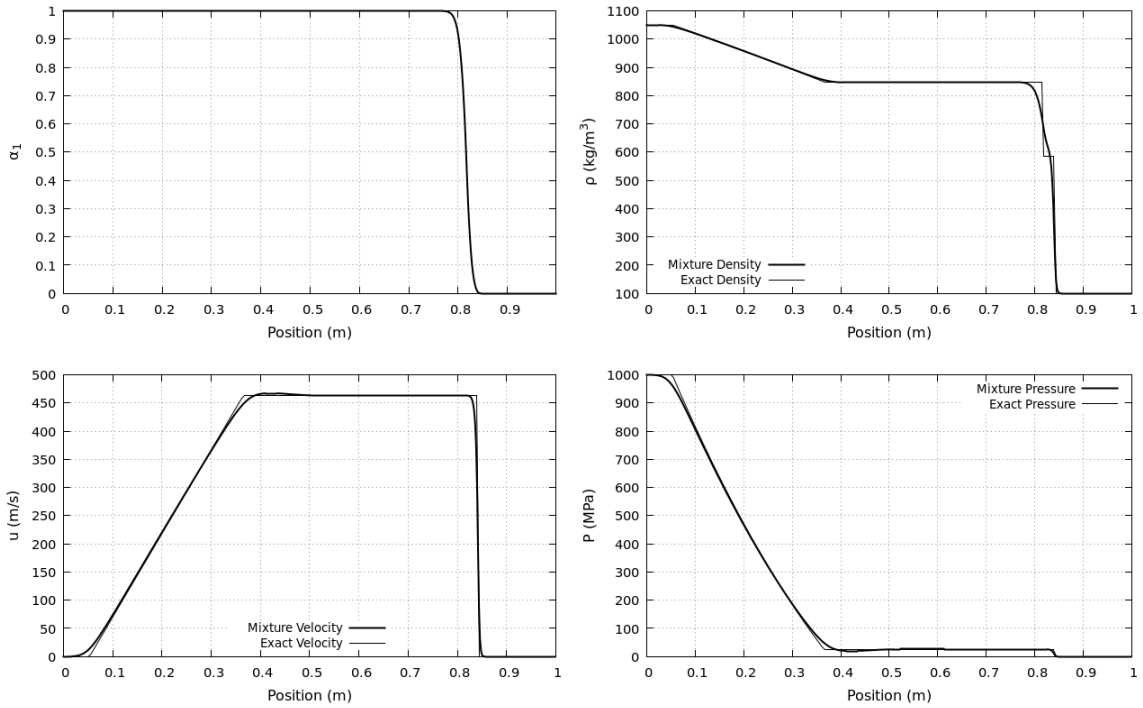

Figure I.10 – Liquid – gas shock tube test solved with the general model with stiff pressure and velocity relaxation. Computations are done with 500 cells, CFL=0.5 and Minmod limiter in the MUSCL method. Results are shown at time 250μs. The numerical solution tends to the exact one and converges better, compared to the original model (Figure I.5).

It is also interesting to address the Rogue test problem with the general model. Corresponding results are shown in Figure I.11.

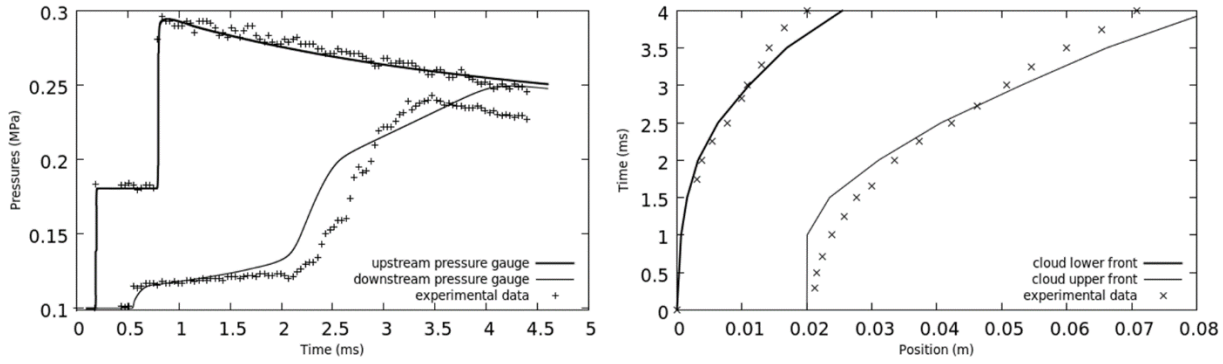

(a) (b)

Figure I.11 – (a): Computed pressure signal of the Rogue test with the general model are compared with experimental pressure records. Computations are done with 1000 cells and CFL=0.5. The various transmitted and reflected waves are correctly computed, and corresponding relative errors are respectively 0.9% and 0.9%. Pressure evolution in the particle cloud has been improved but is still perfectible. (b): Computed cloud fronts trajectories with the general model are compared with experimental records, showing good agreements.

This last test shows slight improvements in the numerical predictions regarding reflected and transmitted waves as well as particle's cloud dynamics. Possibly better agreement against experimental data could be obtained by using sophisticated drag force correlation, but this is not the scope of the present work.

Even if the BN model and the new one have the same limit model (Kapila's model) in the case of infinitely fast pressure and velocity relaxation, the transient wave dynamics between the pure gaseous shock towards a fan of compression waves has to be well captured and seems to depend on the topology of the two-phase flow. Moreover, it can be expected that the dispersive nature of a compression wave from the BN and the new models is different.

Intergranular stress (Bdzil et al., 1999, Saurel et al., 2010) has been considered as a possible effect to improve the computations of Figure I.11. These effects have been added to the present formulation and coded, but no noticeable improvement appeared. The effects of the fluidization limit switch $\alpha^{fluidization}$ as been investigated as well. Various estimates have been tested, from 0.1 to 0.9 without noticeable changes to the results.

I.7 – Conclusion

A new two-phase hyperbolic and thermodynamically consistent model has been built and typical solutions have been computed.

It is able to compute the same flow configurations as the BN model, i.e. interfaces separating pure fluids and non-equilibrium multiphase mixtures. Its acoustic properties sound physical. Moreover, the evolution of the two-phase topology directly influences both number and speed of waves present at a given point of space. The flow dynamics expressed by the model is not only reflected through the change of drag coefficient between phases, through interfacial area evolution.

It is expected that two-phase shock waves structure be easier to analyze in the present frame. It is also expected that multidimensional solutions exhibit extra differences than present one-dimensional computations, in particular regarding interface instabilities.

The present model is not supposed to be more appropriate than the BN model when dealing with packed granular beds, nor stratified and annular flows where both phases are continuous, allowing sound propagation in both phases. Also, it is not appropriate when finite rate relaxation of pressures contains important physical effects, such as pore collapse dynamics, responsible for hot spot appearance and ignition of condensed energetic materials in shock to detonation transition. The present model seems more appropriate when the phases are discontinuous and pressure relaxation stiff.

Appendix I.A. Hyperbolic solver

We address derivation of a Godunov type method for System (I.4.1-I.4.2). In the absence of source terms, it expresses in compact form as,

$$\frac{\partial U}{\partial t}+\frac{\partial F(U)}{\partial x}+H\left(U,\frac{\partial U}{\partial x}\right)=0 \qquad (A.1)$$

where,

$$U=\left(\alpha_1,\alpha_1\rho_1,\alpha_1\rho_1u_1,\alpha_1\rho_1E_1,\alpha_2\rho_2,\alpha_2\rho_2u_2,\alpha_2\rho_2E_2\right)^T,$$

$$F(U)=\begin{pmatrix}\alpha_1u_1\\ \alpha_1\rho_1u_1\\ \alpha_1\left(\rho_1u_1^2+p_1\right)\\ \alpha_1u_1\left(\rho_1E_1+p_1\right)\\ \alpha_2\rho_2u_2\\ \alpha_2\left(\rho_2u_2^2+p_2\right)\\ \alpha_2u_2\left(\rho_2E_2+p_2\right)\end{pmatrix} \text{ and } H\left(U,\frac{\partial U}{\partial x}\right)=\left(0,0,p_I\frac{\partial\alpha_1}{\partial x},p_I\frac{\partial\alpha_1u_1}{\partial x},0,-p_I\frac{\partial\alpha_1}{\partial x},-p_I\frac{\partial\alpha_1u_1}{\partial x}\right)^T.$$

The difficulty with this hyperbolic system relies in the non-conservative term $H\left(U,\frac{\partial U}{\partial x}\right)$.

For the sake of simplicity the Rusanov (1962) approximate Riemann solver is considered. It uses the following estimate for the right facing wave, at a given cell boundary separating cells i and i+1:

$$S=\mathrm{Max}_k\left(\left|\lambda_k\right|_{i+1},\left|\lambda_k\right|_i\right).$$

At a given cell boundary separating left (L) and right (R) states, the approximate flux reads,

$$F^*=\frac{1}{2}\left[F_R+F_L-S\left(U_R-U_L\right)\right] \qquad (A.2)$$

The Godunov scheme for System (A.1) necessarily reads,

$$U_i^{n+1}=U_i^n-\frac{\Delta t}{\Delta x}\left(F_{i+1/2}^*-F_{i-1/2}^*\right)+\Delta tH_i \qquad (A.3)$$

where H_i is the numerical approximation of $H\left(U,\frac{\partial U}{\partial x}\right)$, to be determined.

To determine H_i, we follow Saurel and Abgrall (1999) where a flow in uniform mechanical equilibrium is considered:

$$u_{1,i-1} = u_{1,i} = u_{1,i+1} = u_{2,i-1} = u_{2,i} = u_{2,i+1} = u > 0$$

$$p_{1,i-1} = p_{1,i} = p_{1,i+1} = p_{2,i-1} = p_{2,i} = p_{2,i+1} = p$$

Inserting the Rusanov flux (A.2) in the Godunov method (A.3) for the mass equation of the first phase, the following result is obtained:

$$(\alpha_1\rho_1)_i^{n+1} = (\alpha_1\rho_1)_i^n - \frac{u\Delta t}{2\Delta x}\left[(\alpha_1\rho_1)_{i+1} - (\alpha_1\rho_1)_{i-1}\right] + \frac{S\Delta t}{2\Delta x}\left[(\alpha_1\rho_1)_{i+1} - 2(\alpha_1\rho_1)_i + (\alpha_1\rho_1)_{i-1}\right] \qquad \text{(A.4)}$$

The same procedure is done for the momentum equation of the same phase:

$$(\alpha_1\rho_1u_1)_i^{n+1} = u\overbrace{\left[(\alpha_1\rho_1)_i^n - \frac{u\Delta t}{2\Delta x}\left[(\alpha_1\rho_1)_{i+1} - (\alpha_1\rho_1)_{i-1}\right] + \frac{S\Delta t}{2\Delta x}\left[(\alpha_1\rho_1)_{i+1} - 2(\alpha_1\rho_1)_i + (\alpha_1\rho_1)_{i-1}\right]\right]}^{(\alpha_1\rho_1)_i^{n+1}}$$
$$-\frac{\Delta t}{2\Delta x}p\left[\alpha_{1,i+1} - \alpha_{1,i-1}\right] + \Delta t H_{i,u}$$

In order that $u_{1,i}^{n+1} = u$, the non-conservative term $H_{i,u}$ must be approximated as,

$$H_{i,u} = p_i^n \frac{\alpha_{1,i+1/2}^* - \alpha_{1,i-1/2}^*}{\Delta x} \text{ with } \alpha_{1,i+\frac{1}{2}}^* = \frac{\alpha_{1,i+1} + \alpha_{1,i}}{2}. \qquad \text{(A.5)}$$

Considering the balance energy equation of the same phase the following discrete approximation is obtained:

$$\left(\alpha_1\rho_1E_1\right)_i^{n+1} = \left(\alpha_1\rho_1E_1\right)_i^n - \frac{\Delta t}{2\Delta x}\left[\left(\alpha_1u_1\left(\rho_1E_1 + p_1\right)\right)_{i+1} - \left(\alpha_1u_1\left(\rho_1E_1 + p_1\right)\right)_{i-1}\right]$$
$$+\frac{\Delta tS}{2\Delta x}\left(\left(\alpha_1\rho_1E_1\right)_{i+1} - 2\left(\alpha_1\rho_1E_1\right)_i + \left(\alpha_1\rho_1E_1\right)_{i-1}\right) + p_i^n\frac{\Delta t}{\Delta x}\left[\left(\alpha_1u_1\right)_{i+1/2}^* - \left(\alpha_1u_1\right)_{i-1/2}^*\right]$$

The same analysis as before to maintain mechanical equilibrium provides the following guess:

$$H_{i,E} = p_i^n \frac{\left(\alpha_1u_1\right)_{i+1/2}^* - \left(\alpha_1u_1\right)_{i-1/2}^*}{\Delta x} \text{ with } \left(\alpha_1u_1\right)_{i+1/2}^* = \frac{(\alpha_1u_1)_{i+1} + (\alpha_1u_1)_i}{2} \qquad \text{(A.6)}$$

The flow solver thus consists in (A.3) with (A.2), (A.5) and (A.6).

Appendix I.B. Derivation of the volume fraction numerical scheme for System (I.6.2)

The volume fraction equation,

$$\frac{\partial \alpha_1}{\partial t}+\frac{\partial\left(a\alpha_1 u_1+b\,\alpha_2 u_2\right)}{\partial x}-\left(\alpha_1 u_1+\alpha_2 u_2\right)\frac{\partial a}{\partial x}=0,$$

must have a discretization compatible with the mass equation of the same system,

$$\frac{\partial(\alpha\rho)_1}{\partial t}+\frac{\partial(\alpha\rho u)_1}{\partial x}=0.$$

In uniform velocity flows conditions, using the Rusanov flux (A.2) in the Godunov method (A.3), the discrete mass equation results in (A.4).

The same is done for the volume fraction equation,

$$(\alpha_1)_i^{n+1}=(\alpha_1)_i^n-\frac{u\Delta t}{2\Delta x}\left[(a\alpha_1+b\alpha_2)_{i+1}-(a\alpha_1+b\alpha_2)_{i-1}\right]+\frac{S\Delta t}{2\Delta x}\left[(\alpha_1)_{i+1}-2(\alpha_1)_i+(\alpha_1)_{i-1}\right]+u\Delta t\frac{\Delta a}{\Delta x} \tag{B.1}$$

where $\frac{\Delta a}{\Delta x}$ is the numerical approximation of $\frac{\partial a}{\partial x}$, to be determined.

Rearranging (B.1) with $b=a-1$ and $\alpha_2=1-\alpha_1$ the discrete volume fraction equation becomes,

$$(\alpha_1)_i^{n+1}=(\alpha_1)_i^n-\frac{u\Delta t}{2\Delta x}\left[\alpha_{1i+1}-\alpha_{1i-1}\right]-\frac{u\Delta t}{2\Delta x}\left[a_{i+1}-a_{i-1}\right]+\frac{S\Delta t}{2\Delta x}\left[(\alpha_1)_{i+1}-2(\alpha_1)_i+(\alpha_1)_{i-1}\right]+u\Delta t\frac{\Delta a}{\Delta x} \tag{B.2}$$

Let us now consider the particular case of uniform density field: $\rho_{1,i}^{\,n}=\rho_{1,i+1}^{\,n}=\rho_{1,i-1}^{\,n}$.

Both velocity and density being uniform, the density at the next time step must be invariant: $\rho_{1,i}^{\,n+1}=\rho_{1,i}^{\,n}$. In this context, the mass equation becomes,

$$(\alpha_1\rho_1)_i^{n+1}=\rho_1\left\{(\alpha_1)_i^n-\frac{u\Delta t}{2\Delta x}\left[(\alpha_1)_{i+1}-(\alpha_1)_{i-1}\right]+\frac{S\Delta t}{2\Delta x}\left[(\alpha_1)_{i+1}-2(\alpha_1)_i+(\alpha_1)_{i-1}\right]\right\} \tag{B.3}$$

In order that (B.2) and (B.3) be compatible it is necessary that,

$$-\frac{u\Delta t}{2\Delta x}\left[a_{i+1}-a_{i-1}\right]+u\Delta t\frac{\Delta a}{\Delta x}=0$$

Therefore,

$$\frac{\Delta a}{\Delta x} = \frac{a_{i+1} - a_{i-1}}{2\Delta x} \tag{B.4}$$

or,

$$\frac{\Delta a}{\Delta x} = \frac{a^*_{i+1/2} - a^*_{i-1/2}}{\Delta x},$$

with $a^*_{i+1/2} = \frac{a^n_{i+1} + a^n_i}{2}$.

Consequently the volume fraction scheme reads,

$$\alpha^{n+1}_{1,i} = \alpha^n_{1,i} - \frac{\Delta t}{\Delta x}\left(F^*_{\alpha i+1/2} - F^*_{\alpha i-1/2}\right) + \left(\alpha_1 u_1 + \alpha_2 u_2\right)^n_i \Delta t \frac{\Delta a}{\Delta x} \tag{B.5}$$

with ,

$F^*_{\alpha i+1/2} = \frac{1}{2}\left[\left(a\alpha_1 u_1 + b\alpha_2 u_2\right)^n_{i+1} + \left(a\alpha_1 u_1 + b\alpha_2 u_2\right)^n_i - S\left(\alpha^n_{1,i+1} - \alpha^n_{1,i}\right)\right]$ and $\frac{\Delta a}{\Delta x}$ given by (B.4).

Energy equations have to be considered as well. Let us consider the one of the first phase,

$$\frac{\partial \alpha_1 \rho_1 E_1}{\partial t} + \frac{\partial \alpha_1 u_1 \left(\rho_1 E_1 + p_1\right)}{\partial t} = -p_I \frac{\partial \alpha_1}{\partial t}.$$

Using the volume fraction equation it becomes,

$$\frac{\partial \alpha_1 \rho_1 E_1}{\partial t} + \frac{\partial \alpha_1 u_1 \left(\rho_1 E_1 + p_1\right)}{\partial t} = -p_I \left(-\frac{\partial\left(a\alpha_1 u_1 + b\alpha_2 u_2\right)}{\partial x} + \left(\alpha_1 u_1 + \alpha_2 u_2\right)\frac{\partial a}{\partial x}\right).$$

Discrete approximations of the non-conservative terms $p_I \frac{\partial\left(a\alpha_1 u_1 + b\alpha_2 u_2\right)}{\partial x}$ and $p_I\left(\alpha_1 u_1 + \alpha_2 u_2\right)\frac{\partial a}{\partial x}$ have to be determined. To be compatible with the volume fraction equation of the same system, discretization of the term $\frac{\partial a}{\partial x}$ is given by (B.4).

The discrete approximation of $\frac{\partial\left(a\alpha_1 u_1 + b\alpha_2 u_2\right)}{\partial x}$ reads,

$$\frac{\Delta\left(a\alpha_1 u_1 + b\alpha_2 u_2\right)}{\Delta x} = \frac{\left(a\alpha_1 u_1 + b\alpha_2 u_2\right)^*_{i+1/2} - \left(a\alpha_1 u_1 + b\alpha_2 u_2\right)^*_{i-1/2}}{\Delta x}$$

with $\left(a\alpha_1 u_1 + b\alpha_2 u_2\right)^*_{i+1/2} = \frac{\left(a\alpha_1 u_1 + b\alpha_2 u_2\right)^n_{i+1} + \left(a\alpha_1 u_1 + b\alpha_2 u_2\right)^n_i}{2}$. (B.6)

Chapter II

Riemann solver with internal reconstruction (RSIR) for compressible single-phase and non-equilibrium two-phase flows

Numerical resolution of the new model is addressed in this chapter through a new Riemann solver with internal reconstruction (RSIR), based on the Linde (2002) method.

First, this method is reconsidered and improved in 1D in the frame of the Euler equations.

It is then extended to the new compressible dense and dilute two-phase flows model of the previous chapter. This model poses serious difficulties as it is weakly hyperbolic and only valid in the limit of stiff pressure relaxation, implying non-self-similar solutions. Thanks to the internal reconstruction approach, a low dissipative Riemann solver is built for the new model.

This numerical method is used to solve solid particles jet instabilities, showing possible explanation of their creation process.

Abstract

A new Riemann solver is built to address numerical resolution of complex flow models. The research direction is closely linked to a variant of the Baer and Nunziato (1986) model developed in Saurel et al. (2017a). This recent model provides a link between the Marble (1963) model for two-phase dilute suspensions and dense mixtures. As in the Marble model, Saurel et al. system is weakly hyperbolic with the same 4 characteristic waves, while the system involves 7 partial differential equations. It poses serious theoretical and practical issues to built simple and accurate flow solver. To overcome related difficulties the Riemann solver of Linde (2002) is revisited. The method is first examined in the simplified context of compressible Euler equations. Physical considerations are introduced in the solver improving robustness and accuracy of the Linde method. With these modifications the flow solver appears as accurate as the HLLC solver of Toro et al. (1994). Second the two-phase flow model is considered. A locally conservative formulation is built and validated removing issues related to non-conservative terms. However, two extra major issues appear from numerical experiments: The solution appears not self-similar and multiple contact waves appear in the dispersed phase. Building HLLC-type or any other solver appears consequently challenging. The modified Linde (2002) method is thus examined for the considered flow model. Some basic properties of the equations are used, such as shock relations of the dispersed phase and jump conditions across the contact wave. Thanks to these ingredients the new Riemann solver with internal reconstruction (RSIR), modification of the Linde method, handles stationary volume fraction discontinuities, presents low dissipation for transport waves and handles shocks and expansion waves accurately. It is validated on various test problems showing method's accuracy and versatility for complex flow models. Its capabilities are illustrated on a difficult two-phase flow instability problem, unresolved before.

II.1 – Introduction

The present contribution addresses building of a robust Riemann solver with limited dissipation for complex flow models. The reconstruction method of Linde (2002) is revisited and improved in terms of accuracy and robustness. This effort is mainly motivated by the numerical approximation of a two-phase non-equilibrium flow model developed by the authors that involves a series of theoretical challenges, presented in the following. In the present introduction the modelling context is recalled first, and the numerical approach is introduced secondly.

Modelling context

It is well accepted that hyperbolic models are mandatory to deal with phenomena involving wave propagation. This is the case for multiphase flows in many situations such as in particular shocks and detonations propagation in granular explosives and in fuel suspensions, as well as liquid-gas mixtures with bubbles, cavitating and flashing flows, as soon as motion is intense and governed by pressure gradients. This is thus the case of most unsteady two-phase flow situations.

Wave propagation is important as it carries pressure, density and velocity disturbances. Sound propagation is also very important as it determines critical (choked) flow conditions and associated mass flow rates. It has also fundamental importance on sonic conditions of detonation waves when the two-phase mixture is exothermically reacting (Petitpas et al., 2009).

Hyperbolicity is also related to the causality principle, meaning that initial and boundary conditions are responsible of time evolution of the solution. When dealing with first-order partial differential equations it means that the Riemann problem must have a solution, and the Riemann problem is correctly posed only if the equations are hyperbolic.

However, only a few two-phase flow models are hyperbolic in the whole range of parameters. The Baer and Nunziato (1986) model (BN) seemed the only formulation able to deal with such requirement. However, in the dilute limit at least, the acoustic properties of this model seemed inconsistent (Lhuillier et al., 2013). Indeed, with this model, the dispersed phase sound speed corresponds to the one of the pure phase, while this phase is not continuous and unable to propagate sound in reality, at least at a scale larger than particle's one. When the phase is not continuous (dispersed drops in a gas, dispersed bubbles in a liquid), the associated sound speed should vanish, such effect being absent in the formulation.

In the low particle's concentration limit, the Marble (1963) model is preferred. This model corresponds to the Euler equations with source terms for the gas phase and pressureless gas dynamic equations for the particle phase (see also Zeldovich, 1970). This model is thermodynamically consistent and hyperbolic as well, except that the particle phase equations are weakly hyperbolic. In this model, contrarily to the BN model, sound doesn't propagate in the particles phase, this behaviour being more physical in this limit. However, the Marble model has a limited range of validity as the volume of the dispersed phase is neglected, this assumption having sense only for low (less than per cent) condensed phase volume fraction.

Recently, the gap between these two models has been filled (Saurel et al., 2017a). Modifying the volume fraction equation in the BN model resulted in a flow model where sound propagates only in the carrier

phase. The model is hyperbolic with same 4 wave speeds as Marble's one and is thermodynamically consistent in the stiff pressure relaxation limit. Moreover, in the stiff velocity relaxation limit, the Kapila et al. (2001) model, important for diffuse interface computations (Saurel and Pantano, 2018), is recovered.

Saurel et al. (2017a) model has been solved in the same reference with a Godunov type scheme based on Rusanov (1961) solver. However, as well known, this solver is quite diffusive for stationary discontinuities and linearly degenerate fields, such as in the present context, volume fraction discontinuities and contact waves. This is precisely the motivation of the present work, focused on the building of a Riemann solver with enhanced accuracy.

Riemann solver with internal reconstruction (RSIR)

In the quest of Riemann solver with low dissipation for this flow model several issues appear:

- The flow model, as most two-phase flow models, presents non-conservative terms;
- Numerical experiments of typical initial value problems (IVPs) achieved with the Godunov-Rusanov method exhibit non self-similar solutions. Such behavior appears as a combination of non-conservative terms, acting as a drag force (in differential form), and stiff pressure relaxation, mandatory for this specific flow model.
- Governing equations of the dispersed phase are hyperbolic degenerate, as a single eigenvalue is responsible for characteristic waves propagation. Therefore, it is impossible to determine a basis of eigenvectors and associated Riemann invariants. Moreover, the solution can be multivalued, as for the Marble's model (Saurel et al., 1994). It means that multiple volume fraction waves may be present in the solution, rendering the analysis and design of any Riemann solver intricate.

Several attempts for the building of approximate Riemann solver were done by the authors for this flow model on the basis of,

- characteristic relations for the carrier phase and jump conditions for the dispersed one,
- HLLC-type approximation based on a local conservative formulation, that will be presented later.

None of these attempts yielded efficient solver. The authors consequently move to another type of solver, based on internal reconstruction of intermediate states, computed from a simple and robust intercell state, such as Rusanov (1961) or HLL (Harten et al., 1983). This research direction has been investigated by Linde (2002), Miyoshi and Kusano (2005) and many others, mainly in the frame of

magnetohydrodynamics equations that also involve many waves in the Riemann problem. The aim is to build two intermediate states instead of one. Doing so, the method should maintain stationary discontinuities and reduce numerical diffusion during simple transport.

The underlying philosophy of this approach relies on the assumption that most of the physics is present in the two extreme waves and only one contact wave, that has to be identified. If the contact wave cannot be defined clearly, the method becomes irrelevant. But it seems that in most flow models such as the Euler equations, MHD (e.g. Balsara, 2012), compressible solid mechanics (e.g. Gavrilyuk et al., 2008), and the present two-phase model, identification of the contact wave is possible. The remaining waves, when present, are captured by the scheme during computations even if they are omitted in the RP. This is the same philosophy as the Rusanov and HLL solvers, except that an extra intermediate wave is added.

In the present work the Linde method is revisited, and extra physics is embedded to enhance robustness and accuracy. This is done to the price of generality loss, in the sense that the method becomes model dependent, as most Riemann solvers.

The Linde (2002) method is recalled in Section II.2 in its basic version and computational examples are shown with the Euler equations. It sometimes works perfectly, but oscillations appear depending on the initial conditions. This observation motivates insertion of extra physics in the solver, resulting in significant improvements, yielding robust and accurate solutions. Similar accuracy and robustness as the HLLC solver are observed.

In Section II.3 the internal reconstruction method is extended to the two-phase flow model of interest. As before extra physics is inserted in the closure relations. The (trivial) Rankine-Hugoniot relations of the dispersed phase are used as well as jump conditions across contact wave of the dispersed phase. Thanks to these ingredients the flow solver becomes very efficient. One-dimensional computational examples are shown in the same section.

The method is then embedded in the DALPHADT unstructured meshes code. It is used to compute fingering instability occurring during explosive dispersion of particle clouds. Such instability seems misunderstood and not reproduced by existing flow models. Intensive experimental and numerical studies were done in this area recently, as for example in Rodriguez et al. (2013), McGrath et al. (2018), Osnes et al. (2018) and Xue et al. (2018). Thanks to the new model and present numerical method, the formation stage of this instability seems correctly predicted at least qualitatively. Computational examples are shown in Section II.4. Conclusions are given in Section II.5.

II.2 – Riemann solver with internal reconstruction (RSIR) for the Euler equations

The Riemann solver with internal reconstruction is a modification of the Linde (2002) solver. The original Linde solver is recalled in the frame of the Euler equations and modifications are addressed next.

The Euler equations of compressible fluids consist in a system of conservation laws,

$$\frac{\partial U}{\partial t}+\frac{\partial F}{\partial x}=0 \qquad \text{(II.2.1)}$$

with $U=(\rho, \rho u, \rho E)^T$ and $F=(\rho u, \rho u^2+p, (\rho E+p)u)^T$ where ρ denotes the density, u the velocity and $E(=e+\frac{1}{2}u^2)$ the total energy. The pressure p is given by a convex equation of state (EOS), as a function for example of internal energy e and density ρ : $p=p(\rho,e)$. The stiffened gas (SG) EOS will be used frequently in the present contribution as,

$$p(\rho,e)=(\gamma-1)\rho e-\gamma p_\infty,$$

where γ and p_∞ are typical constants for a given fluid.

This system is strictly hyperbolic with wave's speeds $\lambda_1=u$, $\lambda_2=u-c$ et $\lambda_3=u+c$. The sound speed is defined by $c=\sqrt{\left(\frac{\partial p}{\partial \rho}\right)_s}$ where s denotes the entropy.

The various reconstruction methods considered in the present paper are based on HLL (Harten et al., 1983) approximate solution, or its simplified version by Rusanov (1961). In the HLL solver, the extreme waves only are used, and their speeds are estimated as Davis (1988),

$$S_L=\min(u_L-c_L, u_R-c_R) \text{ and } S_R=\max(u_L+c_L, u_R+c_R), \qquad \text{(II.2.2)}$$

where subscripts L and R denote the left and right states in the initial data of the Riemann problem.

The intermediate HLL state is a consequence of the Rankine-Hugoniot relations of System (II.2.1) applied across the left and right facing waves propagating at speeds S_L and S_R respectively:

$$U^*_{HLL}=\frac{F_R-F_L+S_L U_L-S_R U_R}{S_L-S_R} \qquad \text{(II.2.3)}$$

From this state, the aim is now to reconstruct two intermediate states, as illustrated in Figure II.1 and linked through Relation (II.2.4):

$$(S_R-S_L)U^*_{HLL}=(S_R-S_M)U^*_R+(S_M-S_L)U^*_L. \qquad \text{(II.2.4)}$$

Relation (II.2.4) can be expressed as,

$$U^*_{HLL} = \omega_R U^*_R + \omega_L U^*_L,$$

with $\omega_R = \dfrac{S_R - S_M}{S_R - S_L}$ and $\omega_L = \dfrac{S_M - S_L}{S_R - S_L}$.

The contact wave speed is given by,

$$S_M = \frac{p_R - p_L + (\rho u)_L (S_L - u_L) - (\rho u)_R (S_R - u_R)}{\rho_L (S_L - u_L) - \rho_R (S_R - u_R)},$$

Relation (II.2.4) involves two unknown states, U^*_L and U^*_R. Consequently, an extra relation is needed. Linde (2002) postulate is considered first.

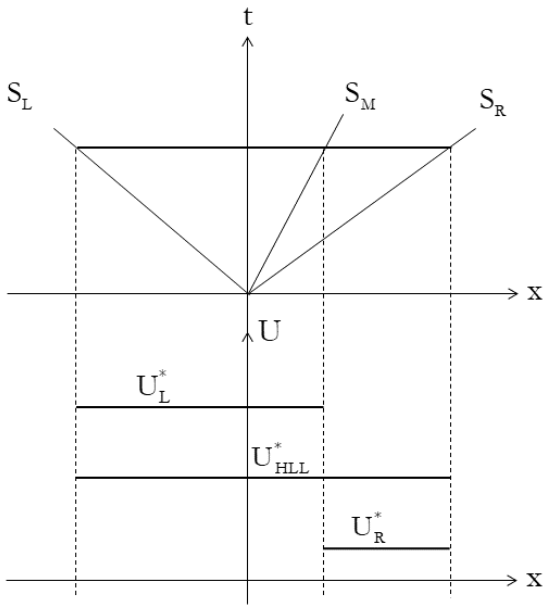

Figure II.1 – Schematic representation of the two intermediate states U^*_L and U^*_R rebuilt from U^*_{HLL}.

II.2.a) Linde reconstruction

Linde reconstruction is based on the following relation,

$$U^*_R - U^*_L = \beta (U_R - U_L) \qquad \text{(II.2.5)}$$

where β represents a viscosity parameter, $0 \le \beta \le 1$.

When β is taken equal to zero, the HLL approximation is recovered. When $\beta = 1$ the reconstruction tends to the HLLC representation but is not equivalent, as interface conditions are ignored in this approach. It is worth to note that when $\beta = 1$, isolated density discontinuities are preserved, an important property in CFD solvers.

Relation (II.2.5) is then combined to Relation (II.2.4) resulting in:

$$\begin{cases} U_L^* = U_{HLL}^* - \omega_R \beta (U_R - U_L) \\ U_R^* = U_{HLL}^* + \omega_L \beta (U_R - U_L) \end{cases} \quad \text{(II.2.6)}$$

Once states U_L^* and U_R^* are computed the various fluxes are computed through the Rankine-Hugoniot relations,

$$\begin{cases} F_R^* = F_R + S_R \left(U_R^* - U_R \right) \\ F_L^* = F_L + S_L \left(U_L^* - U_L \right) \end{cases} . \quad \text{(II.2.7)}$$

Solution sampling is achieved through,

$$F^* = \begin{cases} F_L \ \text{ if } \ S_L \geq 0 \\ F_L^* \ \text{ if } \ S_L < 0 \ \text{ and } \ S_M \geq 0 \\ F_R^* \ \text{ if } \ S_R > 0 \ \text{ and } \ S_M < 0 \\ F_R \ \text{ if } \ S_R \leq 0 \end{cases} .$$

Typical solutions obtained by this solver embedded in a Godunov-type code are shown hereafter. Let us first consider the transport of a density discontinuity in a uniform velocity and pressure flow with a gas governed by the ideal gas EOS with $\gamma = 1.4$. Corresponding results are shown in Figure II.2.

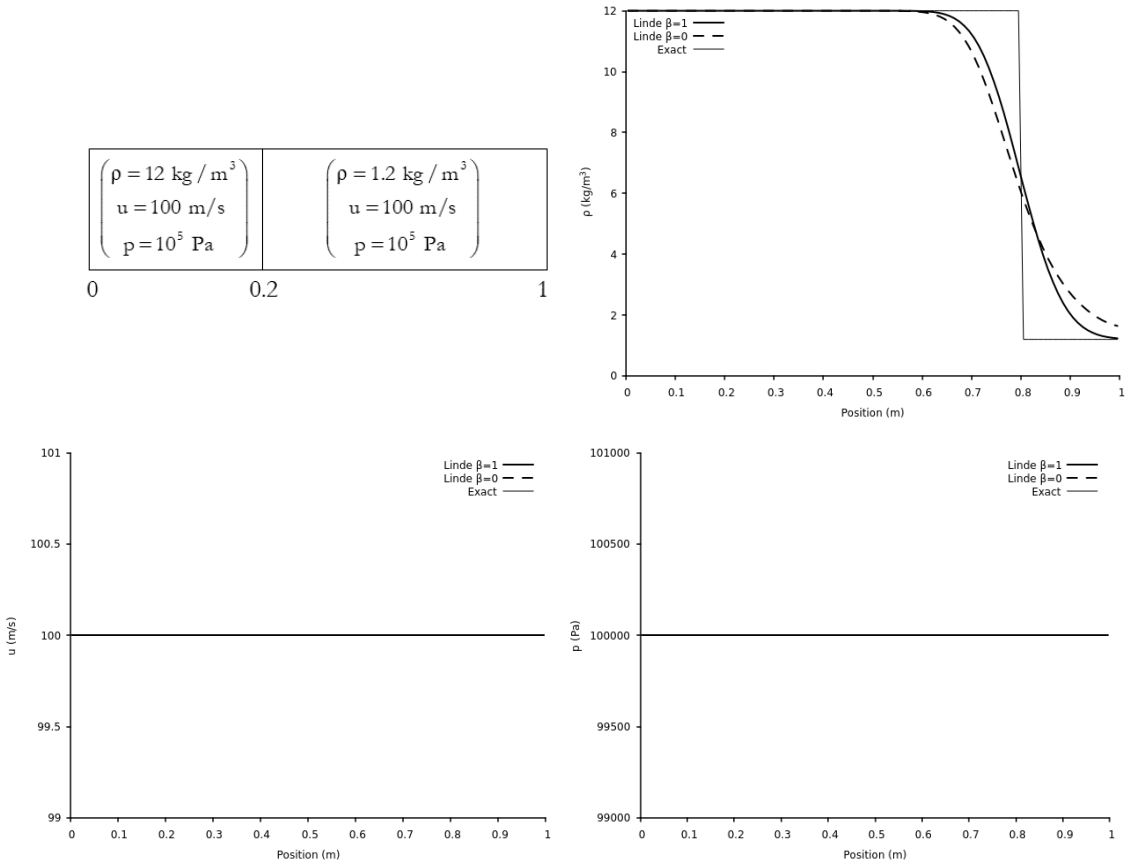

Figure II.**2** – Computed results with the original Linde solver for the transport of a density discontinuity in a uniform pressure and velocity flow. The first-order Godunov scheme is used with 100 computational cells and $\mathbf{CFL = 0.9}$. Results are shown at time t=6 ms. The density discontinuity is correctly transported, and mechanical equilibrium is maintained.

Second, a shock tube test problem is examined in Figure II.3.

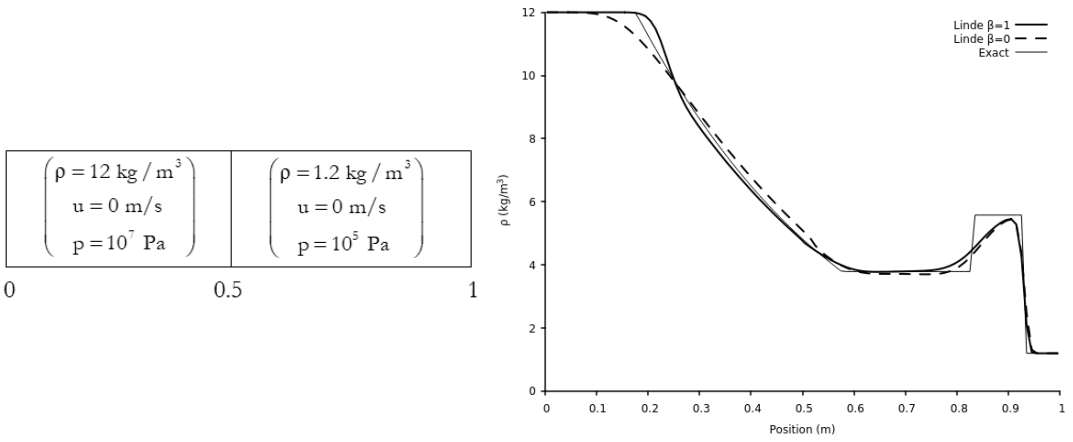

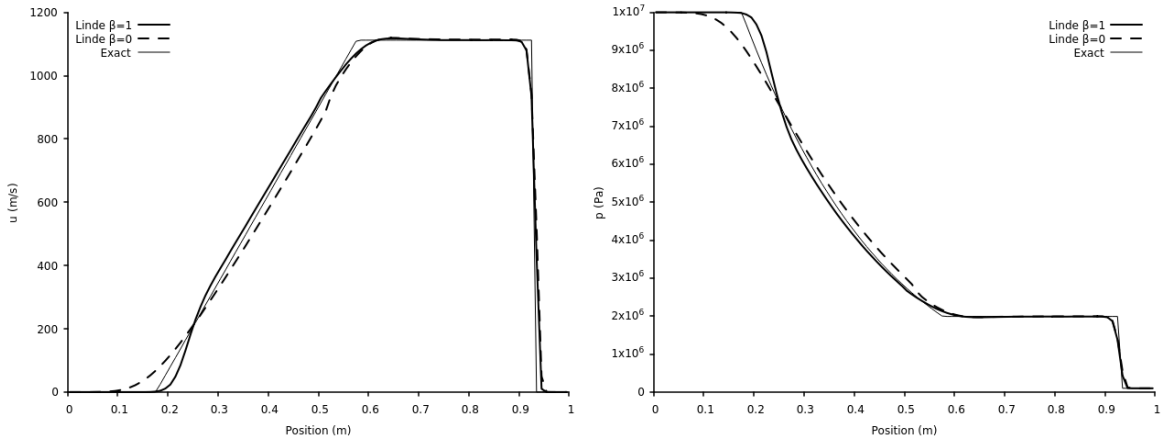

Figure II.3 – Computed results with the original Linde solver for a shock tube test case. The first-order Godunov scheme is used with 100 computational cells and $\mathrm{CFL} = 0.9$. Results are shown at time t=300 μs. The various waves and states are computed correctly.

Third, a double expansion test is considered in Figure II.4.

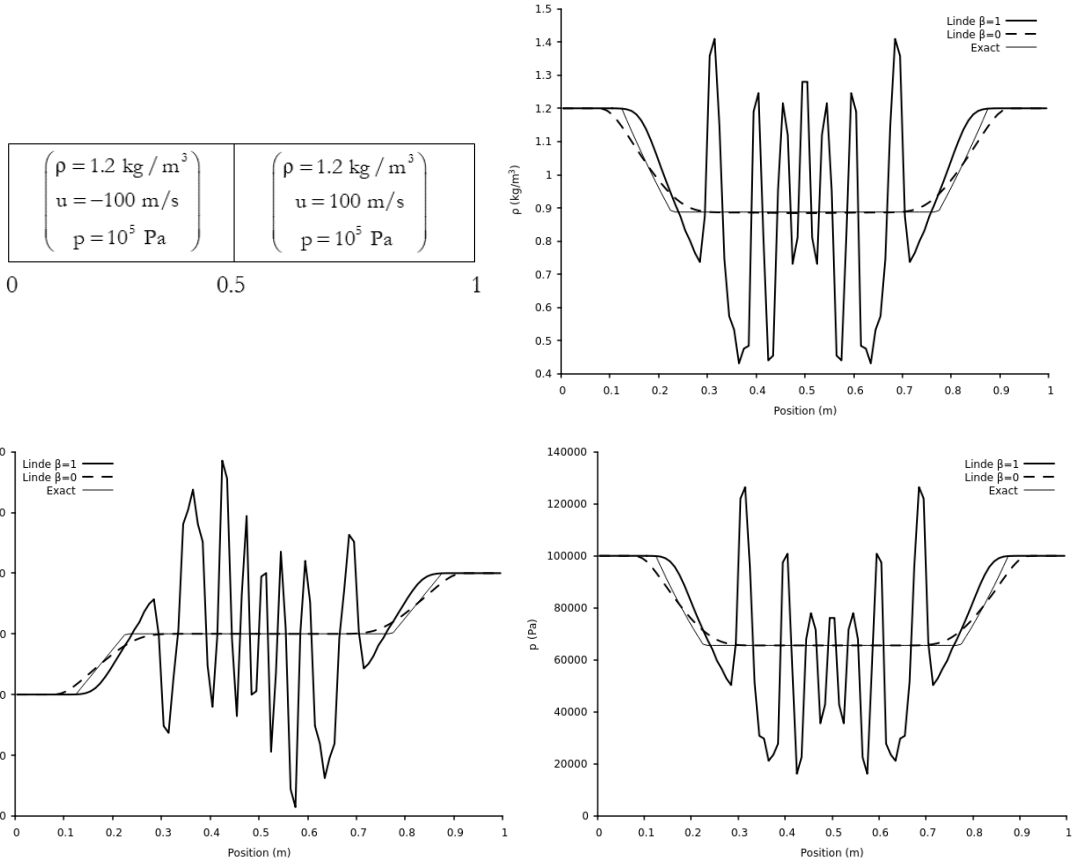

Figure II.4 – Computed results with the original Linde solver for a double expansion test case. The first-order Godunov scheme is used with 100 computational cells and CFL=0.9. Results are shown at time t=850 μs. Oscillations appear when β=1.

Results of Figure II.4 clearly show limitations of the method when (II.2.5) is used as a closure relation. Decreasing parameter β makes the method tend to the HLL solver and yields weaker oscillations but those remain present nonetheless (at least for this test). When $\beta = 0$ the HLL solution state is recovered but so are corresponding deficiencies for stationary contact discontinuities and transport at constant speed.

Same limitations and even more unstable solutions appear for double shock tests, just reversing the velocities in the initial data of Figure II.4 test.

Accuracy of the conventional Linde method is consequently highly dependent on initial data and viscosity parameter β. It is worth mentioning that in Linde (2002) a method is given to determine β as a parameter vector to improve the solution. But it is important to note that as soon as β is strictly less than 1, the solver loses its ability to preserve isolated stationary discontinuities. Modification of this solver is thus addressed in the next paragraph.

II.2.b) New reconstruction method (RSIR)

The reconstruction derived hereafter is based on two ingredients:

- Quasi-isentropic variations across right and left-facing waves;
- Interface conditions across the contact wave.

Although not strictly correct, in particular across strong shocks, thermodynamic evolutions through right and left-facing waves are approximated as isentropic. Isentropic evolutions are themselves approximated through sound speed definition and trapezoidal approximation as,

$$\bar{c}^2 = \frac{p_R^* - p_R}{\rho_R^* - \rho_R}, \qquad \text{(II.2.8)}$$

$$\bar{c}^2 = \frac{p_L^* - p_L}{\rho_L^* - \rho_L},$$

where,

$$\bar{c} = \frac{1}{2}\left(c_L + c_R\right).$$

Across the contact wave S_M, the interface pressure condition reads,

$$p_L^* = p_R^* = p^*.$$

System (II.2.8) becomes,

$$p^* = p_R + \bar{c}^2\left(\rho_R^* - \rho_R\right), \qquad \text{(II.2.9)}$$

$$p^* = p_L + \bar{c}^2\left(\rho_L^* - \rho_L\right).$$

Taking the difference of these two relations, the following one is obtained:

$$\rho_R^* - \rho_L^* = \rho_R - \rho_L - \frac{p_R - p_L}{\bar{c}^2}. \tag{II.2.10}$$

This relation corresponds to a modification of the first relation of System (II.2.5).

To maintain flexibility of the reconstruction method, parameter β is reintroduced as,

$$\rho_R^* - \rho_L^* = \beta\left(\rho_R - \rho_L + \frac{p_L - p_R}{\bar{c}^2}\right) = \Psi_{mass}. \tag{II.2.11}$$

Parameter β can be convenient to control numerical viscosity. In all computational tests addressed in the present contribution, unless stated otherwise, $\beta = 1$.

Combining (II.2.6) and (II.2.11) intermediate density states are obtained as,

$$\begin{cases} \rho_L^* = \rho_{HLL}^* - \omega_R\beta\left(\rho_R - \rho_L + \dfrac{p_L - p_R}{\bar{c}^2}\right), \\ \rho_R^* = \rho_{HLL}^* + \omega_L\beta\left(\rho_R - \rho_L + \dfrac{p_L - p_R}{\bar{c}^2}\right). \end{cases} \tag{II.2.12}$$

Determination of the intermediate states related to the momentum is now addressed. From (II.2.11) similar relation is deduced for momentum jump across the contact wave. As $u_L^* = u_R^* = S_M$, (II.2.11) implies,

$$(\rho u)_R^* - (\rho u)_L^* = \beta\left(\rho_R - \rho_L + \frac{p_L - p_R}{\bar{c}^2}\right)S_M = \Psi_{momentum}. \tag{II.2.13}$$

Combining (II.2.6) and (II.2.13) the intermediate momentum states are obtained as,

$$\begin{cases} (\rho u)_L^* = (\rho u)_{HLL}^* - \omega_R\beta\left(\rho_R - \rho_L + \dfrac{p_L - p_R}{\bar{c}^2}\right)S_M, \\ (\rho u)_R^* = (\rho u)_{HLL}^* + \omega_L\beta\left(\rho_R - \rho_L + \dfrac{p_L - p_R}{\bar{c}^2}\right)S_M. \end{cases} \tag{II.2.14}$$

Determination of the intermediate states related to the energy is now addressed. As star densities are known form (II.2.12), star pressures are determined by same approximate isentropic relations (II.2.9). Summing the two star pressures (II.2.9) to preserve symmetry, the following relation is obtained,

$$p^* = \frac{p_L + p_R}{2} + \bar{c}^2\left(\frac{\rho_L^* + \rho_R^*}{2} - \frac{\rho_L + \rho_R}{2}\right). \tag{II.2.15}$$

The energy jump across the contact wave is approximated thanks to (II.2.12) and (II.2.15) and the EOS,

$$\begin{cases} \left(\rho E\right)_L^* = \rho_L^* \left(e\left(p^*, \rho_L^*\right) + \frac{1}{2} S_M^2 \right), \\ \left(\rho E\right)_R^* = \rho_R^* \left(e\left(p^*, \rho_R^*\right) + \frac{1}{2} S_M^2 \right). \end{cases} \tag{II.2.16}$$

The energy jump finally reads,

$$\left(\rho E\right)_R^* - \left(\rho E\right)_L^* = \rho_R^* \left(e\left(p^*, \rho_R^*\right) + \frac{1}{2} S_M^2 \right) - \rho_L^* \left(e\left(p^*, \rho_L^*\right) + \frac{1}{2} S_M^2 \right) = \Psi_{\text{energy}},$$

(II.2.17)

and the intermediate energy states read,

$$\begin{cases} \left(\rho E\right)_L^* = \left(\rho E\right)_{HLL}^* - \omega_R \left[\rho_R^* \left(e\left(p^*, \rho_R^*\right) + \frac{1}{2} S_M^2 \right) - \rho_L^* \left(e\left(p^*, \rho_L^*\right) + \frac{1}{2} S_M^2 \right) \right], \\ \left(\rho E\right)_R^* = \left(\rho E\right)_{HLL}^* + \omega_L \left[\rho_R^* \left(e\left(p^*, \rho_R^*\right) + \frac{1}{2} S_M^2 \right) - \rho_L^* \left(e\left(p^*, \rho_L^*\right) + \frac{1}{2} S_M^2 \right) \right]. \end{cases} \tag{II.2.18}$$

Note that parameter β is included in $\rho_{L,R}^*$. Note also that (II.2.16) does not depend on the form of the EOS.

Once states $\mathbf{U}_L^*$ and $\mathbf{U}_R^*$ are computed the various fluxes are computed through the Rankine-Hugoniot relations, according to the sign of S_M,

$$\begin{cases} \mathbf{F}_R^* = \mathbf{F}_R + S_R \left(\mathbf{U}_R^* - \mathbf{U}_R \right), \\ \mathbf{F}_L^* = \mathbf{F}_L + S_L \left(\mathbf{U}_L^* - \mathbf{U}_L \right). \end{cases}$$

Intermediate states are given by (II.2.12), (II.2.14) and (II.2.18). In compact form they read,

$$\begin{cases} \mathbf{U}_L^* = \mathbf{U}_{HLL}^* - \omega_R \Psi, \\ \mathbf{U}_R^* = \mathbf{U}_{HLL}^* + \omega_L \Psi, \end{cases} \tag{II.2.19}$$

where $\Psi = \left(\Psi_{\text{mass}}, \Psi_{\text{momentum}}, \Psi_{\text{energy}} \right)^T$, with components given in (II.2.11), (II.2.13) and (II.2.17).

The Riemann solver thus consists in (II.2.3) for the HLL state determination and (II.2.19) to rebuild the two intermediate states.

Comparison with the HLLC solver and exact solution is now addressed on various test problems. Let us recall that, unless mentioned otherwise, $\beta = 1$ in all computations to minimize numerical diffusion. The various test problems are given in Toro (2009, 2019) including the Colella and Woodward (1984)

blast wave test. Extreme wave speeds are approximated following (II.2.2) (Davis, 1988) for both solvers (RSIR and HLLC). Computed results are provided in Figures II.5-II.12. For this test series, all variables are in dimensionless units as done in Toro (2009, 2019). Note that these test problems are all severe and designed to push the methods to the limit with the exception of tests 6 and 7 that involve a stationary discontinuity and a simple advection. Those two last tests remain nonetheless essential to access the methods.

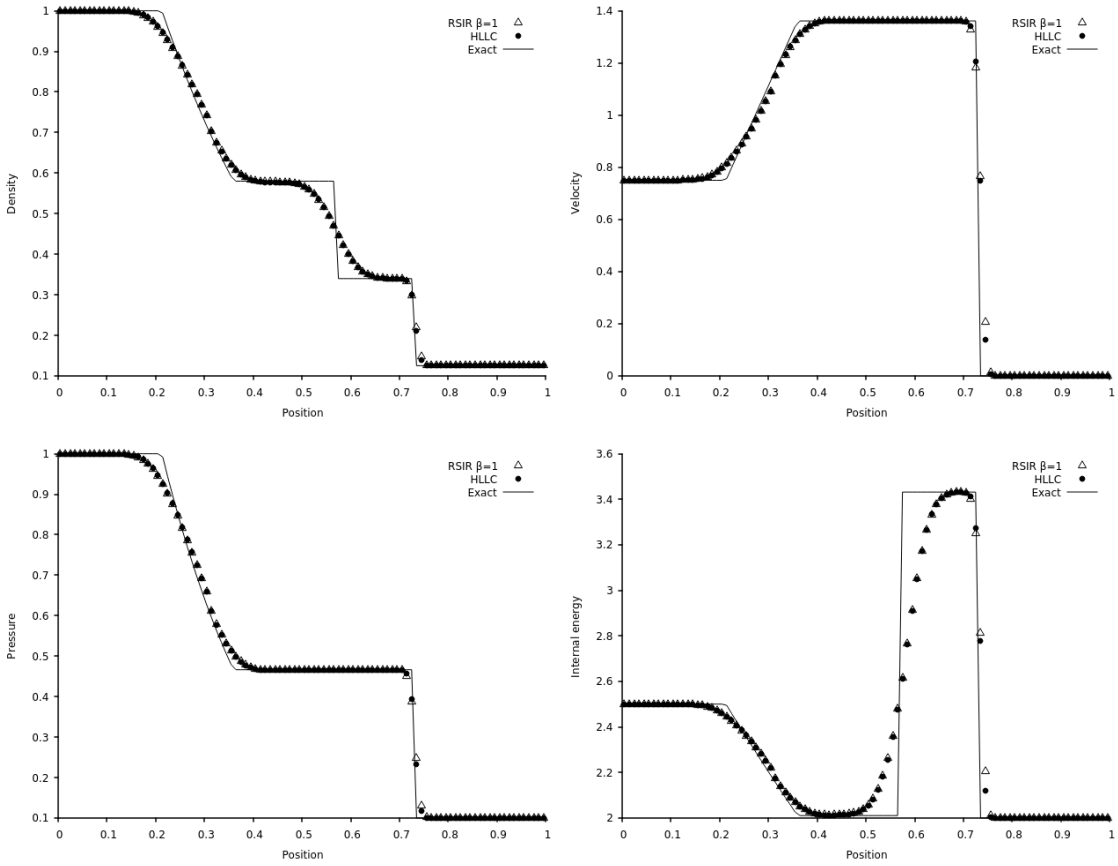

Figure II.5 – Test 1 of Toro (2009) page 334 (shock tube test). Comparison of the RSIR, HLLC and exact solutions. The computational domain involves 100 cells and the first-order Godunov scheme is used with CFL=0.9. Results are shown at time t=0.2. The initial discontinuity is at position $x_0 = 0.3$. Both methods show comparable accuracy.

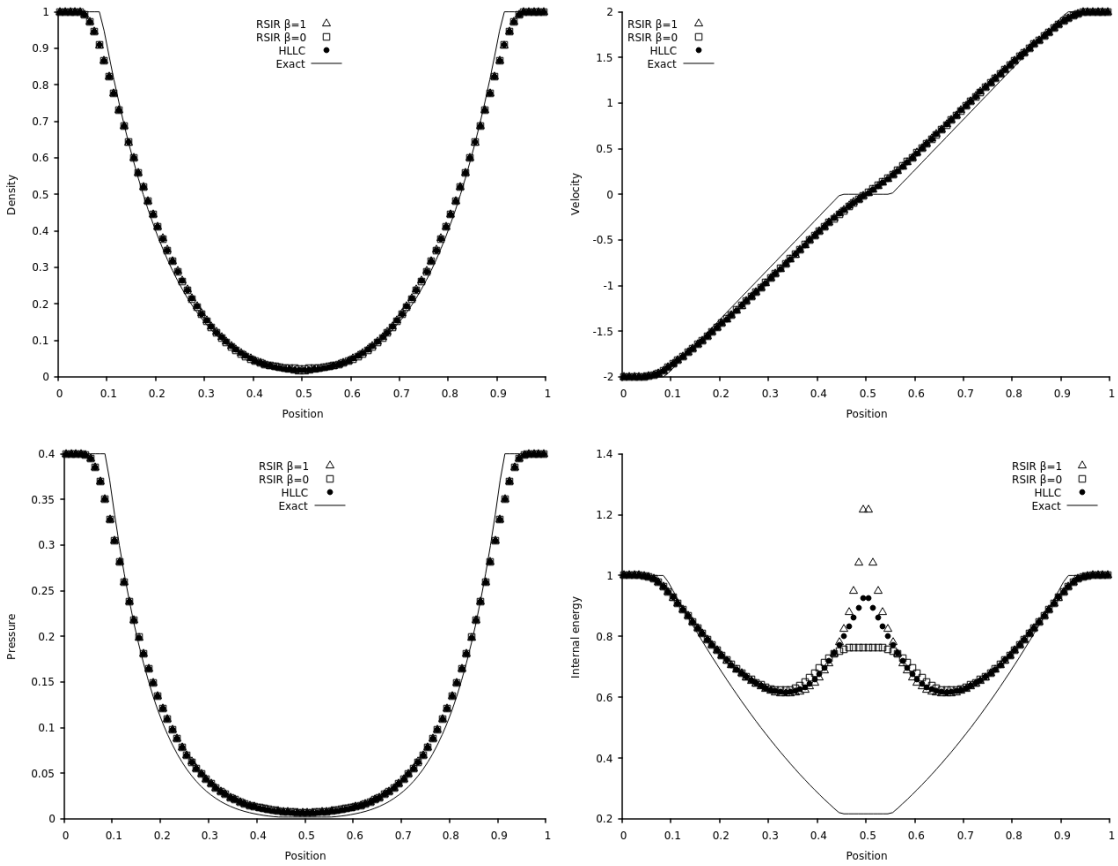

Figure II.6 – Test 2 of Toro (2009) page 334 (double expansion test). Comparison of the RSIR, HLLC and exact solutions. The computational domain involves 100 cells and the first-order Godunov scheme is used with CFL=0.9. Results are shown at time t=0.15. The initial discontinuity is at position $x_0 = 0.5$. Both methods produce unphysical overheating at the center of the domain. HLLC results are less inaccurate than RSIR when $\beta = 1$ while RSIR yields less inaccurate results than those of HLLC when $\beta = 0$.

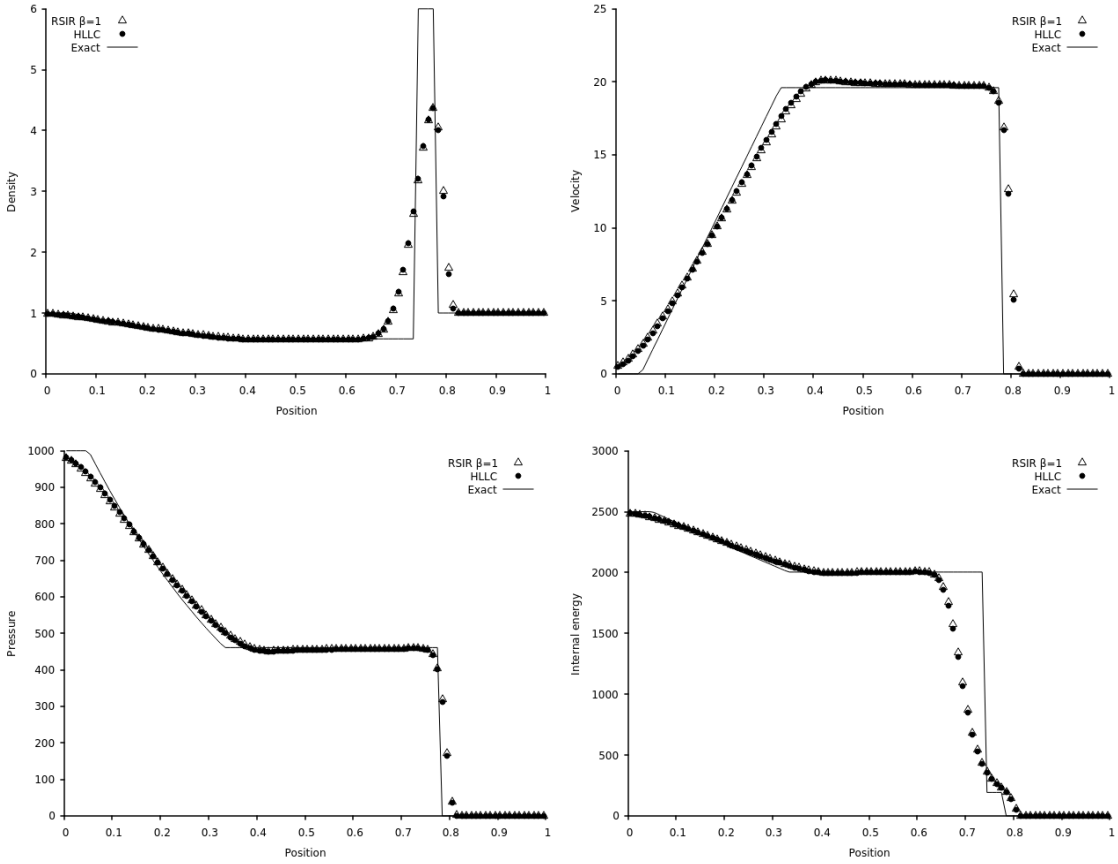

Figure II.7 – Test 3 of Toro (2009) page 334 (strong shock tube test). Comparison of the RSIR, HLLC and exact solutions. The computational domain involves 100 cells and the first-order Godunov scheme is used with CFL=0.9. Results are shown at time t=0.012. The initial discontinuity is at position $x_0 = 0.5$. Both methods show comparable accuracy.

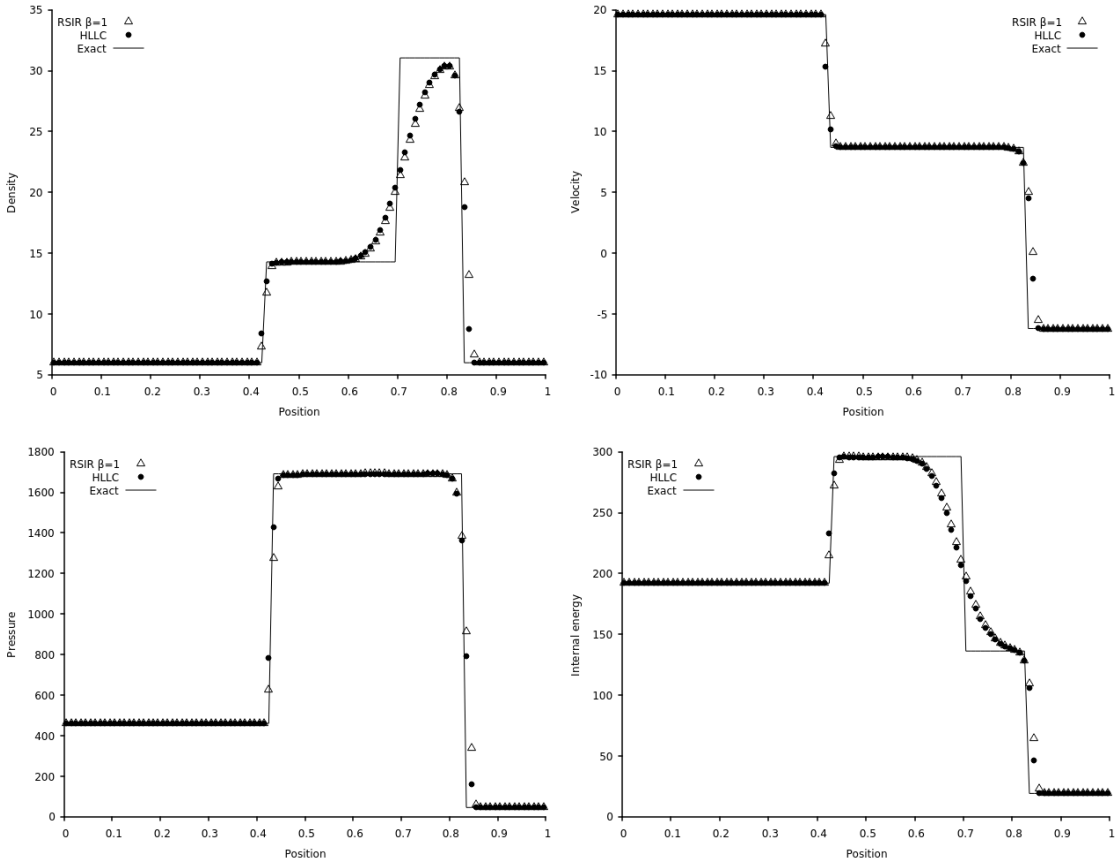

Figure II.8 – Test 4 of Toro (2009) page 334 (double shock test). Comparison of the RSIR, HLLC and exact solutions. The computational domain involves 100 cells and the first-order Godunov scheme is used with CFL=0.9. Results are shown at time t=0.035. The initial discontinuity is at position $x_0 = 0.4$. Both methods show comparable accuracy.

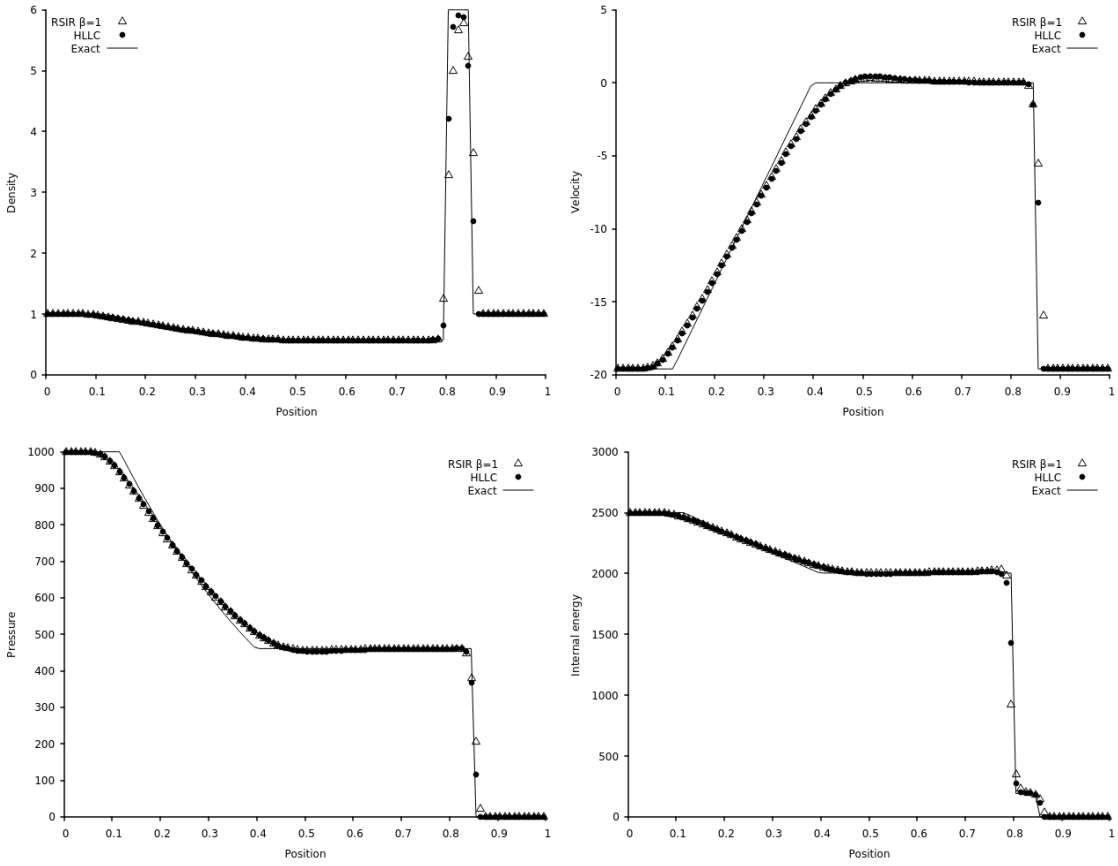

Figure II.9 – Test 5 of Toro (2009) page 334 (strong shock tube test of Test 3 with non-zero initial velocity. Comparison of the RSIR, HLLC and exact solutions. The computational domain involves 100 cells and the first-order Godunov scheme is used with CFL=0.9. Results are shown at time t=0.012. The initial discontinuity is at position $x_0 = 0.8$. Both methods show comparable accuracy.

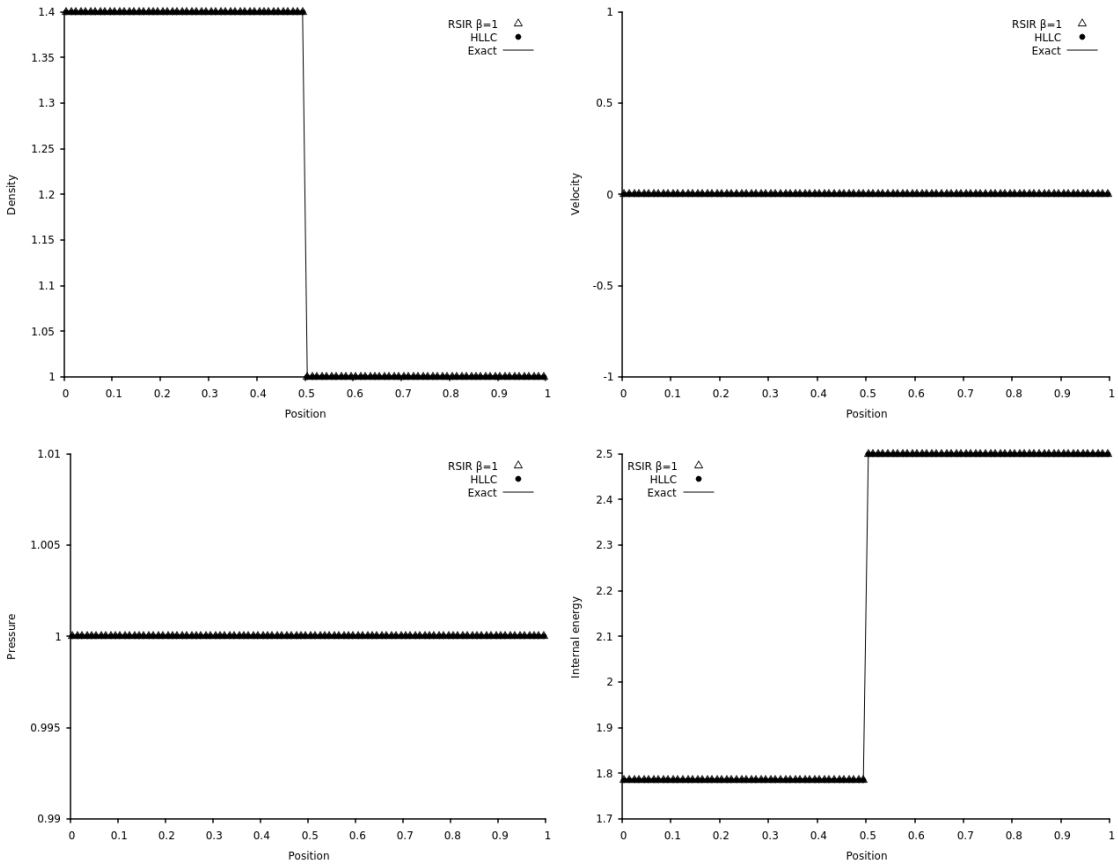

Figure II.10 – Test 6 of Toro (2009) page 334 (stationary contact discontinuity). Comparison of the RSIR, HLLC and exact solutions. The computational domain involves 100 cells and the first-order Godunov scheme is used with CFL=0.9. Results are shown at time t=2. The initial discontinuity is at position $x_0 = 0.5$. Both methods show comparable accuracy.

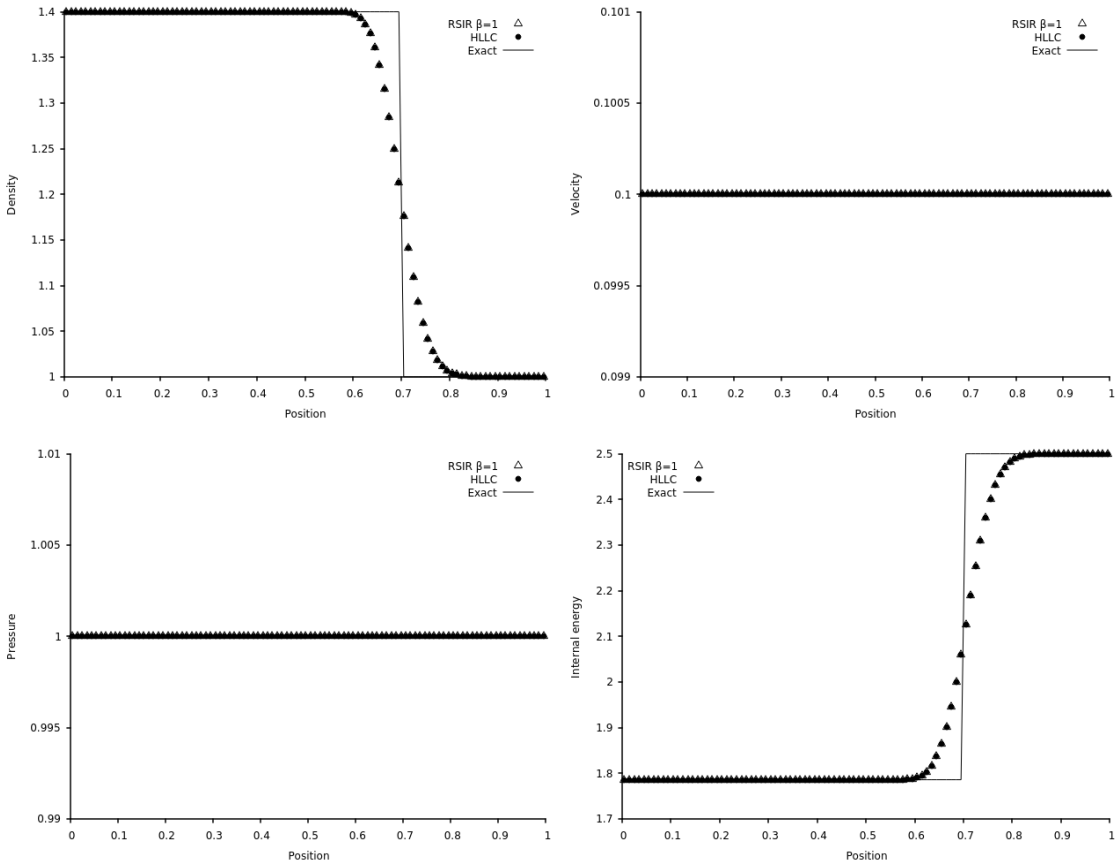

Figure II.11 – Test 7 of Toro (2009) page 334 (moving contact discontinuity). Comparison of the RSIR, HLLC and exact solutions. The computational domain involves 100 cells and first-order Godunov scheme is used with CFL=0.9. Results are shown at time t=2. The initial discontinuity is at position $x_0 = 0.5$. Both methods show comparable accuracy.

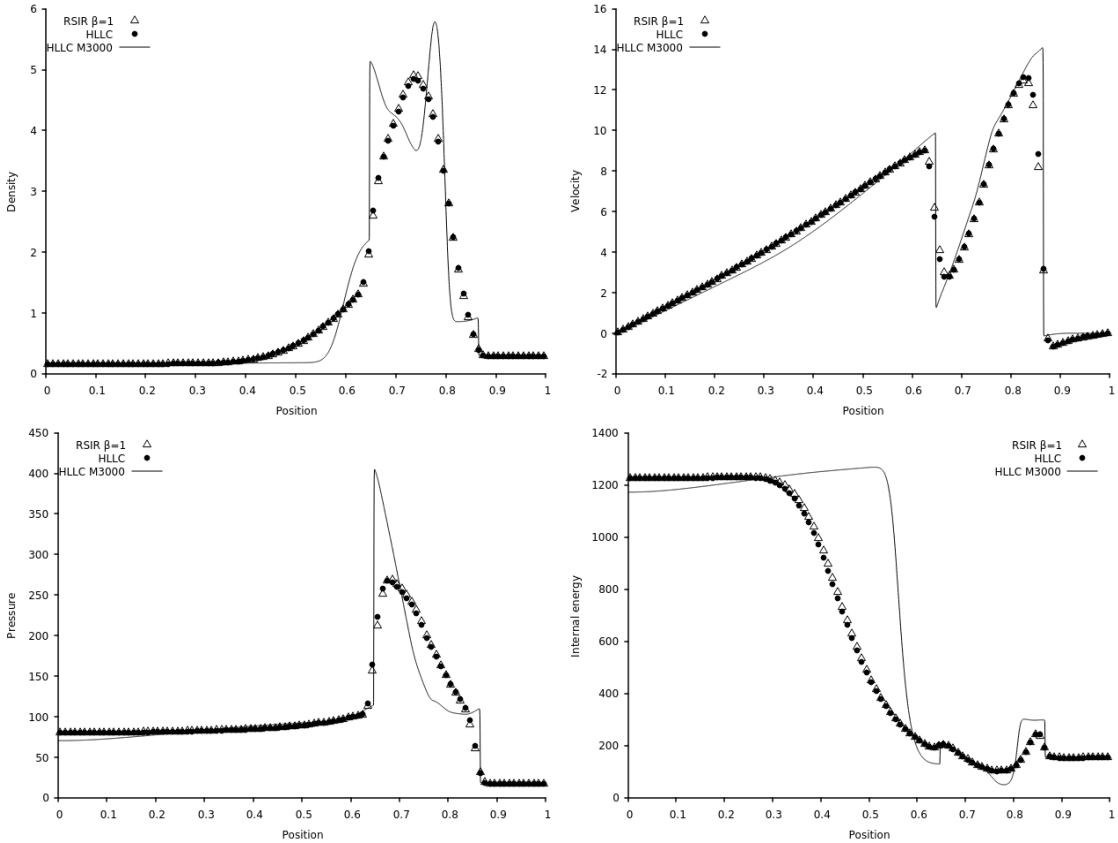

Figure II.12 – Woodward and Colella (1984) blast wave test (provided in Toro 2009 page 612). Comparison of the RSIR and HLLC solutions. The computational domain involves 100 cells and the first-order Godunov scheme is used with CFL=0.9. Results are shown at time t=0.038. Both methods show comparable accuracy. This problem does not have exact solution. Results with the HLLC solver and 3000 cells are shown nonetheless as a reference solution.

The accuracy of the new solver is comparable to the one the HLLC solver, at least for the Euler equations and present test problems. HLLC appears more accurate in the double expansion test of Figure II.6 but this test is challenging as kinetic energy computation is problematic. Indeed, as in all computations based on conservative formulation of the Euler equations, the kinetic energy is computed from the cell average mass and momentum. However, at the center of the domain, the exact kinetic energy is different of the half square mean velocity.

Method extension to the more sophisticated flow model of Saurel et al. (2017a) is now examined. As already mentioned, this system is weakly hyperbolic. Moreover, it will be shown that solutions are not self-similar. For this flow model, the authors tried to derive a HLLC-type Riemann solver, but their attempts failed.

II.3 – Extension to dense-dilute two-phase flow model

The two-phase flow model of Saurel et al. (2017a), considering a dispersed phase 1 in a carrier fluid 2 is recalled hereafter. Pressure and velocity relaxation terms only are considered as interaction effects:

$$
\begin{aligned}
&\frac{\partial \alpha_1}{\partial t}+\frac{\partial (\alpha u)_1}{\partial x}=\mu (p_1-p_2), \qquad \mu \to +\infty \\
&\frac{\partial (\alpha \rho)_1}{\partial t}+\frac{\partial (\alpha \rho u)_1}{\partial x}=0, \\
&\frac{\partial (\alpha \rho u)_1}{\partial t}+\frac{\partial \left(\alpha \rho u^2+\alpha p\right)_1}{\partial x}=p_I \frac{\partial \alpha_1}{\partial x}+\lambda (u_2-u_1), \\
&\frac{\partial (\alpha \rho E)_1}{\partial t}+\frac{\partial \left(\alpha (\rho E+p) u\right)_1}{\partial x}=p_I \frac{\partial (\alpha u)_1}{\partial x}+\lambda u_I (u_2-u_1)-\mu p_I (p_1-p_2), \qquad \text{(II.3.1)} \\
&\frac{\partial (\alpha \rho)_2}{\partial t}+\frac{\partial (\alpha \rho u)_2}{\partial x}=0, \\
&\frac{\partial (\alpha \rho u)_2}{\partial t}+\frac{\partial \left(\alpha \rho u^2+\alpha p\right)_2}{\partial x}=p_I \frac{\partial \alpha_2}{\partial x}-\lambda (u_2-u_1), \\
&\frac{\partial (\alpha \rho E)_2}{\partial t}+\frac{\partial \left(\alpha (\rho E+p) u\right)_2}{\partial x}=-p_I \frac{\partial (\alpha u)_1}{\partial x}-\lambda u_I (u_2-u_1)+\mu p_I (p_1-p_2).
\end{aligned}
$$

Same notations as for the Euler equations are used. Additionally α_k represent the volume fraction of phase k, index I is related to interfacial variables and relaxation parameters are denoted by λ and μ, with respect to velocity and pressure relaxation. Appropriate relations are given for example in Saurel et al. (2017a). It is important to mention that this flow model is valid only in the stiff pressure relaxation limit ($\mu \to +\infty$). Appropriate pressure relaxation solvers are given for example in Lallemand and Saurel (2000). This is not equivalent to strict pressure equilibrium models that are non-hyperbolic, or conditionally hyperbolic. Also, this is not a restrictive assumption for most two-phase flow applications, except possibly extreme situations, such as hot spots ignition in condensed energetic materials (Saurel et al., 2017b), where pressure relaxation is the driving effect for hot spot appearance. The present model is hyperbolic with wave speeds,

$\lambda_{1-4}=u_1$, $\lambda_5=u_2$, $\lambda_6=u_2-c_2$ and $\lambda_7=u_2+c_2$.

These waves speeds are the same as the ones of the Marble (1963) model but are significantly different from those of the Baer and Nunziato (1986) model. Combination of the equations of System (II.3.1) result in the following mixture entropy equation, that guarantees non-negative evolutions,

$$\frac{\partial \alpha_1\rho_1 s_1 + \alpha_2\rho_2 s_2}{\partial t} + \frac{\partial \alpha_1\rho_1 s_1 u_1 + \alpha_2\rho_2 s_2 u_2}{\partial x} = \left(\frac{(u_I - u_1)}{T_1} - \frac{(u_I - u_2)}{T_2} \right) \lambda (u_2 - u_1) \cdot \qquad \text{(II.3.2)}$$

Indeed, admissible estimates for the interfacial velocity are,

$u_I = u_1$ or $u_I = u_2$,

or combinations of them.

System (II.3.1) is obviously non-conservative, as $p_I \frac{\partial \alpha_1}{\partial x}$ and $p_I \frac{\partial (\alpha u)_1}{\partial x}$ terms are present in the right-hand side of the momentum and energy equations. However, assuming $p_I = p_1$ the following Rankine-Hugoniot system is obtained (Saurel et al., 2017a):

$$\begin{aligned}
&\alpha_1 = \alpha_1^0, \\
&\rho_1 = \rho_1^0 \ , \\
&e_1 = e_1^0, \\
&u_1 = u^0, \qquad \text{(II.3.3)} \\
&\rho_2 (u_2 - \sigma) = \rho_2^0 (u^0 - \sigma), \\
&\rho_2 u_2 (u_2 - \sigma) + p_2 = \rho_2^0 u^0 (u^0 - \sigma) + p^0, \\
&\rho_2 E_2 (u_2 - \sigma) + u_2 p_2 = \rho_2^0 E_2^0 (u^0 - \sigma) + u^0 p^0 .
\end{aligned}$$

These relations will be used in the RSIR derivation.

Numerical resolution of System (II.3.1) has been done in Saurel et al. (2017a) with the help of a Rusanov (1961) solver. This solver being quite diffusive, the aim is now to build an improved solver. System (II.3.1) involves however three main difficulties:

- It is non-conservative;
- The eigenvalue u_1 is multiple. Therefore System (II.3.1) admits multivalued solutions (Forestier and Le Floch, 1992, Saurel et al., 1994, Bouchut et al., 2003).
- Solutions are not self-similar, as will be shown later with the help of numerical experiments.

These issues are addressed gradually in the following.

To overcome the non-conservative issue a local conservative of the System (II.3.1) is addressed, which must be tested and validated with the same numerical method as in Chapter I. As the reconstruction is based on the solution given by the local conservative formulation, extra attention is needed to ensure that the new conservative approach does not degrade the previous results obtained in Chapter I. The

reconstruction of the solution is then applied on the local conservative formulation to determine solution of System (II.3.1).

II.3.a) Local conservative formulation and Rusanov-type solvers

In Saurel et al. (2017a) a Rusanov-type method was derived to determine qualitative solutions of the new flow model and validations against both exact solutions and experimental data. This method is recalled hereafter, and an improved version based on a local conservative formulation is built. The aim is to show that non-conservative terms are treated correctly through the local conservative formulation.

II.3.a.i) Basic Rusanov version

System (II.3.1) is considered in non-conservative form and in the absence of relaxation terms as,

$$\frac{\partial U}{\partial t}+\frac{\partial F(U)}{\partial x}+H\left(U,\frac{\partial U}{\partial x}\right)=0, \qquad \text{(II.3.4)}$$

with,

$$U=\left(\alpha_1,\ \ (\alpha\rho)_1,\ \ (\alpha\rho u)_1,\ \ (\alpha\rho E)_1,\ \ (\alpha\rho)_2,\ \ (\alpha\rho u)_2,\ \ (\alpha\rho E)_2\right)^T$$

$$F=\left((\alpha u)_1,\ \ (\alpha\rho u)_1,\ \ \left(\alpha\rho u^2+\alpha p\right)_1\ \ \left(\alpha(\rho E+p)u\right)_1,\ \ (\alpha\rho u)_2,\ \ \left(\alpha\rho u^2+\alpha p\right)_2,\ \ \left(\alpha(\rho E+p)u\right)_2\right)^T$$

$$H=\left(0,\ \ 0,\ \ -p_I\frac{\partial\alpha_1}{\partial x},\ \ -p_I\frac{\partial(\alpha u)_1}{\partial x},\ \ 0,\ \ p_I\frac{\partial\alpha_1}{\partial x},\ \ p_I\frac{\partial(\alpha u)_1}{\partial x}\right)^T$$

Let us denote by,

$$S=\mathrm{Max}_k\left(|\lambda_k|_L,|\lambda_k|_R\right),$$

the maximum wave speed separating two states L and R.

The Rusanov flux reads,

$$F^*=\frac{1}{2}\left[F_R+F_L-S(U_R-U_L)\right],$$

and the Godunov scheme associated to system (II.3.4) reads,

$$U_i^{n+1}=U_i^n-\frac{\Delta t}{\Delta x}\left(F^*_{i+1/2}-F^*_{i-1/2}\right)+\Delta t H_i,$$

where H_i is an approximation of non-conservative terms.

Following Saurel et al. (2017a), based on Saurel and Abgrall (1999) method for a slightly different flow model, approximation of these terms read;

- For the momemtum equation,

$$H_{i,u} = p_i^n \frac{\alpha^*_{1,i+\frac{1}{2}} - \alpha^*_{1,i-\frac{1}{2}}}{\Delta x} \text{ with } \alpha^*_{1,i+\frac{1}{2}} = \frac{\alpha_{1,i} + \alpha_{1,i+1}}{2}.$$

- For the energy equations,

$$H_{i,E} = p_i^n \frac{(\alpha u)^*_{1,i+\frac{1}{2}} - (\alpha u)^*_{1,i-\frac{1}{2}}}{\Delta x} \text{ with } (\alpha u)^*_{1,i+\frac{1}{2}} = \frac{(\alpha u)_{1,i+1} + (\alpha u)_{1,i}}{2}.$$

These formulas are built to respect mechanical equilibrium condition. Another version is examined hereafter.

II.3.a.ii) Local conservative formulation

The interfacial pressure p_I appears in the presence of non-conservative terms, such as $p_I \frac{\partial \alpha_k}{\partial x}$. As p_I has been assumed equal to the dispersed phase pressure, the following assumption is made:

$$p_I = \begin{cases} p_{1,L} & \text{if } \alpha_{1,L} > \alpha_{1,R} \\ p_{1,R} & \text{if } \alpha_{1,L} < \alpha_{1,R} \end{cases}. \qquad \text{(II.3.5)}$$

It means that p_I is taken equal to the pressure of phase 1 when this phase is present. Possible situations are schematized in Figure II.13.

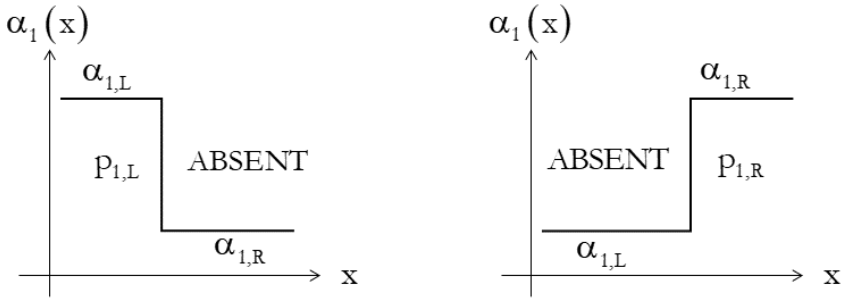

Figure II.13 – Schematic representation of the estimate for p_I. As a consequence of jump conditions (II.3.3) both volume fraction and pressure of phase 1 are invariant across the extreme waves $u_2 - c_2$ and $u_2 + c_2$ in the Riemann problem solution. Therefore, p_I is taken equal to the pressure of phase 1 when this phase is present, as summarized in (II.3.5). As it is constant during time evolution in a given Riemann problem, it becomes a local constant.

As a consequence of Rankine-Hugoniot relations (II.3.3), assuming $p_I = p_1$ implies that p_I becomes a local constant, as p_1 is invariant across right- and left-facing waves.

Thanks to this local constant, System (II.3.1) becomes locally conservative:

$$\frac{\partial \alpha_1}{\partial t} + \frac{\partial (\alpha u)_1}{\partial x} = 0,$$

$$\frac{\partial (\alpha\rho)_1}{\partial t} + \frac{\partial (\alpha\rho u)_1}{\partial x} = 0,$$

$$\frac{\partial (\alpha\rho u)_1}{\partial t} + \frac{\partial \left(\alpha\rho u^2 + \alpha(p - p_I)\right)_1}{\partial x} = 0,$$

$$\frac{\partial (\alpha\rho E)_1}{\partial t} + \frac{\partial \left(\alpha(\rho E + p - p_I)u\right)_1}{\partial x} = 0, \qquad \text{(II.3.6)}$$

$$\frac{\partial \alpha_2}{\partial t} - \frac{\partial (\alpha u)_1}{\partial x} = 0,$$

$$\frac{\partial (\alpha\rho)_2}{\partial t} + \frac{\partial (\alpha\rho u)_2}{\partial x} = 0,$$

$$\frac{\partial (\alpha\rho u)_2}{\partial t} + \frac{\partial \left(\alpha\rho u^2 + \alpha(p - p_I)\right)_2}{\partial x} = 0,$$

$$\frac{\partial (\alpha\rho E)_2}{\partial t} + \frac{\partial \left(\alpha(\rho E + p)u\right)_2 + (\alpha u)_1 p_I}{\partial x} = 0.$$

In compact form it reads,

$$\frac{\partial U}{\partial t} + \frac{\partial \Phi(U)}{\partial x} = 0,$$

with obvious definition for $\Phi(U)$.

The associated Rusanov flux is immediate,

$$\Phi^* = \frac{1}{2}\left[\Phi_R + \Phi_L - S(U_R - U_L)\right]. \qquad \text{(II.3.7)}$$

From Φ^*, the F^* flux of formulation (II.3.4) is deduced as,

$$F_k^* = \Phi_k^* + p_I \begin{pmatrix} 0 \\ 0 \\ \alpha_k^* \\ \Phi^*(\alpha_k) \end{pmatrix}, \; k=1,2. \tag{II.3.8}$$

α_k^* are determined form Rusanov state as,

$$\alpha_k^* = \frac{1}{2}\left[\alpha_{k,R} + \alpha_{k,L} - \frac{\left(\Phi(\alpha_{k,R}) - \Phi(\alpha_{k,L})\right)}{S} \right]. \tag{II.3.9}$$

The fluxes are inserted in the same Godunov scheme as before,

$$U_i^{n+1} = U_i^n - \frac{\Delta t}{\Delta x}\left(F^*_{i+1/2} - F^*_{i-1/2} \right) + \Delta t H_i \,,$$

except that H_i are now given by,

$$H_{i,u} = p_i^n \frac{\alpha^*_{1,i+\frac{1}{2}} - \alpha^*_{1,i-\frac{1}{2}}}{\Delta x}$$

$$H_{i,E} = p_i^n \frac{\Phi^*_{i+\frac{1}{2}}(\alpha_1) - \Phi^*_{i-\frac{1}{2}}(\alpha_1)}{\Delta x}.$$

In these expressions $\alpha^*_{k,i\pm\frac{1}{2}}$ and $\Phi^*_{i+\frac{1}{2}}(\alpha_1)$ are given by (II.3.9) and (II.3.7) respectively.

The overall scheme is consequently quite different of the basic version presented before.

The two Rusanov solvers are now compared on an arbitrary shock tube test problem, in the absence of velocity relaxation, but with stiff pressure relaxation. Corresponding results are shown in Figure II.14.

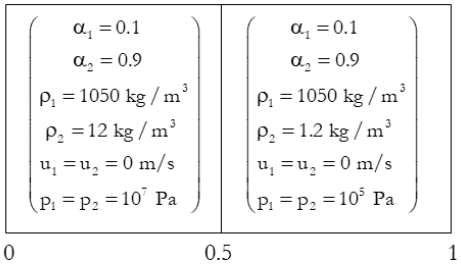
$\alpha_1 = 0.1$
$\alpha_2 = 0.9$
$\rho_1 = 1050\ \mathrm{kg/m^3}$
$\rho_2 = 12\ \mathrm{kg/m^3}$
$u_1 = u_2 = 0\ \mathrm{m/s}$
$p_1 = p_2 = 10^7\ \mathrm{Pa}$
$\alpha_1 = 0.1$
$\alpha_2 = 0.9$
$\rho_1 = 1050\ \mathrm{kg/m^3}$
$\rho_2 = 1.2\ \mathrm{kg/m^3}$
$u_1 = u_2 = 0\ \mathrm{m/s}$
$p_1 = p_2 = 10^5\ \mathrm{Pa}$
0
0.5
1

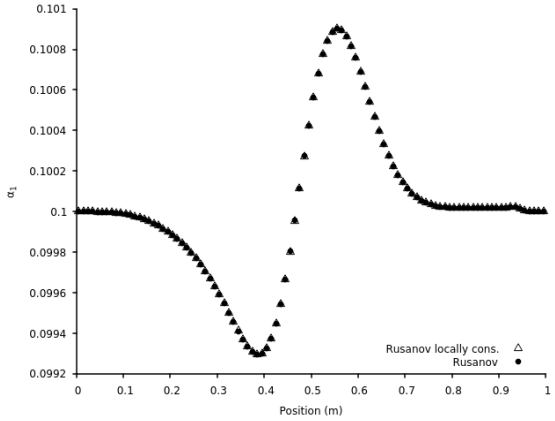
α_1
Position (m)
Rusanov locally cons.
Rusanov

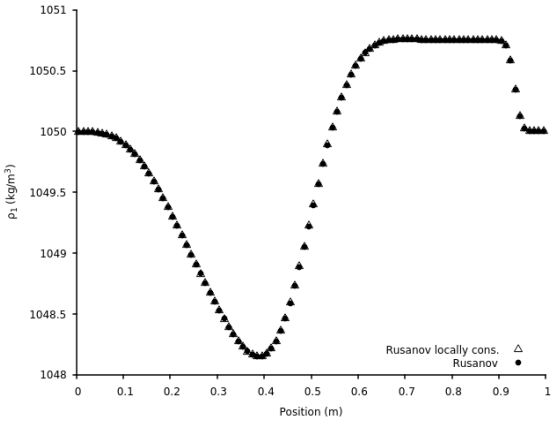
ρ_1 (kg/m^3)
Position (m)
Rusanov locally cons.
Rusanov

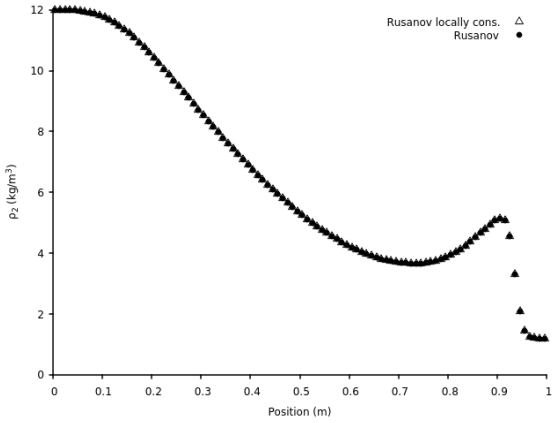
ρ_2 (kg/m^3)
Position (m)
Rusanov locally cons.
Rusanov

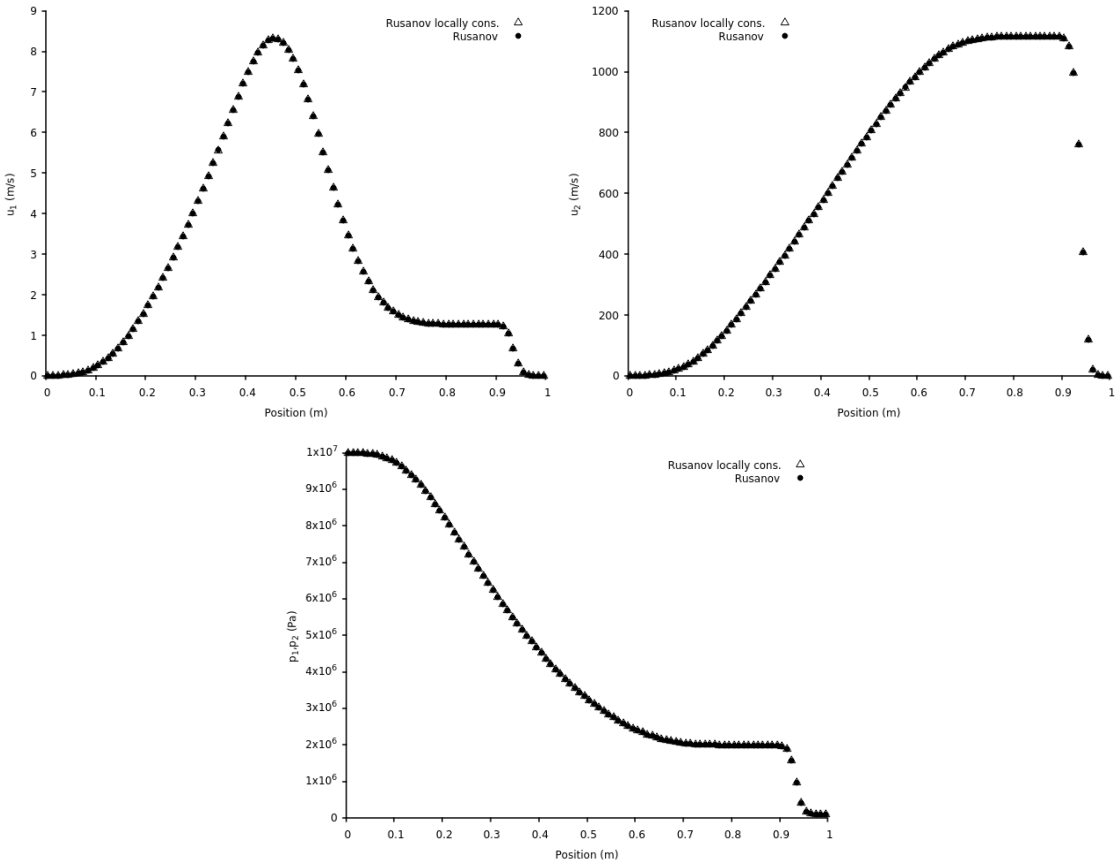

Figure II.14 – Comparison of the two Rusanov solvers on a two-phase shock tube test. Phase 1 corresponds to the dispersed fluid, considered here as liquid water, with SG EOS parameters ($\gamma_1 = 4.4$ and $p_{\infty 1} = 6 \cdot 10^8 \text{Pa}$). Phase 2 represents the carrier phase, here air considered as ideal gas ($\gamma_2 = 1.4$). Stiff pressure relaxation is used at any time. The computational domain involves 100 cells and the first-order Godunov scheme is used with $\text{CFL} = 0.9$. Results are shown at t=300 μs. Both results are perfectly merged validating the approach based on the local conservative formulation.

Extra tests have been done, such as double expansion and double shock tests, always showing the same agreement. The local conservative formulation (II.3.6) with local constant (II.3.5) is consequently robust enough to be considered with the reconstruction method (RSIR).

II.3.a.iii) Non self-similar solutions

Another difficulty is highlighted hereafter. The same shock tube test case as before is reconsidered and the solution obtained by the previous solver is shown at various times in Figure II.15.

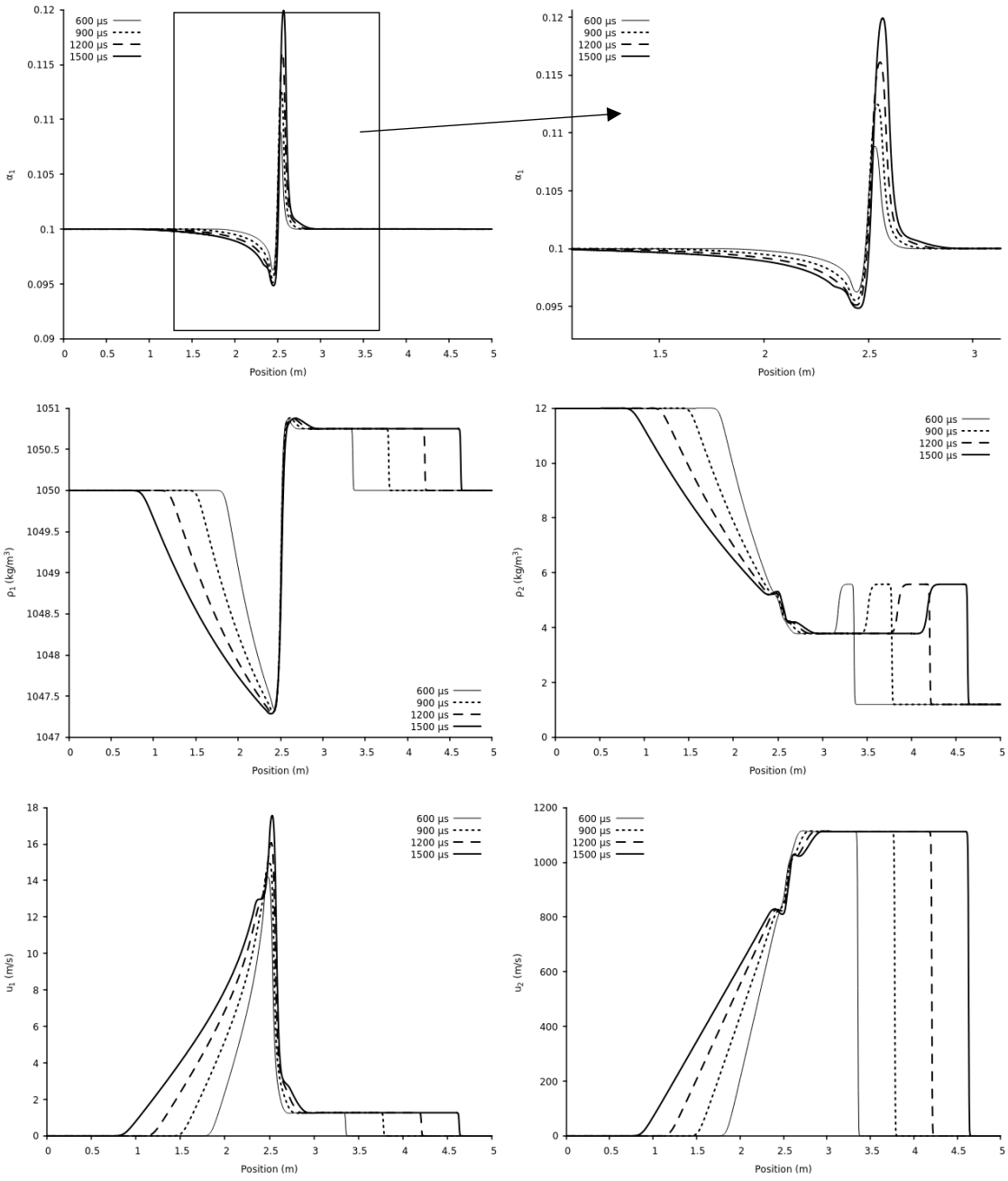
600 µs
900 µs
1200 µs
1500 µs
α_1
ρ_1 (kg/m^3)
ρ_2 (kg/m^3)
u_1 (m/s)
u_2 (m/s)
Position (m)

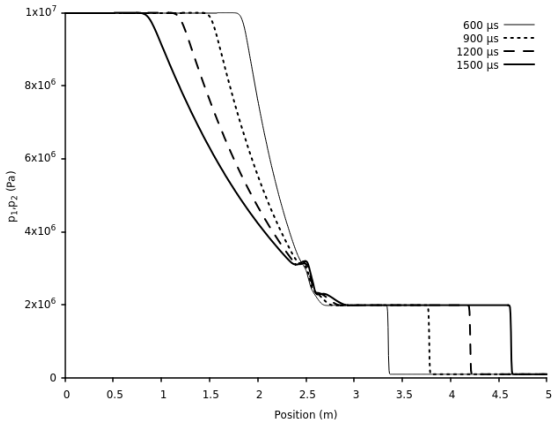

Figure II.15 – Shock tube test problem of Figure II.14 considered at various times. Length of the domain has been increased to 5 m to avoid interaction with the boundaries, and the initial discontinuity is placed at 2.5 m. Stiff pressure relaxation is used at any time. 1 000 computational cells are used with CFL=0.5. Computations are done with the MUSCL method and Minmod limiter and the local conservative Rusanov approximate Riemann solver. Solutions for the carrier phase (2) appear self-similar but solutions of the dilute phase 1 are not, regarding volume fraction and velocity. Volume fraction of the dilute phase keeps increasing without converging towards a constant state. The same tendency is observed in the velocity of the dilute phase. These observations are mesh and solver independent.

Origin of this interesting behavior is examined hereafter with the help of the Baer and Nunziato (1986) model. The same shock tube test problem is rerun with the Baer and Nunziato (1986) model with the help of the HLLC-type solver of Furfaro and Saurel (2015). In the computations of Figure II.16 pressure relaxation is absent.

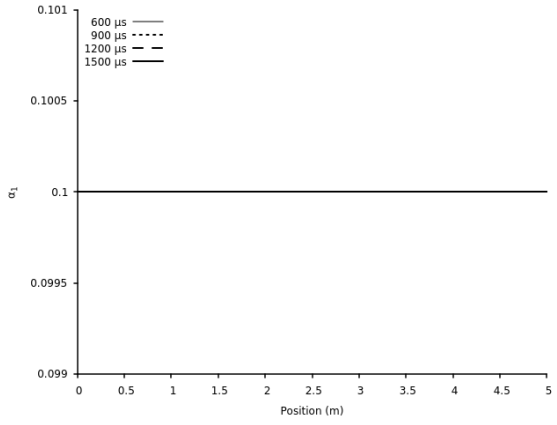

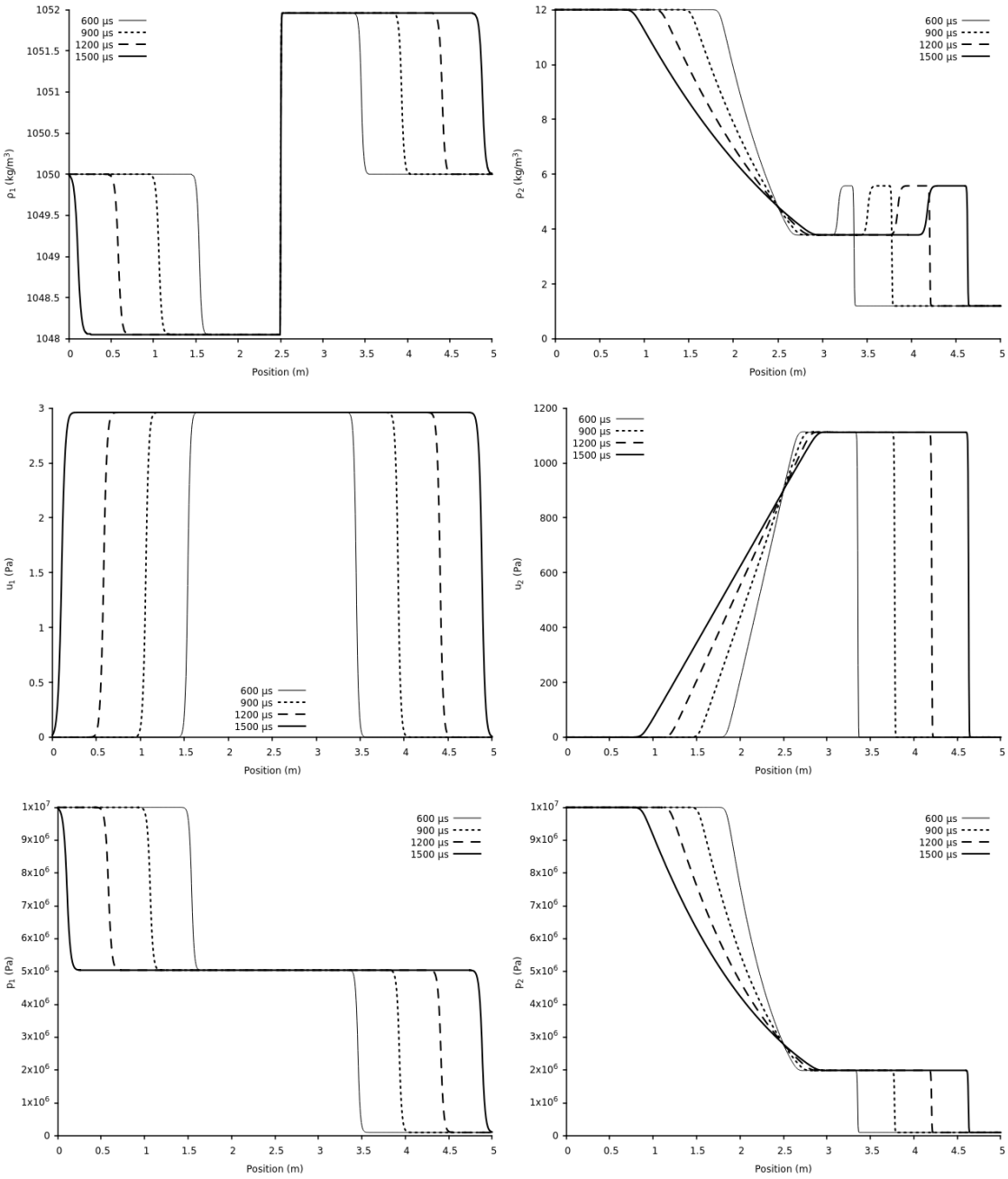

Figure II.16 – Two-phase shock tube problem of Figure II.14 computed with the Baer and Nunziato (1986) model in the absence of pressure relaxation. Length of the domain has been increased to 5m to avoid waves interaction with the boundaries, and the initial discontinuity is placed at 2.5m. 1 000 computational cells are used with CFL=0.5. Computations are done with the MUSCL method and Minmod limiter. The solution is self-similar and consists in two decoupled shock tube solutions, as well known.

The Baer and Nunziato (1986) model, solved with the HLLC-type solver of Furfaro and Saurel (2015) gives self-similar solutions in absence of pressure relaxation. The same shock tube test problem is

reconsidered once more with stiff pressure relaxation in the Baer and Nunziato (1986) model. Corresponding results are shown in Figure II.17.

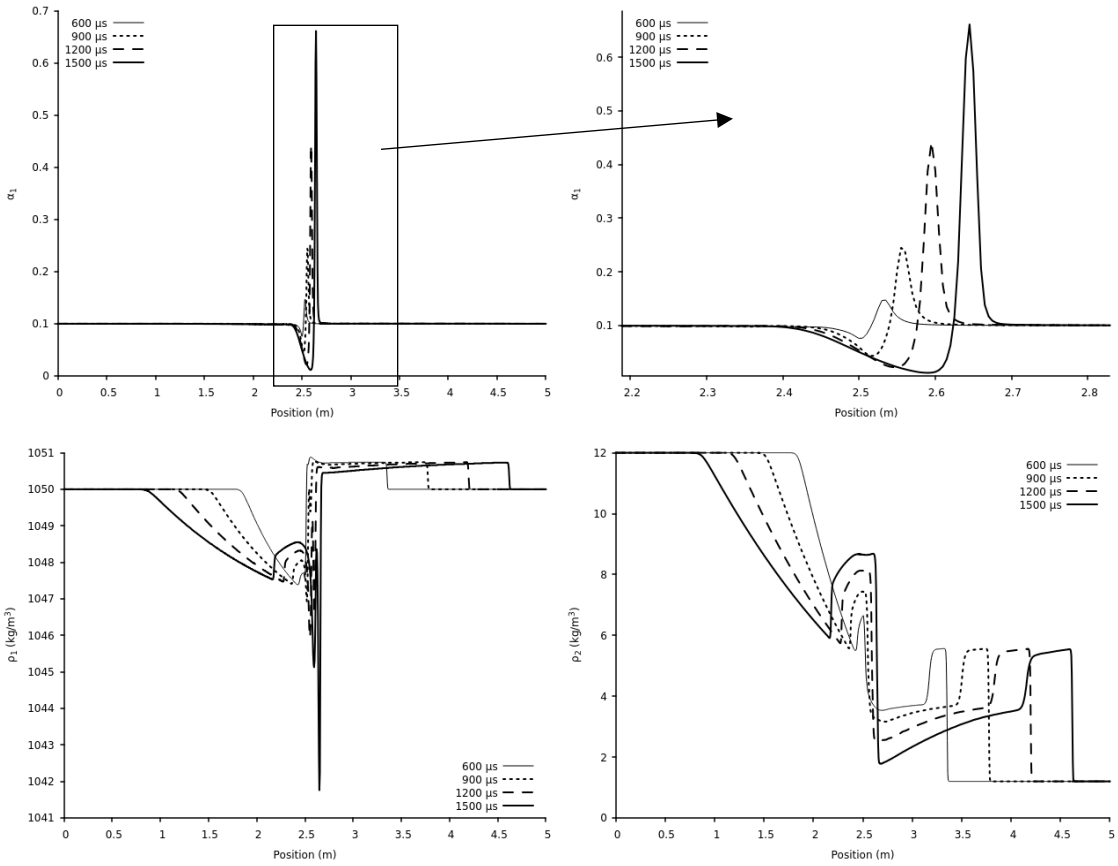

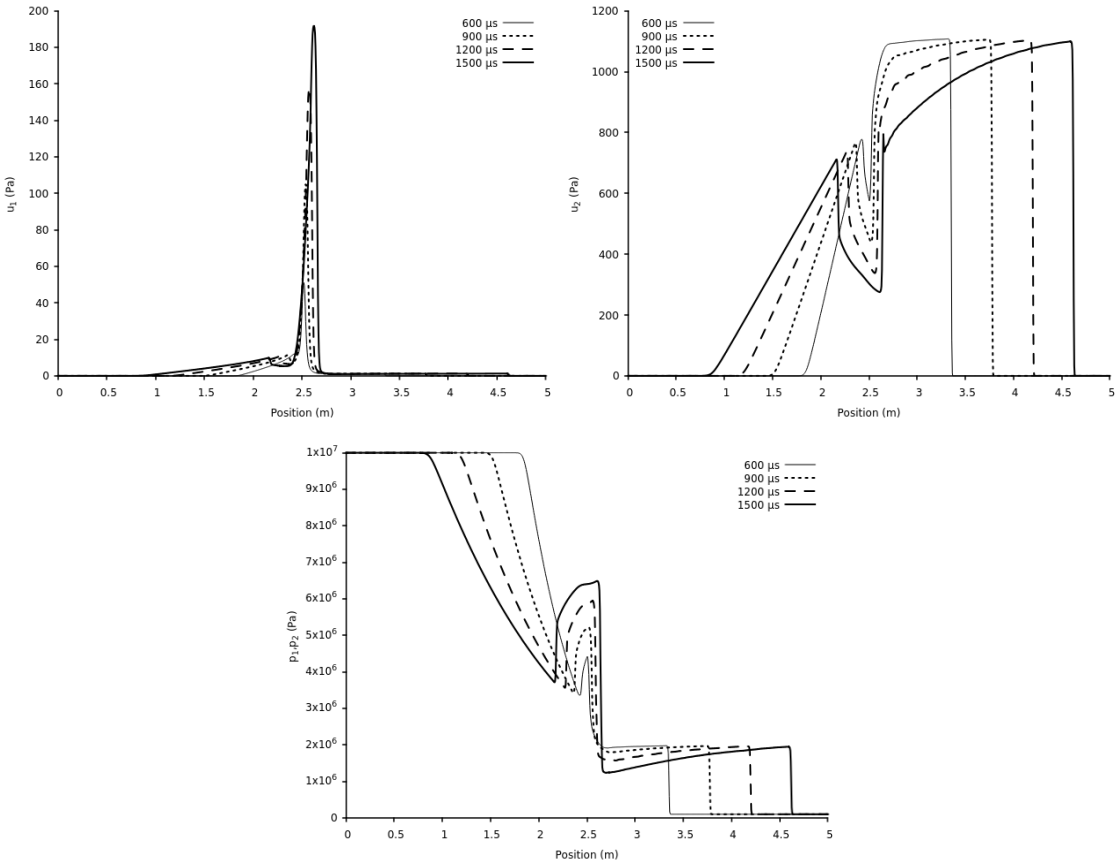

Figure II.17 – Two-phase shock tube problem of Figure II.14 computed with the Baer and Nunziato (1986) model in the presence of stiff pressure relaxation. Length of the domain has been increased to 5m to avoid waves interaction with the boundaries, and the initial discontinuity is placed at 2.5m. 1 000 computational cells are used with CFL=0.5. Computations are done with the MUSCL method and Minmod limiter. The solution is not self-similar. This is not surprising as source terms related to pressure relaxation are present.

When stiff pressure relaxation is considered, solutions of the BN model are no longer self-similar, and this is not surprising. It explains why solutions of flow model (II.3.1) are not self-similar, as this flow model only has sense in the stiff pressure relaxation limit.

Another interesting feature appears with solutions of Figures II.15 and II.17. Solution for the velocity of the dispersed phase appears multivalued, as schematized in Figure II.18. The left and right star velocities are different, implying the creation of a particle's cluster, with a Dirac function type volume fraction profile. Such behavior also happens with the BN model (Figure II.17) as a combination of pressure relaxation and non-conservative terms, acting as a drag force between phases.

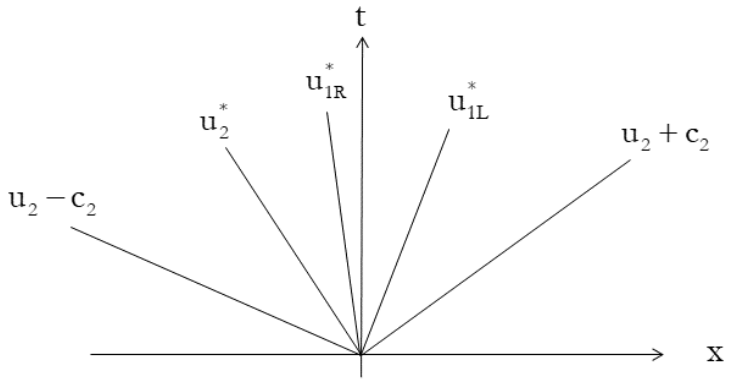

Figure II.18 – Schematic representation of the multivalued phase 1 velocity. Differences in the right and left star velocities of the dispersed phase may result in particle agglomeration as time evolves. This effect is present in the computations of Figure II.15 and II.17.

These difficulties are omitted when dealing with single state Riemann solver, such as HLL or Rusanov. From this robust solution basis, we now address internal reconstruction to reduce numerical smearing.

II.3.b) Riemann solver with internal reconstruction (RSIR) for the two-phase model

The present flow solver is not based on variations across the various waves but only on rebuilding two intermediate states to preserve isolated volume fraction discontinuities and reduce artificial smearing during transport. In this direction, the intermediate wave speed is based on the phase 1 contact wave:

$$S_{M1} = \frac{U^*_{HLL}\left((\alpha\rho u)_1\right)}{U^*_{HLL}\left((\alpha\rho)_1\right)}, \qquad \text{(II.3.10)}$$

with U^*_{HLL} given by (II.3.11) in the context of System (II.3.6) and same wave speed estimates as before. As detailed with the Euler equations the method to solve System (II.3.1) proceeds in two steps:

- Determine average state with HLL based on (II.3.6);
- Rebuild the solution.

Thanks to the local conservative formulation the first step is immediate. System (II.3.6) is expressed as,

$$\frac{\partial U}{\partial t} + \frac{\partial \Phi(U)}{\partial x} = 0,$$

with p_I given by (II.3.5).

The average state is obtained as,

$$U^*_{HLL} = \frac{\Phi_R - \Phi_L + S_L U_L - S_R U_R}{S_L - S_R}. \qquad \text{(II.3.11)}$$

The next step consists in the approximation of states L* and R*. Knowledge of the intermediate wave speed S_{M1} from (II.3.10) enables following decomposition of the average state,

$$U^*_{HLL} = \omega_R U^*_R + \omega_L U^*_L \qquad \text{(II.3.12)}$$

with,

$$\omega_R = \frac{S_R - S_{M1}}{S_R - S_L} \text{ and } \omega_L = \frac{S_{M1} - S_L}{S_R - S_L}.$$

As System (II.3.12) involves two unknown variable vectors, another set of relations is needed.

Reconstruction

For the dispersed phase, the Rankine-Hugoniot relations (III.3) imply, $\alpha^*_{1R} = \alpha_{1R}$ and $\alpha^*_{1L} = \alpha_{1L}$.

The difference of these two relations reads,

$$\alpha^*_{1R} - \alpha^*_{1L} = \alpha_{1R} - \alpha_{1L}.$$

Parameter β is introduced to control numerical diffusion,

$$\alpha^*_{1R} - \alpha^*_{1L} = \beta\left(\alpha_{1R} - \alpha_{1L}\right).$$

As phase 1 density has no jump across left- and right-facing waves, similar relation is obtained:

$$\left(\alpha\rho\right)^*_{1R} - \left(\alpha\rho\right)^*_{1L} = \beta\left(\left(\alpha\rho\right)_{1R} - \left(\alpha\rho\right)_{1L}\right).$$

Regarding momentum jump across the intermediate wave, the same relation is used as in the context of the Euler equations,

$$\left(\alpha\rho u\right)^*_{1R} - \left(\alpha\rho u\right)^*_{1L} = \beta\left(\left(\alpha\rho\right)_{1R} - \left(\alpha\rho\right)_{1L}\right)S_{M1}.$$

The energy jump relation is based on the interface condition related to the momentum equation of phase 1:

$$\left(\alpha\rho\right)^*_{1R} u^*_{1R}\left(u^*_{1R} - S_{M1}\right) + \alpha^*_{1R}\left(p^*_{1R} - p_I\right) = \left(\alpha\rho\right)^*_{1L} u^*_{1L}\left(u^*_{1L} - S_{M1}\right) + \alpha^*_{1L}\left(p^*_{1L} - p_I\right).$$

Velocity jump conditions across left- and right-facing waves of the dispersed phase are introduced as,

$u^*_{1R} = u_{1R}$ and $u^*_{1L} = u_{1L}$.

Momentum jump across the contact wave consequently reads,

$$\left(\alpha\rho\right)^*_{1R} u_{1R}\left(u_{1R} - S_{M1}\right) + \alpha^*_{1R}\left(p^*_{1R} - p_I\right) = \left(\alpha\rho\right)^*_{1L} u_{1L}\left(u_{1L} - S_{M1}\right) + \alpha^*_{1L}\left(p^*_{1L} - p_I\right).$$

Assuming fluid 1 governed by the stiffened gas EOS, it becomes,

$$\alpha_{1R}^{*}\left[(\gamma_1-1)\rho e-\gamma_1 p_{1,\infty}\right]_{1R}^{*}-\alpha_{1L}^{*}\left[(\gamma_1-1)\rho e-\gamma_1 p_{1,\infty}\right]_{1R}^{*}=\left((\alpha\rho)_{1L}^{*}u_{1L}\left(u_{1L}-S_{M1}\right)-(\alpha\rho)_{1R}^{*}u_{1R}\left(u_{1R}-S_{M1}\right)\right)+\left(\alpha_{1R}^{*}-\alpha_{1L}^{*}\right)p_I$$

The internal energy jump thus reads,

$$(\alpha\rho e)_{1R}^{*}-(\alpha\rho e)_{1L}^{*}=(\alpha\rho)_{1L}^{*}u_{1L}\frac{\left(u_{1L}-S_{M1}\right)}{(\gamma_1-1)}-(\alpha\rho)_{1R}^{*}u_{1R}\frac{\left(u_{1R}-S_{M1}\right)}{(\gamma_1-1)}+\left(\alpha_{1R}^{*}-\alpha_{1L}^{*}\right)\frac{p_I+\gamma_1 p_{1,\infty}}{(\gamma_1-1)}.$$

The total energy jump for phase 1 follows,

$$(\alpha\rho E)_{1R}^{*}-(\alpha\rho E)_{1L}^{*}=\left(\alpha_{1R}^{*}-\alpha_{1L}^{*}\right)\frac{p_I+\gamma_1 p_{\infty,1}}{(\gamma_1-1)}+\left[(\alpha\rho)_{1R}^{*}-(\alpha\rho)_{1L}^{*}\right]\frac{S_{M1}^2}{2}+(\alpha\rho)_{1L}^{*}u_{1L}\frac{\left(u_{1L}-S_{M1}\right)}{(\gamma_1-1)}-(\alpha\rho)_{1R}^{*}u_{1R}\frac{\left(u_{1R}-S_{M1}\right)}{(\gamma_1-1)}.$$

For the first phase, these relations summarize as,

$$U_{R,k}^{*}=U_{L,k}^{*}+\psi_k,\ k=1,..,4, \tag{II.3.13}$$

with,

$$\psi=\begin{bmatrix}\beta\left(\alpha_{1R}-\alpha_{1L}\right)\\ \beta\left[(\alpha\rho)_{1R}-(\alpha\rho)_{1L}\right]\\ \beta\left[(\alpha\rho)_{1R}-(\alpha\rho)_{1L}\right]S_{M1}\\ \beta\left(\alpha_{1R}-\alpha_{1L}\right)\frac{p_I+\gamma_1 p_{\infty,1}}{(\gamma_1-1)}+\beta\left[(\alpha\rho)_{1R}-(\alpha\rho)_{1L}\right]\frac{S_{M1}^2}{2}+(\alpha\rho)_{1L}^{*}u_{1L}\frac{\left(u_{1L}-S_{M1}\right)}{(\gamma_1-1)}-(\alpha\rho)_{1R}^{*}u_{1R}\frac{\left(u_{1R}-S_{M1}\right)}{(\gamma_1-1)}\end{bmatrix}$$

For the dispersed phase, combining (II.3.12) and (II.3.13) the intermediate states are computed as,

$$\begin{cases}U_{R,k}^{*}=U_{HLL,k}^{*}+\omega_L\psi_k\\ U_{L,k}^{*}=U_{HLL,k}^{*}-\omega_R\psi_k\end{cases},\quad k=1,..,4. \tag{II.3.14}$$

Reconstruction is now addressed for the second phase. For the sake of simplicity, let us consider that the volume fraction of the second phase is considered additionally. To preserve the saturation constraint ($\alpha_1+\alpha_2=1$) the jump relation across the intermediate wave reads,

$$\alpha_{2R}^{*}-\alpha_{2L}^{*}=\beta\left(\alpha_{2R}-\alpha_{2L}\right).$$

Another assumption is now introduced. The density of the carrier phase is assumed uniform in the two intermediate states. In other words,

$$\bar{\rho}_2 = \frac{(\alpha\rho)^*_{2,\mathrm{HLL}}}{\alpha^*_{2,\mathrm{HLL}}}.$$

This assumption is needed as the flow solver behaves incorrectly when the product of two discontinuous functions are present (volume fraction and density). The assumption made at this level is similar to prolongated formulations used in Ghost Fluid Methods (Fedkiw et al., 1999), immersed boundary methods and diffuse interface methods (Kapila et al., 2001, Allaire et al., 2002, Massoni et al., 2002, Saurel and Pantano, 2018). In diffuse interface methods, numerical diffusion of volume fractions α_k and apparent densities $\alpha_k\rho_k$ results in automatic prolongment of phase's density ρ_k.

In this frame, apparent densities are rebuilt as,

$$(\alpha\rho)^*_{2R} = \alpha^*_{2R}\bar{\rho}_2,$$

$$(\alpha\rho)^*_{2L} = \alpha^*_{2L}\bar{\rho}_2.$$

Consequently,

$$(\alpha\rho)^*_{2R} - (\alpha\rho)^*_{2L} = \beta(\alpha_{2R} - \alpha_{2L})\overline{\rho_2}.$$

Momentum jump across the intermediate wave is rebuilt as,

$$(\alpha\rho u)^*_{2R} - (\alpha\rho u)^*_{2L} = \left[(\alpha\rho)^*_{2R} - (\alpha\rho)^*_{2L}\right]S_M = \beta(\alpha_{2R} - \alpha_{2L})\bar{\rho}_2 S_{M2}$$

where the contact wave speed of the second phase is computed as,

$$S_{M2} = \frac{U^*_{\mathrm{HLL}}\left((\alpha\rho u)_2\right)}{U^*_{\mathrm{HLL}}\left((\alpha\rho)_2\right)}.$$

It remains to determine total energy jump of the second phase. At this level no distinction is made between the left and right velocities of that phase: $u^*_{2L} = u^*_{2R} = S_{M2}$. As before, the energy jump relation is based on the interface condition related to the momentum equation of phase 2:

$$(\alpha\rho)^*_{2R} S_{M2}(S_{M2} - S_{M1}) + \alpha^*_{2R}(p^*_{2R} - p_I) = (\alpha\rho)^*_{2L} S_{M2}(S_{M2} - S_{M1}) + \alpha^*_{2L}(p^*_{2L} - p_I).$$

Alternatively, it reads,

$$\alpha^*_{2R}p^*_{2R} - \alpha^*_{2L}p^*_{2L} = \left((\alpha\rho)^*_{2L} - (\alpha\rho)^*_{2R}\right)S_{M2}(S_{M2} - S_{M1}) + (\alpha^*_{2R} - \alpha^*_{2L})p_I.$$

Assuming fluid 2 governed by the stiffened gas EOS, it becomes,

$$\alpha^*_{2R}\left[(\gamma_2 - 1)\rho e - \gamma_2 p_\infty\right]^*_{2R} - \alpha^*_{2L}\left[(\gamma_2 - 1)\rho e - \gamma_2 p_\infty\right]^*_{2R} = \left((\alpha\rho)^*_{2L} - (\alpha\rho)^*_{2R}\right)S_{M2}(S_{M2} - S_{M1}) + (\alpha^*_{2R} - \alpha^*_{2L})p_I$$

The internal energy jump thus reads,

$$\left(\alpha\rho e\right)_{2R}^{*}-\left(\alpha\rho e\right)_{2L}^{*}=\frac{\left(\left(\alpha\rho\right)_{2L}^{*}-\left(\alpha\rho\right)_{2R}^{*}\right)S_{M2}\left(S_{M2}-S_{M1}\right)+\left(\alpha_{2R}^{*}-\alpha_{2L}^{*}\right)\left(p_{I}+\gamma_{2}p_{\infty,2}\right)}{\left(\gamma_{2}-1\right)}.$$

The total energy jump for phase 2 follows,

$$\left(\alpha\rho E\right)_{2R}^{*}-\left(\alpha\rho E\right)_{2L}^{*}=\left[\left(\alpha\rho\right)_{2R}^{*}-\left(\alpha\rho\right)_{2L}^{*}\right]\left(\frac{S_{M2}^{2}}{2}-S_{M2}\frac{\left(S_{M2}-S_{M1}\right)}{\left(\gamma_{2}-1\right)}\right)+\left(\alpha_{2R}^{*}-\alpha_{2L}^{*}\right)\frac{\left(p_{I}+\gamma_{2}p_{\infty,2}\right)}{\left(\gamma_{2}-1\right)}.$$

The carrier phase is thus rebuilt as,

$$U_{R,k}^{*}=U_{L,k}^{*}+\psi_{k},\quad k=5,..,8, \tag{II.3.15}$$

with,

$$\psi=\beta\left(\alpha_{2R}-\alpha_{2L}\right)\begin{bmatrix}\dfrac{1}{\overline{\rho_{2}}}\\ \overline{\rho_{2}}S_{M2}\\ \overline{\rho_{2}}\left(\dfrac{S_{M2}^{2}}{2}-S_{M2}\dfrac{\left(S_{M2}-S_{M1}\right)}{\left(\gamma_{2}-1\right)}\right)+\dfrac{\left(p_{I}+\gamma_{2}p_{\infty,2}\right)}{\left(\gamma_{2}-1\right)}\end{bmatrix}$$

Last, relations (II.3.14) and (II.3.15) are used to compute $U_{R,k}^{*}$ and $U_{L,k}^{*}$ for $k=5,..,8$.

At this level, states vectors U_{R}^{*} and U_{L}^{*} are determined.

Local conservative fluxes are computed as,

$$\begin{cases}\Phi_{R}^{*}=\Phi_{R}+S_{R}\left(U_{R}^{*}-U_{R}\right)\\ \Phi_{L}^{*}=\Phi_{L}+S_{L}\left(U_{L}^{*}-U_{L}\right)\end{cases}. \tag{II.3.16}$$

Fluxes of System (II.3.1) are computed as,

$$F_{k}^{*}=\Phi_{k}^{*}+\Lambda_{k}\quad k=L,R, \tag{II.3.17}$$

with $\Lambda_{k}=p_{I}\left(0,\quad 0,\quad \alpha_{1k}^{*},\quad \left(\alpha u\right)_{1k}^{*},\quad 0,\quad \left(1-\alpha_{1k}^{*}\right),\quad -\left(\alpha u\right)_{1k}^{*}\right)^{T}$.

α_{k}^{*} are determined from the reconstructed states as,

$$\begin{cases}\alpha_{1L}^{*}=\alpha_{1HLL}^{*}-\omega_{R}\beta\left(\alpha_{1R}-\alpha_{1L}\right),\\ \alpha_{1R}^{*}=\alpha_{1HLL}^{*}+\omega_{L}\beta\left(\alpha_{1R}-\alpha_{1L}\right).\end{cases} \tag{II.3.18}$$

The associated Godunov-type scheme including non-conservative terms reads,

$$U_i^{n+1} = U_i^n - \frac{\Delta t}{\Delta x}\left(F^*_{i+1/2} - F^*_{i-1/2}\right) + \Delta t H_i ,$$

with H_i given by,

$$H_{i,u} = p_i^n \frac{\alpha^*_{1,i+1/2} - \alpha^*_{1,i-1/2}}{\Delta x}$$

$$H_{i,E} = p_i^n \frac{\Phi^*_{i+1/2}(\alpha_1) - \Phi^*_{i-1/2}(\alpha_1)}{\Delta x}.$$

In these expressions $\alpha^*_{k,i\pm 1/2}$ and $\Phi^*_{i+1/2}(\alpha_1)$ are given by (II.3.18) and (II.3.16) respectively.

II.3.c) Examples and validations

Validations of the flow solver and comparisons with the former Rusanov method are addressed first. Second computational examples are shown showing method's capabilities.

A volume fraction discontinuity at rest is considered to check method capability to maintain such stationary wave. Corresponding results are shown in Figure II.19.

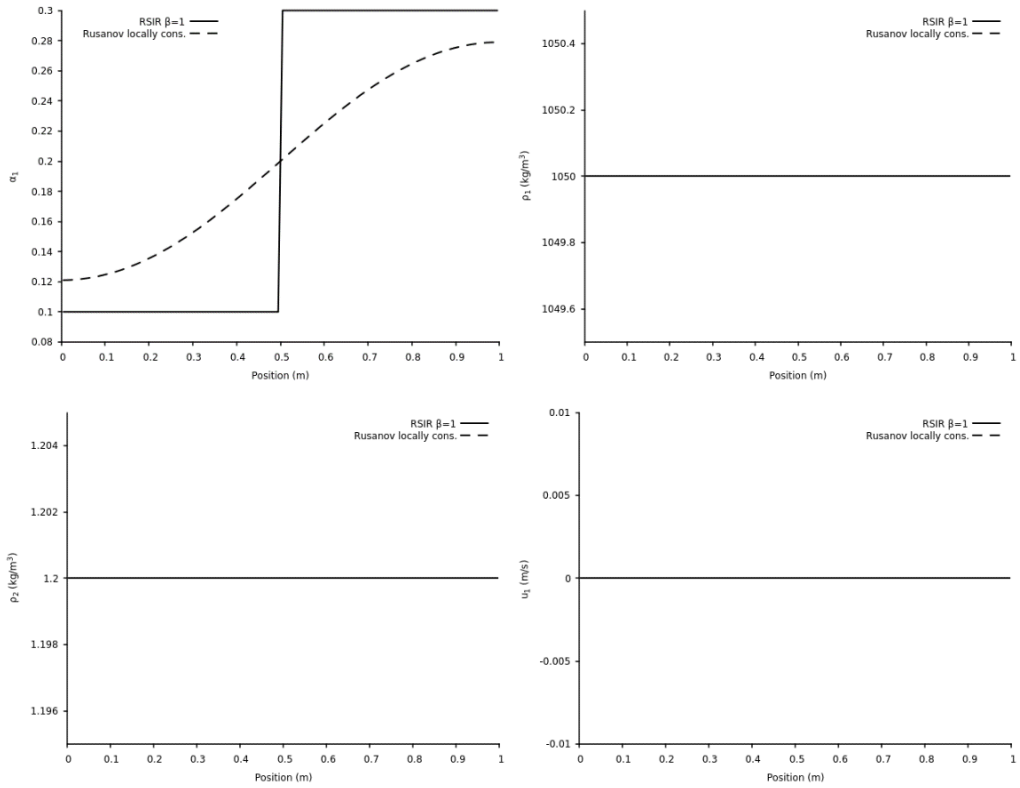

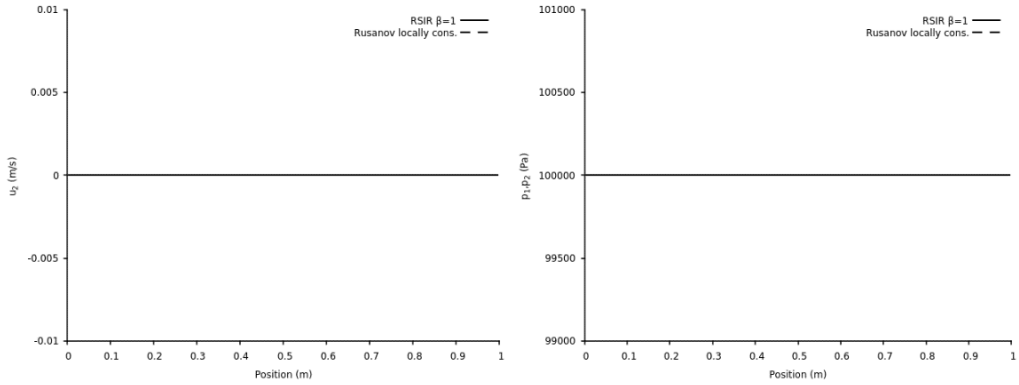

Figure II.19 – Results obtained by the new solver (β=1) for the computation of a contact discontinuity at rest. The computational domain involves 100 cells and first-order Godunov scheme is used with CFL=0.9. Results are shown at time t=6 ms. The volume fraction discontinuity is well preserved and spurious pressure and velocity oscillations are absent.

Transport of the same volume fraction discontinuity is now considered in a flow in uniform pressure and velocity conditions. Corresponding results are shown in Figure II.20.

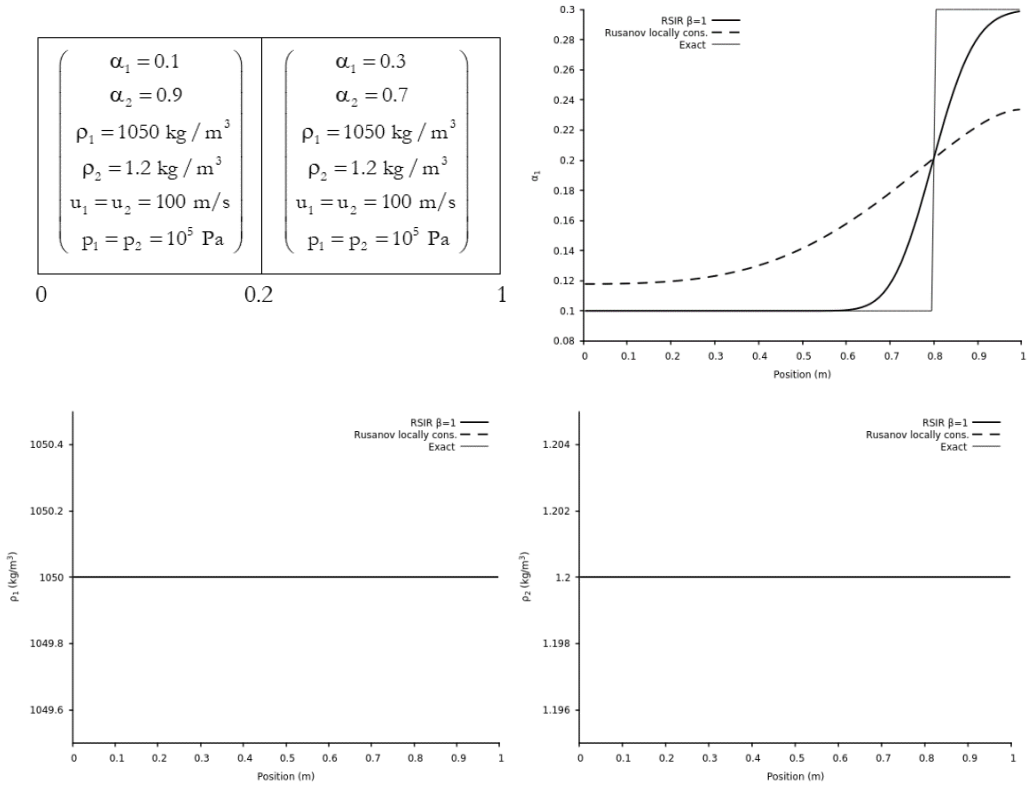

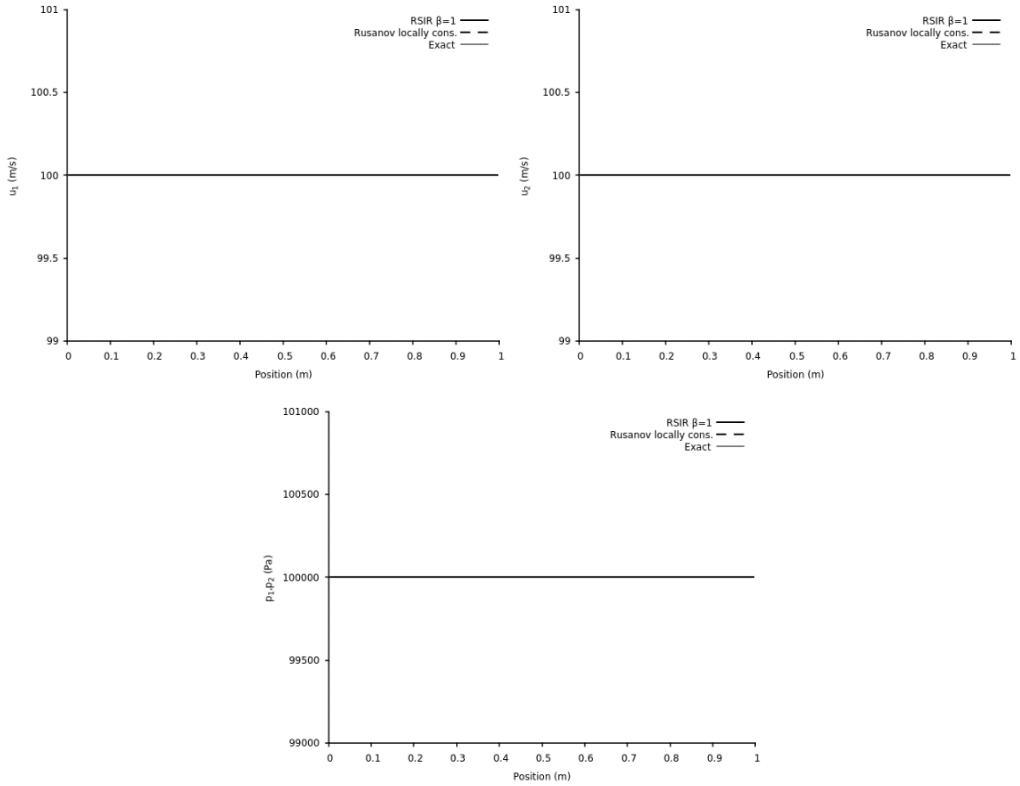

Figure II.20 – Results obtained by the new solver (β=1) for the computation of volume fraction discontinuity transport in a uniform pressure and velocity flow. The computational domain involves 100 cells and first-order Godunov scheme is used with CFL=0.9. Results are shown at time t=6 ms.

The same two-phase shock tube test problem as in Figures II.14 and II.15, in the absence of drag force is now considered. The new method and the Rusanov solver are compared in Figure II.21.

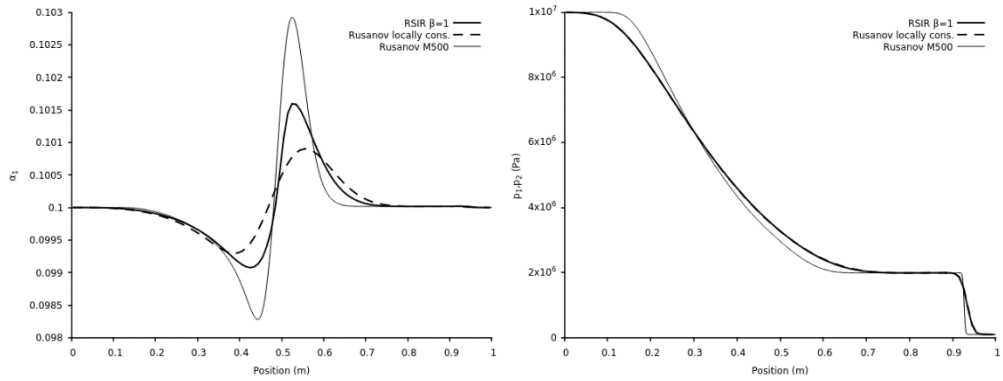

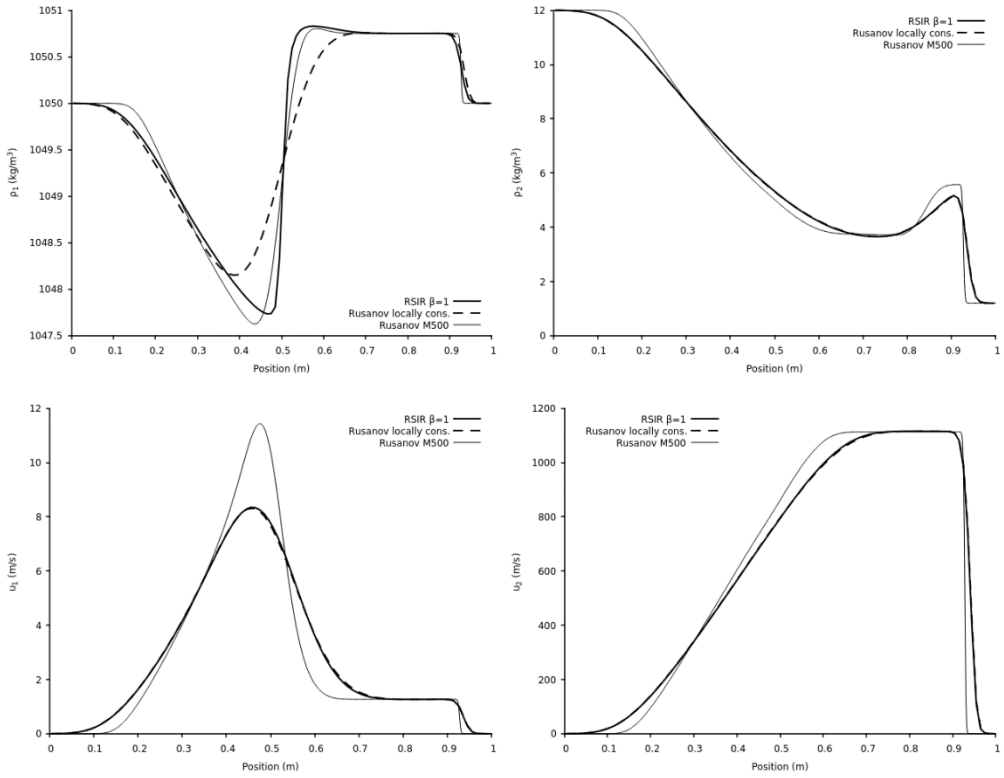

Figure II.21 – Comparison of the results obtained by the new solver (β=1) and the local conservative solver of Rusanov, both embedded in the first-order Godunov scheme with CFL=0.9 for the computation of the shock tube presented in Figure II.14. 100 computational cells are used. Results are shown at time t=300 μs. Stiff pressure relaxation is used. With the RSIR method, significant improvements appear in the volume fraction and phase 1 density computations. Indeed, the RSIR solution lies between computed results with the Rusanov method with 100 and 500 cells.

The RSIR solver is consequently validated and improves accuracy of the Rusanov and HLL solvers. Also, it preserves volume fraction discontinuities at rest. Its capabilities are now illustrated on the computation of a challenging two-phase flow instability.

II.4 – Multi-D example: Particle jetting during radial explosion

When a spherical or cylindrical explosive charge is surrounded by a liquid layer or a granular particle bed the material dispersal occurs through particle jets having well defined size. On the example shown in the Figure II.22 a cylindrical explosive charge is initially surrounded by a liquid layer.

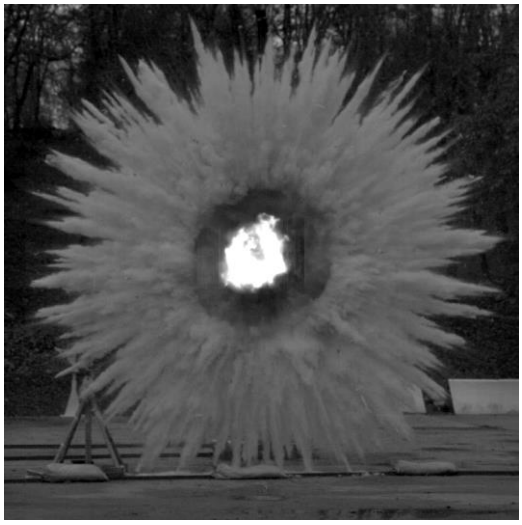

Figure II.22 – A cylindrical explosive charge is initially surrounded by a liquid layer. When the charge explodes the liquid layer transforms to a cloud of droplets forming highly dynamical particle jets.

Gas expansion during explosion fragments the liquid layer to a cloud of droplets that form highly dynamical particle jets. The same observation is reported when a granular bed is used instead of a liquid layer. Dispersion is consequently not spherical or cylindrical in the sense that one-dimensional computations result in significant errors in the predictions of materials presence. Experimental and numerical studies of this phenomenon have been achieved by Zhang et al. (2001), Milne et al. (2010), Frost (2010), Parrish and Worland (2010) to cite a few. Simplified situations have been considered in Rodriguez et al. (2013) and Xue et al. (2018). The explosive is replaced by a shock tube and the matter to disperse is placed between two plates, in a Hele-Shaw cell. Other simplified situations have been considered for example in McGrath et al. (2018), Osnes et al. (2018), Carmouze et al. (2018) to study possible clustering effects due to aerodynamic forces. It seems that jets formation and size selection mechanism is still unidentified.

In the following a configuration like the one considered in Rodriguez et al. (2013) with a Hele-Shaw cell and a particle ring is studied. Typical results reported in Rodriguez thesis are shown in Figure II.23 at times 5 ms, 8 ms and 57 ms after rupture of the shock tube diaphragm, inducing shock wave and gas flow through a ring of flour particles.

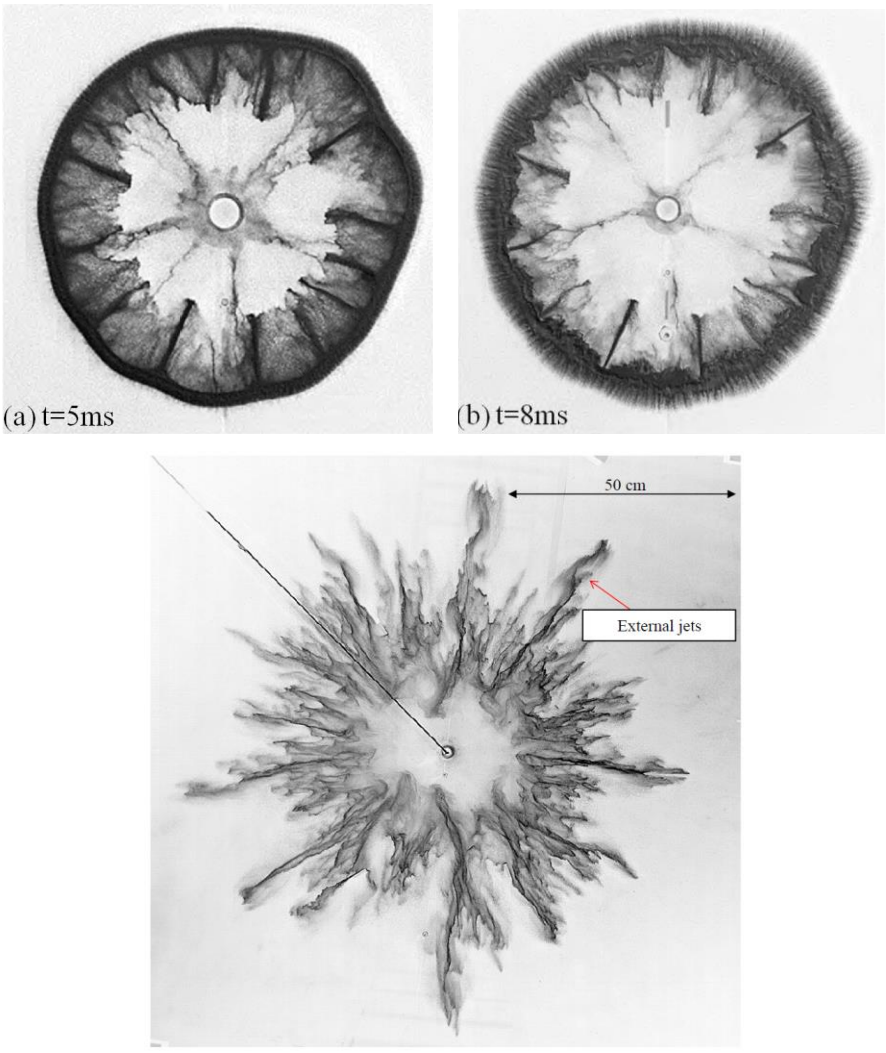

Figure II.23 – Typical interfacial instabilities reported in Rodriguez thesis and papers, as well as in Xue et al. (2018). Impulsive motion of a particle ring by a gas flow induces well defined particles fingers flowing to the center direction, oppositely to the gas flow. At later times, here at 8 ms, short wavelength instabilities also appear at the external surface. As time evolves, external surface instabilities grow and become dominant, as shown in the third picture at time 57 ms. Internal jets are thus observed at early times, followed by external ones at late times.

As reported by Rodriguez et al. (2013) and Xue et al. (2018), instabilities appear first at the inner interface and second at the outer one. Shape of these fingers is singular, in the sense that they do not qualitatively compare to the Richtmyer-Meshov instabilities or Rayleigh-Taylor ones, nor any other known instability. Indeed, mushroom type shape is observed with these two instabilities, while fingers are observed in the present context

With the help of the new model and present RIRS solver attempt is done to reproduce at least qualitatively these instabilities. Former attempts by the authors were based on Marble (1963) model

and fail to reproduce any, inner or outer, instability. In the present attempt computations are based on flow model (II.3.1) extended to 2D and resolved numerically in the DALPHADT code on triangular cells. Compared to the Marble model, the present one has a fundamental difference. Non-conservative terms are present in the momentum and energy equations. These non-conservative terms are often called 'nozzeling terms' in reference to the Euler equations with variable cross section. We prefer howether to interpret them as 'differential drag force'. As shown for example in Figure II.21, phase 1 is set to motion as a result of these terms, in the absence of conventional drag force. Indeed, drag parameter λ is set to zero in these computations. As shown later, it seems that non-conservative terms are responsible for appearance of these instabilities and size selection.

Considered computational domain and initial data are reported in Figure II.24.

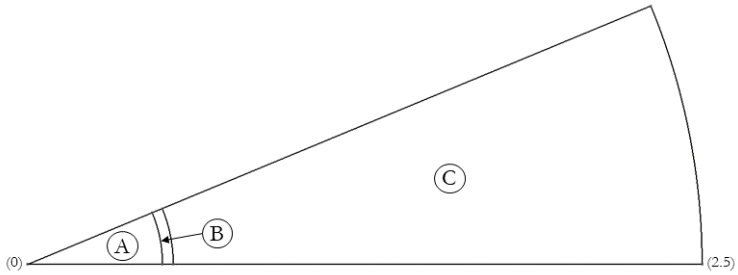

Domain	A	B	C
α_1	0.0001	0.4	0.0001
ρ_1 (kg/m^3)	1050	1050	1050
ρ_2 (kg/m^3)	12	1.2	1.2
$u_1=u_2$ (m/s)	0	0	0
$p_1=p_2$ (Pa)	1.10^7	1.10^5	1.10^5

Figure II.24 – Computational domain and initial data. The portion represents 1/16 of the complete disc with angle $\theta = \pi/8$. The domain denoted A corresponds to the high-pressure chamber, filled with gas only. The domain denoted B represents the initial particles ring of 4cm width. The domain denoted C corresponds to the low-pressure chamber at atmospheric conditions.

The mesh is made of triangles and contains about 15 cells in the radial direction of the particles ring.

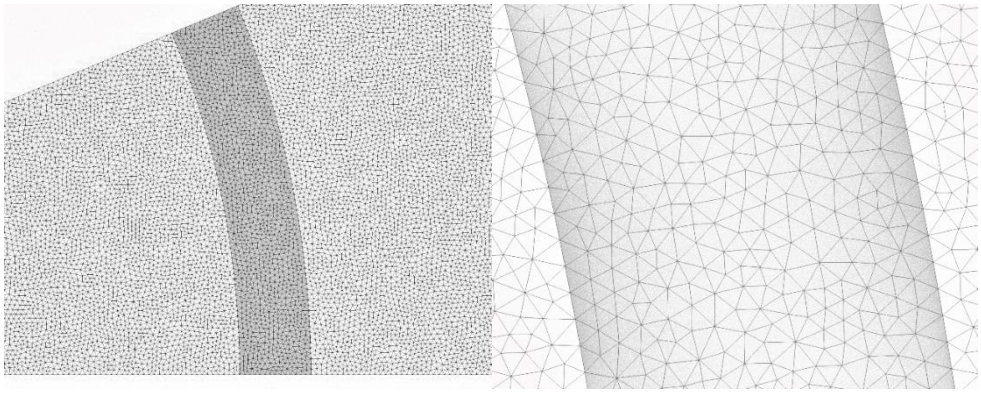

Figure II.25 – Representation of the mesh size used in the particle jetting computations. In the entire domain 361 222 computational cells are used.

Typical computed results are shown in Figures II.26 and II.27 and II.28 at different times. Volume fraction contours are shown. These computations show that the flow model reproduces, at least qualitatively both fingering instabilities issued of the inner and outer surfaces. In these computations drag force is considered with constant particles diameter (2 mm) and air dynamic viscosity (18.10^{-6} Pa.s). Drag force is modelled through Clift and Gauvin (1971) correlation,

$$F_D = \frac{3}{8R_1}\alpha_1 C_d \rho_2 \left\|\vec{u}_2 - \vec{u}_1\right\|\left(u_2 - u_1\right),$$

with,

$$C_d = \begin{cases} \dfrac{24}{Re_1}\left(1+0.15\,Re_1^{0.687}\right) & \text{if } Re_1 < 800 \\ 0.438 & \text{otherwise} \end{cases}$$

and $Re_1 = \dfrac{2R_1\rho_2\left\|\vec{u}_2 - \vec{u}_1\right\|}{\mu_2}$.

Drag force F_D is inserted in the right-hand side of the momentum equation of phase 1 and its opposite in phase 2. The power of this force $F_D.u_1$ is inserted similarly in associated energy equations.

In the absence of drag effects internal particles jets selection is observed as well but quantitative differences appear at later times. It is worth to mention that particle volume fraction is initially uniform in the cloud. No arbitrary wavelength is introduced in the initial data. Computed results at early times are shown in Figure II.26.

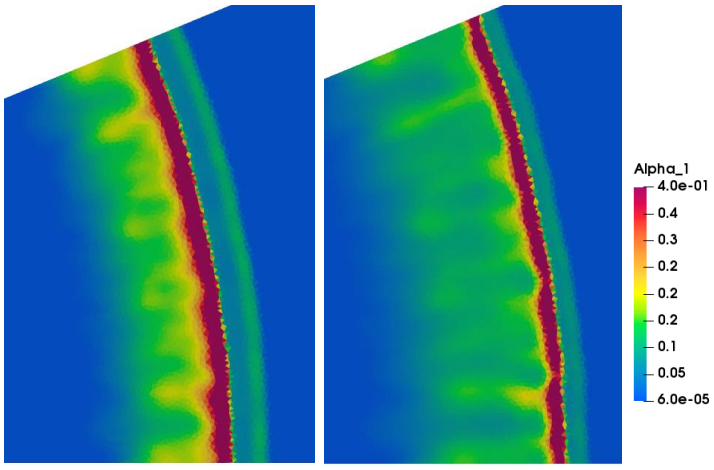

(a) (b)

Figure II.26 – Volume fraction contours of the dispersed phase for the particle jetting simulation, focused on the particles cloud at early times: (a) t=0.6 ms and (b) t=0.75 ms. 361 222 cells are used with CFL=0.5. Results are obtained with the RSIR (β=1) solver embedded in the MUSCL scheme

with Superbee limiter. A compaction zone appears first in the cloud in red color. Particles jets develop at the inner interface and direct to the center domain. Their growth is visible by comparing their length in graphs (a) and (b). They qualitatively look like the instabilities observed in Figure II.23 (a) and (b). Another front appears at the outer surface but appears more like a diffusion zone rather than the short wavelength instabilities visible in Figure II.23 (b). This is possibly due to insufficient special resolution of the present computations.

In Figure II.26 internal jets appear and develop to the center domain direction. A compaction zone appears in the cloud and a detached front with low particles concentration also appears ahead the compaction front. Noticeably the compaction front in red color catches up the detached front. Evolution at intermediate times is reported in Figure II.27.

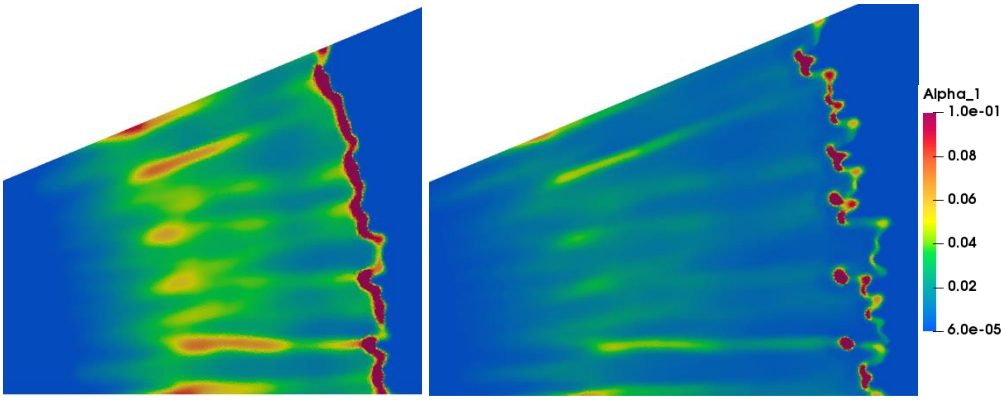

(a) (b)

Figure II.27 – Volume fraction contours of the dispersed phase for the particle jetting simulation, focused on the cloud at intermediate times: (a) t=1.5 ms and (b) t=2.25 ms. Same computational parameters as those of Figure II.26 are used as it corresponds to the same computation. The compaction front and the detached one are now merged and destabilize. Particles concentration zones having cluster type shapes appear in graph (b). Inner jets are still present and continue development.

In Figure II.27 the external front destabilizes, and relatively dense particle clusters appear. The inner front jets flowing to the domain center continue their development. Evolution at later times is reported in Figure II.28.

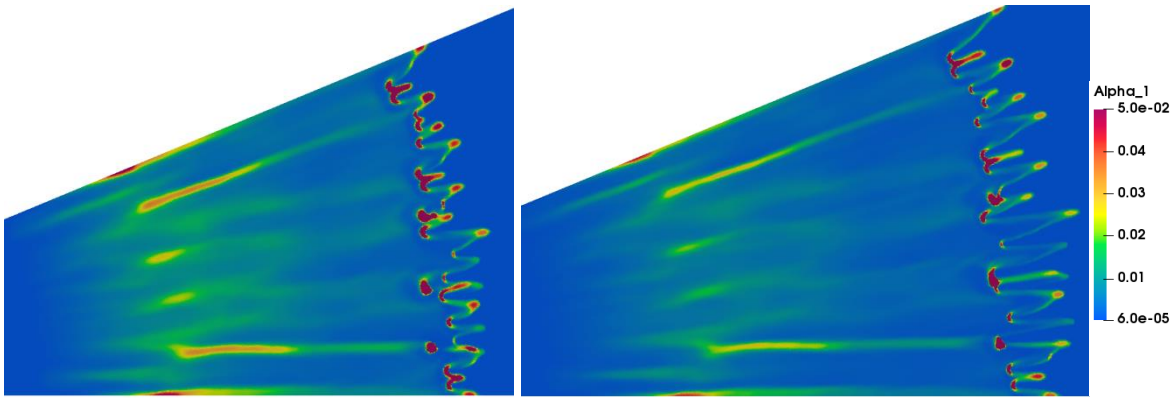

(a) (b)

Figure II.28 – Volume fraction contours of the dispersed phase for the particle jetting simulation, focused on the particles cloud at later times: (a) t=3 ms and (b) t=3.75 ms. Same computational parameters as those of Figure II.26 and II.27 are used. External front instabilities are now created and develop. Dilution of the internal jets happens while external jets develop as a consequence of particles 'dense' zones created at intermediate times. External jets amplitude grows as visible by comparing results of graphs (a) and (b).

In Figure II.28 external front instabilities are created and develop while internal ones tend to vanish. It is also interesting to note that the number of external fingers varies between graphs (a) and (b) as reported by Rodriguez et al. (2013) regarding experimental observations. In graph (b) about 10 leading fingers emerge while in (a) they are about 14.

We now address same type of configuration in 3D. The geometry used to solve particles jet instabilities is presented in Figure II.29, as well as the 3D mesh used in the cloud. Initial data are the same as those of Figure II.24. and 3D computed results are shown in Figure II.30.

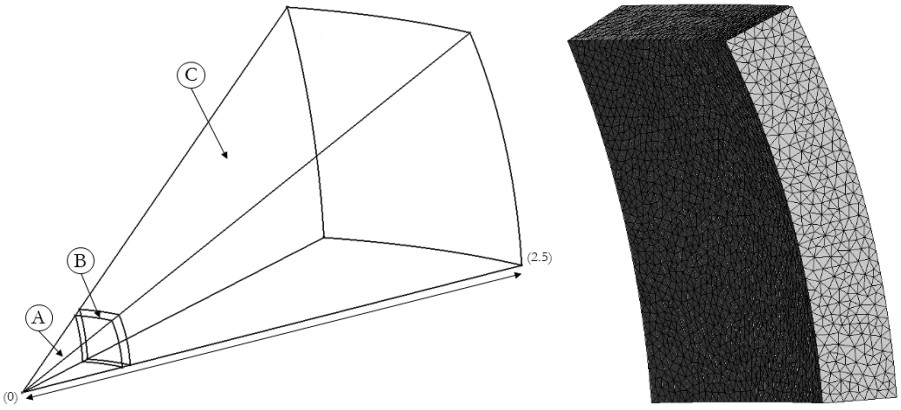

Figure II.29 – Computational domain for the 3D jetting particles test and representation of the mesh focused on the particles initial cloud. The domain is an extrusion of the domain presented in Figure II.24 with angle $\theta = \pi/8$. The mesh is coarser than the 2D one as it is obtained by coarsening the mesh of Figure II.24 from 361 222 to 90 358 cells and then extruding this mesh with angle $\theta = \pi/8$.

3D mesh involves about 11 109 700 cells. Initial data for the domain A, B and C are reported in the table in the Figure II.24.

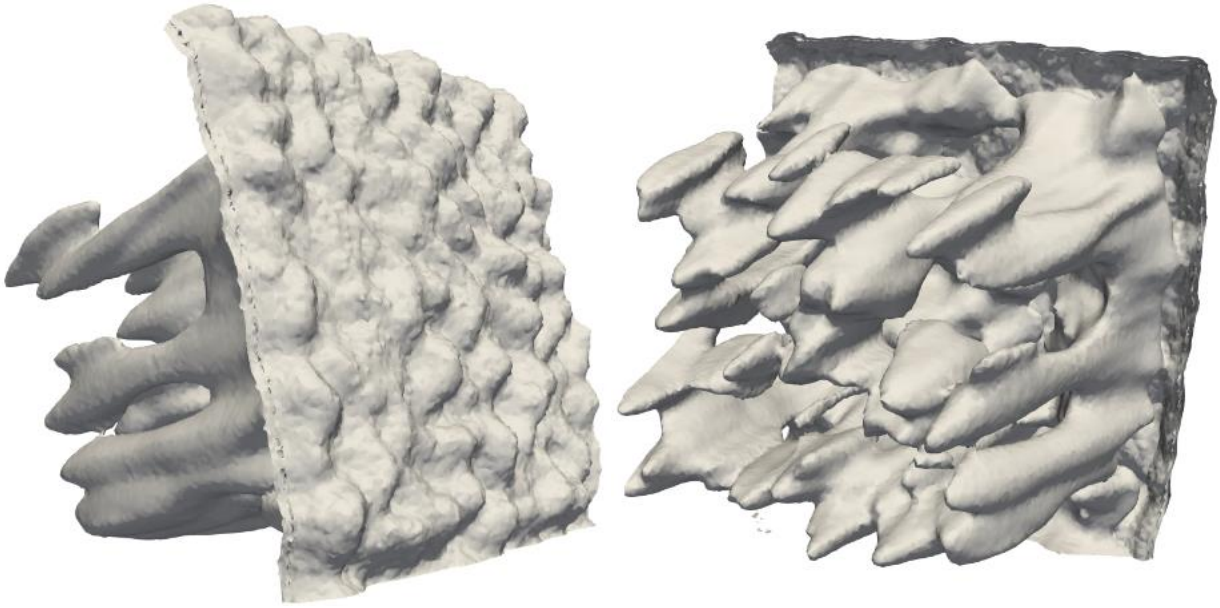

(a) (b)

Figure II.30 – Volume fraction contours of the dispersed phase for the 3D particles jetting simulation, focused on the particles cloud at t=3ms. Results are obtained with the RSIR (β=1) solver embedded in the MUSCL scheme with Superbee limiter and CFL=0.5. The upper cloud boundary is shown in (a) and the inner one is shown in (b). These graphs highlight external and internal jets observed in the experiments of Rodriguez et al. (2013).

Although not precisely identified from the present numerical experiments, the formation mechanism of this fingering instability appears closely related to non-conservative terms. They play the role of a differential drag force, acting intensively at cloud boundaries and vanishing in the wake, when volume fraction gradients disappear.

At the modeling level, non-conservative terms present similar form as capillary ones (Brackbill et al., 1992, Perigaud and Saurel, 2005) except that curvature effects are absent in the present two-phase formulation. Another major difference is that cloud boundaries are obviously highly permeable in the present context, while interfaces are not permeable in conventional hydrodynamic instabilities, except those considering flames and phase transition, where low permeability is present.

II.5 – Conclusion

A Riemann solver with internal reconstruction (RSIR) has been built as an extension of Linde (2002) solver. It has been first developed for the Euler equations and shown to provide similar accuracy and robustness as the HLLC solver, while being not as systematic as this one. The method has been

secondly extended to a two-phase non-equilibrium model developed by the authors. This model presented serious difficulties as it is weakly hyperbolic and valid only in the presence of stiff pressure relaxation, rendering solutions not self-similar. Thanks to the RSIR approach, a low dissipation solver has been developed. It has been validated against solution obtained with more conventional, but dissipative solvers. The new method has been applied in the last section to a difficult problem of fingering instability in granular media and has shown possible explanation of the formation mechanism. Extra work is still needed in this special two-phase flow topic to achieve understanding of this instability.

Regarding the Riemann solver, it seems flexible for many applications where most of the physics is governed by the two extreme waves and an intermediate one. Moreover, a parameter is present to control dissipation when flow conditions are particularly severe. In all present computations the solver appeared robust with parameter ($\beta=1$), corresponding to the minimum dissipation.

Chapter III

Coupling rigid bodies motion with single-phase and two-phase compressible flows on unstructured meshes

In this chapter multidimensional flow around some discrete particles is studied. A Level-Set type method is developed to describe the translation of a rigid body on unstructured meshes. Thanks to the Overbee limiter developed by Chiapolino et al. (2017) a simple and robust solid/fluid coupling method is built.
This method is then extended to 2D and validated through comparisons in the frame of a supersonic flow around a static blunt body. Two-way coupling is then addressed to observe motion of particles induced by shocks and creation of clusters.

Abstract

A simple method is developed to couple accurately translational motion of rigid bodies to compressible fluid flows. Solid rigid bodies are tracked through a Level-Set function. Numerical diffusion is controlled thanks to a compressive limiter (Overbee) in the frame of MUSCL-type-scheme, giving an excellent compromise between accuracy and efficiency on unstructured meshes (Chiapolino et al., 2017b). The method requires low resolution to preserve solid bodies' volume. Several coupling methods are then addressed to couple rigid body motion to fluid flow dynamics: a method based on stiff relaxation and two methods based on Ghost cells (Fedkiw et al., 1999) and immersed boundaries. Their accuracy and convergence rates are compared against an immersed piston problem in 1D having exact solution. The second Ghost cell method is shown to be the most efficient. It is then extended to multidimensional computations on unstructured meshes and its accuracy is checked against flow computations around cylindrical bodies. Reference results are obtained when the flow evolves around a rigid body at rest. The same rigid body is then considered with prescribed velocity moving in a flow at rest. Computed results involving wave dynamics match very well. The method is then extended to two-way coupling and illustrated to several examples involving shock wave interaction with solid particles as well as phase transition induced by projectiles motion in liquid-gas mixtures.

III.1 – Introduction

In fluid mechanics two approaches are used to address the relative motion between a rigid body and a fluid. The first one is also the most commonly used and consists in considering a fluid moving around a body at rest. Setting appropriate boundary conditions at inflows, outflows and walls this method gives reliable results. A fundamental difficulty emerges rapidly as soon as two (or more) rigid bodies are present. For instance, a moving body in the presence of a distant wall at rest is problematic. In the present approach rigid bodies are tracked on a fixed mesh with the help of Level-Set-type functions (Osher and Fedkiw, 2001). This function enables detection of fluids, solids and mixed cells. There are several advantages:

- The method allows solid body motion on fixed meshes and thus eliminates issues related to Lagrangian and ALE methods (Baum et al., 1994, Nkonga and Guillard, 1994, Nkonga, 2000);
- Surfaces are defined implicitly rather than explicitly as in the frame of Front Tracking (Glimm et al., 1998) and Interface Reconstruction methods (Youngs, 1984).

There are obviously drawbacks such as:

- Numerical smearing of the interface contour, that may result in solid body disappearance if the Level-Set function is resolved with insufficient accuracy ;
- Interface roughness effects due to mixed cells.

These issues become pregnant when dealing with unstructured grids as it is more difficult to control artificial smearing and roughness.

To be more precise regarding the state of the art of existing methods, it is worth to mention that accurate results can be obtained with ALE codes as well as cut-cells algorithms. In the frame of ALE methods it is possible to manage mesh deformation in the fluid with linear elasticity equations (Farhat et al., 2001, Barral and Alauzet, 2018). Several subtle operations are necessary to maintain a mesh of high quality. This is done to the price of code complexity and computational cost, but the interface between solid and fluid stays well defined, allowing accurate computation of boundary layers effects. The same remarks hold for cut-cells methods (Muralidharan, B. and Menon, 2018) where the mesh is not distorted, but needs special care with vanishing and emerging cells, as well as AMR (Berger and Colella, 1989) to reduce mesh roughness effects.

With the present alternative, already investigated by Liu et al. (2003), Wang et al. (2006), Liu et al. (2006), Liu et al. (2008), Zeng and Farhat (2012) to cite a few, the quest for simplicity dictates efforts. With the present contribution numerical smearing effects are reduced thanks to a specific limiter, straightforward to implement. Interface roughness effects are reduced with the help of appropriate velocity extrapolation from the fluid to the solid. AMR or mesh refinement of unstructured grids (Shewchuk, 2002) can be used to reach the required level of accuracy but are not addressed in the present work.

Recently a compressive limiter was introduced to sharpen diffuse interfaces in compressible two-phase flow modelling in the frame of 'diffuse interfaces' (Chiapolino et al., 2017b, Saurel and Pantano, 2018). This limiter showed enhanced capturing properties with 2-3 cells only in the interfacial zone, when used in the frame of MUSCL-type-schemes and unstructured meshes. It is thus considered in the present contribution to solve the Level-Set function to control numerical smearing. Its ability to preserve volume and maintain shapes is examined and is shown to be reasonably accurate. In the present frame, translational motion only is considered, excluding rotational one.

The coupling between solid body motion and compressible fluid flow is then examined. It is first examined in one-way, with prescribed solid velocity and action on the surrounding fluid. Three methods of coupling are examined:

- The first one is also the simplest and considers stiff velocity relaxation between the fluid and solid.
- The second one considers Ghost cells in the solid where specific fluid state is prescribed in a given band of cells closed to the interface.
- The third one consists in an improvement of the former to improve its convergence. The Ghost state is modified to improve the surface pressure computation, improving shock and rarefaction waves formation in the fluid during impulsive motion.

Comparison of the various coupling methods is done in 1D with the help of an exact solution of an immersed piston set to impulsive motion, quite similar to the exact shock tube solution.

The coupling method is then extended to multi-D, posing extra difficulties as sliding effects between solid and fluid have to be considered in a context where the interface is arbitrarily rough, as a consequence of unstructured mesh.

The coupling method when the solid is moving in a fluid at rest is validated by comparing computational results when the solid is at rest and the fluid is moving through appropriate boundary conditions, as done in most CFD computation. It is then extended to two-way coupling, through the computation of pressure force integral over the solid surface. It enables update of the solid body velocity which in turn affects the fluid flow. Computational examples of shock – solid particles interaction are shown to illustrate method's capability.

In the area of solid-fluid coupling with Level-Set type methods, many contributions have to be mentioned such as for example, Liu et al. (2003), Wang et al. (2006), Liu et al. (2006), Liu et al. (2008), Zeng and Farhat (2012) this list being certainly not exhaustive. However it seems that important differences appear with the present contribution. First, Cartesian grids are considered instead of unstructured ones. Second, exact or approximate local Riemann problem solution is set in mixture cells to enforce interface conditions. In the present contribution, such ingredient is not used, this detail being important when dealing with sophisticated flow models, such as multiphase flow ones. Last, Ghost Cells in multi-D computations are filled with fluid state normal to the interface in a band (or layer) of cells of finite size. Determination of these cells in the normal direction to the interface may be challenging when dealing with unstructured grids. In the present contribution this issue is replaced by a simple averaging method.

Fluid-fluid and solid-fluid coupling with Level-Set methods have been addressed in the frame of unstructured meshes by Farhat et al. (2008, 2012), Wang et al. (2011) and possibly other authors. It seems that similar restrictions as the former lists with Cartesian grid approaches are present:

- Use of local Riemann problem solution,
- Sophisticated method for setting fluid state in the Ghost-Cell band.

The present approach doesn't seem more accurate than existing ones but seems conceptually simpler and easier to implement.

The paper is organized as follows. The Level-Set method and its numerical resolution are summarized in Section 2. Then, coupling methods are examined in Section 3. The compressible flow model is presented in this section and a reference solution is built to address an immersed piston set to motion impulsively. Three different coupling methods are detailed and tested against the exact solution of the immersed piston test. The method that matches best the results is then extended to multi-dimensions in Section 4. This section ends by validations of the coupling method in 2D with a supersonic flow. Section 5 extends to coupling method to two-way coupling through pressure force computation over each rigid body surface. Conclusions are given in Section 6.

III.2 – Motion of rigid bodies

Rigid bodies are tracked through the Level-Set function denoted by Φ, that is in the present approach aimed to model a Heaviside function. Let us consider a domain Ω having a subdomain Ω_f occupied by the fluid and another sub-domain Ω_s occupied by the solid body, as schematized in Figure III.1.

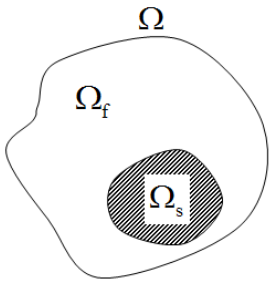

Figure III.1 – Schematic representation of the solid and fluid sub-domains

The Level-Set function Φ indicates the presence of materials and interface at a given point of space **M**. It is defined as,

$$\begin{cases} 1 \geq \Phi > 0 & \text{if } M \in \Omega_s \\ 0 & \text{if } M \in \Omega_f \cap \Omega_s \\ 0 > \Phi \geq -1 & \text{if } M \in \Omega_f \end{cases} \qquad \text{(III.2.1)}$$

With these definitions the zero level pays particular attention as it represents the solid-fluid interface. The Level-Set function obeys the transport equation,

$$\frac{\partial \Phi}{\partial t} + \vec{u_s}.\vec{\nabla}\Phi = 0 \qquad \text{(III.2.2)}$$

where $\vec{u_s}$ denotes the solid body velocity. As it is constant in the rigid body and only time dependent, Eq. (III.2.2) can be expressed in conservation form:

$$\frac{\partial \Phi}{\partial t} + \vec{\nabla}.\left(\Phi \vec{u_s}\right) = 0 \qquad \text{(III.2.3)}$$

Note that considering uniform rigid body velocity excludes rotational motion. The main difficulty with the Level-Set method is to preserve body volume and shape. As a Heaviside function is initially set as $\Phi = 1$ in the solid and $\Phi = -1$ in the fluid, numerical smearing of the discontinuity may result rapidly in solid volume loss. As soon as two interfaces are present and mesh not enough refined solid body may disappear as time evolves. A typical example is shown in Figure III.4 when the MUSCL-Superbee method is used. Several methods are available to balance this weakness:

- When the Level-Set function is used as a distance function (different of definition in Eq. (III.2.1)), a re-initialization procedure is able to restore the correct function profile (Osher and Fedkiw, 2001).
- When it is aimed to model a Heaviside function, as in the present work, the interface can be sharpened with the help of artificial compressibility terms (Olsson et al., 2007, Shukla et al., 2010).

However these procedures require efforts, in particular in unstructured meshes and are consuming in computer resources.

For the sake of simplicity we adopt the method developed in Chiapolino et al. (2017b) in the frame of diffuse interface modelling. This method was precisely designed to lower the numerical diffusion of so called 'diffuse interfaces' through a specific limiter, used to sharpen volume fraction profiles. This limiter (Overbee) is used in MUSCL-type-schemes (Van Leer, 1979) that are quite simple to implement in unstructured codes. Details of the implementation used in the present work are given in Chiapolino et al. (2017b). The Overbee limiter is illustrated in Figure III.2 and corresponds to the upper bound of the first-order TVD region.

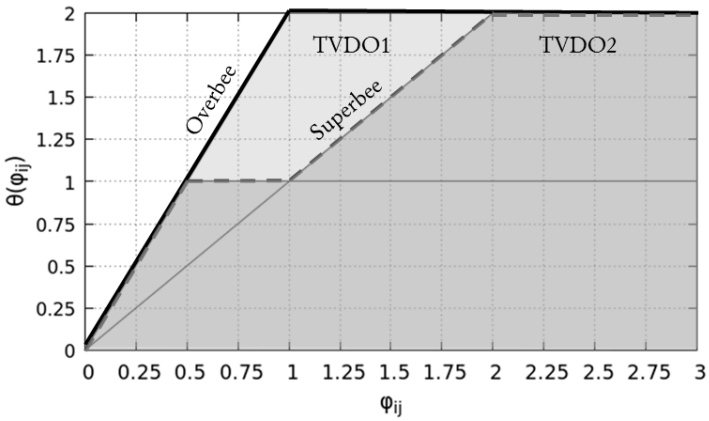

Figure III.2 – First-order and second-order TVD regions. The upper bounds of these regions correspond respectively to the Overbee and Superbee limiters.

The Overbee limiter used in the computational examples of the present paper reads:

$$\theta\left(\varphi_{ij}\right) = \max\left[0, \min\left[2\varphi_{ij}, 2\right]\right], \tag{III.2.4}$$

where φ_{ij} represents the ratio of slopes between cells i and j.

This limiter was originally designed for volume fraction transport, where boundedness of this variable between 0 and 1 is mandatory, and used without modification with the Level-Set function. Thus, the signed property of this function is not used at the discrete level but used only to detect materials through Eq. (III.2.1). Efficiency of this limiter is illustrated in Figure III.3 where a comparison with Superbee is shown for the transport of a Heaviside function at prescribed velocity. Superbee was considered as the optimum bound for the design of limiters (Sweby, 1984). However, when dealing with Heaviside functions only this upper bound can be overpassed, resulting in significant improvements of the solution, free of robustness issues.

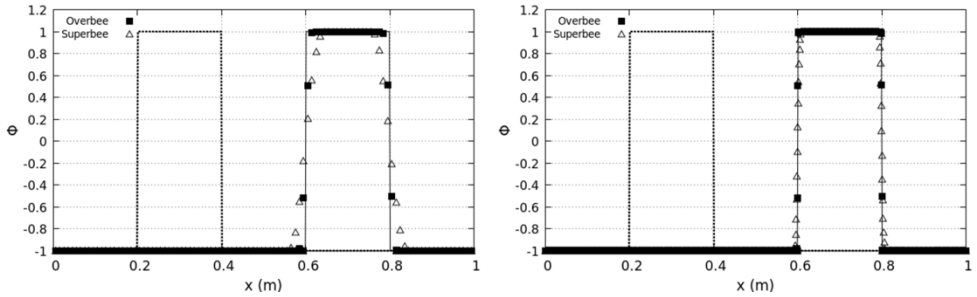

Figure III.3 – Comparison of the Overbee and Superbee limiters for the transport of a Heaviside function, here a Level-Set-type function. The advection speed is 100 m/s. The dashed lines represent the initial condition. The full line represents the exact solution. Gradients of the Heaviside function are computed with the least-squares method, corresponding in the one-dimensional case to central approximations. Final time: t=4 ms, CFL=0.8. On the graph at left 100 cells are used while

on the one at right 1 000 cells are used. Overbee captures the discontinuity with two points only whatever the mesh resolution is.

In these computations, the gradients are computed with central approximations. Indeed, central differences correspond to the least-square approximation method that preserves accuracy and robustness in unstructured meshes codes (Barth and Jespersen, 1989). It appears that the Overbee limiter handles discontinuities in two points only for any mesh refinement and any method of gradient computation (central differencing as well as upwind-downwind). Its capabilities in multi-D are excellent as well, as shown in Figure III.4 where a Zalesak (1979) disc is transported at prescribed velocity (10 m/s) on an unstructured grid made of 16 156 triangles.

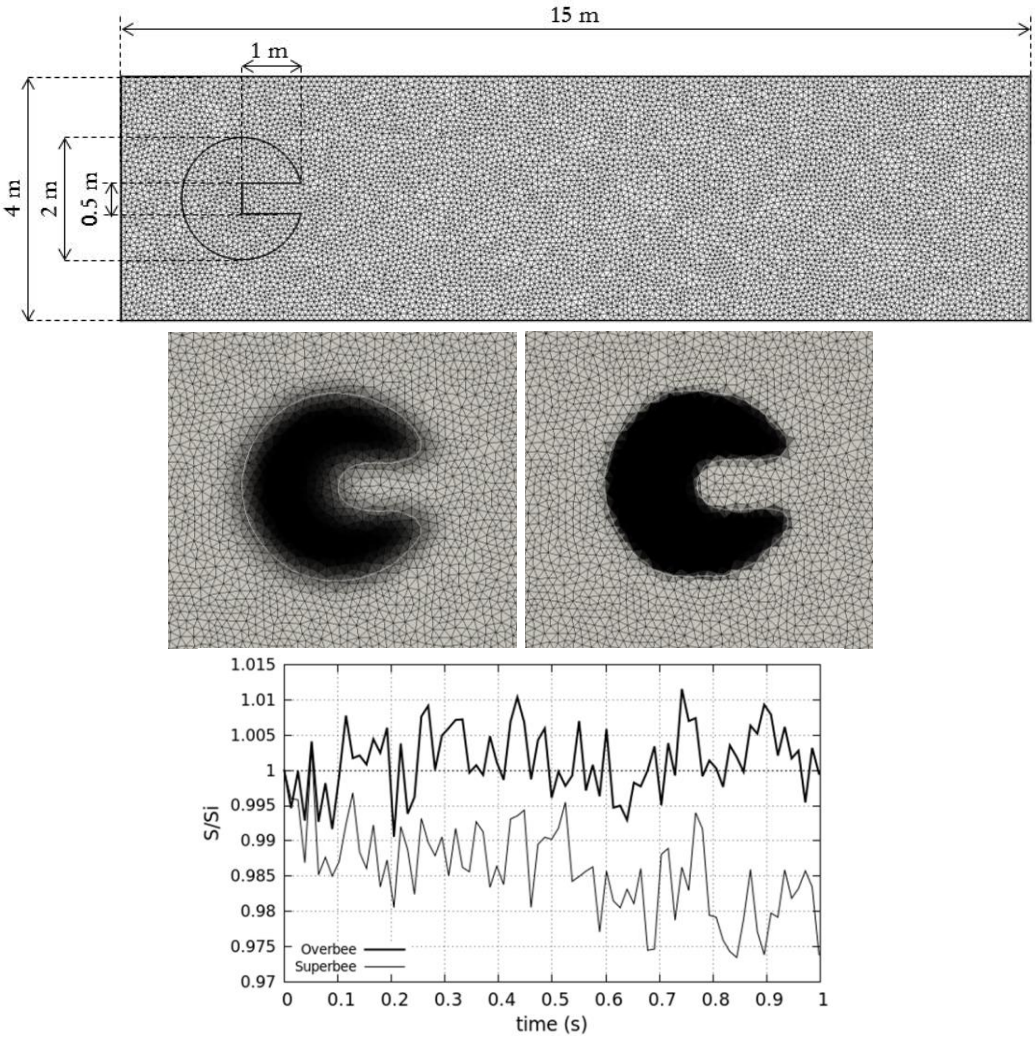

Figure III.4 – Transport of the Zalesak disc on an unstructured grid. The initial data and dimensions are shown on the upper graph. Contours of the Level-Set function and its zero level are shown in the graphs at the middle, at time 1s, before exiting the right boundary of the domain. The graph at

left is obtained with the MUSCL-Superbee scheme while the one at right uses Overbee. The graph at bottom shows surface evolution. Superbee results in surface loss while Overbee preserves surface in the time average sense. All computations use least-square methods for the gradients computation, with an extended set of neighbors as defined in Figure III.6. The same mesh with 16 156 cells is used in both computations, corresponding to an average cell size of 0.05 m. The time step is computed to fulfil CFL restriction of 0.9.

The same computations are rerun on a bigger domain and the results are shown at times 1s, 2s and 3s with the MUSCL-Overbee method in Figure III.5.

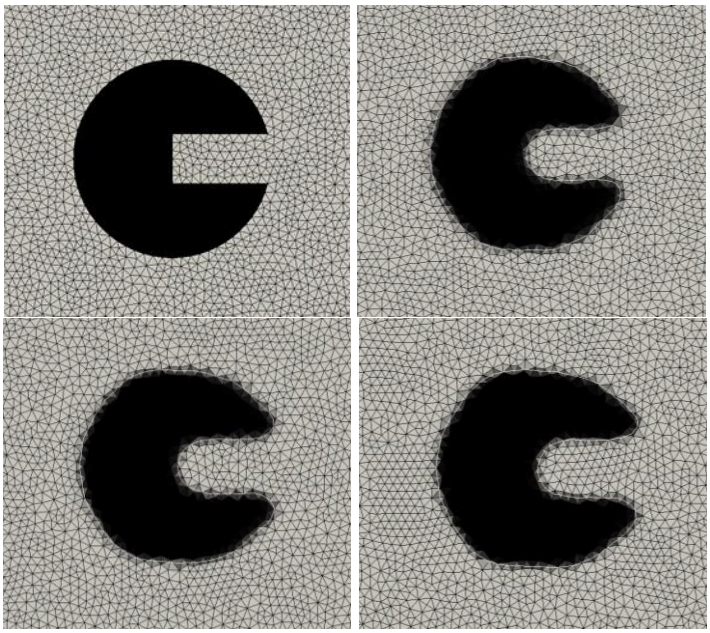

Figure III.5 – Transport of the Zalesak disc on an unstructured grid at times 0s, 1s, 2s and 3s with the MUSCL-Overbee scheme. The upper left graph corresponds to the initial shape of the Zalesak disc. The upper right graph represents the shape of the rigid body at time 1s. The bottom graphs represent respectively the Zalesak disc at time 2s at left and at time 3s at right. All computations use least-square methods for the gradients computation, with an extended set of neighbors as defined in Figure III.6. The average cell size is about 0.05 m. The time step is computed to fulfil CFL restriction of 0.9.

It appears that the overall shape is well preserved. It is worth to mention that the two stencils described in Figure III.6 have been considered for the gradients computation in the least-square method. The results are very similar, the final shape being slightly smoother with extended neighbors. Gradients computed with extended neighbors are always more accurate, having negligible extra cost in 2D computations and about 10% extra cost in 3D. These two stencils are illustrated in the Fig. III.6.

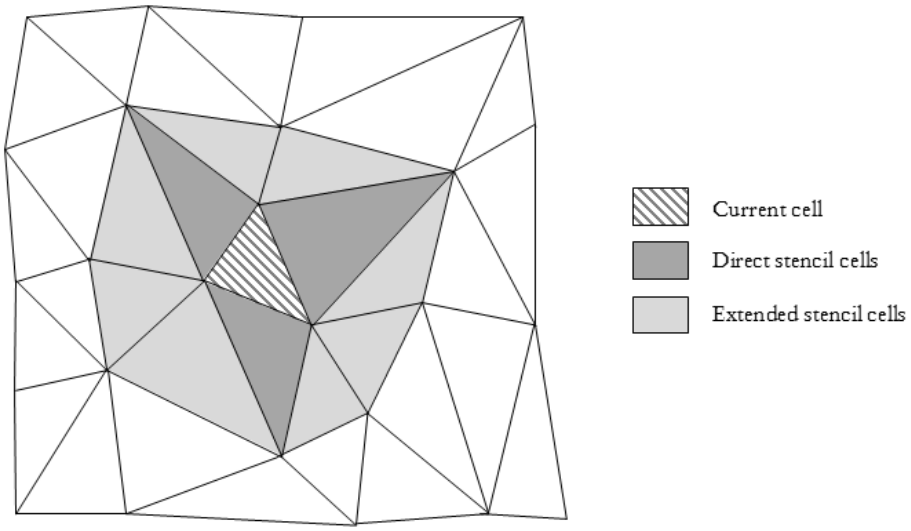

Figure III.6 – Definition of the two stencils: direct and extended neighbors.

Having now in hands a simple and efficient method to track rigid bodies, we now address coupling with the flow dynamics.

III.3 – Coupling methods

Solid-fluid coupling methods are now examined in the frame of a flow model that includes Euler and reactive Euler equations as well as multiphase mixtures in mechanical and thermal equilibrium. This formulation is particularly interesting to address phase transition at interfaces and in finely dispersed mixtures (Le Martelot et al., 2014, Saurel et al., 2016). In the present analysis, phase transition is omitted and coupling methods are analyzed in 1D.

III.3.a) Flow model

The flow model, augmented by Level-Set equation reads,

$$\frac{\partial \rho}{\partial t}+\vec{\nabla}.\left(\rho\vec{u}\right)=0$$
$$\frac{\partial \rho\vec{u}}{\partial t}+\vec{\nabla}.\left(\rho\vec{u}\otimes\vec{u}+p\bar{\bar{I}}\right)=\vec{0}$$
$$\frac{\partial \rho E}{\partial t}+\vec{\nabla}.\left((\rho E+p)\vec{u}\right)=0 \qquad \text{(III.3.1)}$$
$$\frac{\partial \rho Y_k}{\partial t}+\vec{\nabla}.\left(\rho Y_k\vec{u}\right)=0$$
$$\frac{\partial \Phi}{\partial t}+\vec{\nabla}.\left(\Phi\vec{u}_S\right)=0$$

In these notations index k represents a given fluid constituent (liquid or gas). ρ denotes the mixture density, $\vec{u}$ and $\vec{u}_S$ represent the velocity vector of the fluid and the solid respectively, Y_k represent the mass fraction constituent k and E the total energy of the fluid mixture ($E=\sum_k Y_k e_k+\frac{1}{2}\vec{u}.\vec{u}$).

Each fluid is assumed to be governed by a convex equation of state (EOS). Here the stiffened-gas EOS is retained for each constituent as it represents reasonably the thermodynamics of liquids in limited ranges of temperature (typically 300-500K). It also includes the ideal gas EOS when some parameters are set to zero. For a given constituent it reads,

$$p_k=(\gamma_k-1)\rho_k(e_k-q_k)-\gamma_k p_{k,\infty}, \qquad \text{(III.3.2)}$$

where γ_k, q_k and $p_{k,\infty}$ are characteristic of a given constituent. A method to determine these parameters for liquid-vapor systems is given in Le Metayer et al. (2003). The stiffened-gas EOS can be improved to account for short distance repulsive effects, while remaining convex (Le Metayer and Saurel, 2016, Chiapolino and Saurel, 2018).

Under the assumption of temperature and pressure equilibrium among the phases, the following mixture EOS is obtained from the definition of mixture internal energy ($e=\sum_k Y_k e_k(T,p)$) and mixture specific volume ($v=\sum_k Y_k v_k(T,p)$) definitions (Saurel et al., 2016):

$$p(\rho,e,Y_k)=\frac{\sigma+\sqrt{\sigma^2+4\overline{C_v}\omega}}{2\overline{C_v}} \quad \text{with} \quad \begin{cases}\sigma=\dfrac{e-\bar{q}}{v}\left(\overline{C_p}-\overline{C_v}\right)-p_{1,\infty}\overline{C_v}-p_{1,\infty}Y_1\left(C_{p,1}-C_{v,1}\right)\\ \omega=\dfrac{e-\bar{q}}{v}p_{1,\infty}\left(\overline{C_p}-\overline{C_v}-Y_1\left(C_{p,1}-C_{v,1}\right)\right)\end{cases} \qquad \text{(III.3.3)}$$

and $\overline{C_v} = \sum_{k=1}^{N} Y_k C_{v,k}$, $\overline{C_p} = \sum_{k=1}^{N} Y_k C_{p,k}$, $\overline{q} = \sum_{k=1}^{N} Y_k C_{v,k}$.

The mixture temperature $T = T(\rho, p, Y)$ is obtained as,

$$T(\rho, p, Y_k) = \frac{1}{\rho\left(\sum_{k=1}^{N} \frac{Y_k (\gamma_k - 1) C_{v,k}}{p + p_{k,\infty}}\right)} \tag{III.3.4}$$

This EOS is valid when the liquid phase is denoted by index 1, the other constituents being ideal gases ($p_{k,\infty} = 0, k \neq 1$). It is worth to mention that when all constituents are ideal gases, the Dalton's law of ideal gas mixtures is recovered (Chiapolino et al., 2018). Therefore, System (III.3.1) with thermodynamic closure Eq. (III.3.3) can be used for single phase flows and two-phase liquid-gas mixtures in mechanical and thermal equilibrium.

System (III.3.1) is hyperbolic with the sound speed given in Le Martelot et al. (2014) page 65. However this formula is quite complicated and useless, as the Wood (1930) sound speed is simpler and slightly greater than the thermal and mechanical equilibrium sound speed. The Wood speed of sound is consequently a better candidate for numerical computations, with respect to CFL computation as well as wave speeds computation in approximate Riemann solvers. It is given by:

$$\frac{1}{\rho c^2} = \frac{1}{\sum_{k=1}^{N} \left[\frac{\alpha_k}{\rho_k c_k^2}\right]} , \tag{III.3.5}$$

where $\alpha_k = \frac{\rho Y_k}{\rho_k(T, p)}$ denotes the volume fraction of phase k.

In the limit of vanishing mass and volume fractions of the liquid phase and when a single gas constituent is present the Euler equations of gas dynamics are recovered. This remark enables building of a simple 1D reference solution to assess the accuracy of the various coupling methods.

III.3.b) Reference solution

An immersed piston in a fluid, here the air considered as an ideal gas, is set to motion impulsively at time t=0. The impulsive motion to the right induces propagation of a right facing shock wave and a left facing expansion wave. A schematic (x,t) diagram is shown in Figure III.7 as well as qualitative profiles of velocity, pressure and density at a given time. This test problem is reminiscent of the exact Riemann problem solution except that the velocity between the two extreme waves is prescribed.

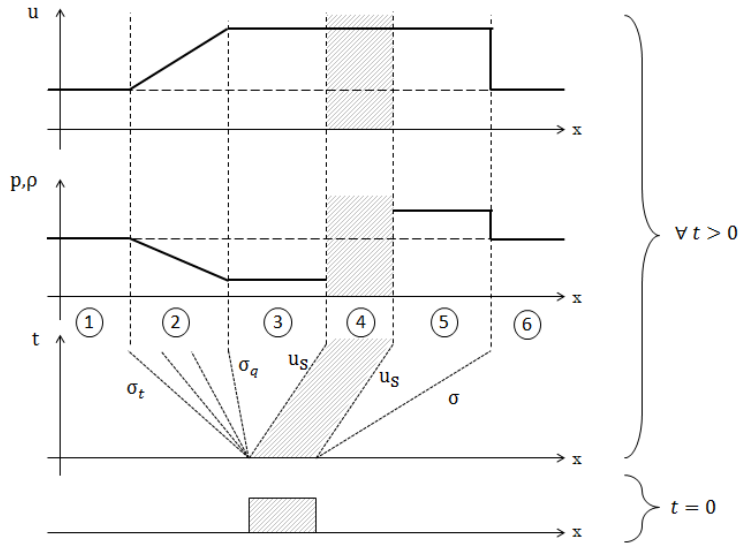

Figure III.7 – Immersed piston test problem. Schematic representation of the (x,t) diagram and associated velocity, pressure and density profiles.

The various states present in the solution are:

- (1) left state initially at rest,
- (2) expansion wave,
- (3) fully expanded fluid,
- (4) piston,
- (5) post shock state,
- (6) right state initially at rest.

The exact solution is straightforward. Knowledge of the piston velocity combined to the Rankine-Hugoniot relations determines fully state (5). The use of the Riemann invariants between state (1) and (3) where the velocity is the one of the piston determines fully state (3) and any point of the expansion wave (2). An example of such solution is given in Figure III.8 with initial data of Table III.1.

Temperatures T_1 and T_6	293 K
Velocities u_1 and u_6	0
Pressures p_1 and p_6	100 000 Pa
Domain lenght	1 m
Initial position of the piston (m)	$0.4 \leq x \leq 0.5$
Velocity of the piston **us**	100 m/s
Final time	1 ms

Table III.1 – Initial data for the immersed piston test problem.

The air thermodynamics is modeled through EOS (III.3.2) with following data: $\gamma = 1.4;\ p_\infty = 0\ \text{Pa};\ q = 0\ \text{J/kg}$.

The corresponding exact solution is shown in Figure III.7. These results will serve as reference for the three coupling methods that are considered hereafter.

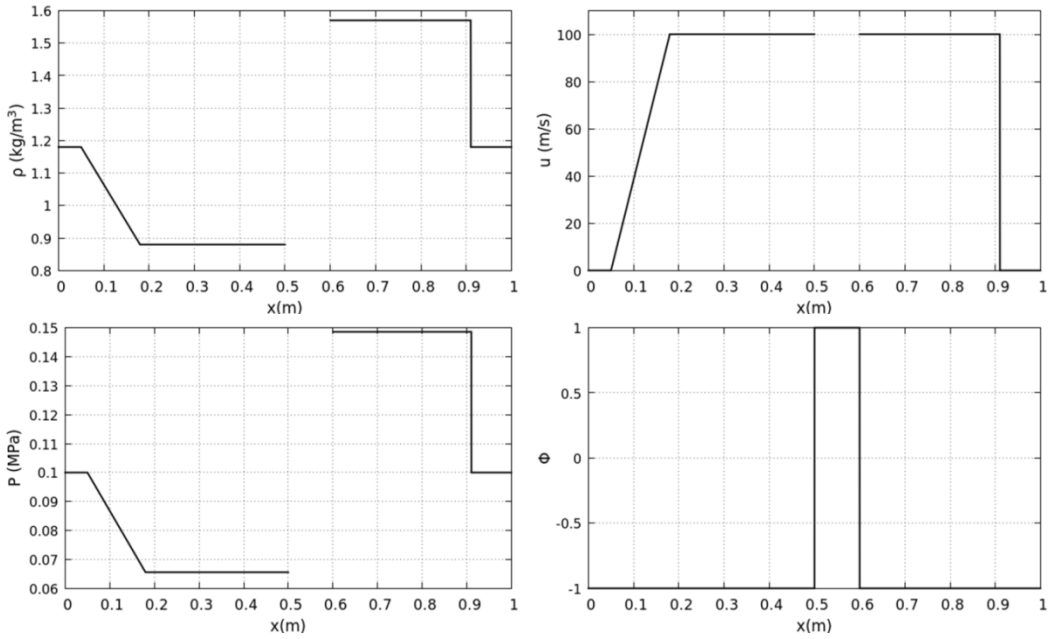

Figure III.8 – Exact solution for the immersed piston test problem moving in an ideal gas associated to initial data of Table III.1.

III.3.c) First coupling method: Velocity penalization

In the present paragraph the coupling method is studied in 1D and the flow model (III.3.1) is reduced to the Euler equations to facilitate both presentation and comparison with the former exact solution. Also, a single moving rigid body is considered. The corresponding flow model with stiff velocity relaxation (penalization) among the body and fluid reads,

$$\begin{aligned}
&\frac{\partial \rho}{\partial t} + \frac{\partial \rho u}{\partial x} = 0 \\
&\frac{\partial \rho u}{\partial t} + \frac{\partial \rho u^2 + p}{\partial x} = F_\Phi \\
&\frac{\partial \rho E}{\partial t} + \frac{\partial (\rho E + p) u}{\partial x} = F_\Phi . u_S \\
&\frac{\partial \Phi}{\partial t} + \frac{\partial \Phi u_S}{\partial x} = 0
\end{aligned} \qquad \text{(III.3.6)}$$

where F_Φ represents the drag force exerted by the fluid on the solid and $F_{\Phi_S}.u_S$ the power of this force.

The coupling force is modelled as,

$$F_\Phi = \rho \frac{1+\tilde{\Phi}}{2} \frac{u_S - u}{\tau} \tag{III.3.7}$$

where the relaxation time tends to zero ($\tau \to 0^+$) and factor $\frac{1+\tilde{\Phi}}{2}$ makes this force present in the numerical diffusion zone of the solid-fluid interface, on the solid side only. Similar approach is examined in Abgrall et al. (2014).

The modified Level-Set function $\tilde{\Phi}$ is defined as:

$$\tilde{\Phi} = \begin{cases} +1 & \text{if} \quad \Phi > 0 \\ -1 & \text{if} \quad \Phi < 0 \end{cases} \tag{III.3.8}$$

This model is thermodynamically consistent as the entropy equation reads,

$$\frac{\partial \rho s}{\partial t} + \frac{\partial \rho s u}{\partial x} = \rho \frac{1+\tilde{\Phi}}{2} \frac{(u_S - u)^2}{\tau} \geq 0 \tag{III.3.9}$$

In the stiff velocity relaxation limit, the production term vanishes, rendering the coupling method isentropic.

System (III.3.6) is solved by a splitting method, where the hyperbolic part is first solved with a MUSCL-type-scheme in the absence of source terms. The HLLC approximate Riemann solver of Toro et al. (1994) is used in all computations of the paper, to solve System (III.3.6) and its multi-D extension, System (III.3.1). The same equations are solved everywhere and the initial fluid state is set in the rigid body, except regarding the velocity, set to the one of the solid body. During this step, the Overbee limiter is used for the Level-Set function and another limiter (Minmod for example) is used for the other flow variables.

Second, the following ODE system is considered:

$$\begin{aligned}
&\frac{\partial \rho}{\partial t} = 0 \\
&\frac{\partial \rho u}{\partial t} = \rho \frac{1+\tilde{\Phi}}{2} \frac{u_S - u}{\tau} \\
&\frac{\partial \rho E}{\partial t} = \rho \frac{1+\tilde{\Phi}}{2} \frac{u_S - u}{\tau} . u_S \\
&\frac{\partial \Phi}{\partial t} = 0
\end{aligned} \qquad \text{(III.3.10)}$$

Rather than solving explicitly this ODE system, its asymptotic solution can be obtained easily as,

$$\rho = \rho^0; \Phi = \Phi^0; u = u_S, \qquad \text{(III.3.11)}$$

where the superscript '0' denotes the variables determined at the end of the hyperbolic step. Update of the total energy only requires specific attention.

Manipulating the equations of System (III.3.10), the internal energy equation is obtained as,

$$\frac{\partial e}{\partial t} = \frac{1+\tilde{\Phi}}{2} \frac{\left(u_S - u\right)^2}{\tau}$$

As $\tau \to 0^+$, asymptotic expansion of the source terms shows immediately, as for the entropy equation, that,

$e = e^0$.

But as the velocity has been reset to the rigid body one, as expressed by Eq. (III.3.11), the total energy has to be corrected as,

$$\left(\rho E\right) = \rho^0 \left(e^0 + \frac{1}{2} u_S^2 \right) \qquad \text{(III.3.12)}$$

The coupling method thus consists in the reset of the velocity and the total energy with the help of Eqs. (III.3.11) and (III.3.12) in zones where $\Phi > 0$. This method is consequently particularly simple. It is tested in Figure III.9 on the immersed piston test case of Figures. III.8-III.7.

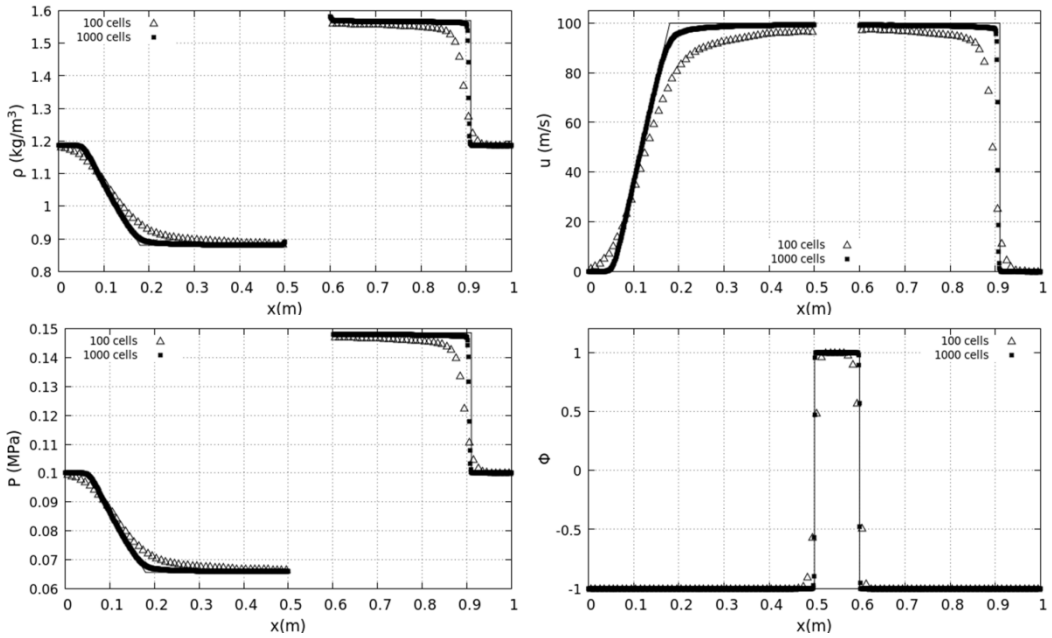

Figure III.9 – Relaxation method results. The first coupling method is used to compute the immersed piston test problem with two meshes, 100 and 1000 cells respectively and CFL=0.9. The Level-Set function is updated with the MUSCL-Overbee method while Minmod is used for the other variables. Numerical results are compared to the exact ones reported here in lines. Poor accuracy is obtained with 100 cells but the method tends to converge to the exact solution under mesh refinement.

This method converges to the exact solution, but the convergence rate seems slow. Another method, closer to the Ghost-Fluid-Method of Fedkiw et al. (1999) is thus addressed to improve convergence and efficiency.

III.3.d) Second coupling method: Ghost-Cell-type method

In this second method, the hyperbolic step is unchanged and based on MUSCL-type-scheme with two limiters, as mentioned above. As in all computations the HLLC solver is used in the hyperbolic step. The coupling step is based on extrapolated variables from the fluid to the solid:

$$\begin{pmatrix} \rho_i \\ u_i \\ p_i \end{pmatrix} = \begin{pmatrix} \rho_j \\ u_s \\ p_j \end{pmatrix} \text{if} \quad \begin{cases} \Phi_i^0 \geq 0 \\ \Phi_j^0 < 0 \end{cases} \tag{III.3.13}$$

where i and j denote two neighboring cells, i being in the solid body and j in the fluid.

In Ghost-Cell (GC) methods the band of cells in which the extrapolation is done has importance. When extrapolation is done with System (III.3.13), interfacial cells only are corrected. But at the next time step the interface may leave the cell and enter another cell occupied formerly by the solid. This

cell must consequently be filled with a consistent set of variables. This issue is illustrated in the Figure III.10.

Let us denote by W the set of primitive variables used during the extrapolation $W = (\rho, u, p)^T$ and U the associated set of conservative variables. The extrapolation is done in the solid cell on the graph on top at left. No precise state is prescribed in cell i+2. Then the Riemann problem is solved everywhere (graph at bottom) and during the time step, the interface changes cell. At the end of the time step cell i+1 is now a fluid cell but the state it contains is wrong, as the Riemann problem solution between cells i+1 and i+2 is wrong too. Therefore, at the next time step, when extrapolation is done from cell i+1 to cell i+2, a wrong state is copied and the solution diverges.

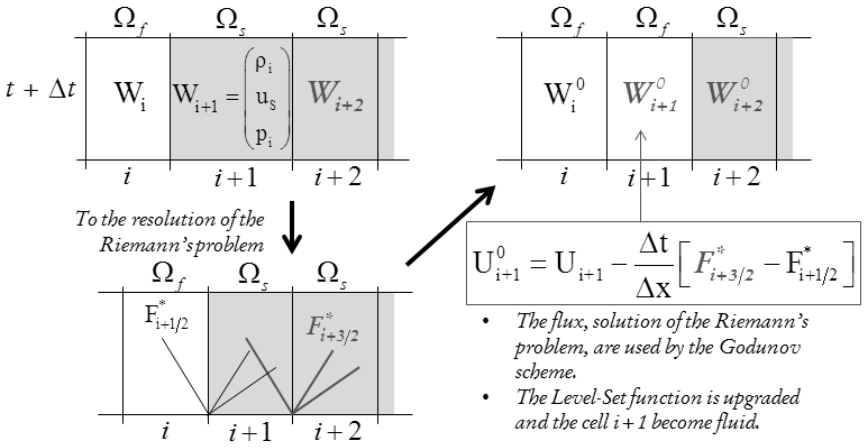

Figure III.10 – Schematic representation of the numerical pollution occurring when the extrapolation is done in a too narrow band of cells.

Typical results obtained with this numerical pollution effect are shown in the Figure III.11 where the same immersed piston test problem as before is rerun. Only the velocity graph is shown for the sake of conciseness.

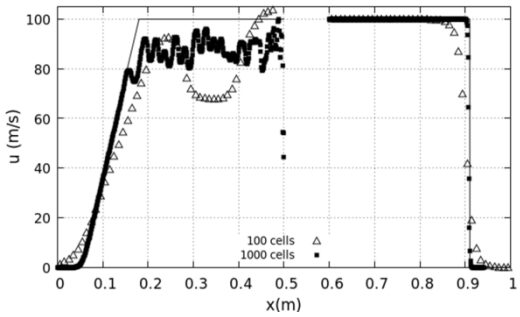

Figure III.11 – Illustration of the numerical pollution effect when a too narrow band of Ghost cells is used for extrapolation. The piston velocity is transmitted to the fluid on the right side but the expansion wave on the left side is wrong. This issue persists when the mesh is refined.

This issue is well known in the literature (Liu et al., 2003, 2006, 2008). Following these references the extrapolation method given by System (III.3.13) is extended to a band of two cells in the solid in the vicinity of the interface. The corrected algorithm is summarized in System (III.3.14):

$$\begin{cases} \begin{pmatrix} \rho_i \\ u_i \\ p_i \end{pmatrix} = \begin{pmatrix} \rho_j \\ u_s \\ p_j \end{pmatrix} \text{if} \quad \begin{cases} \Phi_i^0 \geq 0 \\ \Phi_j^0 < 0 \end{cases} \\ \begin{pmatrix} \rho_{ii} \\ u_{ii} \\ p_{ii} \end{pmatrix} = \begin{pmatrix} \rho_j \\ u_s \\ p_j \end{pmatrix} \text{if} \quad \begin{cases} \Phi_{ii}^0 \geq 0 \\ \Phi_j^0 < 0 \end{cases} \end{cases} \tag{III.3.14}$$

where i denotes the first solid cell in contact with the fluid cell j and ii the second solid cell, neighboring cell i. With this correction the immersed piston test is rerun and the results of Figure III.12 are obtained.

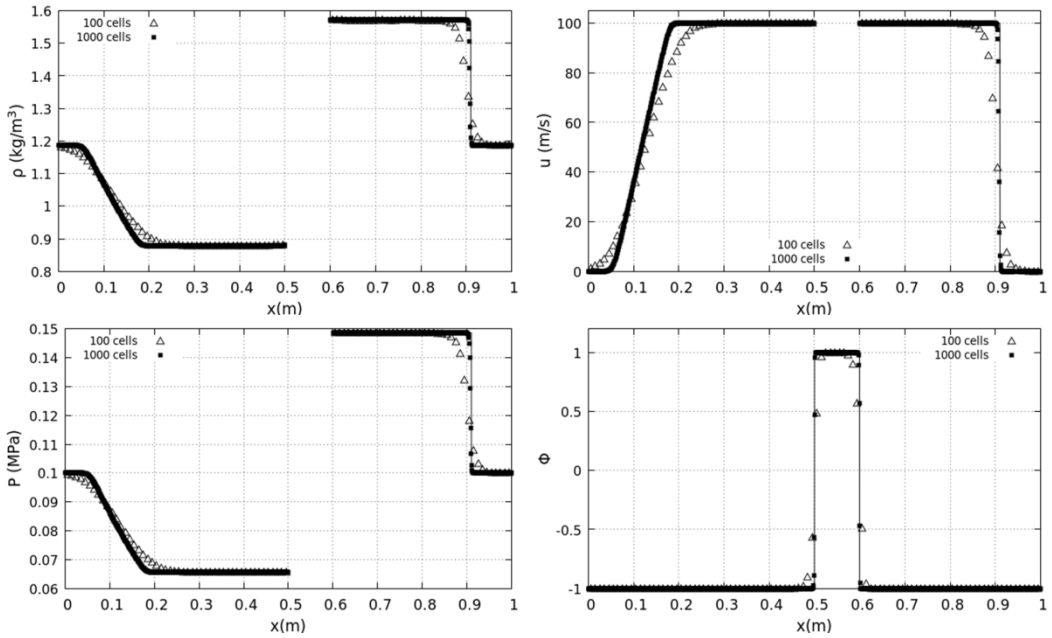

Figure III.12 – Ghost-Cell method with extended band of cells - Results for the immersed piston test. Two meshes are used with 100 and 1000 points respectively. The time step fulfills CFL = 0.9. The MUSCL scheme with Overbee is used for the Level-Set transport and Minmod is used for the other flow variables. The method converges to the exact solution shown in full lines under mesh refinement. With 100 cells, the accuracy is better than with the former relaxation method.

With the Ghost-Cell method summarized in System (III.3.14) interface conditions are matched for the two meshes considered. However, regarding the coarser one (100 cells) the shock is delayed compared to the exact solution of Figure III.8. The method improves efficiency compared to the relaxation one, but seems still perfectible. A refined version is examined in the next paragraph.

III.3.e) Third coupling method: Ghost-Cell-type method with improved velocity extrapolation

The same Ghost-Cell-type method as before is considered, as summarized by System (III.3.14) but the extrapolated state is reconsidered in the aim of convergence improvement.

The present approach follows conventional method for the treatment of piston boundary conditions and avoids local resolution of exact or approximate Riemann problem, as done for example in Liu et al. (2006) and Farhat et al. (2012). It is thus aimed to simplify the related methods and facilitate coupling with more sophisticated flow models, as stated in the Introduction.

Let us consider a fluid at right and a solid at left. To mimic piston motion at prescribed velocity $u^* = u_{piston}$, where u^* denotes solution of the Riemann problem between two fluid states at left and at

right, a fictitious state at left has to be determined. In this approach, the star state solution corresponds to the prescribed piston velocity. This approach is schematized in Figure III.13.

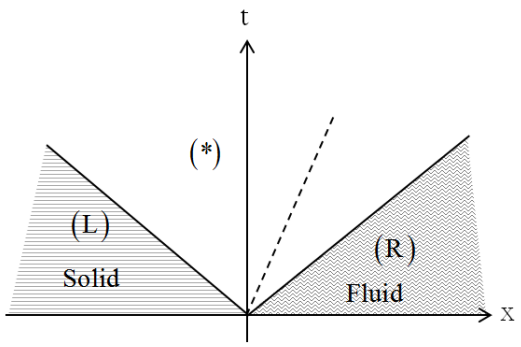

Figure III.13 – Schematic representation of the 'inverse' Riemann problem solved at the interface. The left state has to be determined in order that the star velocity becomes the one of the rigid body.

The right state (R) being known the left state (L) has to be determined in order that $u^* = u_{piston}$.

For the sake of simplicity in the analysis the approximate acoustic solver is considered:

$$\begin{cases} P_L + Z_L u_L = P^* + Z_L u^* \\ P_R - Z_R u_R = P^* - Z_R u^* \end{cases}$$

The pressure and density in the left state are assumed extrapolated from the right state, as done before with the former Ghost-Cell method. Consequently,

$$P_R = P_L = P \; ; \; Z_L = Z_R = Z$$

The Riemann problem solution thus reads,

$$u^* = \frac{u_L - u_R}{2} \; ; \; P^* = P + \frac{Z(u_L - u_R)}{2}$$

As $u^* = u_{piston}$ the left state velocity is determined as,

$$u_L = 2u_{piston} - u_R \qquad \text{(III.3.15)}$$

It also appears that the pressure at the rigid body surface is,

$$P^* = P + Z\left(u_{piston} - u_R\right).$$

The term $Z\left(u_{piston} - u_R\right)$ induces compression or expansion depending on the sign of the velocity difference. In any case it anticipates shock or expansion appearance in the sense that it corresponds to the pressure, solution of the Riemann problem at the interface. However, there is no need to solve explicitly the Riemann problem locally. The HLLC solver (or any other flow solver) used to update

the hyperbolic model will compute correctly the star pressure thanks to Eq. (III.3.15). Doing so, the present treatment provides the same solution as a multi-material or one-sided Riemann solver, without explicit consideration of such solver. Moreover, it is not limited to a specific EOS or a specific flow model.

Thanks to this correction, the extrapolation method, analogue of System (III.3.14) now reads,

$$\begin{cases} \begin{pmatrix} \rho_i \\ u_i \\ p_i \end{pmatrix} = \begin{pmatrix} \rho_j \\ 2u_s - u_j \\ p_j \end{pmatrix} \text{if} \begin{cases} \Phi_i^0 \geq 0 \\ \Phi_j^0 < 0 \end{cases} \\ \begin{pmatrix} \rho_{ii} \\ u_{ii} \\ p_{ii} \end{pmatrix} = \begin{pmatrix} \rho_j \\ 2u_s - u_j \\ p_j \end{pmatrix} \text{if} \begin{cases} \Phi_{ii}^0 \geq 0 \\ \Phi_j^0 < 0 \end{cases} \end{cases} \tag{III.3.16}$$

As before, i denotes the first solid cell in contact with the fluid cell j and ii the second solid cell, neighboring cell i. The immersed piston test problem is now rerun with this modification. Corresponding results are shown in Figure III.14.

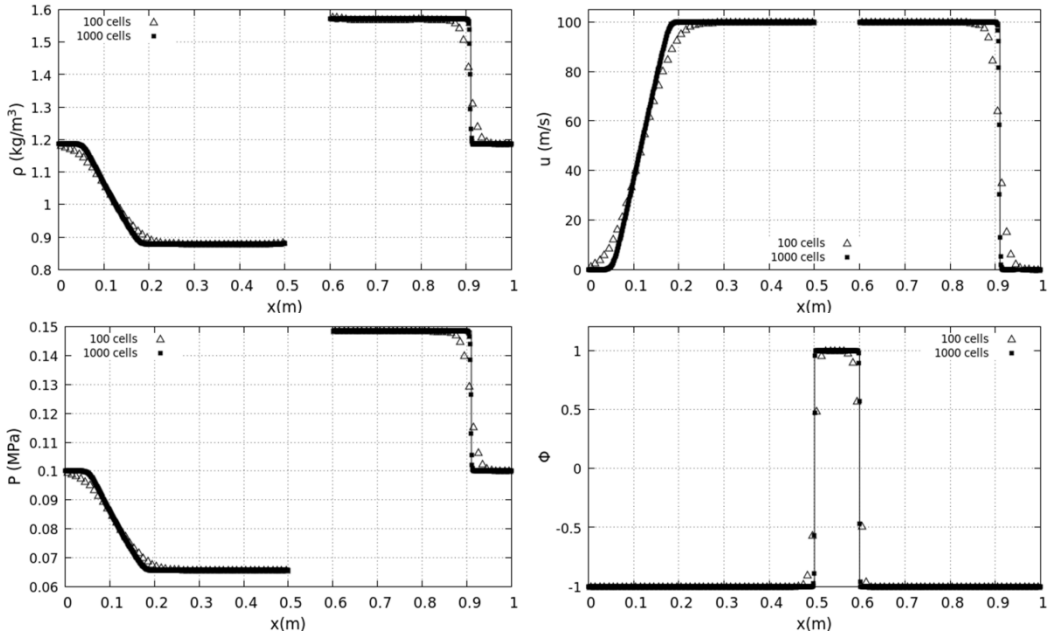

Figure III.14 – Ghost-Cell method with extended band of cells and modified boundary conditions - Results for the immersed piston test. Two meshes are used with 100 and 1000 points respectively. The time step fulfills CFL = 0.9. The MUSCL scheme with Overbee is used for the Level-Set transport and Minmod is used for the other flow variables. The method converges to the exact solution shown in full lines under mesh refinement. With 100 cells, the shock position is now correct.

The three coupling methods are now compared on the same graph with a coarse mesh involving 100 cells. Corresponding results are shown in Figure III.15.

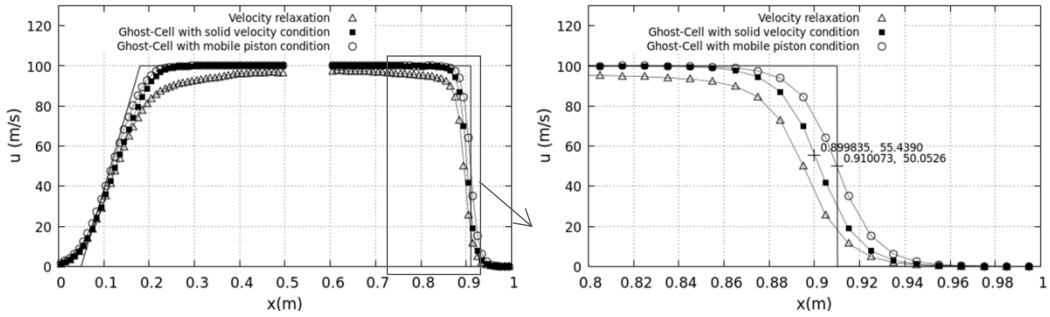

Figure III.15 – Comparison of the various coupling methods with 100 cells against the exact solution. The modified Ghost-Cell method with piston boundary condition improves the results.

We have shown that the three methods tend to converge to the exact solution, but the Ghost-Cell method with modified boundary condition improves the convergence rate. Let us now examine the method's behavior at various times, including very short ones. Corresponding results are shown in Figure III.16.

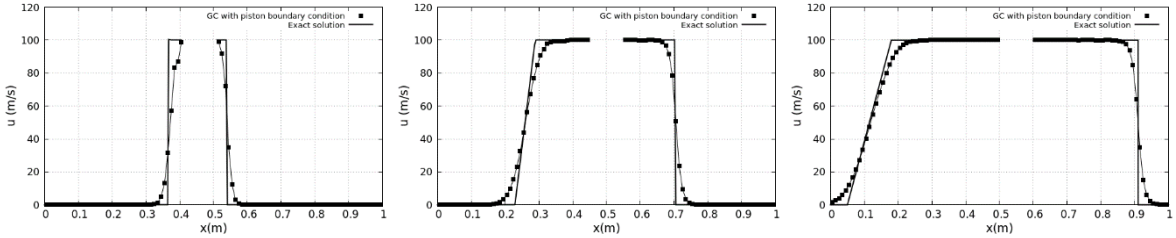

Figure III.16 – Efficiency of the coupling method at various times. Computations are done with 100 cells and compare to the exact immersed piston solution. The modified Ghost-Cell method with piston boundary condition is used in all computations. From the left to the right solutions have been plotted at times 0.1ms, 0.5ms and 1ms. It corresponds to 7, 28 and 53 time steps respectively. The coupling method matches the exact solution, even at short times with similar efficiency as simple phase Euler computations, needing 5 to 10 time steps to build shocks and expansion waves.

The modified Ghost-Cell method with piston boundary condition converges fast towards the exact solution for different times. At short times, waves' speeds are well computed and shocked state is quasi-formed. As time increases, the convergence of the solution is clear. We now address extension of this last method in multi-D on unstructured meshes.

III.4 – Multidimensional extension

The coupling method is now extended to multi-D. Transport of the Level-Set function in multi-D follows the lines of Chiapolino et al. (2017b) regarding the volume fraction transport of their diffuse interface flow model. Therefore, it is not detailed anymore.

III.4.a) Solid-fluid coupling method

Mixed cells have to be defined and to do this solid cells have to be defined first. As already mentioned a cell is considered solid when the Level-Set function Φ is positive at the cell center and fluid otherwise. It becomes a mixed cell when one of its direct neighbors has Φ with opposite sign, as shown in Figure III.17. It is worth mentioning that none of the fluid cells ($\Phi < 0$) are considered as mixed and are solved with the hyperbolic solver routinely. Thus mixed cells are defined as solid one ($\Phi > 0$) that share an edge with at least one fluid cell ($\Phi < 0$).

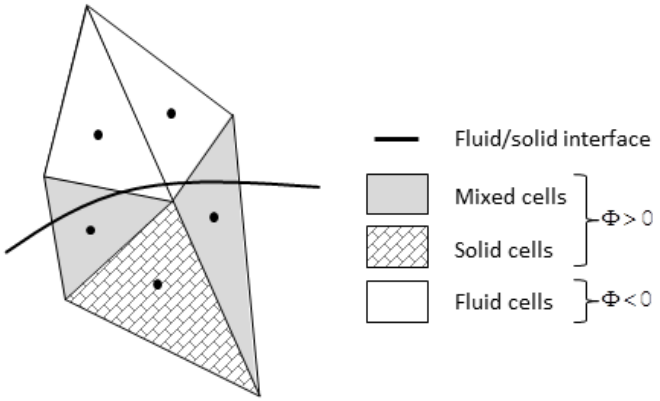

Figure III.17 – Schematic representation of the interface and mixed cells.

2D extension of the Ghost-Cell method proceeds in two-steps.

III.4.a.i) Approximation of the fluid state in mixed cells

When a mixed cell is detected the fluid state in the corresponding cell is computed as a volume average of the neighboring fluid cells. This average is obviously based on conservative variables.

Let's define Ω_{vf} the set of neighboring fluid cells of the considered mixed cell. The set of conservative variable in the mixed cell is obtained as,

$$\overline{\mathbf{U}} = \frac{\sum_{k \in \Omega_{vf}} V_k U_k}{\sum_{k \in \Omega_{vf}} V_k}, \qquad \text{(III.4.1)}$$

where V_k represents the volume of cell k. From this vector of conservative variables, primitive ones are deduced :

$$\tilde{\mathbf{W}} = \left(\tilde{\rho}, \tilde{u}, \tilde{v}, \tilde{p} \right)^T \qquad \text{(III.4.2)}$$

Symbol $\sim$ is used to make distinction with the volume average symbol.

These primitive variables are used during the extrapolation step that follows.

III.4.a.ii) Extrapolation across the interface

The same piston boundary conditions are used in the direction normal to the solid-fluid interface. As the flow model (III.3.1) is inviscid the tangential velocity has to be extrapolated as well.

Let's consider two cells having a common edge and having Level-Set functions of different signs. Necessarily the interface I crosses the line segment connecting the two cell centers, as shown in Figure III.18 where the cell center containing a fluid state is denoted by F, the one containing a solid is denoted by G and the interface point is denoted by S.

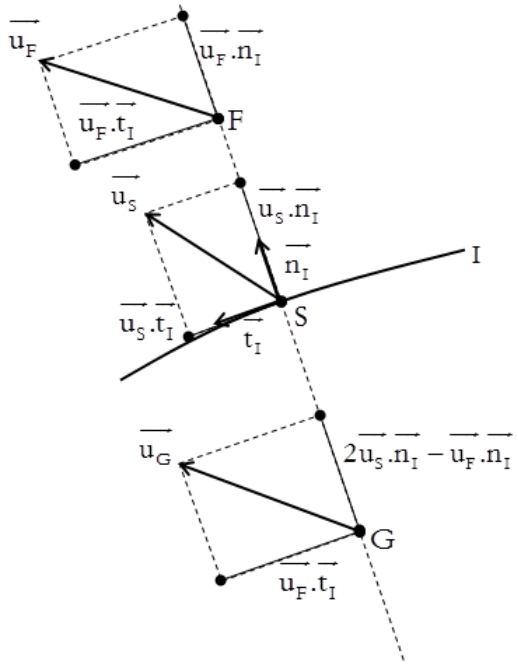

Figure III.18 – Schematic representation of construction of the velocity in the Ghost-Cell G when two mesh points have a common edge and Level-Set function changes sign. The normal velocity component in the Ghost-Cell is computed with both fluid and solid velocities contributions. The tangential component of the velocity at point G is taking equal to the tangential component of the fluid velocity, to mimic slip condition. Velocity at point G is determined following Eq. (III.4.3).

The normal vector to the interface is defined as,

$$\overrightarrow{n_\Phi} = -\frac{\vec{\nabla}\Phi}{\left\|\vec{\nabla}\Phi\right\|}$$

where $\vec{\nabla}\Phi$ is computed in each cell as mentioned in Section III.2 with the least-square method and extended set of neighbors. The normal vector used in the extrapolation procedure is the one computed in the mixed cell, as defined earlier.

The velocity components are extrapolated in the solid as,

$$\overrightarrow{u_G}.\overrightarrow{n_I} = 2\overrightarrow{u_S}.\overrightarrow{n_I} - \overrightarrow{u_F}.\overrightarrow{n_I} \text{ and } \overrightarrow{u_G}.\overrightarrow{t_I} = \overrightarrow{u_F}.\overrightarrow{t_I} \qquad \text{(III.4.3)}$$

along the normal and tangential directions respectively.

The rest of the primitive variable vector is copied in the solid cell.

III.4.a.iii) Extrapolation to the Ghost-Cell band

As previously mentioned in the 1D case and comments related to Figure III.11 additional cells need to be filled with consistent fluid states. Indeed, at the next time step the interface may move away from the current cell and a solid cell may become a fluid one. The extrapolation procedure is extended to a wider stencil to anticipate appearance of extra fluid cells. The 'additional cells' where a fluid state has to be defined are shown in Figure III.19. They are defined as solid cells having a mixed cell as direct neighbor.

A conservative average is performed with the neighboring mixed cells (also defined in Figure III.19), that have been updated with the sequence (III.4.1-III.4.2-III.4.3).

An extra conservative average is done on the mixed cells with the same definitions as Eqs. (III.4.1)-(III.4.2) where the mixed-cells volumes and states are used instead of the fluid ones. The resulting volume average done with the mixed cells is used to update the 'additional cells'.

Two sequences of volume averages are consequently done with the present method:

- First with the fluid cells to update the mixture cells;
- Second with the mixture cells to update the 'additional cells'.

Between these two averaging steps the piston boundary condition (III.4.3) is obviously used.

This simple averaging-extrapolation method simplifies significantly existing solid-fluid coupling methods on unstructured meshes.

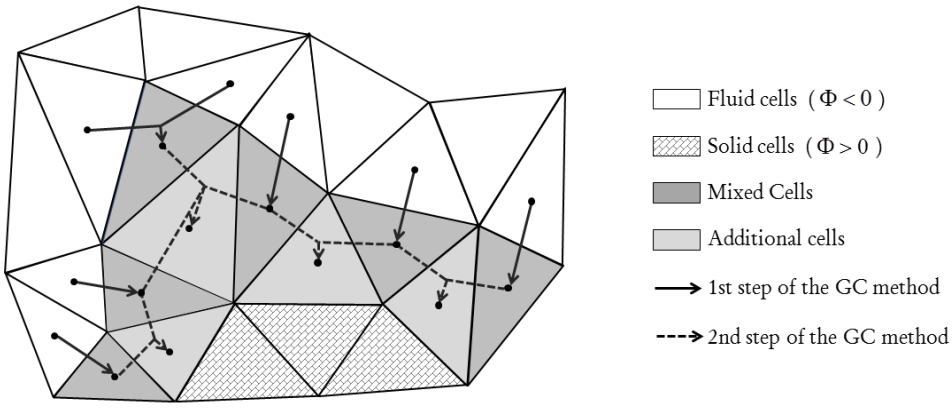

Figure III.19 – Treatment of the Ghost-Cell band in 2D. All grey cells and hatched ones represent solid cells. These solid cells are divided in 3 categories. The first one, in dark grey, corresponds to the mixed cells in which extrapolation is done following (III.4.3) after volume average (III.4.1)-(III.4.2). The second layer, shown in grey, corresponds to the solid direct neighbors of the mixed cells, as defined in Figure III.10. Fluid state is set in these cells by averaging conservative variables of the surrounding mixed cells with the help of (III.4.1)-(III.4.2) definitions. States and volumes of

mixed-cells are used in these formulas. The third one with hatched symbols corresponds to the solid cells that are not modified by the coupling method.

To examine accuracy of the method reference results are determined, as detailed in the next subsection.

III.4.b) Validation

In order to validate the treatment done in the coupling method for multidimensional problems, two computations are considered and compare. In one case, a supersonic flow at Mach number two enters a domain where a cylinder at rest is placed, as shown in Figure III.20(a). The results of this test are compared to the case where the cylinder moves at the same velocity as the inlet flow in a fluid at rest, as shown in Figure III.20(b). Results are compared at two different times. The flow model (III.3.1) is used in the single phase limit, corresponding to the Euler equations, with polytropic coefficient $\gamma_{air} = 1.4$.

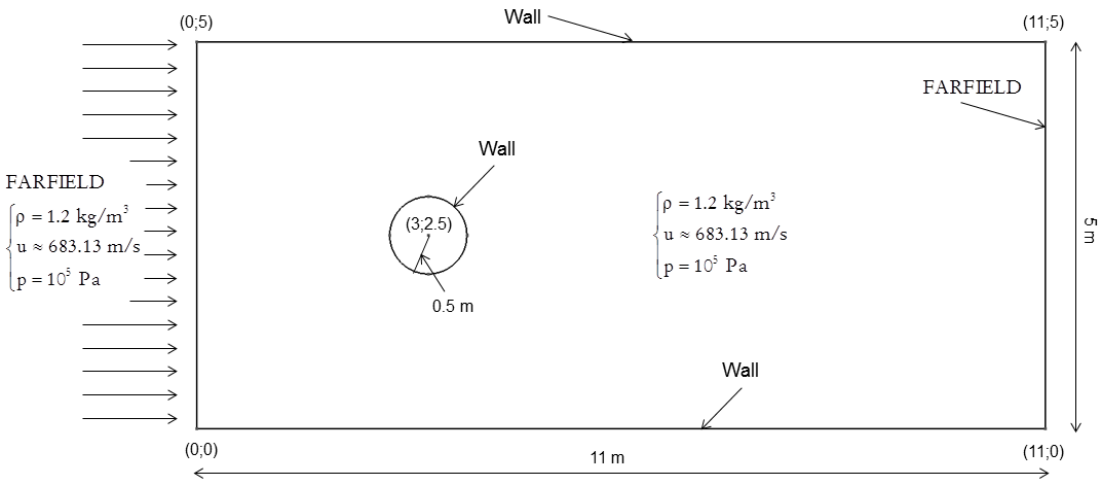

(a)

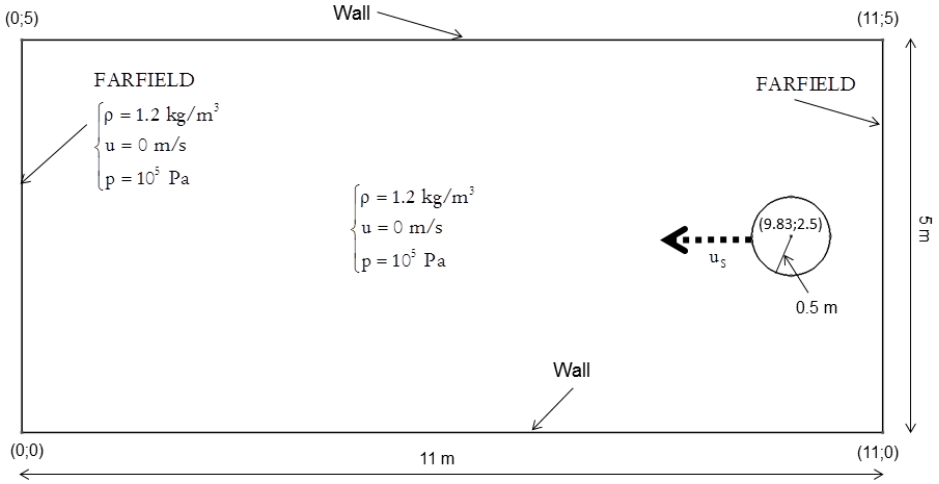

(b)

Figure III.20 – Configurations considered for validation of the coupling method in 2D. (a): A body fitted mesh is used around a cylinder at rest with a supersonic inflow at Mach number two. (b): The same cylinder moves at supersonic speed in a gas flow at rest.

The mesh density is taken with an average space size of 3 cm and Minmod limiter is used for the various flow variables in the MUSCL scheme.

Comparison of computed results is shown in Figure III.21 at times 2ms and 4ms respectively.

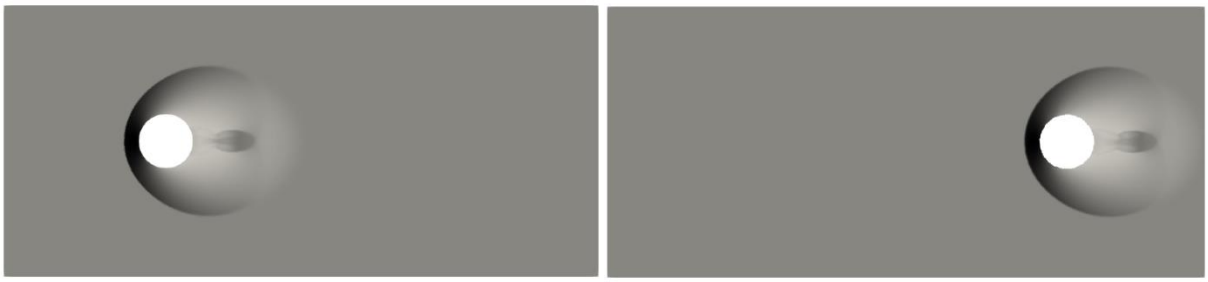

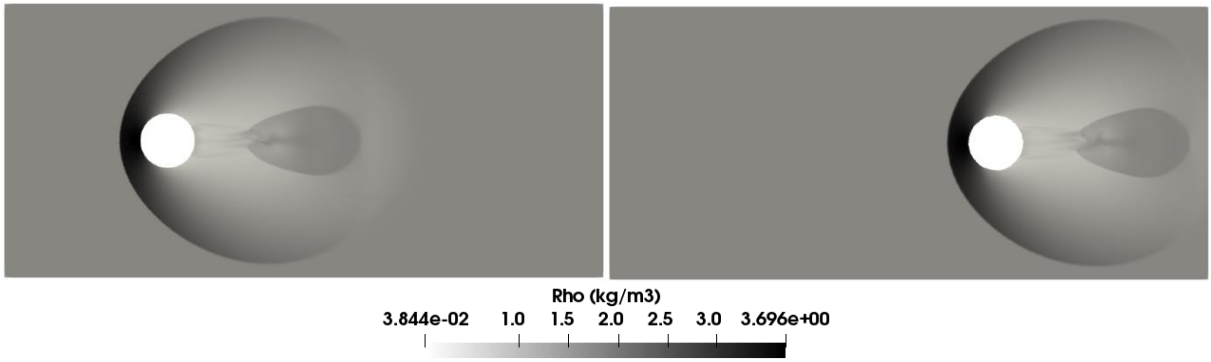

Figure III.21 – Comparison of the results with body at rest (left column) and moving body (right column) related to the configurations depicted in Figure III.20. The Minmod limiter is used in the MUSCL scheme. Upper graphs represent density contours at time 2ms while the lower graphs correspond to the solution at time 4ms. Good agreement is observed between the body-fitted approach and the coupling one.

The mesh of the geometry presented in Figure III.20(a) is composed of 202 716 cells corresponding to an average space step of 3 cm. The mesh of the geometry shown in Figure III.20(b) is composed of 205 628 cells corresponding to the same space step. Computed results of Figure III.21 are in close agreement. First the same detached shock wave is visible as well as expansion zone at rear of the projectile. Second, the shape of the projectile is very well preserved by the Level-Set-Overbee method. Last, it is possible to address quantitative comparison by extracting flow variables from the two sets of results along a given direction, such as the Ox axis for instance. This is done in Figure III.22 and III.23 for the flow variables profiles respectively at time 2ms and 4ms.

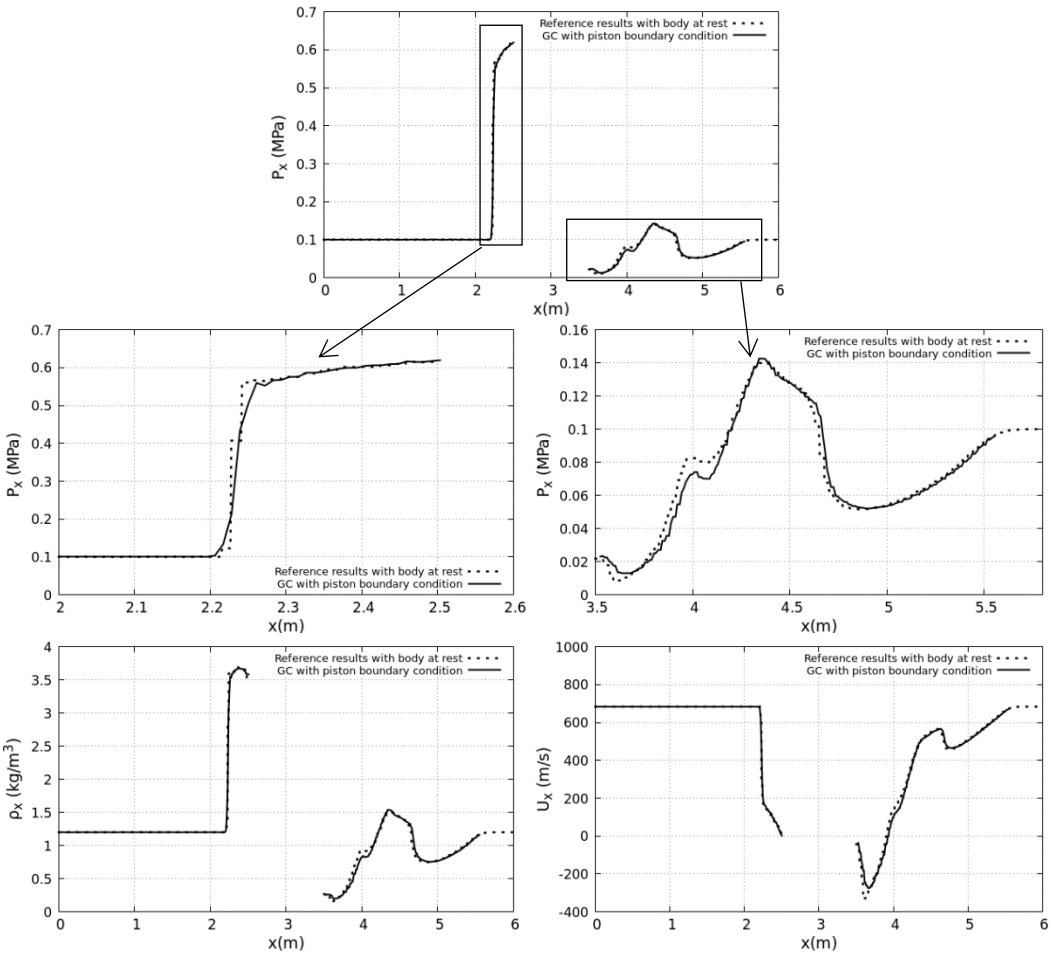

Figure III.22 – Comparison of the variables profiles along the Ox axis related to the computation of Figure III.21, at time 2ms. The range of X-axis has been modified in the moving body computations to compare the results with those related to body at rest. The velocity has been modified to represent relative velocity, for the same reason. Good agreement is observed.

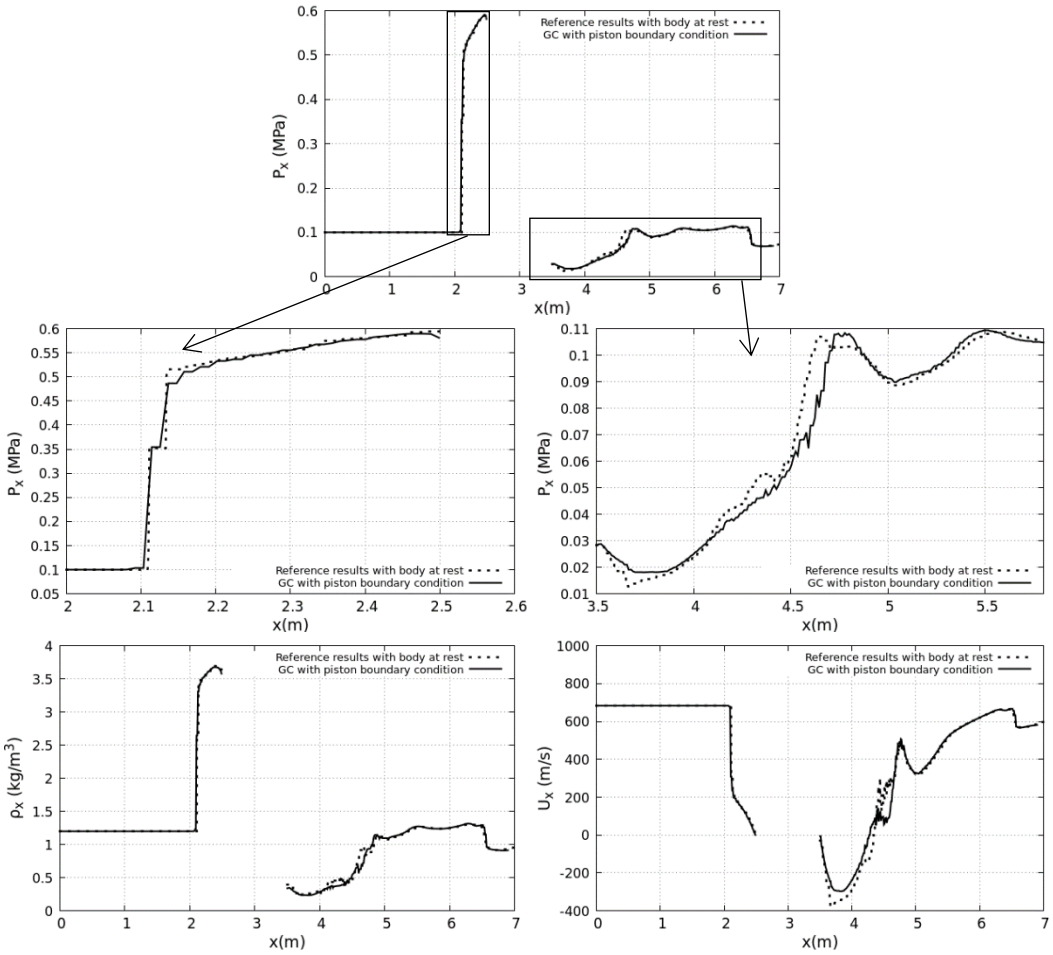

Figure III.23 – Comparison of the variables profiles along the Ox axis related to the computations of Figure III.21, at time 4ms. Good agreement is observed.

The results of Figures III.22 and III.23 confirm validity of the coupling method with comparable accuracy as the one observed in 1D in the Figure III.16. The various profiles do not match perfectly as the meshes are not the same. Also, body roughness effects are present in the moving body computations. Overall agreement is good and the method remains simple to implement. Illustrations of the method's capabilities in the frame of the two-phase flow model (III.3.1) are now addressed.

III.4.c) Illustrations with two-phase flow effects

Two projectiles of 5 mm radius with imposed velocities are considered and move at high velocity through air and impact a liquid water domain settled in the air. The air is considered as an ideal gas and the liquid is assumed governed by the stiffened gas EOS (III.3.2). As material interfaces between the various fluids are present the flow model (III.3.1) with mixture EOS (III.3.3) is an appropriate

candidate, in particular when phase transition is considered (Saurel et al., 2016). Thermodynamic data of the various fluids are given hereafter:

$$\begin{cases} \gamma_{w,liquid} = 2.35 \ ; \ p_{\infty,w,liquid} = 10^9 \text{ Pa} \ ; \ q_{w,liquid} = -1167 \text{ kJ/kg} \ ; \ C_{v,w,liquid} = 1816 \text{ J/kg/K} \\ \gamma_{w,vapor} = 1.43 \ ; \ p_{\infty,w,vapor} = 0 \text{ Pa} \ ; \ q_{w,vapor} = 2030 \text{ kJ/kg} \ ; \ C_{v,w,vapor} = 1040 \text{ J/kg/K} \\ \gamma_{air} = 1.4 \ ; \ p_{\infty,air} = 0 \text{ Pa} \ ; \ q_{air} = 0 \text{ J/kg} \ ; \ C_{v,air} = 719 \text{ J/kg/K} \end{cases}$$

Phase transition is considered through local thermodynamic equilibrium. Simple and fast thermochemical relaxation solver has been developed in Chiapolino et al. (2017a) and is used in the present computations.

Initial and boundary conditions are given in the Figure III.24 as well as geometrical data.

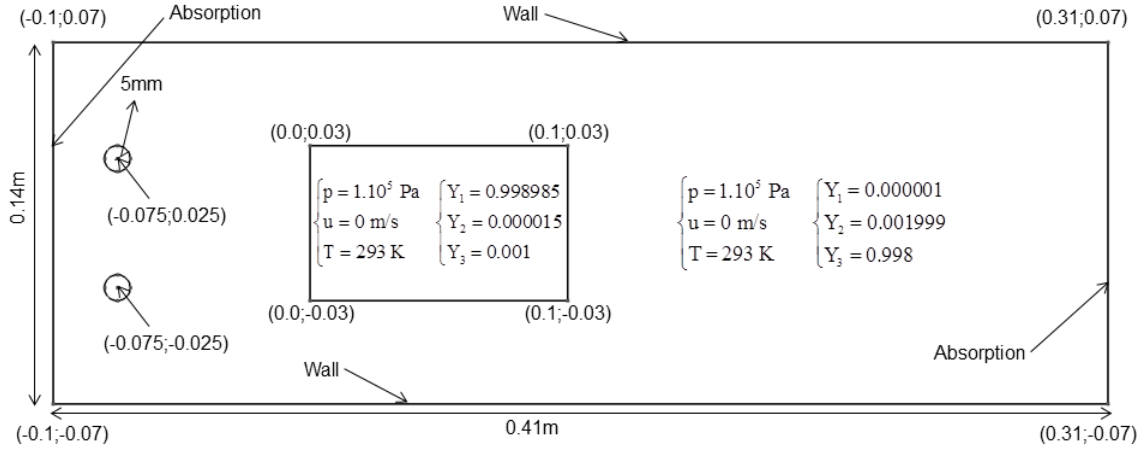

Figure III.24 – Projectiles impact at high velocity onto a water tank in the air. Geometrical data and initial and boundary conditions. The upper projectile has initial velocity components (400, -10) while the lower one has (400 , +10) in m/s units.

Corresponding computational results are shown in Figure III.25 at several times.

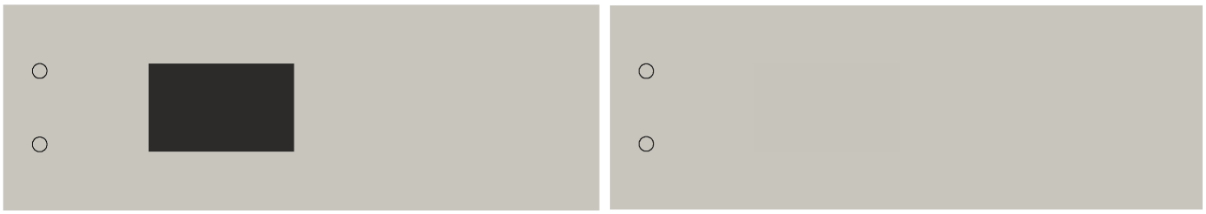

(a)

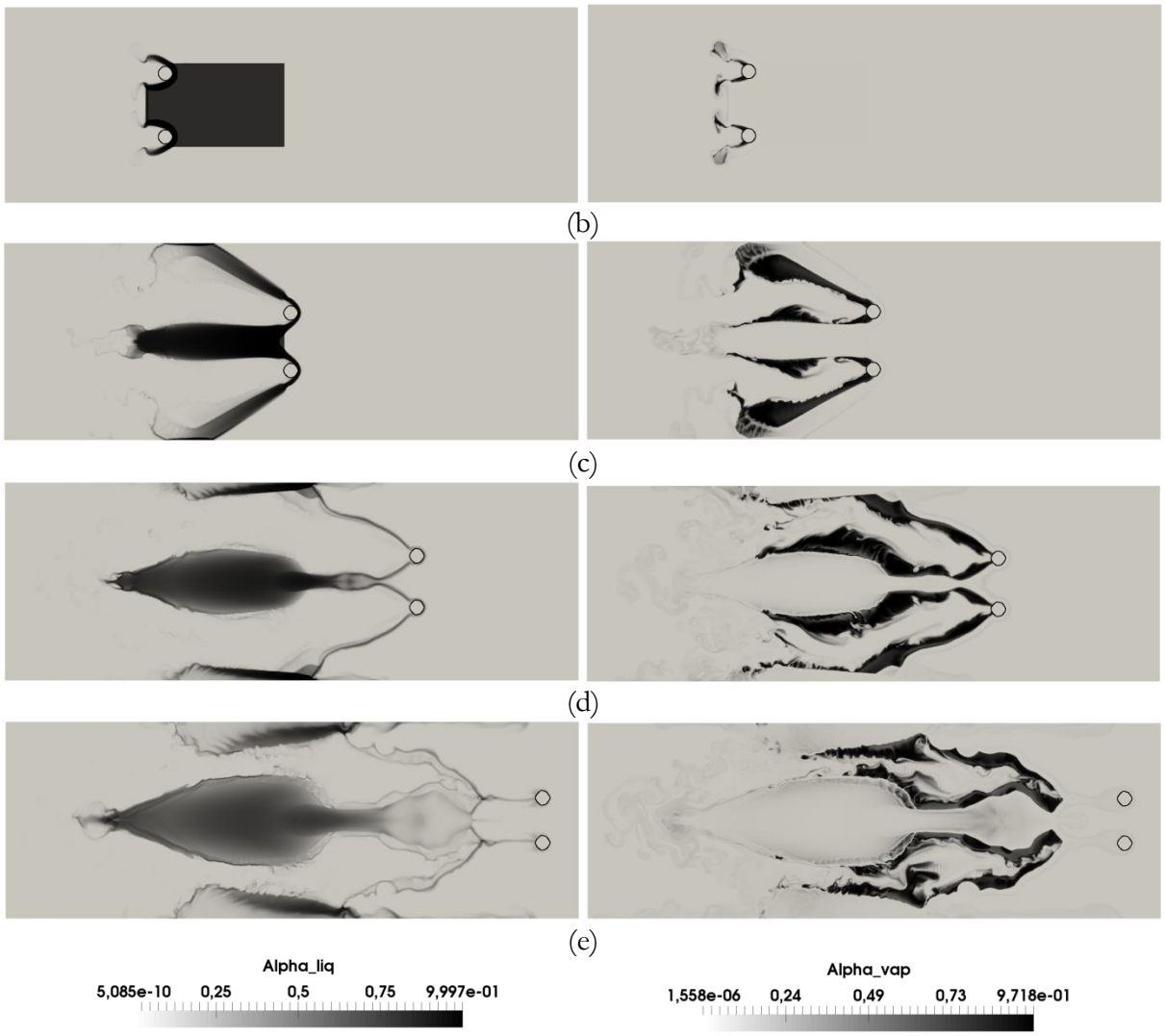

Figure III.25 – Interaction of two projectiles at high speed on a water tank settled in the air. Computed volume fractions of liquid water (left column) and water vapor (right column) appearing during cavitation. Computational parameters: MUSCL scheme with Overbee limiter for the Level-Set functions, Minmod limiter for the other variables, CFL = 0.5, number of cells (triangles) = 1 489 476. Results are shown at times (a) 0 ms ; (b) 0.225 ms ; (c) 0.45 ms ; (d) 0.675 ms ; (e) 0.9 ms.

Figure III.25 illustrates method's capabilities where two-phase effects with phase transition are present, in the presence of liquid gas interfaces and solid-fluid interfaces. These computations show that vapor is produced during the impact and travel of the projectiles in the two-phase cloud. Vapor is produced at approximately 135° from the stagnation point. The related vapor volume fraction is high in this example as it reaches nearly 1 at some locations. Extra extension is now addressed with two-way coupling.

III.5 – Two-way coupling

The motion of rigid bodies is now considered as coupled to the fluid flow through the pressure force integral over the body surface. The pressure force exerted by the fluid on the solid surface is defined as,

$$\vec{F_p} = \int_{\partial\Omega_S} p\vec{n}dS = F_{px}\vec{e_x} + F_{py}\vec{e_y} \qquad \text{(III.5.1)}$$

where $\partial\Omega_S$ denotes the surface of the rigid body.

The cell faces belonging to the rigid boundary surface are detected as:

- For a given face 'f' belonging to the entire set of faces of the overall mesh. This face belongs to two neighboring cells, say for instance cells i and j.
- If the product of the Level-Set functions $\Phi_i.\Phi_j < 0$, then the face belongs to the set of faces of $\partial\Omega_S$.

Consequently the discrete analogue of Eq. (5.1) becomes,

$$\vec{F_p} = \sum_{f\in\partial\Omega_S} p_f \vec{n_f} S_f \qquad \text{(III.5.2)}$$

With the help of pressure force exerted on the rigid body its velocity is updated thanks to the Newton's law:

$$\overrightarrow{u_S^{n+1}} = \overrightarrow{u_S^n} + \Delta t \frac{\vec{F_p}}{M} \qquad \text{(III.5.3)}$$

As the rigid body velocity is time dependent but independent of space, the Level-Set function still obeys the conservation law, Eq. (III.2.3). The overall algorithm described in Sections III.3 and III.4 is thus unchanged.

The method is now illustrated on various flow configurations. An array of 6 cylindrical particles of radius r = 5 mm is considered and set to motion under shock wave interaction. The mass of each particle is arbitrarily set to M=0.8 g and are initially settled in air at atmospheric conditions. Each particle is tracked by its own Level-Set function, different for each particle. At the left boundary of the domain, piston conditions are adopted corresponding to a shock wave emitted to the gas at Mach number 1.24. The various initial and boundary conditions are given in Figure III.26. In the first run, the particles are aligned.

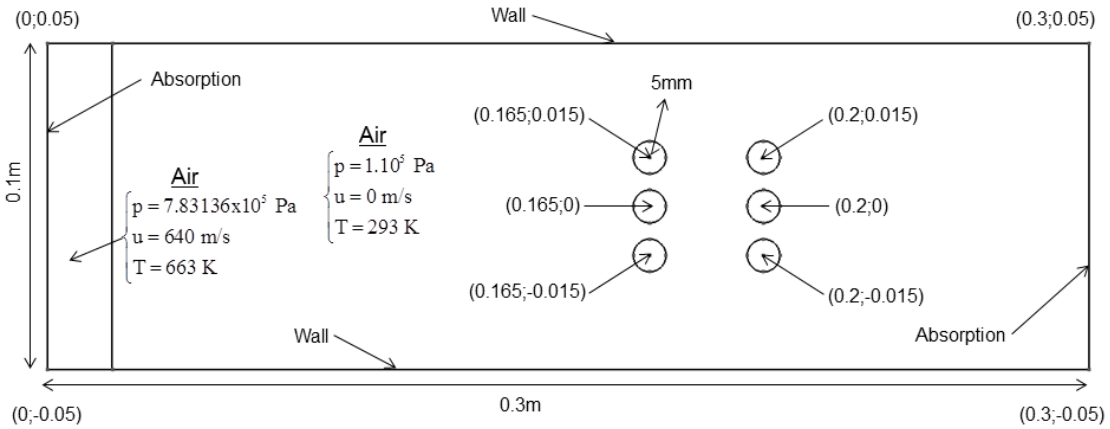

Figure III.26 – Two-way coupling illustration 1 – Shock interaction with an array or aligned particles. Initial data and boundary conditions.

As before, the MUSCL scheme is used with Overbee limiter for the Level-Set function and Minmod for the other flow variables. The pressure contours resulting of the shock interaction are shown at various times in the Figure III.27.

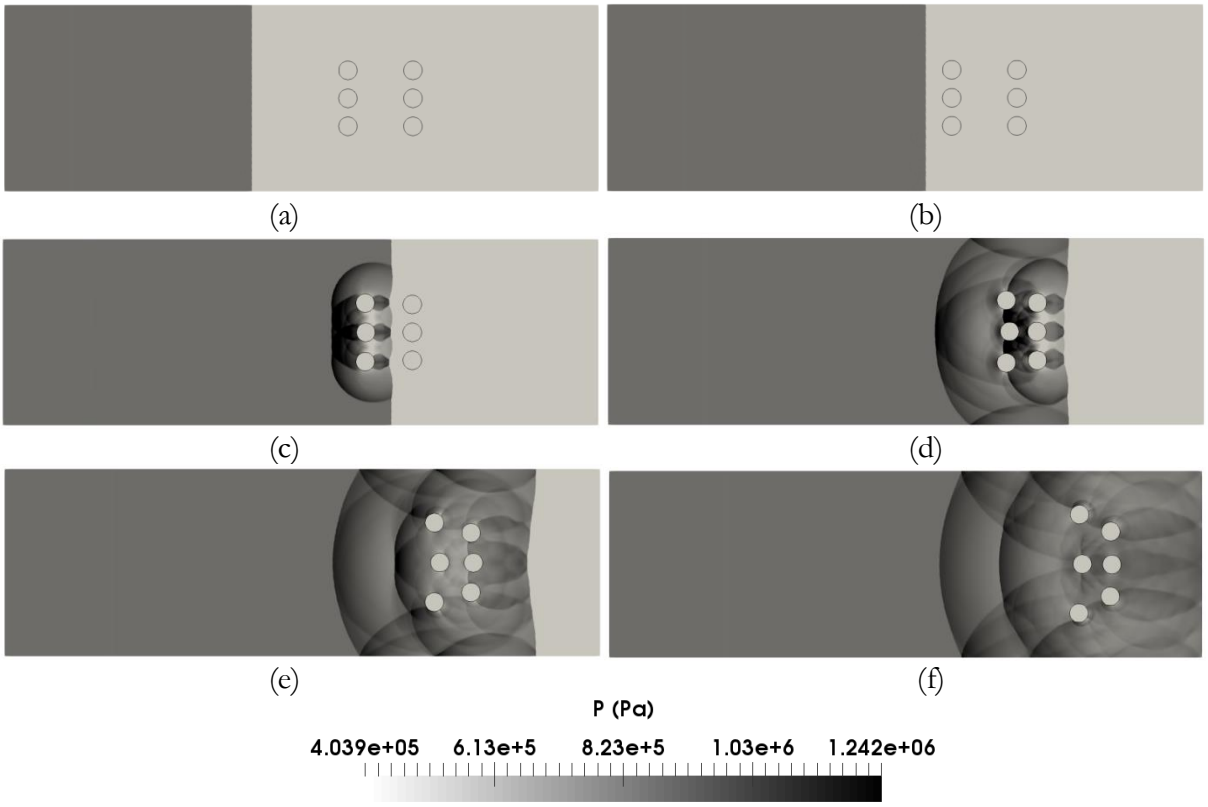

Figure III.27 – Pressure contours resulting of the shock interaction with an array of aligned rigid solid particles. The mesh involves 615 278 cells corresponding to an average space size of 0.2 mm. Both transmitted and reflected shock waves are clearly visible as well as the motion of the various

particles, no longer aligned during time evolution. The results are shown at times (a) 0.126 ms ; (b) 0.168 ms ; (c) 0.21 ms ; (d) 0.252 ms ; (e) 0.294 ms ; (f) 0.336 ms.

At each interaction with a particles layer a reflected shock is emitted. Indeed, after the passage of the first particles layer, the shock reforms very quickly and interacts with the second layer, resulting in both transmitted and reflected shock waves. The transmitted shock reforms quickly to a discontinuous wave, while the reflected one stays a train of shock waves during the physical time observed.

It is interesting to note the very good symmetry of the computations while achieved on unstructured grids, this observation giving confidence to the coupling method.

The same type of initial configuration with staggered particles is considered for a second run, as shown in Figure III.28.

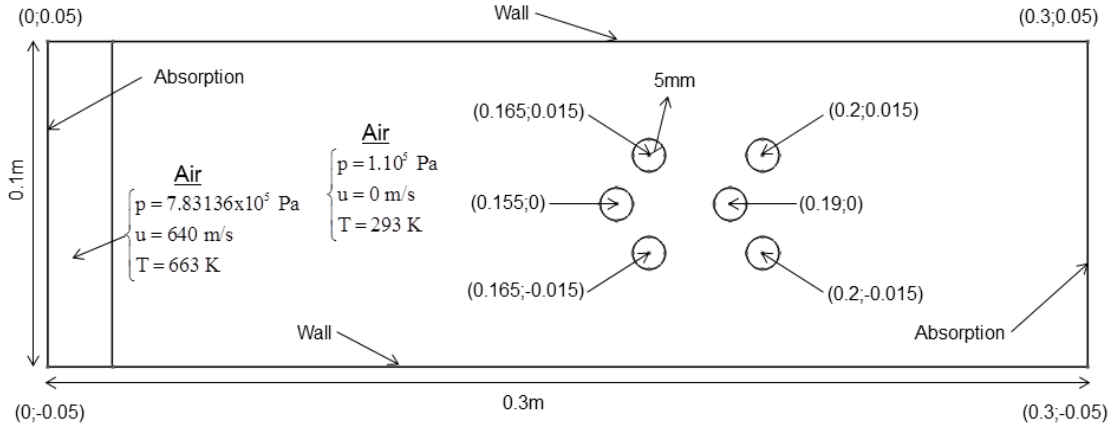

Figure III.28 – Two-way coupling illustration 2 – Shock interaction with an array or staggered particles. Initial data and boundary conditions.

Associated computational results are shown in Figure III.29.

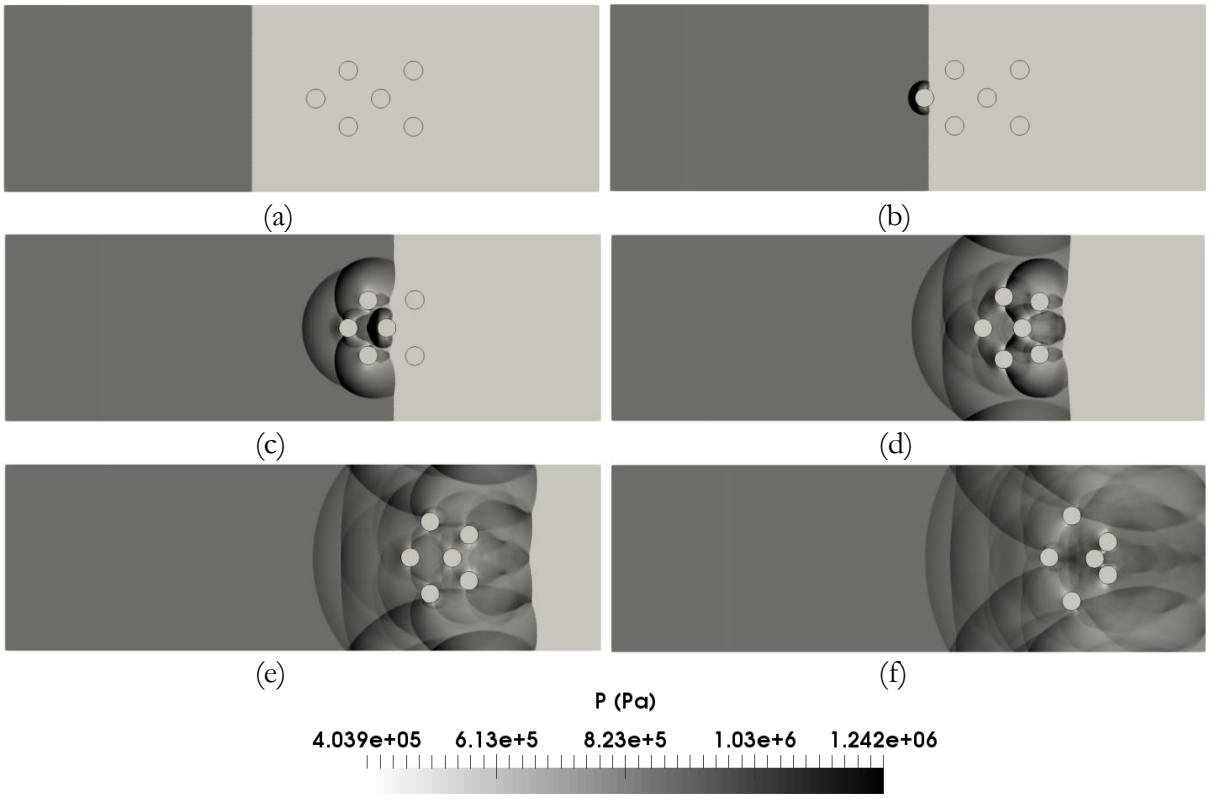

Figure III.29 – Pressure contours resulting of the shock interaction with an array of staggered rigid solid particles. The mesh involves 616 454 cells corresponding to an average space size of 0.2 mm. Both transmitted and reflected shock waves are clearly visible as well as the motion of the various particles that tend to form a cluster. The results are shown at times (a) 0.126 ms ; (b) 0.168 ms ; (c) 0.21 ms ; (d) 0.252 ms ; (e) 0.294 ms ; (f) 0.336 ms.

The same observations as for the previous test are valid. An extra interesting feature appears with the particle layer at right that tends to form a cluster due to the interactions with the fluid flow.

Mesh sensitivity dependence of the results is investigated hereafter. Three meshes are considered : a very coarse one made of 40 222 cells, an intermediate one made of 158 680 cells, a refine one made of 610 454 cells and a very fine one made of 2 424 922 cells. The same computational parameters of the MUSCL and coupling methods as before are used.

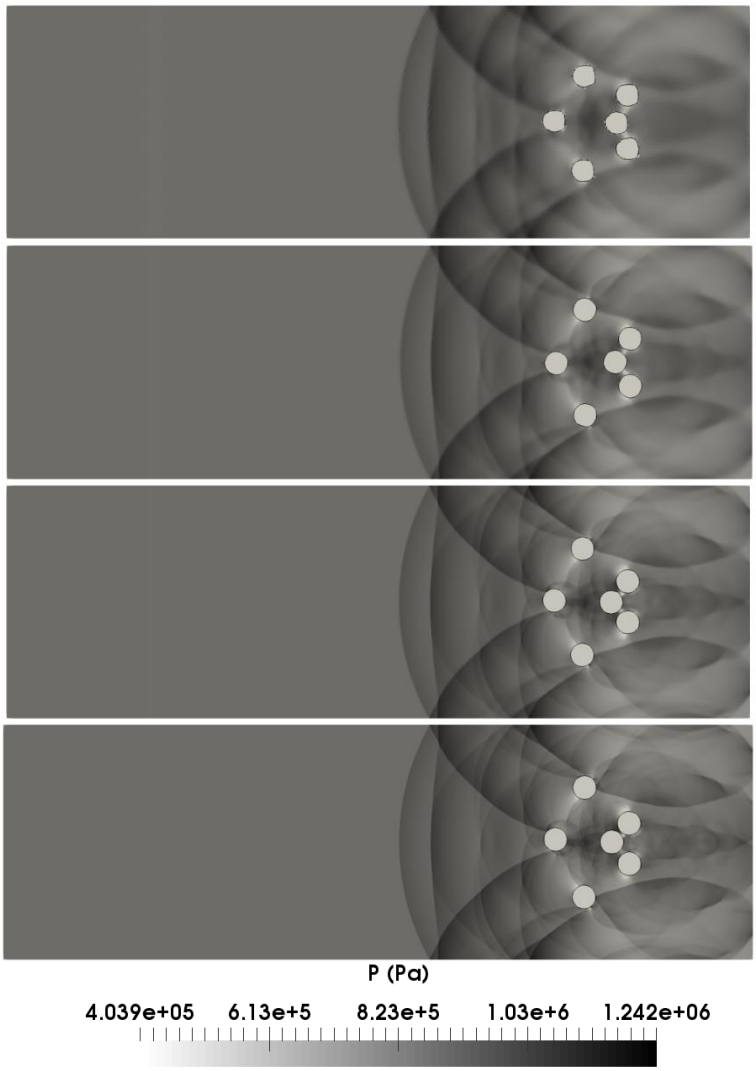

Figure III.30 – Mesh sensitivity analysis related to the computations of Figure III.29. Three meshes are considered: coarse with 40 222 cells, intermediate with 158 680 cells, fine with 616 454 cells and a very fine with 2 424 922 cells. The results are shown at time 0.336ms. The same qualitative evolution for the particle's dynamics is observed, in the direction of cluster formation.

Qualitative evolution regarding wave's dynamics as well as particle's motion is observed for any mesh resolution. Computed results on the last three meshes are very close, showing mesh independent behavior to form particle's cluster, at least in the present flow configuration and related initial data.

III.6 – Conclusion

A Level-Set type method has been developed to track rigid bodies on unstructured meshes. Thanks to the Overbee limiter of Chiapolino et al. (2017b) the method doesn't need reinitialization, nor interface reconstruction. A solid fluid coupling method has been built and compared to other

approaches, based on stiff relaxation and conventional Ghost-Cell extrapolation. It is simple to implement and improves convergence. It has been extended to 2D and validated against 2D computations of supersonic flow around cylindrical body at rest. The overall method has been extended to two-way coupling and illustrations have been shown.

Conclusion Générale

Conclusion des travaux

Cette thèse apporte quelques contributions et voies d'amélioration sur la modélisation et la simulation numérique d'écoulements diphasiques compressibles dans les régimes denses et dilués en particules.

Dans le Chapitre I un nouveau modèle diphasique, hyperbolique dégénéré et thermodynamiquement consistant a été construit. Implémenté dans le cadre d'une méthode numérique robuste, il est capable de résoudre des configurations d'écoulements similaires au modèle de Baer & Nunziato (1986), c'est-à-dire des problèmes d'interfaces entre des fluides purs ou encore dans des mélanges multiphasiques hors d'équilibre.

La nouveauté repose sur la reconsidération de l'équation sur la fraction volumique. Celle-ci provoque des conséquences majeures sur la propagation acoustique, qui semble plus physique par rapport à la topologie de l'écoulement.

Dans le Chapitre II, Un solveur de Riemann avec reconstruction interne des états (RSIR) a été construit, basé sur la méthode de Linde (2002).

D'abord développé et amélioré dans le cadre des équations d'Euler, ce solveur montre une robustesse et des résultats similaires à HLLC. Cette méthode a été étendue au modèle diphasique dense – dilué hors d'équilibre développé dans le Chapitre I. Ce nouveau modèle pose de sérieuses difficultés pour la recherche d'un solveur de Riemann. Ce système est hyperbolique dégénéré et n'est valide que dans le cadre de la relaxation raide des pressions, rendant les solutions non-autosimilaires. Grâce à l'approche avec reconstruction interne, un solveur de Riemann faiblement diffusif a été développé. Il a été validé à l'aide de comparaisons avec d'autres solveurs de Riemann, plus diffusifs. Cette nouvelle méthode numérique, RSIR, a été utilisée pour résoudre une situation complexe d'instabilité de jets de particules solide dans un milieu granulaire et a montré une explication plausible du processus de formation de ces instabilités ou jets de particules.

Un travail supplémentaire sur ce nouveau modèle est cependant nécessaire pour atteindre une compréhension totale de ces phénomènes d'instabilités lors de l'explosion d'une charge entourée de particules.

Concernant le solveur RSIR qui a été développé, il semble approprié pour beaucoup d'applications et systèmes hyperboliques où la physique du phénomène observé est gouvernée par les deux ondes extrêmes et l'onde intermédiaire. De plus, un paramètre est présent dans la formulation afin de contrôler la diffusion numérique du solveur de Riemann. Tous les calculs utilisant ce solveur dans cette thèse ont été réalisés avec $\beta=1$, correspondant au minimum de diffusion de la méthode, sans problème de robustesse.

Dans le Chapitre III on s'est intéressé à l'écoulement multidimensionnel qui se développe autour de quelques particules discrètes. Une méthode de type Level-Set a été développée dans le but de décrire la translation de solides indéformables sur un maillage non-structuré fixe. Grâce à l'utilisation du limiteur de pente Overbee développé par Chiapolino et al. (2017b) cette méthode ne nécessite pas d'étape de réinitialisation ou de reconstruction d'interface. Ainsi, une méthode simple de couplage solide/fluide a été construite et vérifiée à l'aide de comparaisons avec d'autres approches : basée sur une relaxation raide des vitesses, ou encore basée sur l'extrapolation Ghost-Cell. Cette approche, simple à développer permet une amélioration de la convergence de la méthode à l'aide de considérations également simples.

La méthode a été ensuite étendue en 2D et a été validée à l'aide de comparaisons dans le cadre d'un écoulement supersonique autour d'un objet cylindrique immobile. La méthode la plus précise a été ensuite étendue au cas du couplage fort, utilisé pour observer la mise en mouvement de plusieurs particules solides par onde de choc et la formation d'amas de particules.

Perspectives

Les travaux réalisés durant cette thèse représentent une piste de réflexion pour la modélisation et la simulation d'écoulements denses et dilués. Cependant, certains points restent à traiter afin de parfaire la modélisation et la résolution de ces écoulements. Quatre perspectives principales se dégagent de la présente étude :

- Le nouveau modèle est capable de considérer une gamme plus grande de fractions volumique que les modèles de Baer & Nunziato (1986) ou Marble . Cela représente déjà une amélioration des modèles existants notamment en termes de propagation d'ondes de pression. Cependant, une faiblesse apparait dans la limite des écoulements compacts ou stratifiés. En effet, la nouvelle équation conservative sur la fraction volumique devrait tendre vers l'équation de transport sur la fraction volumique du modèle de Baer & Nunziato (1986). Ce point reste à étudier afin de construire un modèle susceptible de traiter toutes les configurations de fractions volumiques.
- A l'aide du nouveau solveur de Riemann avec reconstruction interne (RSIR), la méthode numérique est capable de préserver des discontinuités immobiles. Cependant, ce solveur de Riemann n'a été développé seulement que dans le cadre du modèle où la phase 1 est diluée et la phase 2 est continue. Cette méthode numérique doit être étendue au « modèle global », c'est-à-dire au modèle pouvant considérer la phase 1 comme diluée ou continue. Ce travail demande une attention particulière car le modèle global contient une équation non conservative supplémentaire.
- Dans certaines applications il est nécessaire de considérer un nombre arbitraire de constituants, ou phases. Le modèle et la méthode RSIR nécessitent alors des extensions non-triviales.
- L'étude fine du mécanisme de formation de jets de particules reste à réaliser. Il a été attribué ici aux termes non-conservatifs des équations du mouvement mais une étude plus détaillée s'impose.

Entre autres, ces perspectives encouragent à poursuivre les études sur la modélisation des écoulements diphasiques denses et dilués afin d'analyser et de comprendre la physique mise en jeu dans ces situations.

References

Abgrall, R. & Saurel, R. (2003) Discrete equations for physical and numerical compressible multiphase mixtures. *Journal of Computational Physics*, 186(2), 361-396

Abgrall, R., Beaugendre, H., & Dobrzynski, C. (2014) An immersed boundary method using unstructured anisotropic mesh adaptation combined with level-sets and penalization techniques. *Journal of Computational Physics*, 257, 83-101

Allaire, G., Clerc, S. & Kokh, S. (2002) A five-equation model for the simulation of the interfaces beween compressible fluids. *Journal of Compuational Physics*, 181(2), 577-616

Ambroso, A., Chalons, C. & Raviart, P.A. (2012) A Godunov-type method for the seven-equation model of compressible two-phase flow. *Computers & Fluids*, 54, 67-91

Anderson, T.B. & Jackson, R. (1967) Fluid mechanical description of fluidized beds. Equation of motion. *Industrial & Engineering Chemistry Fundamentals*, 6(4), 527-539

Baer, M. & Nunziato, J.W. (1986) A two-phase mixture theory for the deflagration-to-detonation transition (DDT) in reactive granular materials. *Internation Journal of Multiphase Flow*, 12(6), 861-889

Balsara, D. (2012) A two-dimensinal HLLC Riemann solver for conservation laws: Application to Euler and magnetohydrodynamic flos. *Journal of Computational Physcis,* 231(22), 7476-7503

Barral, N. & Alauzet, F. (2018) Three-dimensional CFD simulations with large displacement of the geometries using a connectivity-change moving mesh approach. . *Engineering with Computers*, 1-26

Barth, T. & Jespersen, D. (1989) The disgn and application of upwind schemes on unnstructured meshes. *In 27th Aerospace sciences meeting*, 366

Baum, J., Luo, H. & Loehner, R. (1994) A new ALE adaptative unstructured methodology for the simulation of the moving bodies. *In 32nd Aerospace Sciences Meeting and Exhibit*, 414

Bdzil, J.B., Menikoff, R., Son, S.F., Kapila, A.K. & Stewart, D.S. (1999) Two-phase modeling of deflagration-to-detonation transition in granular materials: A critical examination of modeling issues. *Physics of Fluids*, 11(2), 378-402

Berger, M.J. & Colella, P. (1989). Local adaptative mesh refinement for shock hydrodynamics. *Journal of Computational Phsycis*, 82(1), 64-84

Bernecker, R.R. & Price, D. (1974) Studies in the transition from deflagration to detonation in granular explosives-II. Transitional characteristics and mechanisms observed in 91/9 RDX/Wax. *Combustion and Flame*, 22(1), 119-129

Bouchut, F., Jin, S. & Li X. (2003) Numerical approximations of pressureless and isothermal gas dynamics. . *SIAM Journal on Numerical Analysis*, 41(1), 135-158

Brackbill, J.U., Kothe, D.B. & Zemach, C. (1992) A continuum method for modeling surface tension. *Journal of Computational Physics*, 100(2), 335-354

Carmouze, Q., Fraysse, F., Saurel, R. & Nkonga, B. (2018) Coupling rigid bodies motion with single phase and two-phase compressible flows on unstructured meshes. *Journal of Computational Physics*, 375, 1314-1338

Chiapolino, A. & Saurel, R. (2018) Extended Noble-Able-Stiffened-Gas equation of state for sub-and-supercritical liquid-gas systems far from the critical point. *Fluids*, 3(3):48

Chiapolino, A., Boivin, P. & Saurel, R. (2017a) A simple and fast phase transition relaxation solver for compressible multicomponent two-phase flows. *Computers and Fluids*, 150, 31-45

Chiapolino, A., Saurel, R. & Nkonga, B. (2017b) Sharpening diffuse interfaces with compressible fluids on unstrutured meshes. *Journal of Computational Physics*, 340,389-417

Chinnayya, A., Daniel, E. & Saurel, R. (2004). Modeling detonation waves in heterogeneous energetic materials. *Journal of Computational Physics*, 196(2), 490-538

Clift, R. & Gauvin, W.H. (1971). Motion of entrained particles in gas stream. *The Canadian Journal of Chemical Engineering*, 49(4), 439-448

Davis, S. (1988). Simplified second-order Godunov-type methods. *SIAM Journal on Scientific and Statistical Computing,* 9(3), 445-473

Deledicque, V. & Papalexandris, M.V. (2007) An exact Riemann solver for compressible two-phase flow models containing non-conservative products. *Journal of Computational Physics*, 222(1), 217-245

Delhaye, J.M. & Achard, J.L. (1976) On the averaging operators introduced in two-phase flow modeling. *In Proceedings CSNI Specialist Meeting in transient two-phase flow*, 1, 5-84

Drew, D.A. & Passman, S.L. (2006) Theory of multicomponent fluids. *Springer Science & Business Media*, 135

Ergun, S. (1952) Fluid flow through packed columns. *Chemical Engineering Progress*, 48, 89-94

Farhat, C., Gerbeau, J.F. & Rallu, A. (2012) FIVER: A finite volume method based on exact two-phase Riemann problems and sparse grids for multi-material flows with large density jumps. *Journal of Computational Physics*, 231(19), 6360-6379

Farhat, C., Lesoinne, M., LeTallec, P., Pierson, K. & Rixen, D. (2001) FETI-DP: a dual-primal unified FETI method - parti I: A faster alternative to the two-level FETI method. *International Journal for Numerical Methods in Engineering*, 50(7), 1523-1544

Farhat, C., Rallu, A. & Shankaran, S. (2008) A higher-order generalized ghost fluid method for the poor for the three-dimensional two-phase flow computation of underwater implosion. *Journal of Computational Physics*, 227(16), 7674-7700

Fedkiw, R.P., Aslam, T., Merriman, B. & Osher, S. (1999) A non-oscillatory Eulerian approach to interfaces in multimaterial flows (the Ghost Fluid method). *Journal of Computational Physics*, 152(2), 457-492

Forestier, A. & Le Floch, P. (1992) Multivalued solutions to some non-linear and non-strictly hyperbolic systems. *Japan Journal of Industrial and Applied Mathematics*, 9(1), 1

Frost. (2010) Jet formation during explosive particle dispersal. *Proceedings of the 21st International Symposium on Military Aspects of Blast and Shocks, Jerusalem, October 3-4*

Furfaro, D. & Saurel, R. (2015) A simple HLLC-type Riemann solver for compressible non-equilibrium two-phase flows. *Computers & Fluids*, 111, 159-178

Gavrilyuk, S. & Saurel, R. (2002) Mathematical and numerical modeling of two-phase compressible flows with micro-inertia. *Journal of Computational Physics*, 175(1), 326-360

Ghidaglia, J.M., Kumbaro, A. & Le Coq, G. (2001) On the numerical solution to two fluid models via cell centered finite volume method. *European Journal of Mechanics-B/Fluids*, 20(6), 841-867

Glimm, J., Grove, J., Li, X., Zeng, Y. & Zhang, Q. (1998) Three-dimensional front tracking. *SIAM Journal of Scientific Computing.*, 19, 703-27

Godunov, S. (1959) A difference method for numerical calculation of discontinuous solution of the equation of hydrodynamics. *Matematicheskii Sbomik*, 89(3), 271-306

Godunov, S. (2008) On approximations for overdetermined hyperbolic equations. *In Hyperbolic Problems: Theory, Numerics, Appplications*, 19-33

Houim, R.W. & Oran, E.S. (2016) A multiphase model for compressible granular-gaseous flows: formulation and initial tests. *Journal of Fluid Mechanics*, 789, 166-220

Kapila, A.K., Menikoff, R., Bdzil, J.B., Son, S.F. & Stewart, D.S. (2001) Two-phase modeling of deflagration-to-detonation transition in granular materials: reduced equation. *Physics of Fluids*, 13(10), 3002-3024

Lallemand, M.H. & Saurel, R. (2000) Pressure relaxation procedures for multiphase compressible flows. *INRIA Report*

Le Martelot, S., Saurel, R. & Nkonga, B. (2014) Towards the direct numerical simulation of nucleate boiling flows. *International of Multiphase Flow*, 66, 62-78

Le Métayer, O. & Saurel, R. (2016) The Noble-Abel stiffened-gas equation of state. *Physics of Fluids*, 28(4), 046102

Le Métayer, O., Massoni, J. & Saurel, R. (2004) Elaboration des lois d'état d'un liquide et de sa vapeur pour les modèles d'écoulements diphasiques. *International Journal of Thermal Sciences*, 43(3), 265-276

Lhuillier, D., Change, C.H. & Theofanous, T.G. (2013) On the quest for a hyperbolic effective-field model of disperse flows. *Journal of Fluid Mechanics*, 731, 184-194

Li, S. (2005) An HLLC Riemann solver for magneto-hydrodynamics. *Journal of Computational Physics*, 203(1), 344-357

Linde, T. (2002) A practical, general-purpose, two-state HLL Riemann solver for hyperbolic conservation laws. *International Journal for Numerical Methods in Fluids*, 40(3-4), 391-402

Liu, T.G., Ho, J.Y., Khoo, B.C. & Chowdhury, A.W. (2008) Numerical simulation of fluid structure interaction using modified ghost fluid method and Naviers equations. *Journal of Scientific Computing*, 36(1), 45-68

Liu, T.G., Khoo, B.C. & Xie, W.F. (2006) The modified ghost fluid method as applied to extreme fluid-structure interaction in the presence of cavitation. . *Communications in Compuational Physics*, 1(5), 898-919

Liu, T.G., Khoo, B.C. & Yeo, K.S. (2003) Ghost fluid method for strong shock impacting on material interface. *Journal of Compuationel Physics.*, 190(2), 651-681

Marble, F. (1963) Dynamics of a gas containing small solid particles. *Combustion and Propulsion (5th AGARD Colloquium), Pergamon Press*, 175

Massoni, J., Saurel, R., Nkonga, B. & Abgrall, R. (2002) Proposition de méthodes et modèles eulériens pour les problèmes à interfaces entre fluides compressibles en présence de transfert de chaleur: some models and Eulerian methods for interface problems between compressible fluids with heat transfer. *Internation Journal of Heat and Mass Transfer*, 45(6), 1287-1307

McGrath, T., Clair, J.S. & Balachandar, S. (2018) Modeling compressible multiphase flows with dispersed particules in both dense and dilute regimes. *Shock Waves*, 28(3), 533-544

Milne, A., Parrish, C. & Worland, I. (2010) Dynamic fragmentation of blast mitigants. *Shock Waves*, 20, 41-51

Miyoshi, T. & Kusano, K. (2005) A multi-state HLL approximate Riemann solver for ideal magnetohydrodynamics. *Journal of Computational Physics*, 208(1), 315-344

Muralidharan, B. & Menon, S. (2018) Simulation of moving boundaries interacting with compressible reacting flows using a second-order adaptative Cartesian cut-cell method. *Journal of Computational Physics*, 357, 230-262

Nkonga, B. & Guillard, H. (1994) Godunov type method on non-structured meshes for three-dimensional moving boundary problems. *Computer Methods in Applied Mechanics and Engineering*, 113(1-2), 183-204

Nkonga, B. (2000) On the conservative and accurate CFD approximations for moving meshes and moving boundaries. *Computer Methods in Applied Mechanics and Engineering*, 190(13-14), 1801-1825

Olsson, E. Kreiss, G. & Zahedi, S. (2007) A conservative level set method for two phase flow II. *Journal of Computational Physics*, 225, 785-807

Osnes, A.N., Vartdal, M. & Reif, B.P. (2018) Numerical simulation of particle jet formation induced by shock wave acceleration in a Hele-Shaw cell. *Shock Waves*, 28(3), 451-461

Parrish, C. & Worland, I. (2010) Dynamic jet formation from mitigation materials. *Proceeding of the 21st International Symposium on Military Aspects of Blast and Shocks, Jerusalem, October 3-4*

Perigaud, G. & Saurel, R. (2005) A compressible flow model with capillary effects. *Journal of Compuational Physics*, 209(1), 139-178

Petitpas, F., Saurel, R., Franquet, E. & Chinnayya, A. (2009) Modelling detonation waves in condensed energetic materials: Multiphase CJ conditions and multidimensional compuations. *Shock Waves*, 19(5), 377-401

Rodriguez, V., Saurel, R., Jourdan, G. & Houas, L. (2013) Solid-particle jet formation under shock-wave acceleration. *Physical Review E*, 88(6), 063011

Romenski, E. & Toro, E.F. (2004) Compressible two-phase flows: two-pressure models and numerical methods. *Computational Fluid Dynamics J*, 13, 403-416

Rossi, T. L. (2019) Détermination de la caractérisation "chef" en milieu scientifique. *Journal des Pébrons*, 0-1.5

Rusanov, V. (1962) The calculation of the interaction of non-stationary shock waves and obstacles. *USSR Computational Mathematics and Mathematical Physics*, 1(2), 304-320

Saurel, R. & Abgrall, R. (1999) A multiphase Godunov method for compressible multifluid and multiphase flows. *Journal of Compuational Physics*, 150(2), 425-467

Saurel, R. & Pantano-Rubio, C. (2018) Diffuse interface capturing methods for compressible two-phase flow. *Annual Review of Fluid Mechanics*, 50(1), 105-130

Saurel, R., Boivin, P. & Le Métayer, O. (2016) A general formulation for caviting, boiling and evaporating flows. *Computers & Fluids*, 128, 53-64

Saurel, R., Chinnayya, A. & Carmouze, Q. (2017a) Modeling compressible dense and dilute two-phase flows. *Physics of Fluids*, 29(6), 063301

Saurel, R., Daniel, E. & Loraud, J.C. (1994) Two-phase flows-second-order schemes and boundary conditions. *AIAA Journal*, 32(6), 1214-1221

Saurel, R., Favrie, N., Petitpas, F., Lallemand, M.H. & Gavrilyuk, S. (2010) Modelling dynamic and irreversible powder compaction. *Journal of Fluid Mechanics*, 664, 348-396

Saurel, R., Franquet, E., Daniel, E. & Le Métayer, O. (2007) A relaxation-projection method for compressible flows. Part I: The numerical equation of state for the Euler equations. *Journal of Computational Physics*, 223(2), 822-845

Saurel, R., Fraysse, F., Furfaro, D. & Lapebie, E. (2017b) Multiscale multiphase modeling of detonations in condensed energetic materials. *Computers & Fluids*, 159, 95-111

Saurel, R., Gavrilyuk, S. & Renaud, F. (2003) A multiphase model with internal degrees of freedom: Application to shock-bubble interaction. *Journal of Fluid Mechanics*, 495, 283-321

Saurel, R., Le Martelot, S., Tosello, R. & Lapebie, E. (2014) Symmetric model of compressible granular mixtures with permeable interfaces. *Physics of Fluids*, 26(12), 123304

Schwendeman, D.W., Wahle, C.W. & Kapila, A.K. (2006) The Riemann problem and a high-resolution Godunov method for a model of compressible two-phase flow. *Journal of Computational Physics*, 212(2), 490-526

Shewchuk, J. (2002) Delaunay refinement algorithms for triangular mesh generation. *Computational Geometry*, 22(1-3), 21-74

Shukla, R.K., Pantano-Rubio, C. & Freund, J.B. (2010) An interface capturing method for the simulation of multi-phase compressible flows. *Journal of Computational Physics*, 229, 7411-39

Sweby, P. (1984) High resolution schemes using flux limiters for hyperbolic conservation laws. *SIAM Journal on Numerical Analysis*, 21(5), 995-1011

Toro, E. (2009) *Riemann solvers and numerical methods for fluid dynamics. A practical introduction. Third edition.* Springer-Verlag, Berlin Heidelberg

Toro, E.F., Spruce, M. & Speares, W. (1994) Restoration of the contact surface in the HLL-Riemann solver. *Shock Waves*, 4(1), 25-34

Van Leer, B. (1979) Towards the ultimate conservative difference scheme. V. A second-order sequel to Godunov's method. *Journal of Computational Physics*, 32(1), 101-136

Wang, C.W., Liu, T.G. & Khoo, B.C. (2006) A real ghost fluid method for the simulationof multimedium compressible flow. *SIAM Journal on Scientific Computing*, 28(1), 278-302

Wang, K., Rallu, A., Gerbeau, J.F. & Farhat, C. (2011) Algorithms for interface treatment and load computation in embedded boundary methods for fluid and fluid-structure interaction problems. *International Journal for Numerical Methods in Fluids*, 67(9), 1175-1206

Wood, A. (1930) A Textbook of Sound. *G. Bell and Sons Ltd., London*

Woodward, P. & Colella, P. (1984) The Numerical Simulation of Two-Dimensional Fluid with Strong Shocks. *Journal of Computational Physics,* 54, 115-173

Xue, K., Du, K., Shi, X., Gan, Y. & Bai, C. (2018) Dual hierarchical particle jetting of a particle ring undergoing radial explosion. *Soft Matter*, 14, 4422

Youngs, D. (1984) An interface tracking method for a 3D Eulerian hydrodynamics code. *Atomic Weapons Research Establishment (AWRE) Technical Report* , (44/92), 35

Zalesak, S. (1979) Fully multidimensional flux-corrected transport algorithms for fluids. *Journal of Computational Physics*, 31(3), 335-362

Zeldovich, Y. (1970) Gravitational instability: An approximate theory for large density perturbations. *Astronomy and Astrophysics*, 5, 84-89

Zeng, X. & Farhat, C. (2012) A systematic approach for constructing higher-order immersed boundary and ghost fluid methods for fluid-structure interaction problems. *Journal of Computational Physics*, 231(7), 2892-2923

Zhang, F., Frost, D.L., Thibault, P.A. & Murray, S.B. (2001) Explosive dispersal of solid particles. *Shock Waves*, 10, 431-443